

**Doctoral Dissertation (Shinshu University)**

**Carbon Materials Supported Metal Nanostructures for Efficient  
Catalytic Organic Transformations**

**March 2014**

**MAYAKRISHNAN GOPIRAMAN**

**Interdisciplinary Graduate School of Science and Technology**

**Shinshu University**

**This Thesis Is Dedicated To My Parents  
For Their Endless Support, Love  
And Encouragement**

## **BONAFIDE CERTIFICATE**

This is to certify that the thesis entitled “**Carbon Materials Supported Metal Nanostructures for Efficient Catalytic Organic Transformations**” is a bonafide record of the work done by

**MAYAKRISHNAN GOPIRAMAN (11ST107J)**

in partial fulfillment of the requirements for the award of the degree of **Doctor of Philosophy in Chemistry** of the **SHINSHU UNIVERSITY, UEDA CAMPAUS, JAPAN**, during the year 2011-2014.

**Prof. Dr. Ick Soo Kim**  
**(Guide)**

Thesis viva-voce held on 29-01-2014

**Japanese Examiner**

**External Examiner**

## THESIS CERTIFICATE

This is to certify that the thesis entitled “**Carbon Materials Supported Metal Nanostructures for Efficient Catalytic Organic Transformations**” submitted by **MAYAKRISHNAN GOPIRAMAN** to the **SHINSHU UNIVERSITY, UEDA CAMPAUS, JAPAN** for the award of the degree of **Doctor of Philosophy** is a bonafide record of research work carried out by him under my supervision. The contents of this thesis, in full or in parts, have not been submitted to any other Institute or University for the award of any degree or diploma.

Ueda – 620015, Japan

Date: 29-01-2014

**Prof. Dr. Ick Soo Kim**

Guide

Associate Professor

## ABSTARCT

### **Carbon Materials Supported Metal Nanostructures for Efficient Catalytic Organic Transformations**

My research is focused on two main objectives, the preparation and characterization of carbon materials (CMs) supported metal nanostructures (MNSs), and apply them to catalyze various organic transformations.

A very simple and cost-efficient “dry synthesis” method has been used to decorate the MNSs over CMs. Copper oxide nanoparticles (CuONPs) have been successfully decorated on multi-wall carbon nanotubes (MWCNTs) using copper acetate precursor, and was used as a heterogeneous nanocatalyst (CuO/MWCNT) for the *N*-arylation of imidazole. In the same way, ultrafine ruthenium dioxide nanoparticles (RuO<sub>2</sub>NPs) with mean diameter of 0.9 nm have been decorated on single-walled carbon nanotubes (SWCNTs), and used as a nanocatalyst (RuO<sub>2</sub>/SWCNT) for the Heck-type olefination of aryl halides under mild reaction conditions. For the transfer hydrogenation of aromatic aldehydes and ketones, graphene nanoplatelets (GNPs) supported ruthenium oxide nanorods (RuNRs) catalyst was found to be an effective and reusable heterogeneous catalyst. Alike, ruthenium nanoparticles (RuNPs) have been decorated on graphene nanosheets (GNS), and the resultant material has been used as a nanocatalyst (GNS-RuNPs) for the aerial oxidation of alcohols. It was found that, RuO<sub>2</sub>NPs anchored GNPs catalyst (GNP-RuO<sub>2</sub>NPs) is highly efficient for the *N*-oxidation of tertiary amines. Before going for the catalytic applications, all the prepared nanocatalysts are characterized in

detail by various microscopic and spectroscopic techniques. The morphology and particles size of the metal nanostructures (MNSs) have been investigated by HR-TEM and TEM techniques. SEM-EDX and ICP-MS are taken to determine the factual weight percentage of the metals loaded in nanocatalysts. Raman spectroscopy has been recorded to study the nature of interaction between MNSs and CMs. Chemical states of the MNSs in nanocatalysts have been identified by XPS and XRD techniques. In all the catalytic systems, initially, reaction condition is optimized and then the substrate scope of the catalytic system has been extended. Chemoselectivity, regioselectivity, heterogeneity and reusability tests have been performed. GC is recorded to calculate the conversion and selectivity of the reactants and products, respectively. Catalytic products have been analyzed by  $^1\text{H}$  and  $^{13}\text{C}$  NMR, FT-IR and Mass spectra. In order to reveal the physical as well as chemical stability, after the completion of catalytic reactions, the nanocatalysts are separated out from the reaction mixture and analyzed by TEM, XRD, Raman and SEM-EDS. Here, it is worth mentioning that, after the catalytic reactions, MWCNTs and GNPs supporters have been successfully recovered from the used nanocatalysts (*u*-CuO/MWCNT or *u*-GNPs-RuNRs) and confirmed by TEM, Raman and WAXD.

Keywords: CuO/MWCNT; RuO<sub>2</sub>/SWCNT; GNPs-RuNRs; GNS-RuNPs; GNP-RuO<sub>2</sub>NPs; *N*-Arylation; Heck-Type Olefination; Transfer Hydrogenation; Aerial Oxidation; *N*-Oxidation.

## ACKNOWLEDGEMENTS

All praises and thanks are to **SARADA DEVI**, the Lord and the most merciful, for helping me to complete this work. I would like to express my sincere gratitude to my advisor, **Prof. Dr. Ick Soo Kim** for his encouragement, kind support, enthusiastic attention, critical discussions, valuable advice and guidance. Also, I would like to express my sincere gratitude to **Prof. Dr. R. Karvembu**, Department of Chemistry, NIT-Trichy, for his encouragement, kind support, enthusiastic attention, critical discussions, valuable advice and guidance. My special acknowledgement is to Prof. Dr. Byoung Suhk Kim and Dr. Kai Wei, for their valuable suggestions and kind help during my research.

I deserve my special thanks to Mr. Kazushige Fujimori for his great assistance that really made my life very easy in Japan. Also I would like to extend my special thanks to Mr. Matsui Takushi and Mr. Mori Yuuki for their kind support and help in handling instrumentations.

I gratefully acknowledge the support of Global COE program by the Ministry of Education, Culture, Sports, Science, and Technology, Japan that made my work possible. Especially, my sincere thanks are to Professor Toshihiro Hirai, Professor Koji Abe and Ms. Naoko Suguta for their kind support.

I would like to express my sincere thanks to Dr. Zeeshan Kathir, Dr. Watanabe Kei, Mr. Naotaka Kimura, Ms. Gu Jalam, Mr. Bang Hyun-Sik, Ms. Akada Yaeko, Mr. Nakajima Youtarou, Mr. Matsui Takushi, Mr. Mori Yuuki, Mr. Saito Hiroki, Mr. Sato Ko, Mr. Suzuki Kota, Mr. Ishihaha Yutaro and Mr. Seki Hiromiti for their help and kind

support. Also, my thanks are to my past lab members Ms. Yujin Lee, Mr. Nakamura Taiki, Mr. Nakasima Ryu, Mr. Satou Hidekazu for their help and kind support.

I wish to give my special thanks to one of my best friends, Senior Assistant Professor Dr. D. Kesavan, for his very special care, help, kind support and constant encouragement during my research. Also, my special thanks to Mr. K. Karthikeyan, Mr. S. Senthil Selvam and Mr. G. Ayyannan for their constant support and understanding.

I would like to say my very special thanks to Dr. S. Ganesh Babu for his help, valuable advices, encouragement and support. Also I thank Dr. M. Saravana Kumar, Dr. S. L. Ashok Kumar, Mr. R. Tamilarasan, Mr. S. Saravanamorthy and Mr. M. Muneeswaran for their help and encouragement. My deep gratitude is to my all seniors, friends and juniors for their constant encouragement.

My special thanks to my friends, Mr. V. Ashok Kumar, Mr. K. Arun, Mr. V. Ramkumar, Mr. P. Iniyavan, Mr. S. Vivekananthan, Mr. K.P. Annamalai, Ms. P. Aruna Priyadarsini, Ms. N. Bhuvanewari, Ms. S. Priyadarsini and Ms. S. Suganya for their encouragement and constant support.

I can't forget to praise my mother and father, who gave me the vision to pursue for higher studies and provided a ground to succeed in my life; it's more than the words of acknowledgement. Also I would like to give my very special thanks to my sisters and brother for their deep love, real care and encouragement at all times.

Mayakarishnan Gopiraman  
Shinshu University  
March 2014

# TABLE OF CONTENTS

	Title	Page no.
	<b>ABSTRACT</b> .....	v
	<b>ACKNOWLEDGEMENTS</b> .....	vii
	<b>TABLE OF CONTENTS</b> .....	ix
	<b>LIST OF TABLES</b> .....	xiv
	<b>LIST OF FIGURES</b> .....	xv
	<b>LIST OF SCHEMES</b> .....	xx
	<b>ABBREVIATIONS</b> .....	xxi
	<b>NOTATIONS</b> .....	xxiii
<b>CHAPTER 1</b>	<b>Introduction</b>	
1.1	Background.....	2
1.2	Role of carbon materials as supports in heterogeneous catalysis.....	3
1.3	Dry synthesis of CMs supported MNPs catalysts.....	4
1.4	Literature survey.....	4
1.5	Objectives.....	7
<b>CHAPTER 2</b>	<b>An efficient, reusable copper-oxide/carbon-nanotube catalyst for <i>N</i>-arylation of imidazole</b>	
2.1	Introduction.....	14
2.2	Experimental section.....	16
2.2.1	Materials and characterization.....	16
2.2.2	Preparation of nanocatalyst (CuO/MWCNT).....	17
2.2.3	<i>N</i> -Arylation of imidazole with aryl halides.....	19
2.2.4	Product analysis.....	19
2.2.5	Recovery of MWCNTs from the used nanocatalyst.....	20
2.3	Results and discussion.....	20
2.3.1	Characterization of CuO/MWCNT.....	20

2.3.2	Optimization of reaction conditions.....	29
2.3.3	Extension of scope.....	31
2.3.4	Effect of particle size on catalytic efficiency.....	33
2.3.5	Heterogeneous nature of CuO/MWCNT.....	36
2.3.6	Reusability of CuO/MWCNT.....	36
2.3.7	Recovery of MWCNTs from the used nanocatalyst.....	39
2.3.8	Proposed catalytic mechanism.....	40
2.4	Conclusions.....	42

**CHAPTER 3**      **Highly active, selective and reusable RuO<sub>2</sub>/SWCNT catalyst for Heck olefination of aryl halides**

3.1	Introduction.....	51
3.2	Experimental section.....	53
3.2.1	Materials and characterization.....	53
3.2.2	Dry synthesis of RuO <sub>2</sub> /SWCNT.....	54
3.2.3	Procedure for Heck olefination reaction.....	55
3.2.4	Product analysis.....	56
3.3	Results and discussion.....	56
3.3.1	Characterization of RuO <sub>2</sub> /SWCNT.....	56
3.3.2	Screening for optimal reaction conditions.....	61
3.3.3	Substrate scope.....	63
3.3.4	Regioselectivity.....	67
3.3.5	Chemoselectivity.....	67
3.3.6	Heterogeneity, reusability and stability of RuO <sub>2</sub> /SWCNT.....	68
3.3.7	Proposed mechanism.....	70
3.4	Conclusions.....	72

**CHAPTER 4**      **Facile and homogeneous decoration of RuO<sub>2</sub> nanorods on graphene nanoplatelets for transfer hydrogenation of carbonyl compounds**

4.1	Introduction.....	78
4.2	Experimental section.....	80
4.2.1	Materials and characterization.....	80
4.2.2	Typical procedure of oxidation of GNPs.....	81
4.2.3	Preparation of nanocatalyst.....	81
4.2.4	Transfer hydrogenation of carbonyl compounds.....	82
4.2.5	Typical procedure for reusability of GNPs-RuNRs.....	82
4.2.6	Typical procedure for recovery of GNPs.....	83
4.2.7	Product confirmation and analysis.....	83
4.3	Results and discussion.....	84
4.3.1	Characterization of GNPs-RuNRs.....	84
4.3.2	Optimization of reaction conditions.....	87
4.3.3	Extension of scope.....	88
4.3.4	Chemoselectivity of GNPs-RuNRs.....	93
4.3.5	Heterogeneity and reusability of GNPs-RuNRs.....	94
4.3.6	Proposed mechanism.....	97
4.4	Conclusions.....	100

**CHAPTER 5**      **Dry synthesis of easily tunable nano ruthenium supported on graphene – novel nanocatalysts for aerial oxidation of alcohols and transfer hydrogenation of ketones**

5.1	Introduction.....	106
5.2	Experimental section.....	108
5.2.1	Materials and characterization.....	108
5.2.2	Dry synthesis of nanocatalyst (GNS-RuNPs).....	110
5.2.3	Aerial oxidation of alcohols.....	111
5.2.4	Transfer hydrogenation of ketones.....	112

5.3	Results and discussion.....	112
5.3.1	Characterization of GNS-RuNPs.....	112
5.3.2	Optimization of reaction conditions for the oxidation of alcohols.....	122
5.3.3	Extension of scope.....	124
5.3.4	Chemoselective nature of GNS-RuNPs.....	128
5.3.5	Heterogeneity of GNS-RuNPs.....	130
5.3.6	Reusability of GNS-RuNPs.....	131
5.3.7	Effect of particle size on catalytic activity.....	132
5.3.8	Proposed mechanism.....	135
5.3.9	Versatility of GNS-RuNPs.....	137
5.3.9.1	Preparation and Characterization of <i>u</i> -GNS- RuO <sub>2</sub> NRs.....	137
5.3.9.1	Transfer hydrogenation of ketones catalyzed by <i>u</i> - GNS-RuO <sub>2</sub> NRs.....	139
5.4	Conclusions.....	140

**CHAPTER 6      Catalytic *N*-oxidation of tertiary amines on RuO<sub>2</sub>NPs anchored  
graphene nanoplatelets**

6.1	Introduction.....	155
6.2	Experimental section.....	157
6.2.1	Materials and characterization.....	157
6.2.2	Dry synthesis of nanocatalyst (GNP-RuO <sub>2</sub> NPs).....	158
6.2.3	Oxidation of tertiary amines.....	159
6.3	Results and discussion.....	161
6.3.1	Characterization of GNP-RuO <sub>2</sub> NPs.....	161
6.3.2	Optimization of reaction conditions.....	168
6.3.3	Extension of scope.....	169
6.3.4	Heterogeneity and reusability of GNP-RuO <sub>2</sub> NPs.....	173
6.3.5	Proposed mechanism.....	174

6.4	Conclusions.....	175
<b>CHAPTER 7 Conclusions</b>		
7.1	Conclusions.....	183
	<b>Accomplishments.....</b>	<b>187</b>

## LIST OF TABLES

Table No.	Title	Page No.
2.1	Optimization of reaction conditions for the CuO/MWCNT catalyzed <i>N</i> -arylation of imidazole (1a) with 4-chlorobenzonitrile (1b) to obtain <i>N</i> -arylated imidazole (1c) <sup>a</sup> .....	30
2.2	CuO/MWCNT catalyzed <i>N</i> -arylation of imidazole with various aryl halides <sup>a</sup> .....	32
2.3	Catalytic activity of CuO/MWCNT (having 10-26 nm CuONPs) and CuO/MWCNT (having 60-80 nm CuONPs) on <i>N</i> -arylation of imidazole with various aryl halides <sup>a</sup> .....	35
3.1	Screening for optimal reaction conditions <sup>a</sup> .....	62
3.2	Substrate scope of the RuO <sub>2</sub> /SWCNT-catalyzed Heck-type olefination of aryl halides <sup>a</sup> .....	65
4.1	Transfer hydrogenation of carbonyl compounds catalyzed by GNPs-RuNRs <sup>a</sup> .....	89
4.2	Selective transfer hydrogenation of carbonyl compounds catalyzed by GNPs-RuNRs <sup>a</sup> .....	92
5.1	Optimization of the reaction conditions for oxidation of 1-phenylethanol <sup>a</sup> .....	123
5.2	Oxidation of alcohols <sup>a</sup> .....	125
5.3	Oxidation of alcohols using GNS-RuNPs having 10-20 nm RuNPs <sup>a</sup> .....	135
5.4	Transfer hydrogenation of ketones catalyzed by <i>u</i> -GNPs-RuO <sub>2</sub> NRs <sup>a</sup> .....	140
6.1	<i>N</i> -oxidation of tertiary amines catalyzed by GNP-RuO <sub>2</sub> NPs <sup>a</sup> .....	170

## LIST OF FIGURES

Figure No.	Title	Page No.
2.1	Schematic illustration for the preparation of CuO/MWCNT.....	18
2.2	TEM images of (i) pure MWCNTs and (ii and iii) CuO/MWCNT (inset in ii; the size distribution of CuONPs); (iv), (v) and (iv) are high-resolution TEM images of CuO/MWCNT.....	21
2.3	(i) SEM image and (ii) corresponding EDS spectrum of CuO/MWCNT, and EDS mapping of (iii) C, (iv) Cu and (v) O (inset in i, ii and iii, bottom, right: weight percentage).....	22
2.4	(i) SEM image and the corresponding (ii) EDS spectrm of <i>f</i> -MWCNTs.....	23
2.5	(i) Full and (ii) magnified Raman spectra of (a) pure MWCNTs, (b) <i>f</i> -MWCNTs, (c) MWCNTs + Cu(OAc) <sub>2</sub> mixture before calcination, and (d) CuO/MWCNT.....	24
2.6	(i) WAXD patterns of (a) pure MWCNTs, (b) <i>f</i> -MWCNTs, (c) MWCNTs + Cu(OAc) <sub>2</sub> , and (d) CuO/MWCNT and (ii) magnified WAXD pattern of CuO/MWCNT.....	25
2.7	(i) XPS spectra (a) MWCNTs, (b) <i>f</i> -MWCNTs and (c) CuO/MWCNT, (ii) magnified C 1s peak of <i>f</i> -MWCNTs, (iii) magnified C 1s peak of a, b and c, and (iv) main peaks of Cu 3p of CuO/MWCNT.....	27
2.8	TPR profiles of (a) <i>f</i> -MWCNTs and (b) CuO/MWCNT.....	28
2.9	(i and ii) TEM images, (iii) EDS and (iv) XPS spectra survey (main and satellite peaks of Cu 2p <sub>3/2</sub> and Cu 2p <sub>1/2</sub> of the XPS spectra of Cu) of CuO/MWCNT (having 60-80 nm CuONPs)...	34
2.10	(i) Heterogeneity and (ii) recyclability of CuO/MWCNT for <i>N</i> -arylation of imidazole with 4-chlorobenzonitrile [Reaction condition: 81 mg of imidazole (1.2 mmol), 137 mg of 4-chlorobenzonitrile (1 mmol), CuO/MWCNT (0.98 mol % or 5	37

	mg), 2 mmol of K <sub>2</sub> CO <sub>3</sub> (276 mg) and 5 mL of DMAc at 120°C for 24 h].....	
2.11	(i) TEM image, (ii) EDS and (iii) XPS spectra of used CuO/MWCNT.....	38
2.12	(i and ii) TEM images, (iii) Raman spectrum and (iv) WAXD pattern of R-MWCNTs.....	39
2.13	Possible mechanism of <i>N</i> -arylation of imidazole with aryl halide.....	41
3.1	Schematic illustration for the preparation of RuO <sub>2</sub> /SWCNT	54
3.2	(i and ii) Low and (iii-v) high magnification HR-TEM images of RuO <sub>2</sub> /SWCNT, and (vi) the particle size distribution of RuO <sub>2</sub> NPs in RuO <sub>2</sub> /SWCNT.....	57
3.3	(i) SEM image and (ii) EDS spectrum of RuO <sub>2</sub> /SWCNT, and corresponding EDS mapping of (iii) C, (iv) Ru and (v) O.....	58
3.4	Raman spectra of (a) pure SWCNTs, (b) <i>f</i> -SWCNTs, and (c) RuO <sub>2</sub> /SWCNT (left: magnified D band region; right: magnified G band region).....	59
3.5	(i) C 1s peak of <i>f</i> -SWCNTs, (ii) O 1s peak of <i>f</i> -SWCNTs, (iii) C 1s peak and O 1s peak of SWCNTs (a), <i>f</i> -SWCNTs (b) and RuO <sub>2</sub> /SWCNT (c), and (iv) main peaks of Ru 3p of RuO <sub>2</sub> /SWCNT.....	61
3.6	(i) Heterogeneity test and recyclability of RuO <sub>2</sub> /SWCNT [styrene (343 μL, 3.0 mmol), iodobenzene (111 μL, 1.0 mmol), (CH <sub>3</sub> ) <sub>3</sub> COK (224 mg, 2.0 mmol) and RuO <sub>2</sub> /SWCNT (0.9 mol%) at 110°C in 5 mL of DMF].....	69
3.7	Proposed mechanism for Heck-type olefination of iodobenzene with styrene.....	71
4.1	Preparation of nanocatalyst, GNPs-RuNRs.....	81
4.2	(i) TEM image of the GNPs-RuNRs (inset: magnified TEM image); (ii) XPS for catalyst (insert, above, right: Ru <sub>1/2</sub> and Ru <sub>3/2</sub> spectrum; left: Ru 3d <sub>5/2</sub> spectrum).....	84

4.3	(i) Full and (ii) magnified (right) region of XRD patterns of GNP (a), <i>f</i> -GNPs (b), GNP-Ru(acac) <sub>3</sub> (c) and GNP-RuNRs (d).....	85
4.4	(i) SEM and (ii) corresponding EDS images of GNP-RuNRs, and EDX mapping observations of (iii) C, (iv) Ru and (v) O (inset in iii, iv and v, bottom, right: weight percentage).....	85
4.5	(i) Full and (ii) magnified region of Raman spectra of GNP (a), <i>f</i> -GNPs (b), GNP-Ru(acac) <sub>3</sub> (c) and GNP-RuNRs (d).....	86
4.6	Effect of (i) catalyst amount, (ii) reaction time, (iii) temperature and (iv) base on transfer hydrogenation of acetophenone.....	87
4.7	(i) Reusability test and (ii) heterogeneity test of GNP-RuNRs for transfer hydrogenation of acetophenone.....	94
4.8	TEM images of used GNP-RuNRs: (i) cycle 1, (ii) cycle 2, (iii) cycle 3 and (iv) cycle 4.....	95
4.9	XRD (a), Raman (b), XPS (c and d) and SEM-EDX (e and f) of used GNP-RuNRs.....	96
4.10	Proposed catalytic mechanism.....	97
4.11	(i) FT-IR spectra (ii) of pure catalyst (a) and catalyst after stirred with 2-propanal and (CH <sub>3</sub> ) <sub>3</sub> COK for 6 h at 82°C (b).....	98
4.12	(i) Raman spectra (ii) of pure catalyst (a) and catalyst after stirred with 2-propanal and (CH <sub>3</sub> ) <sub>3</sub> COK for 6 h at 82°C (b).....	99
4.13	TEM image (a), Raman spectrum (b) and WAXD pattern (c) of recovered GNP.....	99
5.1	Schematic illustration for the preparation of GNS-RuNPs.....	110
5.2	(i and v) TEM images of GNP, (ii and vi) GNS, (iii) <i>f</i> -GNS and (iv, vii and viii) GNS-RuNPs.....	114
5.3	High resolution TEM images of GNS.....	114
5.4	(i) SEM image and (ii) EDS spectrum of GNS-RuNPs, and corresponding elemental mapping observations of (iii) C, (iv) Ru and (v) O.....	115
5.5	(i) Full and (ii, iii and iv) magnified Raman spectra of GNP.....	117

	( <b>a</b> ), GNS ( <b>b</b> ), <i>f</i> -GNS ( <b>c</b> ), GNS+Ru(acac) <sub>3</sub> ( <b>d</b> ), and GNS-RuNPs ( <b>e</b> ).....	
5.6	(i) XRD patterns of GNPs ( <b>a</b> ), GNS ( <b>b</b> ), <i>f</i> -GNS ( <b>c</b> ), ( <b>d</b> ) GNS+Ru(acac) <sub>3</sub> and ( <b>e</b> ) GNS-RuNPs, and (ii) magnified XRD pattern of GNS-RuNPs.....	118
5.7	Magnified C 1s peaks of (i) GNS and <i>f</i> -GNS, and (ii) <i>f</i> -GNS and GNS-RuNPs.....	119
5.8	(i) XPS spectra of ( <b>a</b> ) GNS, ( <b>b</b> ) <i>f</i> -GNS and ( <b>c</b> ) GNS-RuNPs, (iii and iv) magnified C 1s peak of <i>f</i> -GNS and GNS-RuNPs, and (ii and vi) main peaks of Ru 3d and 3p of GNS-RuNPs.....	120
5.9	Heterogeneity and reusability tests of GNS-RuNPs.....	130
5.10	(i) TEM, (ii) SEM-EDS, (iii) Raman and (iv) XRD of <i>u</i> -GNS-RuNPs.....	131
5.11	(i and ii) TEM images, (iii and iv) SEM-EDS, (v) Raman and (vi) XRD of GNS-RuNPs having 10-20 nm RuNPs.....	134
5.12	(i) FT-IR, (ii) Raman and (iii) XPS spectra of pure GNS-RuNPs ( <b>a</b> ) and <i>o</i> -GNS-RuNPs ( <b>b</b> ).....	136
5.13	Proposed mechanism for GNS-RuNPs catalyzed oxidation of alcohols.....	137
5.14	(i and ii) TEM images, (iii) SEM-EDS, (iv) Raman, (v) XPS and (iv) XRD of <i>u</i> -GNS-RuO <sub>2</sub> NRs, and (iv-vi) elemental mapping of C (iv), Ru (v) and O (vi).....	138
6.1	Schematic diagram of the procedure for preparation of GNP-RuO <sub>2</sub> NPs.....	159
6.2	TEM images of (i) pure GNP and (ii, iii, iv and v) GNP-RuO <sub>2</sub> NPs, and (vi) the particle size distribution of RuO <sub>2</sub> NPs.....	162
6.3	(i) SEM images and (ii) corresponding EDS spectrum of GNP-RuO <sub>2</sub> NPs, and EDS mapping of (iii) C, (iv) Ru and (v) O.....	163
6.4	XPS spectrum of <i>f</i> -GNP; magnified (i) C 1s and (ii) O 1s peaks	165
6.5	XPS spectrum of GNP-RuO <sub>2</sub> NPs; magnified (i) C 1s and (ii) Ru 3p peaks .....	166

6.6	(i) XRD pattern of GNP-RuO <sub>2</sub> NPs and (ii) Raman spectra of <i>f</i> -GNP and GNP-RuO <sub>2</sub> NPs.....	167
6.7	Effect of (i) solvent, (ii) temperature, (iii) amount of oxidant and (iv) time on the oxidation of triethylamine.....	168
6.8	(i) Reusability of GNP-RuO <sub>2</sub> NPs, (ii) TEM image, (iii) EDS and (iv) XPS of <i>u</i> -GNP-RuO <sub>2</sub> NPs.....	174
6.9	Proposed catalytic mechanism for the <i>N</i> -oxidation of triethylamine using GNP-RuO <sub>2</sub> NPs.....	175

## LIST OF SCHEMES

<b>Scheme No.</b>	<b>Title</b>	<b>Page No.</b>
3.1	Regioselectivity of RuO <sub>2</sub> /SWCNT-catalyzed Heck coupling reaction.....	67
3.2	Chemoselectivity of RuO <sub>2</sub> /SWCNT-catalyzed Heck coupling reaction.....	68
4.1	Chemoselectivity of catalyst, GNPs-RuNRs.....	98
5.1	Chemoselectivity of nanocatalyst, GNS-RuNPs.....	129

## ABBREVIATIONS

BET	Brunner Emmett Teller
Ca.	Calculated value
CMs	Carbon Materials
CNTs	Carbon Nanotubes
Conv.	Conversion
CVD	Chemical Vapor Deposition
DMAc	<i>N,N</i> -Dimethylacetamide
DMF	<i>N,N</i> -Dimethylformamide
DMSO	Dimethyl Sulphoxide
Equiv.	Equivalent
FID	Flame Ionization Detector
FT-IR	Fourier Transform Infrared
<i>f</i> -GNPs	Functionalized Graphene Nanoplatelets
<i>f</i> -GNSs	Functionalized Graphene Nanosheets
<i>f</i> -MWCNTs	Functionalized Multi Walled Carbon Nanotubes
<i>f</i> -SWCNTs	Functionalized Single Walled Carbon Nanotubes
GC	Gas Chromatography
GNPs	Graphene Nanoplatelets
GNSs	Graphene Nanosheets
HPLC	High Pressure Liquid Chromatography
HR-TEM	High Resolution Transmission Electron Microscopy
ICP-MS	Inductively Coupled Plasma – Mass Spectroscopy
Min.	Minutes
MNPs	Metal Nanoparticles
MNSs	Metal Nanostructures
MWCNTs	Multi Walled Carbon Nanotubes
NMR	Nuclear Magnetic Resonance
NPs	Nanoparticles
ppm	Parts per million

SEM	Scanning Electron Microscopy
Sel.	Selectivity
SWCNTs	Single Walled Carbon Nanotubes
TEM	Transmission Electron Microscopy
Temp.	Temperature
TMS	Tetramethylsilane
TLC	Thin Layer Chromatography
TPR	Temperature Programmed Reduction
XPS	X-ray Photoelectron Spectroscopy
WAXD	Wide Angle X-ray Diffraction

## NOTATIONS

$^1\text{H}$	Hydrogen isotope – 1
$^{13}\text{C}$	Carbon isotope – 13
%	Percentage
$^{\circ}\text{C}$	Degree Celsius
$\text{\AA}$	Angstrom
$\text{cm}^{-1}$	Reciprocal centimeter
d	Doublet
$\delta$	Chemical shift
h	Hour
Hz	Hertz
$J$	Coupling constant
$\lambda$	Wavelength
mol %	Mole percentage
$\nu$	Frequency
nm	Nanometer
s	Singlet
kV	Kilo volt
mA	Microampere
eV	Electron volt
m/z	Molecular mass
t	Triplet

# **CHAPTER 1**

## **Introduction**

# CHAPTER 1

## Introduction

### 1.1 Background

Research in catalysis has undergone remarkable development and continues to expand since the word ‘catalysis’ was coined by Berzelius in 1836. One of the most important driving forces for this amazing development is the increasing demand of the catalytic products in various fields such as biomedical, pharmaceutical, material sciences and agricultural. There are several transition metal complexes-based homogeneous catalytic systems have been reported. However, recently, owing to the high recyclability and easy separation from the reaction mixture, transition metal nanoparticles (MNPs) have gained vast interest in heterogeneous catalysis [1]. Among them, supported MNPs based on Cu- and RuNPs have played a tremendous role in various organic transformations; the results have been well-documented [2, 3]. Silica, alumina and polymers are well known supports for these active metal catalysts [4]. In fact, supported Cu- and RuNPs are cost-effective, environmental friendly and highly versatile when compared to other supported MNPs. In spite of their advantages, these catalytic systems often require higher stoichiometric amounts of Cu or Ru catalysts (typically 10-5 mol%) and the scope is also very limited. In addition, most of the common supports are not stable under both acidic and basic reaction conditions [5]. These are the problems mainly affect the productivity of the chemical industries. Therefore, several researchers focus on

the development of efficient, stable and recyclable supported catalysts for the organic reactions with the use of catalytic amount of Cu or Ru.

## **1.2 Role of carbon materials as support in heterogeneous catalysis**

In heterogeneous catalysis, carbon materials (CMs) have been used as a support to disperse and stabilize small MNPs [6]. In fact, they provide an access to a much larger number of catalytically active sites than in the corresponding bulk metal. Indeed, the catalytic activity of these active MNPs is also highly dependent on the interaction between CMs and MNPs. To date, there are numerous publications have been written about the CMs and its use as supports in heterogeneous catalysis [7]. Very recently, owing to the astounding properties such as unique structure, high surface area, and chemical as well as electrochemical inertness, carbon nanotubes (CNTs) and graphene nanosheets (GNSs) have been receiving a great deal of attention as a support in heterogeneous catalysis [8]. Krashennnikov *et al.*, demonstrated that the inert GNSs/CNTs can be transformed to a very active catalyst through the interactions between the active metal clusters and carbon vacancies [9, 10]. The transition MNPs supported on CMs-catalyzed reactions provide the advantages of high atom efficiency, simplified isolation of product, and easy recovery and recyclability of the catalyst. Moreover, the decoration of transition MNPs onto the CMs support has shown a more versatility in carrying out the highly selective catalytic processes. These outstanding catalytic activities of CMs-supported MNPs are mainly due to the effective dispersion in various solvents, very less aggregation of MNPs and larger surface area of the nanocatalyst. These are the

very important points to choose the CMs including CNTs and GNSs as supports for Ru and Cu NPs.

### **1.3 Dry synthesis of CMs supported MNPs catalysts**

Owing to the hydrophobic nature and chemical inertness of the CMs, the decoration of MNPs over the CMs is a challenging task [11]. Previous studies almost used solution-based techniques i.e. wet synthesis [12]. In order to obtain a homogeneous distribution and very good adhesion of MNPs on CMs, many factors such as type of organic solvents, concentration of metal precursors, reducing agents, deposition time and temperature need to be controlled very carefully, therefore, a wet synthesis approach is very limited [13]. In contrast to wet synthesis, the solventless bulk synthesis so called ‘dry synthesis’ has been attracting greater interest due to its simplicity, better adhesion and advantages of least parameters to control; the results have been well documented [14]. Very recently, Li *et al.*, [13] demonstrated a rapid, solventless, bulk synthesis method for the preparation of MNPs-decorated CNTs. They found that the procedure is very simple, highly effective, scalable to multigram quantities and generally applicable to various carbon substrates (*e.g.*, CNFs, expanded graphite, CNTs and carbon black) and many metal salts (*e.g.*, Ag, Au, Co, Ni, and Pd acetates) [15].

Well known that the oxygen functional groups (C–OH, C–O–C, C=O and COOH) play a significant role in the decoration of MNPs on CMs [13]. In fact, the presence of oxygen functional groups can play a bridging role between the MNPs and support; consequently, can exhibit good attachment of MNPs with supports such as CMs. However, in case of other CMs such as activated carbon, creation of the oxygen

functional groups is very difficult whereas inert metal supports such as silica have only –OH groups [13]. Since the ‘dry decoration’ methods need more nucleation centers (oxygen functional groups) on the CMs, we believed that the CNTs and GNSs would be the better option. Moreover, the functionalization of the C–OH, C–O–C, C=O and COOH groups on GNSs and CNTs is very easy. Furthermore, the high surface area, versatility and its physicochemical stability also attracted to chose these smart materials (GNSs and CNTs) as catalyst support in our work.

## 1.4 Literature survey

There are several reviews and book chapters dealing with the preparation and catalytic applications of CMs-supported MNPs have been published. However, we found only few reports on CMs/MNPs for the organic reactions.

The formation of C-C bonds *via* Heck reaction is one of the very important reactions in organic synthesis. CuONPs has been very commonly used as a catalyst for this transformation. Saberi *et al.*, have prepared CNT@ $\alpha$ -Fe<sub>2</sub>O<sub>3</sub>@CuO catalyst by a simple solution phase reduction method [16]. They found that the catalyst is highly active in Ullmann type coupling of aryl iodides and bromides with phenols in very shorter reaction time. Moreover, they realized the merit of the CNTs support from the recyclability and stability of the CNT@ $\alpha$ -Fe<sub>2</sub>O<sub>3</sub>@CuO catalyst.

Papageorgiou *et al.*, have reported a simple and one step carbonization-reduction procedure based on the modified polyol process for the preparation of carbon supported CuNPs catalyst [17]. The prepared material has showed a very good dispersion of CuNPs of fairly uniform size. Even at high metal loading, no visible aggregation of CuNPs is

evident due to the dispersion of the active metal binding sites on carbon support. The catalyst was used for the NO catalytic abatement and showed high efficiency even at low temperatures compared to other carbon supported catalysts.

Since the MNPs decorated MWCNTs composites display an excellent catalytic activity and selectivity in various organic transformation reactions, Ye *et al.*, have developed a new, rapid, convenient and environmentally benign method for the fabrication of MNPs-MWCNTs composites [18]. They found that the MNPs decorated MWCNTs composites exhibit a high catalytic activity for hydrogenation of olefins in CO<sub>2</sub> as well as a high electrocatalytic activity for oxygen reduction for potential fuel cell applications.

In organic synthesis, oxidation of alcohols to carbonyl compounds is one of the very important reactions. Yang *et al.*, have transformed a variety of alcohols to the corresponding oxygenated products in good yield with high selectivity using RuNPs supported on MWCNTs catalyst [19]. They found that the Ru/CNTs can be easily recoverable and reusable for several cycles.

RuNPs supported MWCNTs with different loadings (1% wt, 3% wt, 5% wt) have been prepared by Guo *et al.* [20]. The activity of this RuNPs/MWCNTs catalyst towards the hydrogenation of oils and fats is much higher than that of conventional Ni catalyst. More interestingly, they found that the catalyst is highly *cis*-selective and this selectivity can be easily tunable.

Matsumoto *et al.*, have reported that 5% Ru/C catalyst affords over 98% yield of cinnamaldehyde in the slow oxidation of cinnamyl alcohol [21]. However, the drawback in this process is that 2,6-di-tert-butyl-p-cresol additive was required to prevent further

oxidation to cinnamic acid. Moreover, reactivity of primary and secondary allylic alcohols, R-keto alcohols, R-hydroxy-lactones, and saturated alcohols decreased in this order.

MNPs-catalyzed carbon-carbon (C–C) cross coupling reactions is a key step in the synthesis of organic building blocks, agricultural derivatives and natural products. Although this transformation reaction is highly dominated by Pd-based catalysts, very recently, RuNPs-catalyzed cross coupling reactions are proven to be an effective tool for the construction of C–C bond. However, the results have been disclosed in very few examples. Na *et al.*, employed Ru/Al<sub>2</sub>O<sub>3</sub> catalyst for both the Heck-type olefination and Suzuki-type coupling reactions [22]. They found that the Ru/Al<sub>2</sub>O<sub>3</sub> catalyst is highly effective and reusable, but, bromo- and chloroarenes are unreactive under the catalytic system. Soon after, polymers supported RuNPs catalyst also reported for the olefination reactions.

## 1.5 Objectives

In spite of the advantages of the MNPs/CMs in heterogeneous catalysis, drawbacks still remain in these catalysts as higher stoichiometric amounts of metal catalysts (typically 10-2 mol %) are often required. Moreover, in most of the cases, scope of the catalytic system is very limited and, the stability and reusability of these catalysts under harsh reaction conditions are also questionable. Our main aim of this work is to overcome the above discussed drawbacks.

Chapter 2 concentrates on the preparation of CuO/MWCNT using copper acetate precursor by a very simple “dry synthesis” method. The resultant material has been used

as a heterogeneous nanocatalyst for the *N*-arylation of imidazole. Previously reported CuONPs-based methods for this transformation required a stoichiometric amount of Cu catalyst and, in some cases, the scope of the methods is also highly limited. These drawbacks have been addressed.

In chapter 3, a mild and highly efficient SWCNTs-supported RuO<sub>2</sub>NPs based catalytic system for the Heck-type olefination of aryl halides is reported. We demonstrate that the substrate scope of the reactions could be efficiently carried out with as low as 0.9 mol % of the supported RuO<sub>2</sub> catalyst over a wide range of substrates in short reaction times. Unreactive bromo- and chloroarenes are also effectively olefinated under the present catalytic reaction condition. Regioselectivity, chemoselectivity, heterogeneity, reusability and stability of RuO<sub>2</sub>/SWCNT are also tested.

In chapter 4, we report the preparation of a novel RuNRs/GNPs catalyst for the transfer hydrogenation of carbonyl compounds. We demonstrate that a wide range of substrates can be hydrogenated in good yield with excellent selectivity. Chemoselectivity, heterogeneity and reusability are also tested.

In chapter 5, decoration of RuNPs on GNS by dry synthesis method is reported. After the complete characterization, the prepared material (GNS-RuNPs) is used as catalyst for the aerial oxidation of alcohols. The scope of the catalytic system has been extended with various aliphatic, aromatic, alicyclic, benzylic, allylic, amino and heterocyclic alcohols. We have shown that 0.036 mol% (5 mg) of catalyst was enough for aerial oxidation of alcohols; lowest amount of catalyst among so far reported. Chemoselectivity, heterogeneity, reusability and stability of RuO<sub>2</sub>/SWCNT are also tested. The GNS-RuNPs were separated out from the reaction mixture and analyzed by

TEM, XRD, Raman and SEM-EDS; the results revealed that the nanocatalyst is physically as well as chemically stable. Owing to the high stability of used catalyst (*u*-GNS-RuNPs), it was further applied in transfer hydrogenation, after suitable modifications. We obtained ruthenium oxide nanorods hybrid GNS (*u*-GNS-RuO<sub>2</sub>NRs) from *u*-GNS-RuNPs by simple calcination. The catalytic activity of *u*-GNS-RuO<sub>2</sub>NRs toward the transfer hydrogenation of various aromatic, alicyclic and heterocyclic ketones was found to be an excellent.

Finally in chapter 6, anchoring of ultrafine RuO<sub>2</sub>NPs (1.3 nm) on GNP using Ru(acac)<sub>3</sub> precursor by a very simple dry synthesis method is presented. The resultant material (GNP-RuO<sub>2</sub>NPs) has been used as a heterogeneous nanocatalyst for the *N*-oxidation of tertiary amines. We have achieved an excellent yields even at a very low amount of Ru catalyst (0.13 mol%). The GNP-RuO<sub>2</sub>NPs is heterogeneous in nature, chemically as well as physically very stable and the catalyst can be reused for up to 5 times.

## Reference

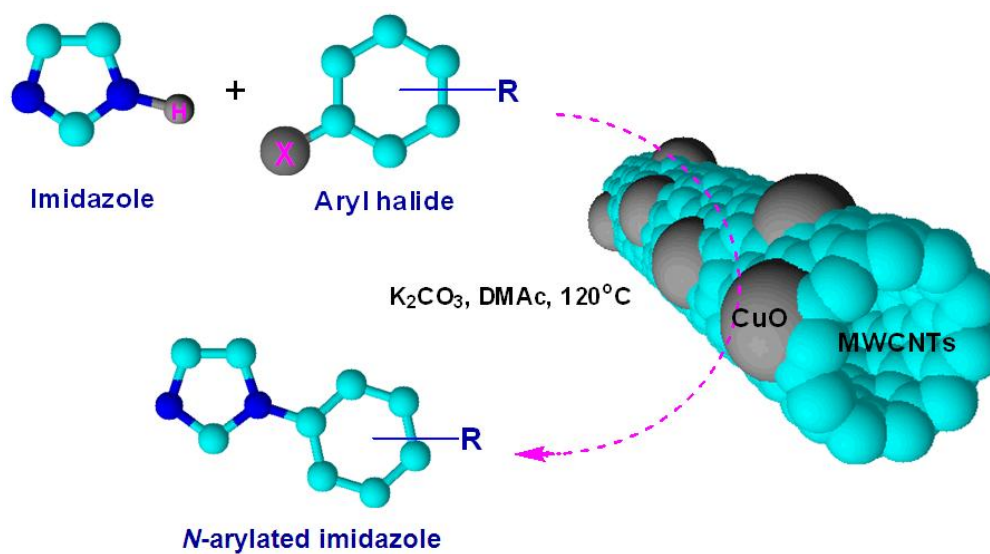
- [1] Astruc, D.; Lu, F.; Aranzaes, J. R. Nanoparticles as Recyclable Catalysts: The Frontier between Homogeneous and Heterogeneous Catalysis. *Angew. Chem. Int. Ed.* **2005**, *44*, 7852–7872.
- [2] Ganesh Babu, S.; Karvembu, R. Copper Based Nanoparticles-Catalyzed Organic Transformations. *Catal. Surv. Asia.* **2013**, *17*, 156–176.
- [3] Polshettiwar, V.; Luque, R.; Fihri, A.; Zhu, H.; Bouhrara, M.; Basset, J. M. Magnetically Recoverable Nanocatalysts. *Chem. Rev.* **2011**, *111*, 3036–3075.
- [4] Silica Gel-alumina Supported Catalyst, US patent 2487564.
- [5] Mandal, S.; Roy, D.; Chaudhari, R. V.; Sastry, M. Pt and Pd Nanoparticles Immobilized on Amine-Functionalized Zeolite: Excellent Catalysts for Hydrogenation and Heck Reactions. *Chem. Mater.* **2004**, *16*, 3714–3724.
- [6] Reinoso, F. R. The Role of Carbon Materials in Heterogeneous Catalysis. *Carbon* **1998**, *36*, 159–175.
- [7] Serp, P.; Figueiredo, J. L. Carbon Materials for Catalysis. John Wiley and Sons, 2008, 579.
- [8] Planeix, J. M.; Coustel, N.; Coq, J B.; Bretons, J V.; Kumbhar, P. S.; Dutartre, R.; Geneste, P.; Bernier, P.; Ajayan, P. M. Application of Carbon Nanotubes as Supports in Heterogeneous Catalysis. *J. Am. Chem. Soc.* **1994**, *116*, 7935–7936.
- [9] Huang, C.; Lia, C.; Shi, G. Graphene Based Catalysts. *Energy Environ. Sci.* **2012**, *5*, 8848–8868.

- [10] Krashennnikov, A. V.; Lehtinen, P. O.; Foster, A. S.; Pyykko, P.; Nieminen, R. M. Embedding Transition-Metal Atoms in Graphene: Structure, Bonding, and Magnetism. *Phys. Rev. Lett.* **2009**, *102*, 126807–126810.
- [11] Sanjib, B.; Lawrence, T. D. A Novel Approach to Create a Highly Ordered Monolayer Film of Graphene Nanosheets at the Liquid–Liquid Interface. *Nano Lett.* **2009**, *9*, 167–172.
- [12] Xiaozhu, Z.; Xiao, H.; Xiaoying, Q.; Shixin, W.; Can, X.; Freddy, Y. C. B.; Qingyu, Y.; Peng, C.; Hua, Z. In Situ Synthesis of Metal Nanoparticles on Single-Layer Graphene Oxide and Reduced Graphene Oxide Surfaces. *J. Phys. Chem. C* **2009**, *113*, 10842–10846.
- [13] Li, J.; Liu, C. Y. Ag/Graphene Heterostructures: Synthesis, Characterization and Optical Properties. *Eur. J. Inorg. Chem.* **2010**, *2010*, 1244–1248.
- [14] Tien, H. W.; Huang, Y. L.; Yang, S. Y.; Wang, J. Y.; Ma, C. C. M. The Production of Graphene Nanosheets Decorated with Silver Nanoparticles for use in Transparent, Conductive Films. *Carbon* **2011**, *49*, 1550–1560.
- [15] Lin, Y.; Watson, K. A.; Fallbach, M. J.; Ghose, S.; Smith, J. G.; Delozier, D. M.; Cao, W.; Crooks, R. E.; Connell, J. W. Rapid, Solventless, Bulk Preparation of Metal Nanoparticle-Decorated Carbon Nanotubes. *ACS Nano* **2009**, *3*, 871–884.
- [16] Saberi, D.; Sheykhani, M.; Niknam, K.; Heydari, A. Preparation of Carbon Nanotube-Supported  $\gamma$ -Fe<sub>2</sub>O<sub>3</sub>@CuO Nanocomposite: a Highly Efficient and Magnetically Separable Catalyst in Cross-coupling of Aryl Halides with Phenols. *Catal. Sci. Technol.* **2013**, *3*, 2025–2031.

- [17] Papageorgiou, S. K.; Favvas, E. P.; Sapalidis, A. A.; Romanos, G. E.; Katsaros, F. K. Facile Synthesis of Carbon Supported Copper Nanoparticles from Alginate Precursor with Controlled Metal Content and Catalytic NO Reduction Properties. *J. Hazard. Mater.* **2011**, *189*, 384–390.
- [18] Ye, X. R.; Lin, Y.; Wang, C.; Engelhard, M. H.; Wang, Y.; Waix, C. M. Supercritical Fluid Synthesis and Characterization of Catalytic Metal Nanoparticles on Carbon Nanotubes. *J. Mater. Chem.* **2004**, *14*, 908–913.
- [19] Lin, Y.; Watson, K. A.; Fallbach, M. J.; Ghose, S.; Smith, J. G.; Delozier, D. M.; Cao, W.; Crooks, R. E.; Connell, J. W. Rapid, Solventless, Bulk Preparation of Metal Nanoparticle-Decorated Carbon Nanotubes. *ACS Nano* **2009**, *3*, 871–884.
- [20] Yang, X.; Wang, X.; Qiu, J. Aerobic Oxidation of Alcohols over Carbon Nanotube-Supported Ru Catalysts Assembled at the Interfaces of Emulsion Droplets. *Appl. Catal. A: Gen.* **2010**, *382*, 131–137.
- [21] Matsumoto, M.; Ito, S. *Synth. Commun.* **1984**, *14*, 697–701.
- [22] Na, Y.; Park, S.; Han, S. B.; Han, H.; Ko, S.; Chang, S. Ruthenium-Catalyzed Heck-Type Olefination and Suzuki Coupling Reactions: Studies on the Nature of Catalytic Species. *J. Am. Chem. Soc.* **2004**, *126*, 250–258.

## CHAPTER 2

### An efficient, reusable copper-oxide/carbon-nanotube catalyst for *N*-arylation of imidazole



## CHAPTER 2

# **An efficient, reusable copper-oxide/carbon-nanotube catalyst for *N*-arylation of imidazole**

### **2.1 Introduction**

Nitrogen-containing heterocycles are prevalent structural motifs in various fields such as biological, pharmaceutical and material sciences [1]. Particularly, imidazole and its derivatives are consigned as privileged structures in drug development because they possess salt formation property and often exhibit good solubility, which are the prime requirements for bioavailability and oral absorption in medicinal research [2]. In addition, imidazole derivatives are efficient antibacterial, antimalarial, antiviral, antimycobacterial and antifungal compounds [3, 4]. However, the traditional methods employed for *N*-arylation of heterocycles are very limited because it often requires harsh conditions such as high reaction temperatures (typically 150-200°C), extended reaction time, and in some cases over-stoichiometric amount of Cu reagents, which lead to the environmental problem of waste disposal [5-8]. To circumvent these issues, newer and milder homogeneous transition metal catalysts have been developed for this reaction but the preparation methods are complex and difficult to recycle [9, 10]. Recently, heterogeneous catalysts particularly MNPs including CuO and Cu<sub>2</sub>O with high surface area are getting so much attention from both economic and industrial point of view because they possess very good activity and are highly recyclable [11, 12]. In spite of their advantages, drawbacks remain in these catalysts too, as the MNPs effortlessly agglomerate during the

reaction and also less stability under severe reaction conditions, which lead to low catalytic activity as well as poor reusability of the catalyst [13]. In addition, higher stoichiometric amounts of Cu catalyst (typically 20-10 mol%) are often required [11, 12, 14-16]. To prevent the agglomeration of MNPs and the over-stoichiometric use of Cu reagents, several inorganic materials such as alumina and silica have been used as a support for MNPs but again they have limited stability under both acidic and basic conditions [17]. Therefore, developing an efficient and recyclable catalyst for the *N*-arylation of heterocycles with the use of lower amount of Cu remains a challenging one.

Recently, owing to the astounding properties of CNTs such as unique structure, high surface area, and chemical as well as electrochemical inertness [18, 19], it has been receiving a great deal of attention as a support in heterogeneous catalysis [20, 21]. Particularly, transition MNPs supported on CNTs-catalyzed reactions provide the advantages of high atom efficiency, simplified isolation of product, and easy recovery and recyclability of the catalyst [22, 23]. Moreover, the decoration of transition MNPs onto the CNTs support has shown a more versatility in carrying out the highly selective catalytic processes [24, 25]. These outstanding catalytic activities of CNTs-supported MNPs are mainly due to the effective dispersion in various solvents, very less aggregation of MNPs and larger surface area of the nanocatalyst [26]. Recently, Cano *et al.*, prepared CNTs supported PdNPs and used as a catalyst for the Heck and Suzuki coupling reactions [27]. They have found that the prepared CNTs-PdNPs showed very high conversions and good recyclability. Byunghoon *et al.*, described an unusual high catalytic activity of the CNTs-supported bimetallic Pd/Rh NPs for the hydrogenation of anthracene [28]. We believe that the CuONPs based on multi-wall carbon nanotubes

(MWCNTs) composite could overcome the drawbacks exist in the *N*-arylation of heterocycles, especially higher stoichiometric amounts of Cu and the limited reusability. Herein, we report the simple preparation of MWCNTs supported CuONPs and its catalytic property towards *N*-arylation of imidazole with various aryl halides. Reusability and heterogeneity of CuO/MWCNT are also described. In addition, MWCNTs were successfully recovered from the used CuO/MWCNT by a simple acid treatment method.

## **2.2 Experimental section**

### **2.2.1 Materials and characterization**

High-purity MWCNTs with diameters ranging from 15 to 20 nm were used in this study. The MWCNTs were produced in large scale through the optimal combination of chemical vapor deposition (CVD) method [29], and subsequent thermal treatment at 2800°C in an argon atmosphere [19]. Cu(OAc)<sub>2</sub> (97%), H<sub>2</sub>SO<sub>4</sub> (98%), HNO<sub>3</sub> (70%) and HCl (70%) were purchased from Wako pure chemicals, Japan. All other chemicals were purchased from Aldrich and used without further purification.

The morphology of CuO/MWCNT was investigated on a JEOL JEM-2100F TEM with accelerating voltage of 120 kV. To quantify the weight percentage of Cu in CuO/MWCNT, SEM-EDS was recorded using Hitachi 3000H SEM. The same field of view was then scanned using an EDS spectrometer to acquire a set of X-ray maps for Cu, C, and O using 1 ms point acquisition for approximately one million counts. The definite quantity of Cu in the CuO/MWCNT was determined using ICP-MS (7500CS, Agilent). Raman spectrometer (Hololab 5000, Kaiser Optical Systems Inc., USA) was applied to

examine the interaction between CuONPs and MWCNTs. The argon laser was operated at 532 nm with a Kaiser holographic edge filter. WAXD experiment was performed at room temperature using a Rotaflex RTP300 (Rigaku Co., Japan) diffractometer at 50 kV and 200 mA. Nickel-filtered Cu  $K_{\alpha}$  radiation ( $10 < 2\theta < 80^{\circ}$ ) was used for the measurements. XPS (Kratos Axis-Ultra DLD, Kratos Analytical Ltd, Japan) was recorded to confirm the chemical state of Cu in CuO/MWCNT. During the XPS analysis, the sample was irradiated with Mg  $K_{\alpha}$  ray source. Temperature programmed reduction tests were conducted in a Micromeritics TPD/TPR 2900 instrument. For the measurement, 80 mg of sample was reduced under flowing  $H_2/Ar$  (10%) at 60 mL/min, from 50 to 800°C with a ramping rate of 10°C/min. NMR spectra were recorded on a 400 MHz Bruker spectrometer in  $CDCl_3$  using TMS as a standard. The conversion of the reactants and the yield of *N*-arylated products were determined using Shimadzu-2010 gas chromatograph.

### **2.2.2 Preparation of nanocatalyst (CuO/MWCNT)**

Chemical vapor deposition (CVD) and wet chemical processing (WCP) are the most common approaches to decorate the MNPs on the surface of CMs including CNTs. However, these approaches require extremely high temperature and long reaction time, and also the percentage of filled CNTs is very low [29]. To overcome these, a method involving the reduction of metal precursors in solution phase using reducing agents has been developed. Due to the inert and poor hydrophilic nature of CNTs surface, these approaches are also limited because of the unsatisfactory coverage control and adhesion of MNPs on the surface of CNTs [25]. Hence, in this study, the CuONPs were decorated on MWCNTs surface by a very simple “mix-and-heat” process without the use of any

solvent, reducing agent, or electric current. Before mix-and-heat, MWCNTs were functionalized with carboxylic ( $\text{O}=\text{C}-\text{OH}$ ), carbonyl ( $-\text{C}=\text{O}$ ), and hydroxyl ( $-\text{C}-\text{OH}$ ) groups to achieve good adhesion of CuONPs on MWCNTs [30-32]. In a typical procedure, 0.5 g of pure MWCNTs were treated with a 3:1 mixture of conc.  $\text{H}_2\text{SO}_4$  and  $\text{HNO}_3$ , and then the mixture was sonicated at  $40^\circ\text{C}$  for 3 h in an ultrasonic bath. After cooling to  $27^\circ\text{C}$ , the mixture was diluted with 500 mL of deionized water and then vacuum-filtered through a filter paper of  $3\ \mu\text{m}$  porosity. The resultant solid filtrate (*f*-MWCNTs) was repeatedly washed with deionized water until the pH became neutral and then dried in *vacuo* at  $60^\circ\text{C}$ . After that, 0.1 g of  $\text{Cu}(\text{OAc})_2$  was added into 0.5 g of *f*-MWCNTs and mixed well by a mortar and pestle. The homogeneous mixture of *f*-MWCNTs and  $\text{Cu}(\text{OAc})_2$  was obtained in 10-15 minutes. Then the mixture was calcinated under argon atmosphere at  $350^\circ\text{C}$  for 3 h in a muffle furnace. Figure 2.1 shows schematic illustration of the procedure for the preparation of CuO/MWCNT.

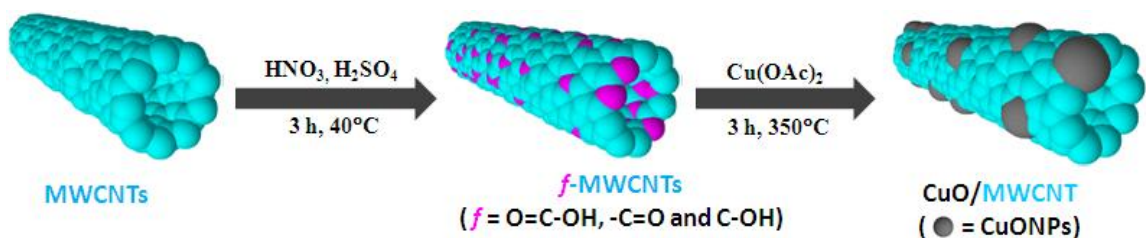


**Figure 2.1** – Schematic illustration for the preparation of CuO/MWCNT.

### 2.2.3 *N*-Arylation of imidazole with aryl halides

In a typical procedure, CuO/MWCNT (5 mg, 0.98 mol%) were added into a mixture of imidazole (81 mg, 1.2 mmol), 4-chlorobenzonitrile (137 mg, 1 mmol) and  $\text{K}_2\text{CO}_3$  (276 mg, 2 mmol), and stirred under air atmosphere at  $120^\circ\text{C}$  for 24 h. After the

completion of the reaction, the nanocatalyst was separated out from the reaction mixture *via* centrifugation and then the separated nanocatalyst was washed well with diethyl ether and dried in an oven at 135°C for 3 h. The centrifugate was partitioned between 10 mL of ethyl acetate and 5 mL of saturated aqueous sodium hydrogen carbonate solutions. Then the organic layer was separated out and dried over anhydrous sodium sulphate. The yield of product was determined by GC. Finally, the organic layer was concentrated to obtain *N*-arylated imidazole. **4-(1H-imidazol-1-yl)benzotrile:** <sup>1</sup>H NMR (400 MHz, CDCl<sub>3</sub>): δ 7.28 (s, 1H), 7.39 (s, 1H), 7.59 (d, *J* = 7.2 Hz, 2H), 8.02 (s, 1H), 8.37 (d, *J* = 7.2 Hz, 2H) ppm; <sup>13</sup>C NMR (150 MHz, CDCl<sub>3</sub>): δ 117.6, 121.0, 125.7, 131.7, 135.4, 141.9, 146.2 ppm; MS (GC) *m/z* 169.06 (M<sup>+</sup>); melting point 142-144°C.

#### 2.2.4 Product analysis

In order to confirm the formation of the product, samples of both reactants and products were dissolved in ethyl acetate. The samples were then analyzed by GC, which was equipped with 5 % diphenyl and 95 % dimethyl siloxane, Restek-5 capillary column (0.32 mm dia, 60 m in length) and a flame ionization detector (FID). Nitrogen gas was used as a carrier gas. The initial column temperature was increased from 60 to 150°C at the rate of 10°C/min and then further increased to 220°C at the rate of 40°C/min. During the product analysis, the temperatures of the FID and injection port were kept constant at 150 and 250°C respectively.

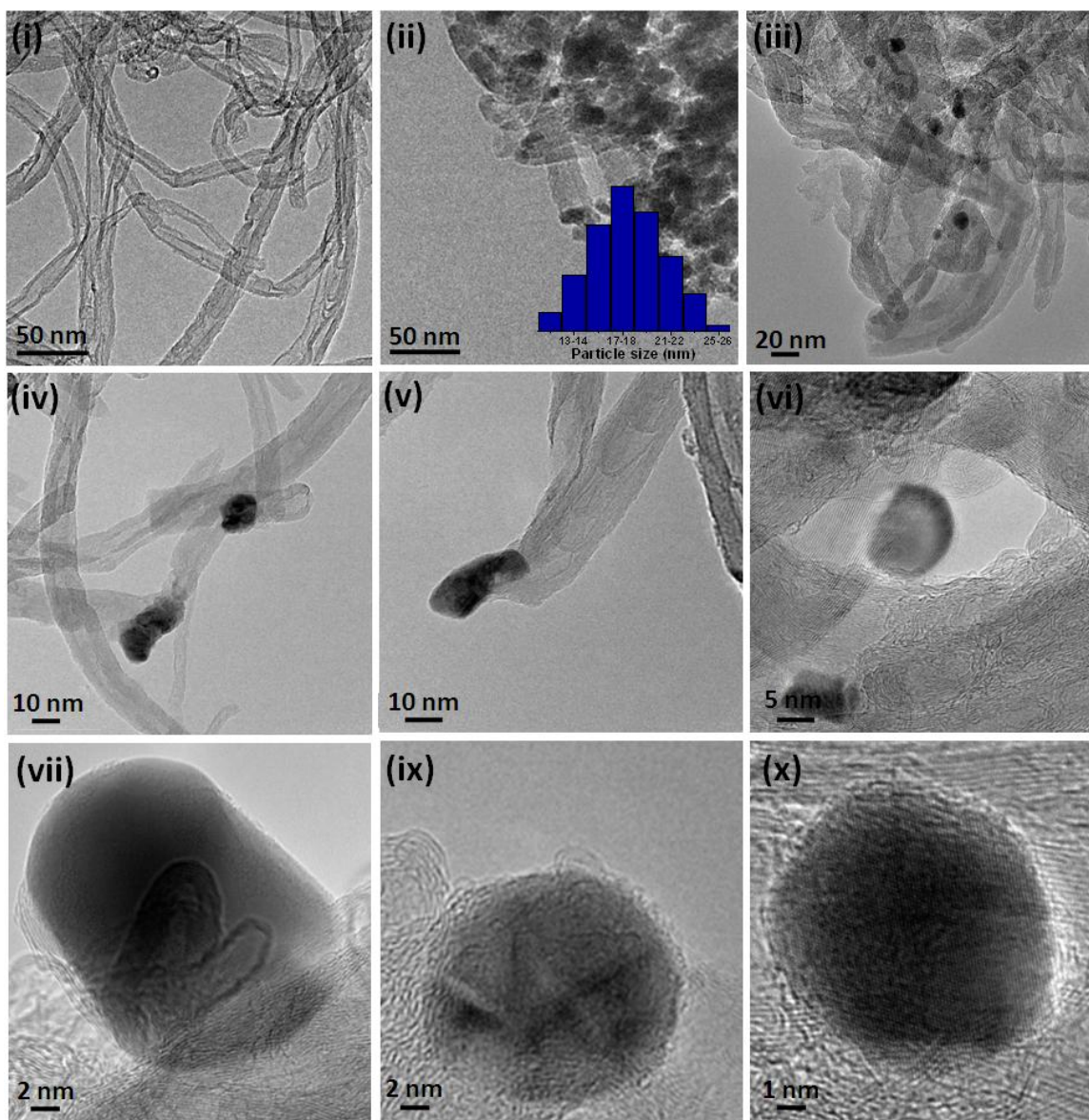
### **2.2.5 Recovery of MWCNTs from the used nanocatalyst**

In a typical experiment, used CuO/MWCNT were washed with ethyl acetate and then treated with a 3:1 mixture of conc. H<sub>2</sub>SO<sub>4</sub> and HNO<sub>3</sub> (40 mL), then the mixture was sonicated for 30 minutes at 40°C in an ultrasonic bath followed by stirring for 3 h at 60°C. After cooling to room temperature, the mixture was diluted with 500 mL of deionized water and then vacuum-filtered through a filter paper of 3 μm porosity. The resultant precipitate (R-MWCNTs) was repeatedly washed with deionized water until the pH became neutral followed by drying in *vacuo*.

## **2.3. Results and discussion**

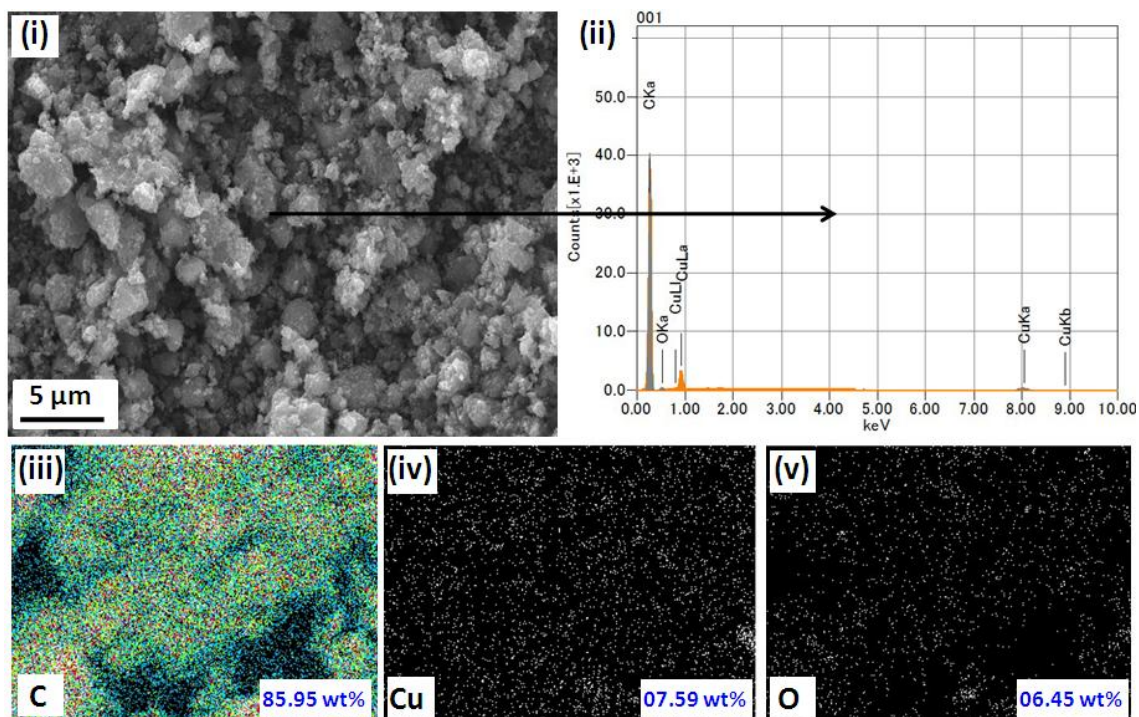
### **2.3.1 Characterization of CuO/MWCNT**

To investigate the morphology of CuO/MWCNT, TEM images were taken for pure MWCNTs [Figure 2.2(i)] and CuO/MWCNT [Figure 2.2(ii-x)]. As seen from Figure 2.2, very small and well dispersed CuONPs were anchored tightly onto the external walls of MWCNTs. The histogram of CuONPs [Figure 2.2(ii), inset] demonstrates that the CuONPs have a fairly broader size distribution ranging from 10 to 26 nm with a peak centered at ca. 18.7 nm. The average diameter and its standard deviation of CuONPs were found to be ca. 18.5 and ca. 5 nm, respectively. In addition, the crystalline structure of CuONPs can be noticed clearly in Figure 2.2(x).



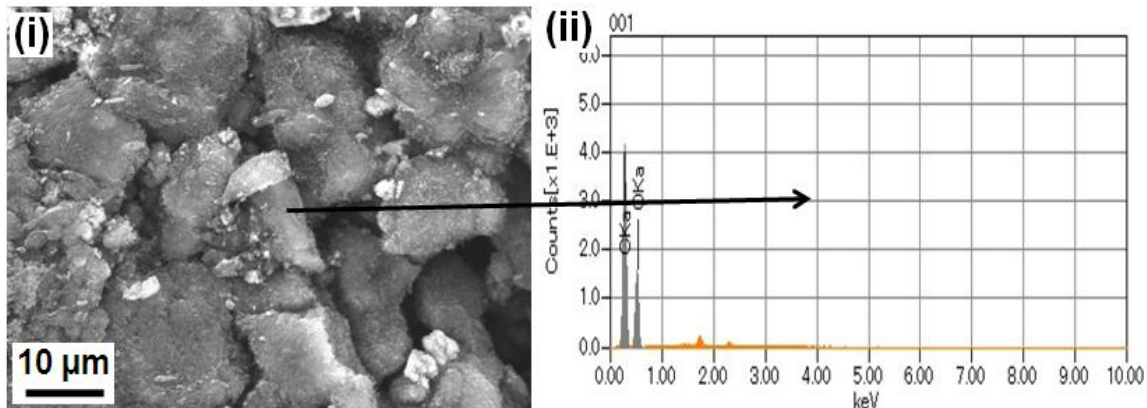
**Figure 2.2** – TEM images of (i) pure MWCNTs and (ii and iii) CuO/MWCNT (inset in ii; the size distribution of CuONPs); (iv), (v) and (iv) are high-resolution TEM images of CuO/MWCNT.

In order to determine the weight percentage of Cu and homogeneous distribution of CuONPs in CuO/MWCNT, SEM-EDS images [Figure 2.3(i) and (ii)] and their corresponding elemental mapping were taken for CuO/MWCNT [Figure 2.3(iii-v)].



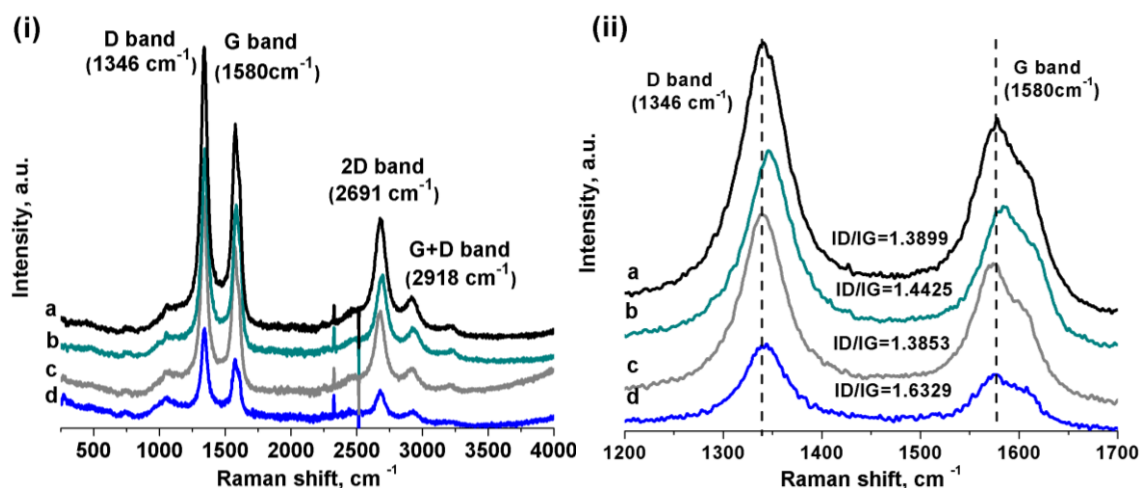
**Figure 2.3** – (i) SEM image and (ii) corresponding EDS spectrum of CuO/MWCNT, and EDS mapping of (iii) C, (iv) Cu and (v) O (inset in i, ii and iii, bottom, right: weight percentage).

The weight percentage of Cu was found to be 7.59 wt%. The ICP-MS result confirmed that the actual loading of Cu in CuO/MWCNT was 7.64 wt%, which agrees well with the SEM-EDS result. Interestingly, the reliability of the proposed method can be realized from the purity of CuO/MWCNT that contain only carbon, oxygen and copper as revealed by EDS analysis [Figure 2.3(iii-v)]. Similarly, SEM-EDS was also taken for *f*-MWCNTs in order to determine the presence of residual catalyst (Figure 2.4). The result showed that the *f*-MWCNTs contain only carbon and oxygen which confirmed the high purity of *f*-MWCNTs without any residual metal catalyst.



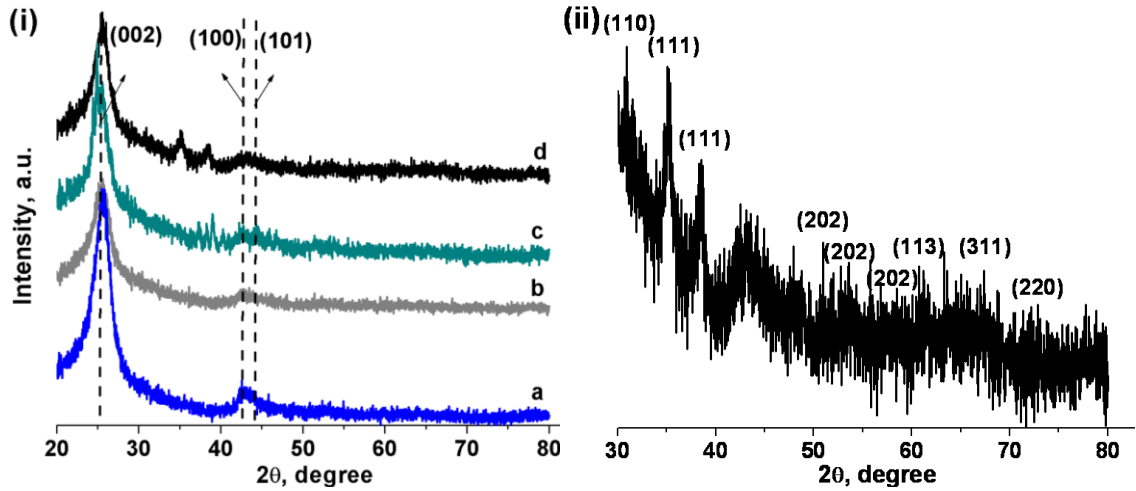
**Figure 2.4** – (i) SEM image and the corresponding (ii) EDS spectrum of *f*-MWCNTs.

Since the CuONPs were externally attached to the MWCNTs, it was vital to investigate the interaction between CuONPs and MWCNTs surface, therefore, Raman spectra were recorded for pure MWCNTs (a), *f*-MWCNTs (b), MWCNTs-Cu(OAc)<sub>2</sub> [MWCNTs and Cu(OAc)<sub>2</sub> mixture before calcination] (c) and CuO/MWCNT (d), under 532 nm excitation over the Raman shift interval of 250-4000 cm<sup>-1</sup> [Figure 2.5(i)]. The D and G bands observed at 1346 and 1580 cm<sup>-1</sup> corresponding to the sp<sup>3</sup>- and sp<sup>2</sup>-hybridized carbons in all the four samples [Figure 2.5(ii)] indicate the disordered graphite (D band) and the ordered state graphite (G band) of MWCNTs [33]. The two phonon D-band secondary peak (2D band) [34] was observed at 2691 cm<sup>-1</sup> which is the overtone of the D mode, and D+G-band was appeared at 2918 cm<sup>-1</sup>. It is well known that the ratios of D and G bands (*ID/IG*) intensities are often used as a diagnostic tool to measure the defect concentration in carbon materials including MWCNTs [33]. This intensity ratio was calculated for all the four samples and the calculated values were given in Figure 2.5(ii).



**Figure 2.5** – (i) Full and (ii) magnified Raman spectra of (a) pure MWCNTs, (b) *f*-MWCNTs, (c) MWCNTs + Cu(OAc)<sub>2</sub> mixture before calcination, and (d) CuO/MWCNT.

The data revealed that MWCNTs surface was functionalized by O=C–OH, –C=O and –C–OH groups as the *ID/IG* ratio was reasonably high for *f*-MWCNTs (1.4425) when compared to that of pure MWCNTs (1.3898). In addition, red shift was observed in the D band (1346 cm<sup>-1</sup> to 1351 cm<sup>-1</sup>) and G band (1580 cm<sup>-1</sup> to 1588 cm<sup>-1</sup>) for *f*-MWCNTs [35]. It is well known that the oxidative treatment introduces functional groups on the MWCNTs as well as responsible for shortening of the MWCNTs, which create more defect sites for further oxidation [36]. In fact, these functional groups can act as additional nucleation centers for CuONPs, which favor more homogeneous nucleation [31]. The calculated *ID/IG* ratio was very high for sample **d** (1.6329), which indicates the strong attachment of CuONPs with MWCNTs surface [37]. This higher *ID/IG* ratio of CuO/MWCNT is also an indication that the CuONPs prefer anchoring sites in the defect structures rather than in the perfect structures of MWCNTs [36]. Moreover, in all the cases analyzed, the absence of peaks around 1700 cm<sup>-1</sup> suggested that the present process produces fairly pure MWCNTs [38].



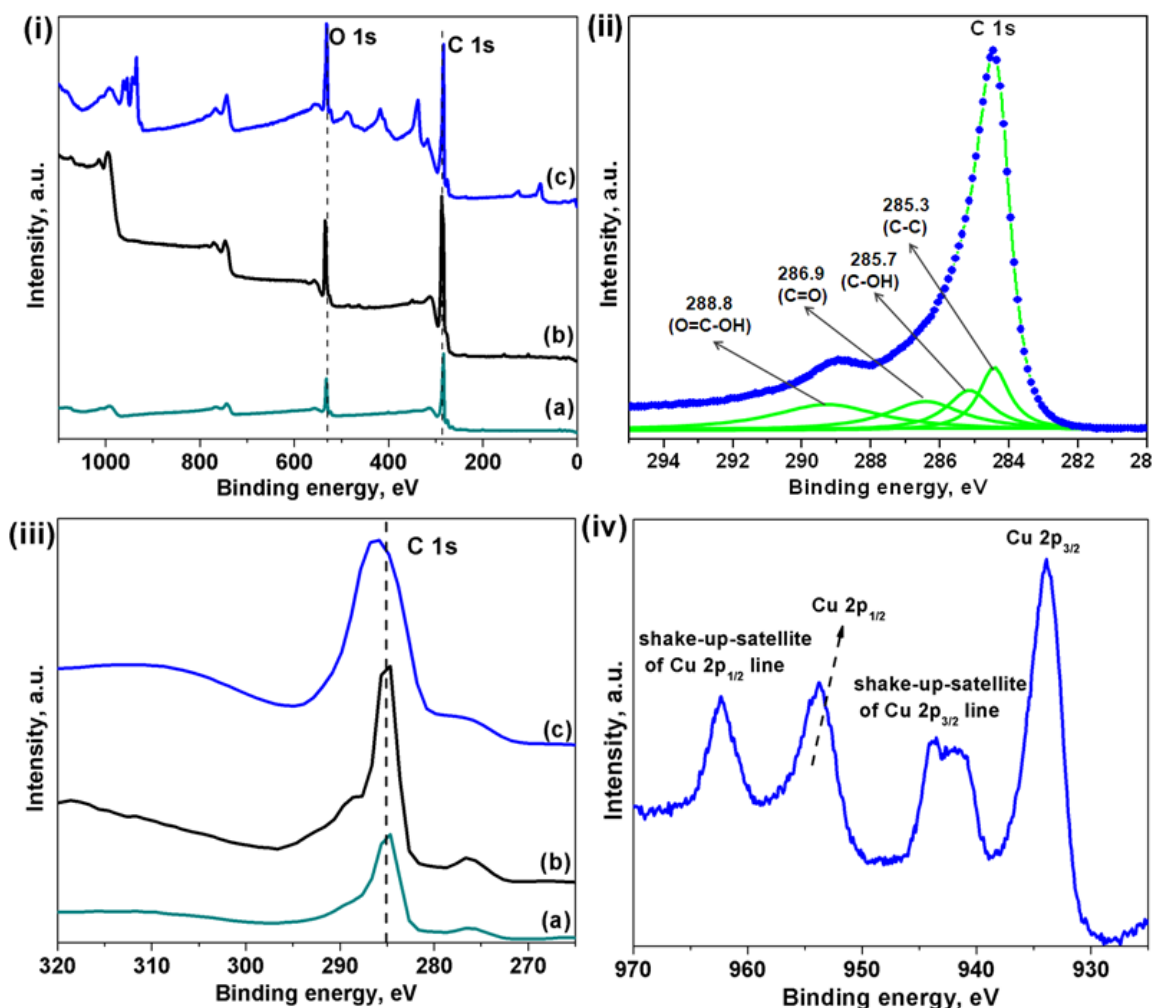
**Figure 2.6** – (i) WAXD pattern of (a) pure MWCNTs, (b) *f*-MWCNTs, (c) MWCNTs + Cu(OAc)<sub>2</sub>, and (d) CuO/MWCNT and (ii) magnified WAXD pattern of CuO/MWCNT.

Figure 2.6 shows WAXD patterns of pure MWCNTs (a), *f*-MWCNTs (b), MWCNTs + Cu(OAc)<sub>2</sub> (c), and CuO/MWCNT (d). In all the four samples the diffraction peaks are observed at 26.5°, 42.4°, and 44.2°, corresponding to the (002), (100) and (110) crystal planes of MWCNTs, respectively, which are attributed to the hexagonal graphite structures of MWCNTs [39]. The sample c exhibited a typical WAXD patterns for acetate groups (JCPDS 14-0733) at 40.0°, whereas the sample d [Figure 2.6(ii)] showed signature patterns (JCPDS 41-0254) at 32.0°, 35.5°, 38.5°, 48.5°, 53.5°, 58.0°, 61.5°, 66.0° and 67.5°, corresponding to the (110), (111), (111), (202), (020), (202), (113), (311) and (220) crystal planes of monoclinic phase of the CuO, respectively [40]. The absence of peaks at 40.0° in the sample d confirmed the complete conversion of Cu(OAc)<sub>2</sub> into CuO on the surface of MWCNTs. In addition, broadness of the diffraction peaks for the sample d revealed nano-crystalline nature of CuONPs. The crystallite size of CuO on MWCNTs was calculated using Scherrer's formula.

$$\text{Crystallite size} = K\lambda / \beta \text{ Cos } \theta \quad (1)$$

Where K is the shape factor (0.9),  $\lambda$  is the wavelength of X-rays (1.541 Å) and  $\beta$  is the full width half maxima. The crystallite size of CuO was found to be 22 nm, which agrees well with the results of TEM.

In order to investigate the formation of functional groups ( $\text{-C-OH}$ ,  $\text{-C=O}$  and  $\text{O=C-OH}$  groups) on MWCNTs and the chemical state of CuONPs, XPS spectra were recorded for MWCNTs, *f*-MWCNTs and CuO/MWCNT; the results are shown in Figure 2.7. As expected, all the three samples showed a C 1s peak and O 1s peak at 284.5 and 532.5 eV respectively. As can be seen from Figure 2.7(ii), the binding energy (BE) of the C-C and C-H bonds are assigned at 284.5–285 eV and the peaks at 285.7, 286.9 and 288.8 eV are attributed to  $\text{-C-OH}$ ,  $\text{-C=O}$  and  $\text{O=C-OH}$  groups respectively. The presence of oxygen functional groups makes MWCNTs hydrophilic and supports homogeneous decoration and good adhesion of CuONPs. In addition, this oxygen functional groups play a bridging role between the CuONPs and MWCNTs, hence, heterogeneous nucleation of CuONPs on the surface of MWCNTs obtained [36]. Particularly,  $\text{O=C-OH}$  group assists well decoration and adhesion of charged CuONPs by replacing the proton of carboxylic group of the *f*-MWCNTs [41].



**Figure 2.7** – (i) XPS spectra (a) MWCNTs, (b) *f*-MWCNTs and (c) CuO/MWCNT, (ii) magnified C 1s peak of *f*-MWCNTs, (iii) magnified C 1s peak of a, b and c, and (iv) main peaks of Cu 3p of CuO/MWCNT.

The XPS spectrum of the CuO/MWCNT in Cu 2p region [Figure 2.7(iii)] showed BE of Cu 2p<sub>3/2</sub> at 934.2 eV and Cu 2p<sub>1/2</sub> at 954.1 eV (with splitting of 19.9 eV) which correspond to the photoemission from CuO (Cu<sup>2+</sup>). Furthermore, the shake-up satellite peaks of the Cu 2p<sub>3/2</sub> and Cu 2p<sub>1/2</sub> at 942.4 and 962.6 eV (~9 eV greater than the corresponding main peaks) respectively, confirmed the formation of Cu<sup>2+</sup> [42]. In fact, the shake-up satellite feature is peculiar to the CuO that relates to d<sup>9</sup> configuration of

ground state of the Cu. However, in the case of  $\text{Cu}_2\text{O}$ , the d shell is completely filled, therefore, the screening *via* a charge transfer into the d states is not possible and hence the satellite peaks were absent. It is worth to mention that a positive shift in C 1s peak was observed for CuO/MWCNT in comparison with that of the *f*-MWCNTs; this proves there has been a strong interaction between MWCNTs and CuONPs. This positive shift also provides evidence for the decoration of CuONPs mainly on the defect sites of MWCNTs.

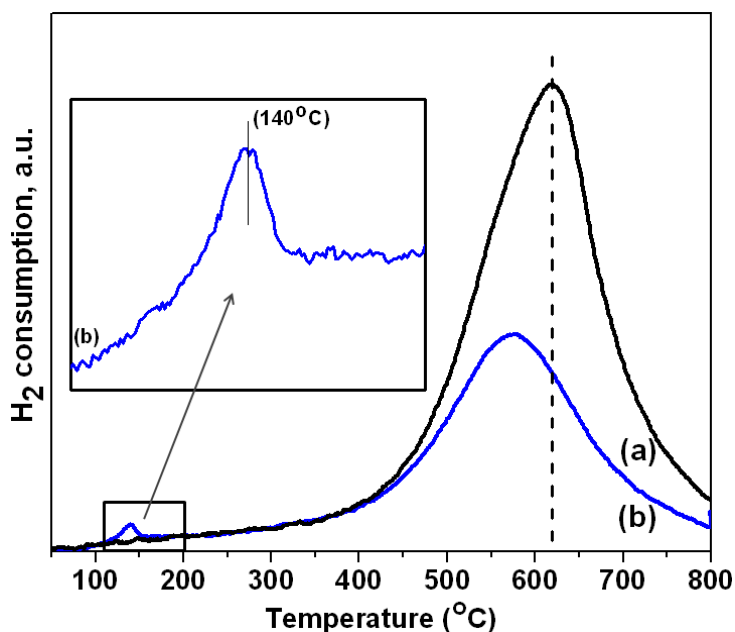


**Figure 2.8** – TPR profiles of (a) *f*-MWCNTs and (b) CuO/MWCNT.

The structure of CuO/MWCNT was further investigated in detail by TPR method. Figure 2.8 shows the TPR profile of pure *f*-MWCNTs and CuO/MWCNT. As can be seen from Figure 2.8, the characteristic reduction was observed between 110 and 190°C (maximum at 140°C) in CuO/MWCNT, which is ascribed to a two-step reduction of CuO by  $\text{H}_2$  as  $\text{CuO} \rightarrow \text{Cu}_2\text{O} \rightarrow \text{Cu}$  [43]. Whereas no peak was observed between 100 and

500°C in *f*-MWCNTs, which shows the absence of metal residues and confirms the high purity of *f*-MWCNTs as verified by SEM-EDS results. In comparison to bulk CuO (230°C), the reduction peak of CuO/MWCNT was found to be shifted to lower temperature; this implies that the CuONPs are very small, highly dispersed and strongly interacted with the MWCNTs support [43]. In addition, the CuONPs are attached mainly on the defect site of MWCNTs that could be easily reduced to Cu, because these defect sites have an ability to promote the electron transfer during the reduction process of CuONPs [44]. In the case of *f*-MWCNTs, only one broad peak between 500 and 750°C (maximum at 621°C) was observed, which may be due to the gasification of MWCNTs [43]. Interestingly, the reduction temperature of MWCNTs in the CuO/MWCNT (maximum at 575°C) was lower than that of *f*-MWCNTs (maximum at 621°C), which confirms a possible interaction of CuONPs with the defect sites on MWCNTs.

### 2.3.2 Optimization of reaction condition

In a preliminary study, we used imidazole and 4-chlorobenzonitrile as substrates and varied the solvent, base, amount of Cu and amount of catalyst, to find out the most effective reaction condition for *N*-arylation of imidazole (Table 2.1). In solvent optimization, various organic solvents such as dimethyl sulfoxide (DMSO), *N,N*-dimethylacetamide (DMAc), toluene and *N,N*-dimethylformamide (DMF) were used and the results are given in Table 2.1 (entries 1–4). The yield of 87% was obtained when DMAc was used (Table 2.1, entry 3).

**Table 2.1 – Optimization of reaction conditions for the CuO/MWCNT catalyzed *N*-arylation of imidazole (1a) with 4-chlorobenzonitrile (1b) to obtain *N*-arylated imidazole (1c)<sup>a</sup>**

entry	solvent	base	wt % of Cu	amount of catalyst (mol %)	yield <sup>b</sup> (%)
1	toluene	K <sub>2</sub> CO <sub>3</sub>	7.59	0.98	trace
2	DMSO	K <sub>2</sub> CO <sub>3</sub>	7.59	0.98	31
<b>3</b>	<b>DMAc</b>	<b>K<sub>2</sub>CO<sub>3</sub></b>	<b>7.59</b>	<b>0.98</b>	<b>87</b>
4	DMF	K <sub>2</sub> CO <sub>3</sub>	7.59	0.98	16
5	DMAc	KOH	7.59	0.98	no reaction
6	DMAc	K <sub>2</sub> PO <sub>4</sub>	7.59	0.98	3
7	DMAc	K- <sup>t</sup> OBu	7.59	0.98	5
8	DMAc	K <sub>2</sub> CO <sub>3</sub>	1.20	0.98	5
9	DMAc	K <sub>2</sub> CO <sub>3</sub>	3.31	0.98	12
10	DMAc	K <sub>2</sub> CO <sub>3</sub>	7.59	0	no reaction
11	DMAc	K <sub>2</sub> CO <sub>3</sub>	7.59	0.48	14
12	DMAc	K <sub>2</sub> CO <sub>3</sub>	7.59	1.44	21

<sup>a</sup>All the reactions were performed with CuO/MWCNT, 1 mmol (137 mg) of 4-chlorobenzonitrile, 1.2 mmol (81 mg) of imidazole, 2.0 mmol of base in 5 mL of solvent at 120°C for 24 h. <sup>b</sup>GC yield.

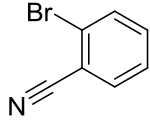
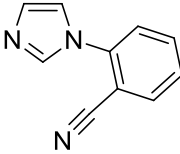
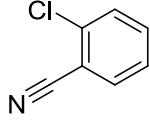
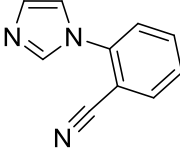
Subsequently, in base optimization (Table 2.1, entries 3, 5–7), potassium carbonate (2 mmol) was found to be the most efficient one (Table 2.1, entry 3) over other bases such as potassium hydroxide (KOH), potassium phosphate (K<sub>3</sub>PO<sub>4</sub>), and potassium tert-butoxide (K-<sup>t</sup>OBu). Different wt% of Cu supported on MWCNTs were investigated (Table 2.1, entries 3, 8 and 9) and the optimum quantity was found to be 7.59 wt% (Table

2.1, entry 3). As expected, no *N*-arylated product was obtained in the absence of CuO/MWCNT (Table 2.1, entry 10). The catalyst containing 7.59 wt% of Cu was used in different quantities to optimize the amount of the catalyst (Table 2.1, entries 3, 11 and 12). The optimum amount of CuO/MWCNT catalyst was found as low as 5 mg (0.98 mol%) and to the best of our knowledge, this is the lowest amount of Cu used for this reaction. Either less than or greater than 5 mg of CuO/MWCNT, decreased the yield of *N*-arylated imidazole (Table 2.1, entries 11 and 12). Finally, a blank run i.e., the reaction was carried out in the presence of pure *f*-MWCNTs, which showed no conversion after stirring at 120°C for 24 h. The optimized reaction conditions were opted to extend the scope of the *N*-arylation of imidazole with various aryl halides (Table 2.2).

### 2.3.3 Extension of scope

In an attempt to extend the scope of the above optimized methodology, the catalyst was applied to *N*-arylation of imidazole with various aryl halides and the results are presented in Table 2.2. It can be seen that the present catalytic system tolerates wide range of functional groups including –NO<sub>2</sub>, –CF<sub>3</sub>, –CHO and –COOH (Table 2.2). Both aryl bromides and aryl chlorides reacted with imidazole to yield *N*-arylated product in good yields (Table 2.2, entries 1-9). However, the yield obtained for aryl bromides (Table 2.2, entries 4, 5, 7 and 8) was better than the aryl chlorides (Table 2.2, entries 1-3), because the bromo group is a better leaving group compared to chloro.



10			47
11			44

<sup>a</sup>All the reactions were performed with 0.98 mol % of Cu (5.0 mg of CuO/MWCNT), 1 mmol of ArX, 1.2 mmol (81 mg) of imidazole, 2.0 mmol (276 mg) of K<sub>2</sub>CO<sub>3</sub> in 5 mL of DMAc at 120°C for 24 h. <sup>b</sup>GC yield. <sup>c</sup>Isolated yield.

Whereas inspections of entries 1, 10 and 11 in Table 2.2, confirmed that the *para*-substituted aryl halides provided a better yield in comparison to the *ortho*-substituted aryl halides. The poor yield of *ortho*-substituted aryl halides may be due to the steric-effect of cyano group in the *ortho* position [11]. The results obtained are promising in terms of catalytic activity under the optimized condition. The good catalytic activity of CuO/MWCNT may be due to two possible reasons: (i) higher surface area of MWCNTs and (ii) effective dispersion of the CuO/MWCNT in the reaction medium.

### 2.3.4 Effect of particle size on catalytic efficiency

The size of MNPs plays a very important role in heterogeneous catalysis. Therefore, we have investigated the effect of particle size of CuONPs in CuO/MWCNT on catalytic efficiency in terms of yields. For this purpose, another nanocatalyst with CuONPs size of around 60-80 nm [Figure 2.9(i) and (ii)] have been prepared using the procedure pursued for the preparation of CuO/MWCNT, however the calcination was carried out under air atmosphere at 450°C [46]. The weight percentage of Cu was 7.95 in

this catalyst [Figure 2.9(iii)]. The shake-up satellite peaks of the Cu  $2p_{3/2}$  and Cu  $2p_{1/2}$  observed at 942.4 and 962.6 eV respectively, confirmed the chemical state of Cu as +2 [Figure 2.9(iv)].

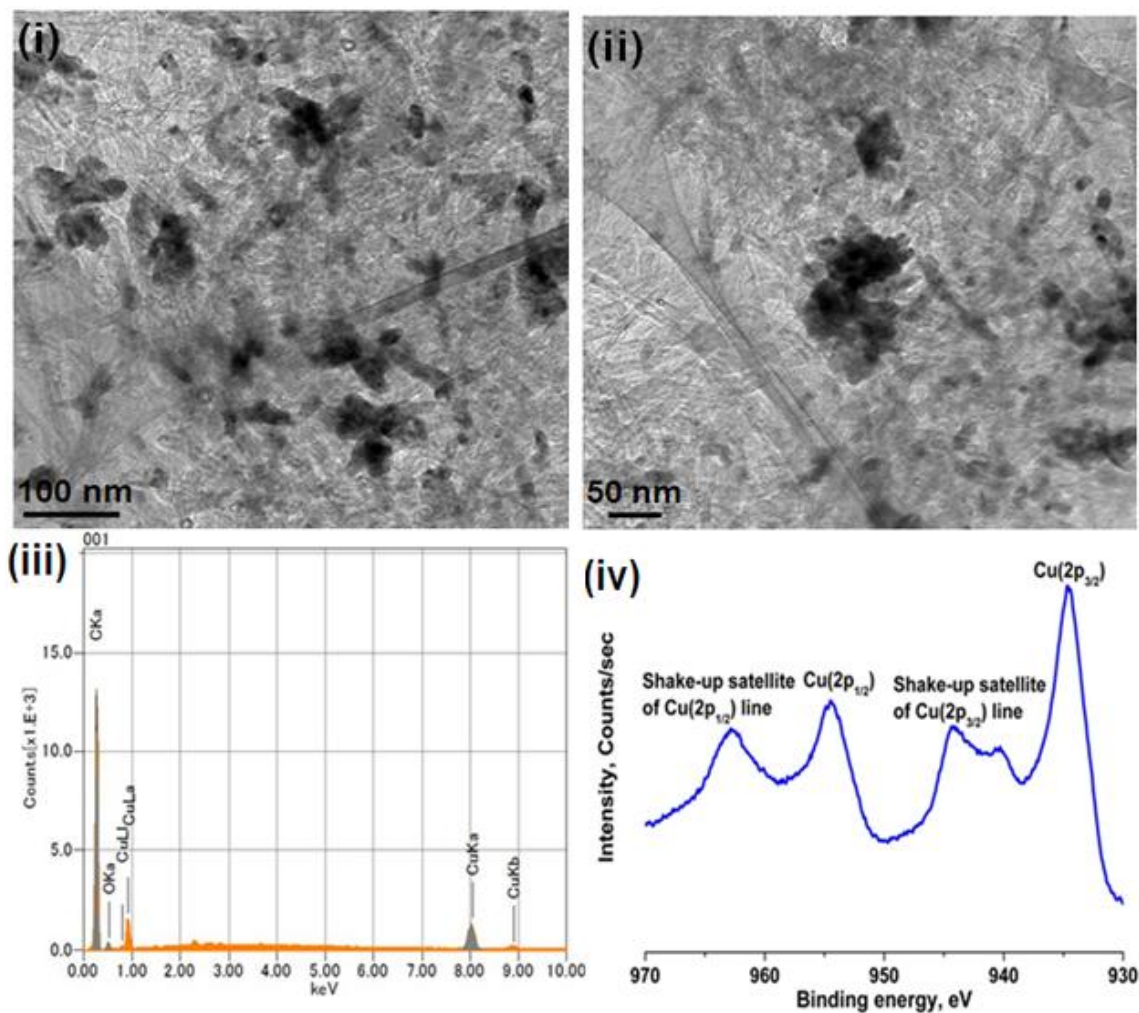


**Figure 2.9** – (i and ii) TEM images, (iii) EDS and (iv) XPS spectra survey (main and satellite peaks of Cu  $2p_{3/2}$  and Cu  $2p_{1/2}$  of the XPS spectra of Cu) of CuO/MWCNT (having 60-80 nm CuONPs).



surface area to volume ratio increases, obviously more number of active sites per unit area are available [11, 47]. Thus, the proposed catalyst exhibited better catalytic activity in terms of yields.

### **2.3.5 Heterogeneous nature of CuO/MWCNT**

In order to confirm the factual heterogeneity of the nanocatalyst, a hot-filtration test was performed for *N*-arylation of imidazole with 4-chlorobenzonitrile. In a typical experiment of 24 h, the nanocatalyst was separated out by simple centrifugation after 16 h when GC yield was 5%. Then stirring was continued without the catalyst for another 8 h and the reaction conversion was monitored at 2 h intervals; the results are shown in Figure 2.10(i). It is obvious from the results that no further conversion occurred after the nanocatalyst was separated out from the reaction mixture, which indicates that the *N*-arylation reaction of imidazole occurred only due to the solid CuO/MWCNT. Moreover, the conversion remained 5% even after 24 h of reaction time, which revealed that the Cu was not leached out from CuO/MWCNT during the *N*-arylation reaction. The filtrate was further analyzed by ICP-MS; only a negligible amount of Cu (10 ppb) was detected, which confirms the heterogeneous nature of the present catalytic system [45].

### **2.3.6 Reusability of CuO/MWCNT**

One of the unique features of nanocatalysts is their recovery and reusability, which make these viable and economical. In a typical experiment, the catalyst was recovered from the reaction mixture by simple centrifugation, and washed well with ethyl

acetate, dried in *vacuo* at 130°C and reused for *N*-arylation of imidazole with 4-chlorobenzonitrile; the results are shown in Figure 2.10(ii). Interestingly, the present catalytic system provided a good yield of 69% even at the 8<sup>th</sup> cycle, which indicates its good reusability. It is worth to mention that the reused CuO/MWCNT showed improved yields after calcination under argon atmosphere at 350°C for 2 h. At the 8<sup>th</sup> cycle, the calcined catalyst showed a better yield of 78% [Figure 2.10(ii)]. This may be due to complete or effective removal of adsorbed species or coupled products from CuONPs active sites during the calcination process, as a consequence, more number of active sites are available. Furthermore, in order to investigate the stability of CuO/MWCNT, the reused catalyst was investigated by TEM, SEM-EDS and XPS (Figure 2.11).

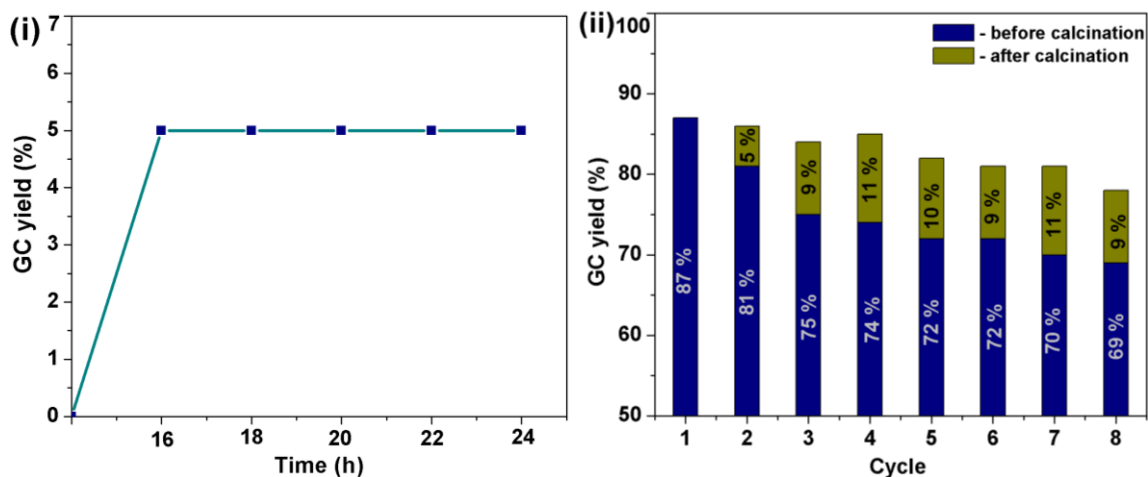


**Figure 2.10** – (i) Heterogeneity and (ii) recyclability of CuO/MWCNT for *N*-arylation of imidazole with 4-chlorobenzonitrile [Reaction condition: 81 mg of imidazole (1.2 mmol), 137 mg of 4-chlorobenzonitrile (1 mmol), CuO/MWCNT (0.98 mol % or 5 mg), 2 mmol of  $K_2CO_3$  (276 mg) and 5 mL of DMAc at 120°C for 24 h].

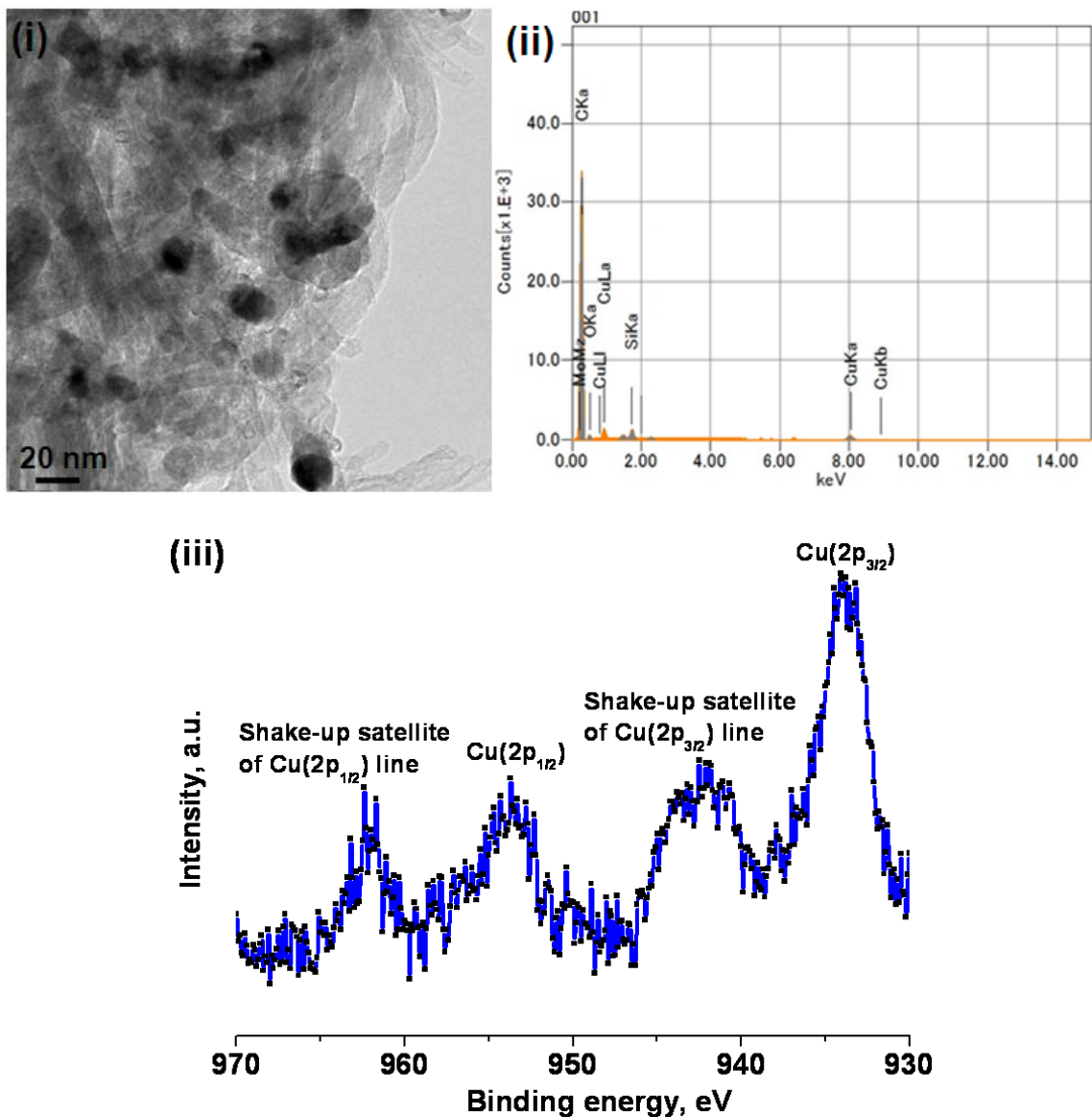


**Figure 2.11** – (i) TEM image, (ii) EDS and (iii) XPS spectrum of used CuO/MWCNT.

TEM images confirmed that the morphology has not been changed [Figure 2.11(i)]. The weight percentage of Cu was almost same as in the fresh catalyst as determined by EDS [Figure 2.11(ii)]. XPS of the used catalyst showed +2 oxidation state for Cu [Figure 2.11(iii)]. Hence it is concluded that CuO/MWCNT are physically and chemically stable.

### 2.3.7 Recovery of MWCNTs from the used nanocatalyst

As a matter of fact the MWCNTs are quite expensive and it is worth to be recovered after catalytic reactions. To the best of our knowledge, MWCNTs based nanocatalysts have limited versatility in terms of its recovery, which in our opinion, make many MWCNTs based nanocatalysts less affordable [46]. We report here the good recovery (4.3 mg of R-MWCNTs was recovered from the 5.0 mg of used CuO/MWCNT) of MWCNTs from used nanocatalyst; this is the hallmark of CuO/MWCNT.

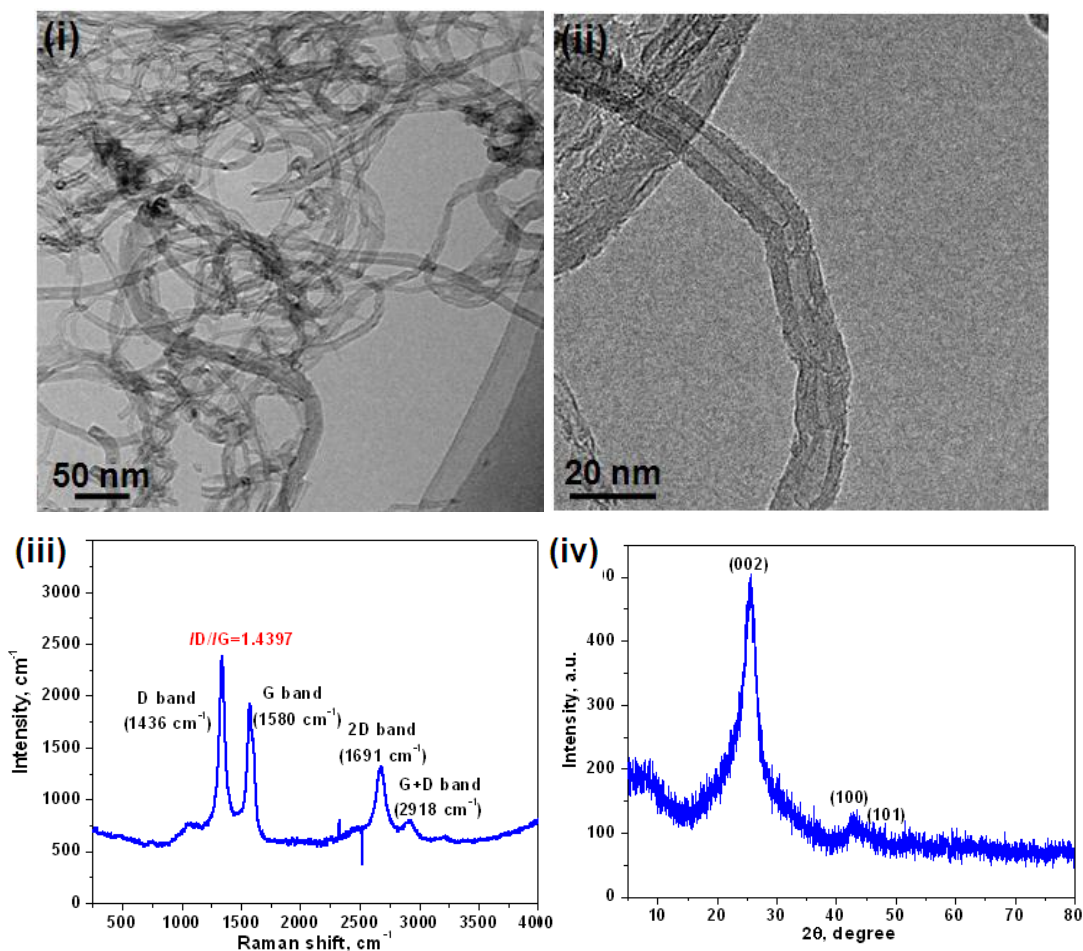


**Figure 2.12** – (i and ii) TEM images, (iii) Raman spectrum and (iv) WAXD pattern of R-MWCNTs.

The MWCNTs were recovered by simple chemical treatment and was further confirmed by TEM, Raman and WAXD. The TEM morphology of R-MWCNTs [Figure 2.12(i) and (ii)] showed that the R-MWCNTs did not contain residues of CuONPs; this purity confirms the successful recovery of MWCNTs from the used CuO/MWCNT. The diffraction peaks observed at 26.5°, 42.4°, and 44.2° for R-MWCNTs [Figure 2.12(iv)], are well correlated with the peaks observed for pure MWCNTs (Figure 2.6). The D and G bands in the Raman spectrum of R-MWCNTs [Figure 2.12(iii)] were observed at 1346 and 1580 cm<sup>-1</sup>, which correspond to the sp<sup>3</sup>- and sp<sup>2</sup>-hybridized carbons, which also agree well with the results obtained for MWCNTs (Figure 2.4). Moreover, the *ID/IG* ratio of R-MWCNTs is found to be 1.4425.

### 2.3.8 Proposed catalytic mechanism

The proposed mechanism for CuO/MWCNT-catalyzed *N*-arylation reaction has been provided in Figure 2.13. The catalytic reaction is expected to take place *via* adsorption followed by desorption (Figure 2.13). Firstly, heating the mixture of CuO/MWCNT and aryl halide may lead to the adsorption of the aryl halide species on the surface of the CuONPs. Due to the adsorption of aryl halide species on CuONPs, the positive charge was developed and the excess charge might be shared among the CuONPs. Since the MWCNTs are highly conductive the created excess charge may assist good dispersion of charged CuONPs on MWCNTs support and consequently exhibit more feasible adsorption of the aryl halide species on the surface of CuONPs [47, 48]. Secondly, the adsorbed aryl halide species undergoes reaction with imidazole and base. Thirdly, the catalytic cycle is completed by the desorption of coupled products.

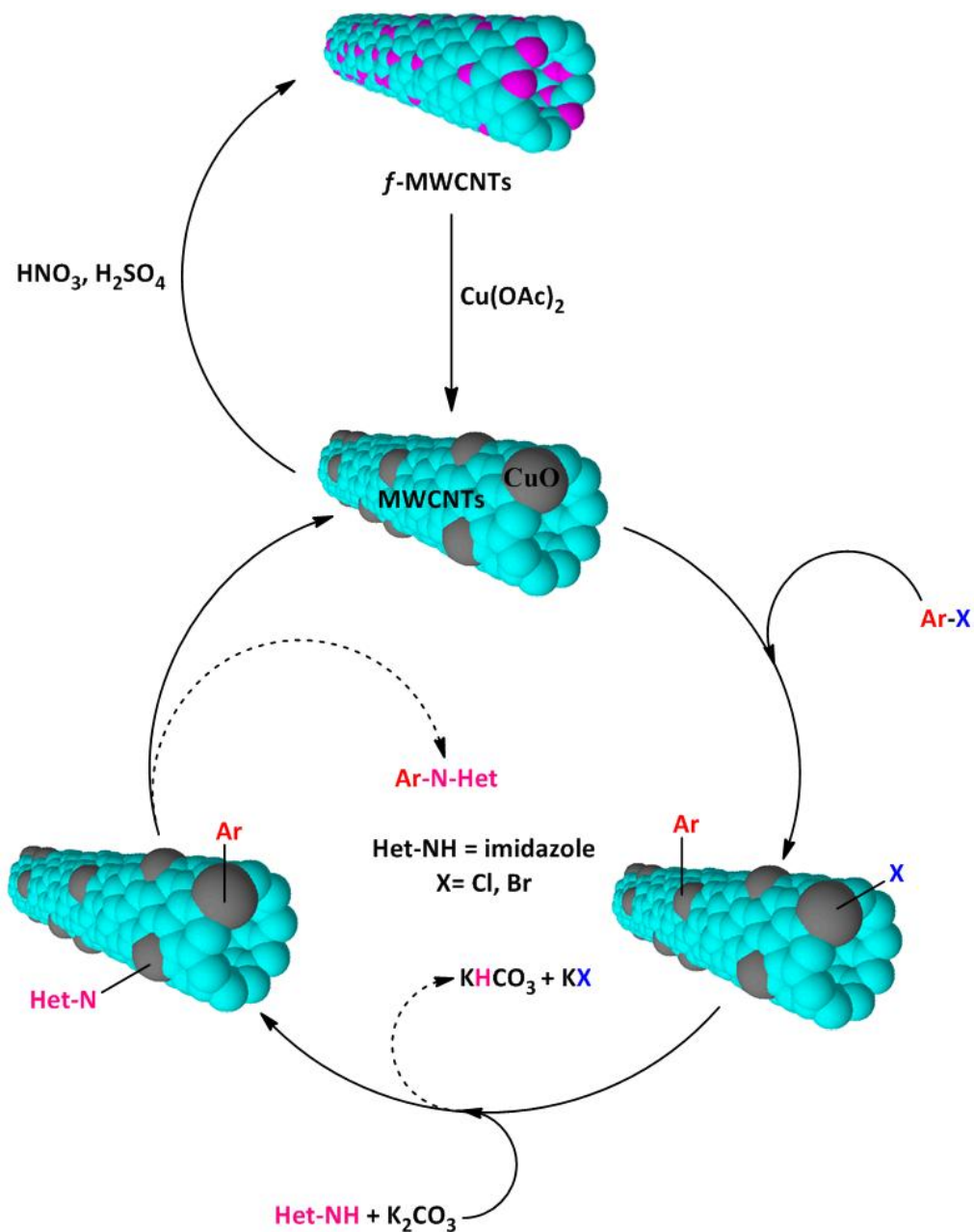


**Figure 2.13** – Possible mechanism of *N*-arylation of imidazole with aryl halide.

Either less than or greater than 5 mg of catalyst, decreased the yield of products (Table 2.1, entries 14 and 16); this observation well supports the proposed mechanism. When the amount of CuO/MWCNT is increased, imidazole and aryl ions might not be adsorbed close enough to interact effectively. In the same way, while the catalyst amount

is decreased, there may not be adequate number of active sites for the adsorption of substrates. Apart from the catalytic reaction, the *f*-MWCNTs can be recovered from the used CuO/MWCNT by simple acid treatment.

## 2.4 Conclusions

We have successfully decorated CuONPs on MWCNTs by a straight forward “mix and heat” method. The resultant material behaves as efficient catalysts for *N*-arylation of imidazole with various aryl halides. The stoichiometric amount of CuO/MWCNT catalyst was found as low as 5 mg (0.98 mol % of Cu) and to the best of our knowledge, this is the lowest amount of Cu used for this reaction. The good yields of products are mainly due to the smaller particle size of the CuONPs. The proposed catalyst is chemically as well as physically very stable, heterogenous in nature and reusable. The main feature of CuO/MWCNT nanocatalysts is the recovery of pure MWCNTs from the used nanocatalyst by the simple acid treatment. The recovered MWCNTs can be used for any further applications. In summary, we have developed a ligand free and heterogeneous Cu based nanocatalytic system for *N*-arylation of imidazole, which requires a lower amount of catalyst (0.98 mol% of Cu) to be effective.

## References

- [1] Gungor, T.; Fouquet, A.; Teulon, J. M.; Provost, D.; Cazes, M.; Cloarec, A.; Cardiotoxic Agents, Synthesis and Cardiovascular Properties of Novel 2-Arylbenzimidazoles and Azabenzimidazoles. *J. Med. Chem.* **1992**, *35*, 4455–4463.
- [2] Leeson, P. D.; Springthorpe, B. The Influence of Drug-Like Concepts on Decision-Making in Medicinal Chemistry. *Nat. Rev. Drug Discov.* **2007**, *6*, 881–890.
- [3] Zhang, W.; Ramamoorthy, Y.; Kilicarslan, T.; Nolte, H.; Tyndale, R. F.; Sellers, E. M. Inhibition of Cytochrome P450 by Antifungal Imidazole Derivatives. *Drug. Metab. Dispos.* **2002**, *30*, 314–318.
- [4] Silverman, R. M. *The Organic Chemistry of Drug Design and Drug Action*, Academic Press, New York, **1992**.
- [5] Ullmann, F. Ueber Eine Neue Bildungsweise Von Diphenylaminderivaten. *Chem. Ber.* **1903**, *36*, 2382–2384.
- [6] Goldberg, I. Ueber Phenylirungen Bei Gegenwart Von Kupfer Als Katalysator. *Chem. Ber.* **1906**, *39*, 1691–1692.
- [7] Strieter, E. R.; Bhayana, B.; Buchwald, S. L. Mechanistic Studies on the Copper-Catalyzed *N*-Arylation of Amides. *J. Am. Chem. Soc.* **2009**, *131*, 78–88.
- [8] Lindley, J. Copper Assisted Nucleophilic Substitution of Aryl Halogen. *Tetrahedron* **1984**, *40*, 1433–1456.
- [9] Ayumu, K.; Jean-Francois, M.; Stephen, L. B. An Efficient Copper-Catalyzed Coupling of Aryl Halides with Imidazoles. *Tetrahedron. Lett.* **1999**, *40*, 2657–2660.

- [10] Yi, W.; Zhiqing, W.; Lixia, W.; Zhengkai, L.; Xiangge, Z. A Simple and Efficient Catalytic System for *N*-Arylation of Imidazoles in Water. *Chem. Eur. J.* **2009**, *15*, 8971–8974.
- [11] Ganesh Babu, S.; Karvembu, R. CuO Nanoparticles: A Simple, Effective, Ligand Free, and Reusable Heterogeneous Catalyst for *N*-Arylation of Benzimidazole. *Ind. Eng. Chem. Res.* **2011**, *50*, 9594–9600.
- [12] Lakshmi Kantam, M.; Jagjit, Y.; Soumi, L.; Bojja, S.; Shailendra, J. *N*-Arylation of Heterocycles with Activated Chloro- and Fluoroarenes Using Nanocrystalline Copper(II) Oxide. *Adv. Synth. Catal.* **2007**, *349*, 1938–1942.
- [13] Mandal, S.; Roy, D.; Chaudhari, R. V.; Sastry, M. Pt and Pd Nanoparticles Immobilized on Amine-Functionalized Zeolite: Excellent Catalysts for Hydrogenation and Heck Reactions. *Chem. Mater.* **2004**, *16*, 3714–3724.
- [14] Michael, T. W.; Brian, J. H.; Rajesh, M. K.; Philip, D. W.; Marisa, C. K. Copper-Catalyzed *N*-Arylation of Hindered Substrates under Mild Conditions. *Adv. Synth. Catal.* **2009**, *351*, 931–937.
- [15] Ley, S. V.; Thomas, A. W. Modern Synthetic Methods for Copper-Mediated C(aryl)–O, C(aryl)–N, and C(aryl)–S Bond Formation. *Angew. Chem. Int. Ed.* **2003**, *42*, 5400–5449.
- [16] Mark, K.; Koen Bekedam, E.; Gerben, M. V.; Hoogenband, A. V. D.; Terpstra, J. W.; Kamer, P. C. J.; Piet van Leeuwena, W. N. M.; Gino van Strijdoncka, P. F. Mild Copper-Catalyzed *N*-Arylation of Azaheterocycles with Aryl Halides. *Tetrahedron. Lett.* **2005**, *46*, 2405–2409.
- [17] Roisson, P.; Brunelle, J. P.; Nortier, P. Catalyst Supports and Supported Catalysts,

Butterworth, Boston, **1987**.

- [18] Ando, Y.; Zhao, X.; Kataura, H.; Achiba, Y.; Kaneto, K.; Tsuruta, M.; Uemura, S.; Iijima S. Multiwalled Carbon Nanotubes Prepared by Hydrogen Arc. *Diam. Relat. Mater.* **2000**, *9*, 847–851.
- [19] Endo, M.; Kim, Y. A.; Hayashi, T.; Nishimura, K.; Matusita, T.; Miyashita, K.; Dresselhaus, M. S. Vapor-Grown Carbon Fibers (VGCFs): Basic Properties and Their Battery Applications. *Carbon* **2011**, *39*, 1287–1297.
- [20] Planeix, J. M.; Coustel, N.; Coq, B.; Bretons, V.; Kumbhar, P. S.; Geneste, R. D. P.; Bernier, P.; Ajayan, P. M. Application of Carbon Nanotubes as Supports in Heterogeneous Catalysis. *J. Am. Chem. Soc.* **1994**, *116*, 7935–7936.
- [21] Philippe, S.; Eva, C. Catalysis in Carbon Nanotubes. *Chem. Cat. Chem.* **2010**, *2*, 1–47.
- [22] Ovejero, G.; Sotelo, J. L.; Rodriguez, A.; Diaz, C.; Sanz, R.; Garcia, J. Platinum Catalyst on Multiwalled Carbon Nanotubes for the Catalytic Wet Air Oxidation of Phenol. *Ind. Eng. Chem. Res.* **2007**, *46*, 6449–6455.
- [23] Yoon, B.; Pan, H. B.; Wai, C. M. Relative Catalytic Activities of Carbon Nanotube-Supported Metallic Nanoparticles for Room-Temperature Hydrogenation of Benzene. *J. Phys. Chem. C* **2009**, *113*, 1520–1525.
- [24] Wu, G.; Xu, B. Q. Carbon Nanotube Supported Pt Electrodes for Methanol Oxidation: A Comparison between Multi- and Single-Walled Carbon Nanotubes. *J. Power. Sour.* **2007**, *174*, 148–158.
- [25] Wu, B.; Kuang, Y.; Zhang, X.; Chen, J. Noble Metal Nanoparticles/Carbon Nanotubes Nanohybrids: Synthesis and Applications. *Nano Today* **2011**, *6*, 75–90.

- [27] Tessonnier, J. P.; Pesant, L.; Ehret, G.; Ledoux, M.; Pham-Huu, C. Pd Nanoparticles Introduced Inside Multi-Walled Carbon Nanotubes for Selective Hydrogenation of Cinnamaldehyde into Hydrocinnamaldehyde. *Appl. Catal. A: Gen.* **2005**, *288*, 203–210.
- [28] Cano, M.; Benito, A.; Maser, W. K.; Urriolabeitia, E. P. One-Step Microwave Synthesis of Palladium–Carbon Nanotube Hybrids with Improved Catalytic Performance. *Carbon* **2011**, *49*, 652–658.
- [29] Yoon, B.; Wai, C. M. Microemulsion-Templated Synthesis of Carbon Nanotube-Supported Pd and Rh Nanoparticles for Catalytic Applications. *J. Am. Chem. Soc.* **2005**, *127*, 17174–17175.
- [30] Wildgoose, G. G.; Banks, C. E.; Compton, R. G. Metal Nanoparticles and Related Materials Supported on Carbon Nanotubes: Methods and Applications. *Small* **2006**, *2*, 182–193.
- [31] Lin, Y.; Watson, K. A.; Fallbach, M. J.; Ghose, S.; Smith, J. G.; Delozier, D. M.; Cao, W.; Crooks, R. E.; Connell, J. W. Rapid, Solventless, Bulk Preparation of Metal Nanoparticle-Decorated Carbon Nanotubes. *ACS Nano* **2009**, *3*, 871–884.
- [32] Tsang, S. C.; Chen, Y. K.; Harris, P. J. F.; Green, M. L. H. A Simple Chemical Method of Opening and Filling Carbon Nanotubes. *Nature* **1994**, *372*, 159–162.
- [33] Liu, J.; Rinzler, A. G.; Dai, H.; Hafner, J. H.; Bradley, R. K.; Boul, P. J.; Lu, A.; Iverson, T.; Shelimov, K.; Huffman, C. B.; Rodriguez-Macias, F.; Shon, Y. S.; Lee, T. R.; Colbert, D. T.; Smalley, R. Fullerene Pipes. *Science* **1998**, *280*, 1253–1255.
- [34] Dresselhaus, M. S.; Dresselhaus, G.; Saito, R.; Jorio, A. Raman Spectroscopy of Carbon Nanotubes. *Phys. Rep.* **2005**, *409*, 47–99.

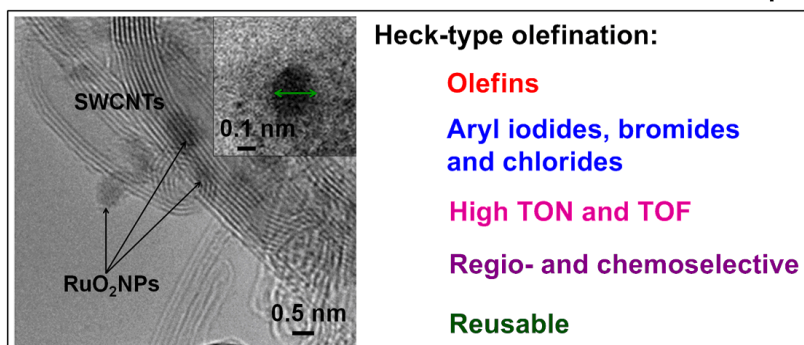
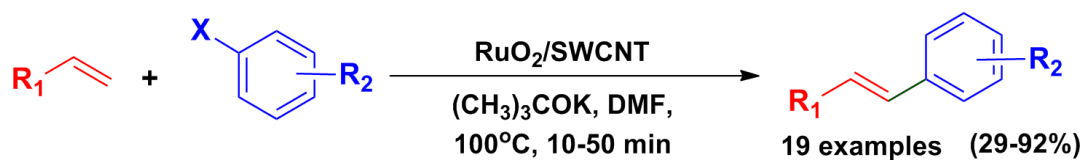
- [35] Moreno, J. M. C.; Yoshimura, M. Hydrothermal Processing of High-Quality Multiwall Nanotubes from Amorphous Carbon. *J. Am. Chem. Soc.* **2001**, *123*, 741–742.
- [36] Simmons, T. J.; Bult, J.; Hashim, D. P.; Linhardt, R. J.; Ajayan, P. M. Noncovalent Functionalization as an Alternative to Oxidative Acid Treatment of Single Wall Carbon Nanotubes with Applications for Polymer Composites. *ACS Nano* **2009**, *3*, 865–870.
- [37] Datsyuk, V.; Kalyva, M.; Papagelis, K.; Parthenios, J.; Tasis, D.; Siokou, A.; Kallitsis, I.; Galiotis, C. Chemical Oxidation of Multiwalled Carbon Nanotubes. *Carbon* **2008**, *46*, 833–840.
- [38] Souza Filho, A. G.; Meunier, V.; Terrones, M.; Sumpter, B. G.; Barros, E. B.; Villalpando-Paez, F.; Filho, J. M.; Kim, Y. A.; Muramatsu, H.; Hayashi, T.; Endo, M.; Dresselhaus, M. S.; Selective Tuning of the Electronic Properties of Coaxial Nanocables through Exohedral Doping. *Nano Lett.* **2007**, *7*, 2383–2388.
- [39] Delzeit, L.; Nguyen, C. V.; Chen, B.; Stevens, R.; Cassell, A.; Han, J.; Meyyappan, M.; Multiwalled Carbon Nanotubes by Chemical Vapor Deposition using Multilayered Metal Catalysts. *J. Phys. Chem. B* **2002**, *106*, 5629–5635.
- [40] Li, W.; Liang, C.; Zhou, W.; Qiu, J.; Zhou, Z.; Sun, G.; Qin, X. Preparation and Characterization of Multiwalled Carbon Nanotube-Supported Platinum for Cathode Catalysts of Direct Methanol Fuel Cells. *J. Phys. Chem. B* **2003**, *107*, 6292–6299.
- [41] Zhang, P.; Zhang, L.; Zhao, G.; Feng, F. A Highly Sensitive Nonenzymatic Glucose Sensor Based on CuO Nanowires. *Microchim. Acta.* **2012**, *176*, 411–417.

- [42] Shrestha, S.; Choi, W. C.; Song, W.; Kwon, Y. T.; Shrestha, S. P.; Park, C. Y.; Preparation and Field Emission Properties of Er-Decorated Multiwalled Carbon Nanotubes. *Carbon* **2010**, *48*, 54–59.
- [43] Chusuei, C. C.; Brookshier, M. A.; Goodman, D. W. Correlation of Relative X-ray Photoelectron Spectroscopy Shake-up Intensity with CuO Particle Size. *Langmuir* **1999**, *15*, 2806–2808.
- [44] Bian, J.; Xiao, M.; Wang, S. J.; Lu, Y. X.; Meng, Y. Z. Carbon Nanotubes Supported Cu–Ni Bimetallic Catalysts and their Properties for the Direct Synthesis of Dimethyl Carbonate from Methanol and Carbon Dioxide. *Appl. Surf. Sci.* **2009**, *255*, 7188–7196.
- [45] Shaoqing, S.; Shujuan, J. Selective Catalytic Oxidation of Ammonia to Nitrogen Over CuO/CNTs: The Promoting Effect of the Defects of CNTs on the Catalytic Activity and Selectivity. *Appl. Catal. B: Environ.* **2012**, *117*, 346–350.
- [46] Webb, J. D.; MacQuarrie, S.; McEleney, K.; Crudden, C. M.; Mesoporous Silica-Supported Pd Catalysts: An Investigation into Structure, Activity, Leaching and Heterogeneity. *J. Catal.* **2007**, *252*, 97–109.
- [47] Oh, S. W.; Bang, H. J.; Bae, Y. C.; Sun, Y. K. Effect of Calcination Temperature on Morphology, Crystallinity and Electrochemical Properties of Nano-Crystalline Metal Oxides (Co<sub>3</sub>O<sub>4</sub>, CuO, and NiO) Prepared *via* Ultrasonic Spray Pyrolysis. *J. Power. Sour.* **2007**, *173*, 502–509.

- [48] Bell, A. T. The Impact of Nanoscience on Heterogeneous Catalysis. *Science* **2003**, 299, 1688–1691.

## CHAPTER 3

### Highly active, selective and reusable RuO<sub>2</sub>/SWCNT catalyst for Heck olefination of aryl halides



## CHAPTER 3

### Highly active, selective and reusable RuO<sub>2</sub>/SWCNT catalyst for Heck olefination of aryl halides

#### 3.1 Introduction

The transition metal-catalyzed C–C cross coupling reaction is a key step in the synthesis of organic building blocks, natural products, pharmaceuticals, and agricultural derivatives [1]. Certainly, Pd-catalyzed olefination of aryl halides (Heck-Mizoroki reaction) is one of the most powerful tools for the construction of C–C bonds [2]. In fact, the Pd-based catalytic systems are highly efficient and they generally offer excellent product yields with good selectivity. In spite of that, they often suffer from three major problems: (i) the use of expensive phosphine ligands for the stabilization of Pd active species, (ii) utilization of highly volatile solvents, and (iii) very low reactivity towards aryl chlorides [3]. Moreover, homogeneous Pd catalysts can be easily precipitated in the reaction mixtures; therefore, the recovery and the reusability of the catalysts are highly complicated [4]. To overcome these issues, polymers [5] and metal oxides [6] have been used as supports for the immobilization of Pd complexes. Later, due to high activity, easy separation and reusability, Pd nanoparticles (NPs) gained importance [7]. Nevertheless, the catalytic systems require hindered phosphines and amines as ancillary ligands with a stoichiometric amount of the catalyst for the activation of aryl chlorides. Recently, the use of other MNPs such as Cu [8], Ni [9], Fe [10], Rh [11] and Ir [12] has been reported for the Heck-type olefination of aryl halides. Although they have shown good catalytic activity

in the Heck coupling reactions, the scope and functional group tolerance of these catalytic systems are generally limited. Therefore, developing an efficient catalytic system for the Heck-type olefination is a challenging task.

In the past few years, RuNPs-catalyzed cross coupling reactions were found to be an effective tool for the construction of C–C bond [13]. Na *et al.*, [14] employed Ru/Al<sub>2</sub>O<sub>3</sub> catalyst for both the Heck olefination and Suzuki coupling reactions. They found that Ru/Al<sub>2</sub>O<sub>3</sub> catalyst is highly effective and reusable; but, bromo- and chloroarenes are less reactive. Hence, there is a continuous exploration for a better heterogeneous Ru-based catalytic system for the Heck coupling reaction. According to Joo *et al.*, [15] activity of the supported MNPs catalyst is dependent on three main factors: (i) nature of the support, (ii) metal-support interaction, and (iii) particle size. Indeed, single-walled carbon nanotube (SWCNT) is one of the promising supports for active metal catalysts in heterogeneous catalysis and trustable due to its astounding properties such as high specific surface area, and chemical as well as electrochemical inertness [16]. Recently, Krashennnikov *et al.*, [17] demonstrated that the inert SWCNT can be transformed to a very active catalyst through the interactions between the active metal clusters and carbon vacancies. We presumed that the decoration of a very fine RuO<sub>2</sub>NPs can transform the SWCNT to a very active catalyst for the Heck olefination reaction. In this study, ultrafine RuO<sub>2</sub>NPs were decorated over SWCNT by a simple ‘dry synthesis’ method and used as a nanocatalyst for the Heck olefination of aryl halides. Regioselectivity and chemoselectivity of RuO<sub>2</sub>/SWCNT-catalyzed Heck olefination reaction were investigated. Moreover, heterogeneity, reusability and stability of RuO<sub>2</sub>/SWCNT were also examined.

## 3.2 Experimental section

### 3.2.1 Materials and characterization

High-purity SWCNT (>90%) with diameter ranging from 0.7 to 1.3 nm was purchased from Sigma Aldrich and used as received. All other chemicals were purchased from Sigma Aldrich or Wako pure chemicals, Japan.

The surface morphology of RuO<sub>2</sub>/SWCNT was investigated on a JEOL JEM-2100F HR-TEM with the accelerating voltage of 200 kV. To quantify the weight percentage of Ru in RuO<sub>2</sub>/SWCNT, SEM-EDS was recorded using Hitachi 3000H SEM. The same field of view was then scanned using an EDS spectrometer to acquire a set of X-ray maps for Ru, C, and O using 1 ms point acquisition for approximately one million counts. Raman spectrometer (Hololab 5000, Kaiser Optical Systems Inc., USA) was applied to examine the interaction between RuO<sub>2</sub>NPs and SWCNT. The Ar laser was operated at 532 nm with a Kaiser holographic edge filter. XRD experiment was performed at room temperature using a Rotaflex RTP300 (Rigaku Co., Japan) diffractometer at 50 kV and 200 mA. Nickel-filtered Cu K<sub>α</sub> radiation ( $5 < 2\theta < 80^\circ$ ) was used for XRD measurements. XPS (Kratos Axis-Ultra DLD, Kratos Analytical Ltd, Japan) was recorded to confirm the chemical state of Ru in RuO<sub>2</sub>/SWCNT. During the XPS analysis, the sample was irradiated with Mg K<sub>α</sub> ray source. The conversion of the reactants and the yield of coupled products were determined using gas chromatograph (Shimadzu, GC-2014). The heterogeneity of the RuO<sub>2</sub>/SWCNT was tested using inductively coupled plasma-mass spectrometer (ICP-MS, 7500CS, Agilent). NMR

spectra were recorded on a 400 MHz Bruker spectrometer using tetramethylsilane (TMS) as a standard.

### 3.2.2 Dry Synthesis of RuO<sub>2</sub>/SWCNT

Functional groups such as C=O, COOH, C–OH and C–O–C are very important anchoring sites for metal NPs, which assists homogeneous decoration and good adhesion of metal NPs on SWCNT [18]. Hence, at first, SWCNTs were treated with acid. In a typical procedure, 1.0 g of SWCNTs were chemically treated with a 3:1 mixture of conc. H<sub>2</sub>SO<sub>4</sub> and HNO<sub>3</sub>, and then the mixture was sonicated at 40°C for 4 h in ultrasonic bath. After cooling to 21°C, the solution mixture was diluted with 1000 mL of deionized water and then vacuum-filtered through a filter paper of 0.65 μm porosity. The resultant solid (*f*-SWCNTs) was washed with deionized water until the pH became neutral and then dried in *vacuo* at 60°C. After that, 0.13 g of Ru(acac)<sub>3</sub> was added into 0.5 g of *f*-SWCNTs and mixed well by a mortar and pestle. The homogeneous mixture of *f*-SWCNTs and Ru(acac)<sub>3</sub> was obtained in 13-15 minutes. Finally, the mixture was calcinated under nitrogen atmosphere at 350°C for 3 h in a muffle furnace. Figure 3.1 shows schematic illustration of the procedure for the preparation of RuO<sub>2</sub>/SWCNT.

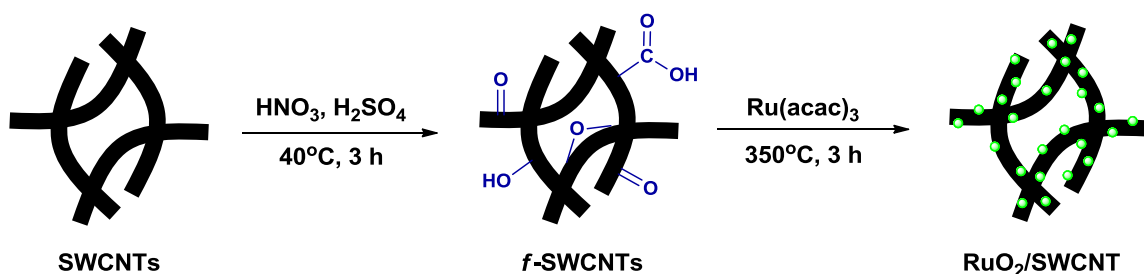


**Figure 3.1** – Schematic illustration for the preparation of RuO<sub>2</sub>/SWCNT.

### 3.2.3 Procedure for Heck olefination reaction

In a typical procedure, RuO<sub>2</sub>/SWCNT (5 mg, 0.9 mol%) was added into a mixture of styrene (343 μL, 3.0 mmol), iodobenzene (111 μL, 1.0 mmol) and (CH<sub>3</sub>)<sub>3</sub>COK (224 mg, 2.0 mmol) in DMF, and stirred at 100°C for 10 minutes. After the completion of reaction, the RuO<sub>2</sub>/SWCNT was separated out from the reaction mixture *via* centrifugation and then the separated nanocatalyst was washed well with diethyl ether and dried in an oven at 60°C for 5 h. On the other hand, the centrifugate was partitioned between 15 mL of ethyl acetate and 10 mL of saturated aqueous sodium hydrogen carbonate. Subsequently, the organic layer was separated out and dried over anhydrous magnesium sulphate. The yield of olefinated product was determined by GC. Finally, the organic layer was concentrated to obtain the coupled product. The products were confirmed by <sup>1</sup>H and <sup>13</sup>C NMR spectra.

***trans*-Stilbene (3a):** <sup>1</sup>H NMR (400 MHz, DMSO-d<sub>6</sub>): δ (ppm) 7.12 (s, 2H), 7.26 (t, 2H), 7.36 (t, 4H), 7.72 (d, *J* = 8.0 Hz, 4H); <sup>13</sup>C NMR (400 MHz, DMSO-d<sub>6</sub>): δ (ppm) 126.5, 127.5, 129.0, 130.0, 137.7.

**1-Isopropyl-4-styrylbenzene (3b):** <sup>1</sup>H NMR (400 MHz, DMSO-d<sub>6</sub>): δ (ppm) 1.31 (d, *J* = 8.0 Hz, 6H), 2.79 (m, 1H), 6.78 (2, 2H), 7.12-7.15 (m, 3H), 7.35-7.38 (m, 2H), 7.58-7.61 (m, 4H); <sup>13</sup>C NMR (400 MHz, DMSO-d<sub>6</sub>): δ (ppm) 28.7, 34.5, 115.3, 118.5, 128.6, 128.8, 129.9, 130.9, 133.3, 137.4, 149.9.

**4-Methoxy-*trans*-stilbene (3d):** <sup>1</sup>H NMR (400 MHz, DMSO-d<sub>6</sub>): δ (ppm) 3.64 (s, 3H), 6.84 (d, *J* = 8.0 Hz, 2H), 6.97 (d, *J* = 16.0 Hz, 1H), 7.05 (d, *J* = 16.0 Hz, 1H), 7.10 (t, 1H), 7.23 (t, 2H), 7.35-7.45 (m, 4H); <sup>13</sup>C NMR (400 MHz, DMSO-d<sub>6</sub>): δ (ppm) 60.2, 114.2, 126.5, 127.5, 128.4, 129.0, 130.0, 137.7, 159.4.

**4-Styrylbenzotrile [3h(i) and (ii)]:**  $^1\text{H}$  NMR (400 MHz, DMSO- $d_6$ ):  $\delta$  (ppm) 6.83 (s, 2H), 7.32-7.55 (m, 3H), 7.71-7.78 (m, 4H), 7.85 (m, 2H);  $^{13}\text{C}$  NMR (400 MHz, DMSO- $d_6$ ):  $\delta$  (ppm) 110.0, 118.5, 127.1, 127.3, 127.5, 128.5, 129.1, 130.36, 132.6, 136.7, 142.2.

**Ethyl-3-(4-cyanophenyl)acrylate [3i(i) and (ii)]:**  $^1\text{H}$  NMR (400 MHz, DMSO- $d_6$ ):  $\delta$  (ppm) 1.37 (m, 3H), 4.23 (m, 2H), 7.23-7.28 (m, 3H), 7.82 (d,  $J = 8.0$  Hz, 2H);  $^{13}\text{C}$  NMR (400 MHz, DMSO- $d_6$ ):  $\delta$  (ppm) 14.6, 61.4, 112.6, 119.6, 120.1, 128.7, 132.5, 139.6, 140.1, 166.5.

### 3.2.4 Product analysis

In order to confirm the formation of the product, samples of both reactants and products were dissolved in ethyl acetate and then analyzed by GC. GC was equipped with 5 % diphenyl and 95 % dimethyl siloxane, Restek capillary column (0.32 mm dia, 60 m in length) and a flame ionization detector (FID). He gas was used as a carrier gas. The initial column temperature was increased from 60 to 150°C at the rate of 10°C/min and then to 280°C at the rate of 40°C/min. During the product analysis, the temperatures of the FID and injection port were kept constant at 150 and 280°C, respectively.

## 3.3 Results and discussion

### 3.3.1 Characterization of RuO<sub>2</sub>/SWCNT

Figure 3.2 shows the HR-TEM images of RuO<sub>2</sub>/SWCNT and the particle size distribution histogram of RuO<sub>2</sub>NPs in RuO<sub>2</sub>/SWCNT. As seen from Figure 3.2(i-v), a

very fine and homogeneously dispersed RuO<sub>2</sub>NPs were externally attached on anchoring sites of SWCNT. The size distribution histogram of RuO<sub>2</sub>NPs revealed that the diameter of RuO<sub>2</sub>NPs ranges from 0.1 to 3.0 nm, with a mean diameter of 0.9 nm [Figure 3.2(vi)]. It is worth to mention that no free RuO<sub>2</sub>NPs were observed in the background of the HR-TEM images, which shows a complete utilization of the RuO<sub>2</sub>NPs by the SWCNT.

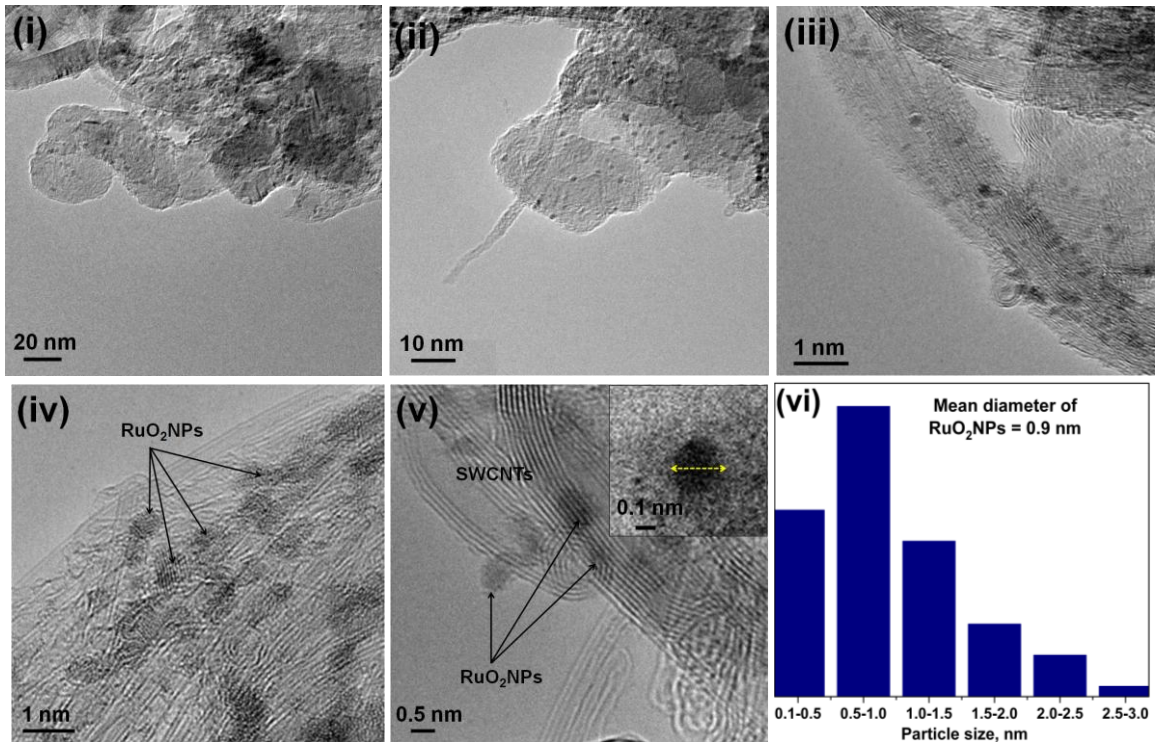


**Figure 3.2** – (i and ii) Low and (iii-v) high magnification HR-TEM images of RuO<sub>2</sub>/SWCNT, and (vi) the particle size distribution of RuO<sub>2</sub>NPs in RuO<sub>2</sub>/SWCNT.

The RuO<sub>2</sub>/SWCNT has a BET surface area of 415.74 m<sup>2</sup> g<sup>-1</sup> with a pore volume of 0.6541 cm<sup>3</sup> g<sup>-1</sup> and a BJH desorption average pore diameter of 1.2 nm. Moreover, the surface area per unit mass (*S*) of RuO<sub>2</sub>NPs was calculated to be 956.5 m<sup>2</sup> g<sup>-1</sup> based on the equation  $S = 6000/(\rho \times d)$ , where *d* is the mean diameter, and  $\rho$  is the density of RuO<sub>2</sub>

( $6.97 \text{ g cm}^{-3}$ ). The weight percentage of Ru in  $\text{RuO}_2/\text{SWCNT}$  was 13.79 wt%, as determined by EDS analysis [Figure 3.3(ii)]. Figures 3.3(iv) and (v) show the homogeneous distribution of  $\text{RuO}_2\text{NPs}$  in  $\text{RuO}_2/\text{SWCNT}$ .  $\text{RuO}_2/\text{SWCNT}$  contains only C, Ru and O elements as shown by EDS analysis, which indicates the reliability of the proposed method.

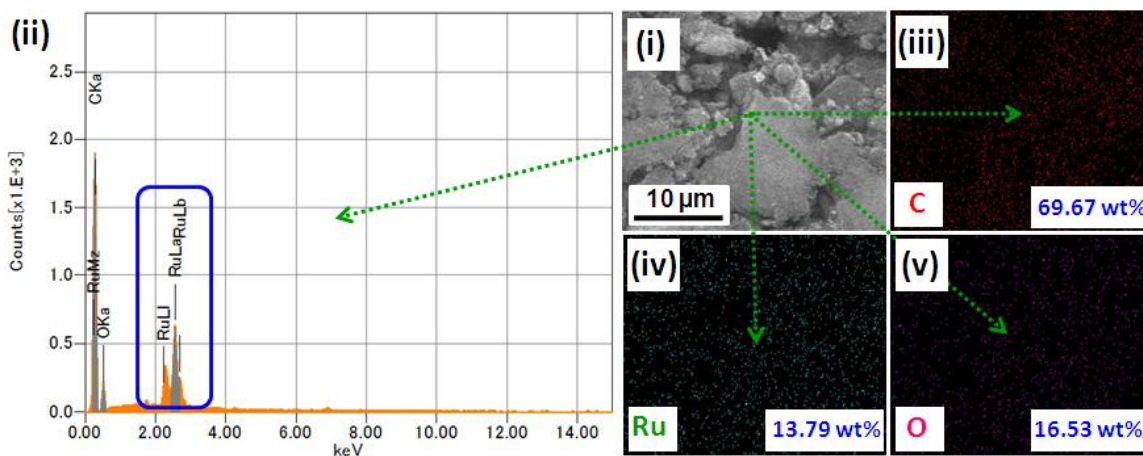


**Figure 3.3** – (i) SEM image and (ii) EDS spectrum of  $\text{RuO}_2/\text{SWCNT}$ , and corresponding EDS mapping of (iii) C, (iv) Ru and (v) O.

To investigate the interaction of  $\text{RuO}_2\text{NPs}$  on SWCNTs, Raman spectra were recorded for pure SWCNT (a), *f*-SWCNT (b) and  $\text{RuO}_2/\text{SWCNT}$  (c) over the Raman shift interval of 200-4000  $\text{cm}^{-1}$ . As can be seen in Figure 3.4, all the three samples showed two characteristic peaks at 1345 and 1592  $\text{cm}^{-1}$ , corresponding to the  $\text{sp}^3$  and  $\text{sp}^2$  hybridized carbons respectively, which confirm the presence of disordered graphite (D band) and ordered state graphite (G band) in SWCNT [19]. Since the ratio of D and G bands ( $I_D/I_G$ ) intensities is often used as a diagnostic tool to measure the defect concentration in SWCNT, the  $I_D/I_G$  ratio was calculated for all the three samples; the

values are given in Figure 3.4 [19]. It was found that the  $I_D/I_G$  ratio of pure SWCNT is 0.5267, whereas, after acid treatment, the  $I_D/I_G$  value increased to 0.7317 (*f*-SWCNT) which confirms the successful functionalization of SWCNT. In addition, positive shift was observed in the D (1342 to 1351  $\text{cm}^{-1}$ ) and G bands (1587 to 1591  $\text{cm}^{-1}$ ) of *f*-SWCNT. This is due to the shortening of SWCNT as well as the creation of oxygen functional groups on SWCNT during the oxidative treatment, which create more anchoring sites for  $\text{RuO}_2$ NPs [20]. In fact, the oxygen functional groups make the SWCNT hydrophilic and support homogeneous decoration and good adhesion of  $\text{RuO}_2$ NPs [21]. The calculated  $I_D/I_G$  ratio was low for  $\text{RuO}_2$ /SWCNT (0.1875) when compared to that of *f*-SWCNT (0.7317). Negative and positive shifts were also observed in the D (1342 to 1331  $\text{cm}^{-1}$ ) and G bands (1587 to 1593  $\text{cm}^{-1}$ ) respectively. The results reveal that the  $\text{RuO}_2$ NPs were strongly attached on to the anchoring sites in the defect structure as well as in the perfect structure of SWCNT [20].

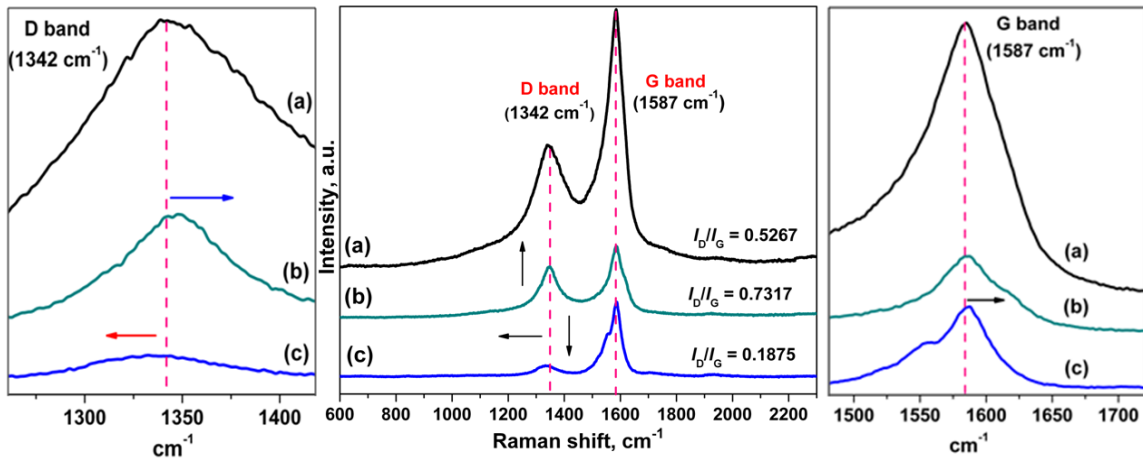


**Figure 3.4** – Raman spectra of (a) pure SWCNTs, (b) *f*-SWCNTs, and (c)  $\text{RuO}_2$ /SWCNT (left: magnified D band region; right: magnified G band region).

XPS spectra were recorded for SWCNT (a), *f*-SWCNT (b) and RuO<sub>2</sub>/SWCNT (c) and the results are shown in Figure 3.5. As expected, all the three samples displayed C 1s and O 1s peaks at 284.4 and 532.5 eV respectively. Figures 3.5(i) and (ii) show the deconvoluted C 1s and O 1s XPS spectra of *f*-SWCNT. In C 1s spectrum, the binding energy of C–C/C=C, C–OH, C–O–C, C=O and COOH groups are assigned at 284.3, 285.0, 285.8, 286.7 and 288.3 eV respectively [21]. Alike, deconvolution of the O 1s spectrum of *f*-SWCNT resulted in five peaks located at 529.8, 530.7, 531.5, 532.2 and 533.5 eV, which were assigned to C=O, COOH, C–OH, C–O–C and H<sub>2</sub>O respectively [21]. Moreover, in comparison to the C 1s spectrum of SWCNT [Figure 3.5(i) insert], the p→p\* shake-up satellite peak at 291.5 eV was completely disappeared in that of *f*-SWCNT. These results confirm the successful creation of the functional groups on the SWCNT. According to Fuller *et al.*, [22] the reactivity of SWCNT is directly decided by the concentration of functional groups. Among the functional groups, mainly, COOH assists well dispersion and adhesion of RuO<sub>2</sub>NPs by replacing its proton. The XPS spectrum of RuO<sub>2</sub>/SWCNT in Ru 3p region [Figure 3.5(iv)] showed BE of Ru 3p<sub>3/2</sub> at 462.5 eV and Ru 3p<sub>1/2</sub> at 485.2 eV, which are attributed to the photoemission from RuO<sub>2</sub> (Ru<sup>4+</sup>) [23]. The intensity of the peaks in both O 1s and C 1s spectra of RuO<sub>2</sub>/SWCNT dramatically decreased which shows a virtually complete reduction of the functional groups [Figure 3.5(iii)]. Interestingly, the strong interaction of RuO<sub>2</sub>NPs on SWCNT was also confirmed from the positive shift in C 1s peak of RuO<sub>2</sub>/SWCNT [Figure 3.5(iii)] when compared to that of *f*-SWCNT [24].

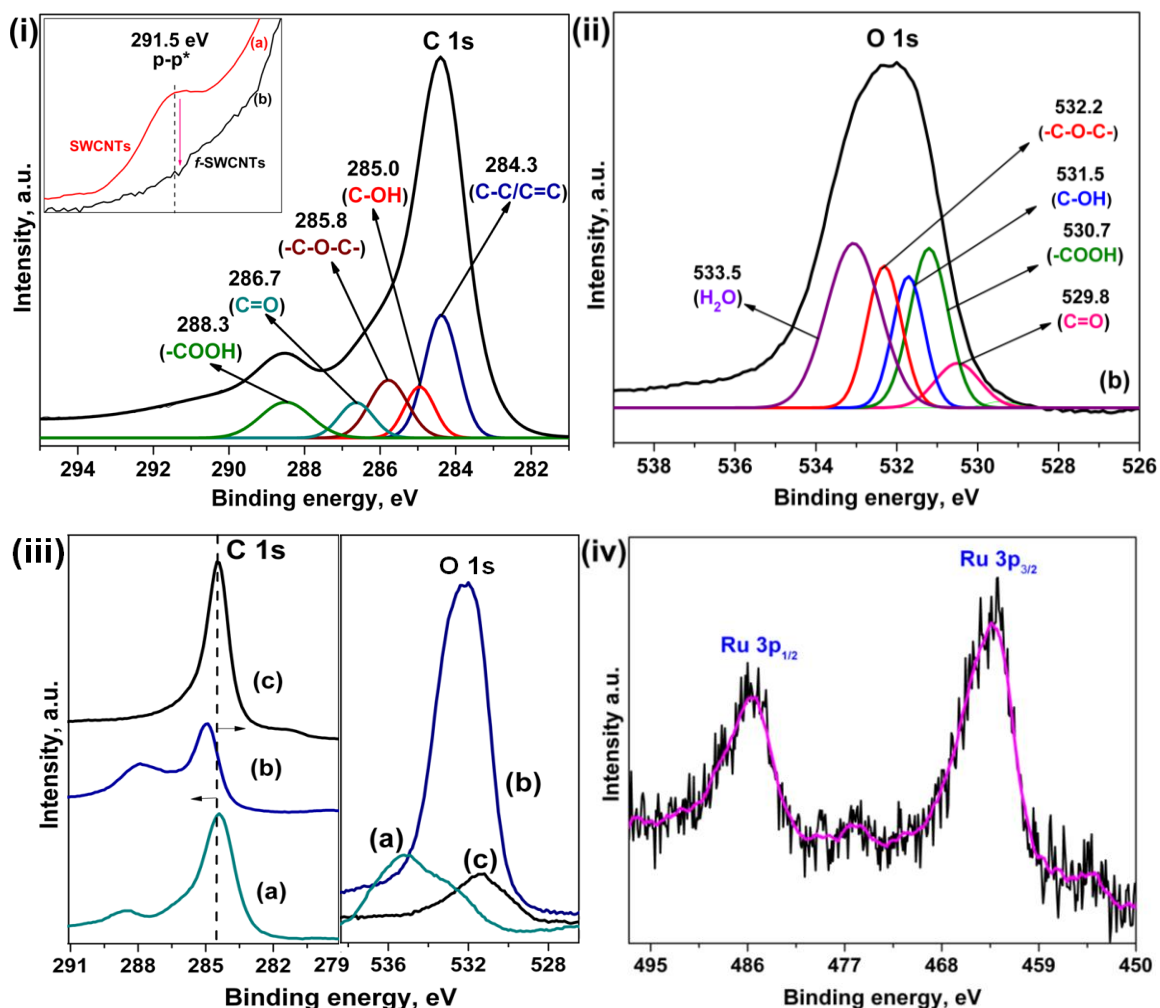
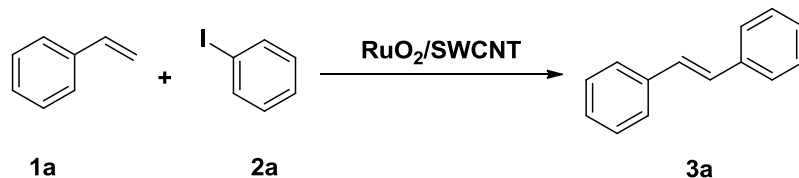


**Figure 3.5** – (i) C 1s peak of *f*-SWCNTs, (ii) O 1s peak of *f*-SWCNTs, (iii) C 1s peak and O 1s peak of (a) SWCNTs, (b) *f*-SWCNTs and (c) RuO<sub>2</sub>/SWCNT, and (iv) main peaks of Ru 3p of RuO<sub>2</sub>/SWCNT.

### 3.3.2 Screening for optimal reaction conditions

Initially, the reaction of styrene (**1a**) with iodobenzene (**2a**) was chosen as the model reaction to screen the reaction conditions (Table 3.1). In this screening, reaction variables such as solvent, base, amount of base, amount of catalyst, temperature and time were optimized to find out the most effective reaction conditions.

**Table 3.1 – Screening for optimal reaction conditions<sup>a</sup>**



entry	solvent <sup>b</sup>	base	amount of base (mmol)	amount of catalyst (mol%)	temp. (°C)	time (min)	yield <sup>c</sup> (%)	(TON/TOF h <sup>-1</sup> ) <sup>d</sup>
1	DMSO	(CH <sub>3</sub> ) <sub>3</sub> COK	2.0	0.9	100	10	47	313/1874
2	Toluene	(CH <sub>3</sub> ) <sub>3</sub> COK	2.0	0.9	100	10	32	213/1275
<b>3</b>	<b>DMF</b>	<b>(CH<sub>3</sub>)<sub>3</sub>COK</b>	<b>2.0</b>	<b>0.9</b>	<b>100</b>	<b>10</b>	<b>91</b>	<b>606/3651</b>
4	DMAc	(CH <sub>3</sub> ) <sub>3</sub> COK	2.0	0.9	100	10	57	380/2276
5	DMF	KOH	2.0	0.9	100	10	19	127/760
6	DMF	NaOH	2.0	0.9	100	10	39	260/1557
7	DMF	K <sub>2</sub> CO <sub>3</sub>	2.0	0.9	100	10	55	367/2198
8	DMF	NaOAc	2.0	0.9	100	10	14	93/557
9	DMF	(CH <sub>3</sub> ) <sub>3</sub> COK	1.5	0.9	100	10	69	460/2755
10	DMF	(CH <sub>3</sub> ) <sub>3</sub> COK	2.5	0.9	100	10	90	600/3593
11	DMF	(CH <sub>3</sub> ) <sub>3</sub> COK	2.0	0.45	100	10	71	95/569
12	DMF	(CH <sub>3</sub> ) <sub>3</sub> COK	2.0	1.35	100	10	91	413/2473
13	DMF	(CH <sub>3</sub> ) <sub>3</sub> COK	2.0	0.9	60	10	32	213/1276
14	DMF	(CH <sub>3</sub> ) <sub>3</sub> COK	2.0	0.9	80	10	56	373/2234
15	DMF	(CH <sub>3</sub> ) <sub>3</sub> COK	2.0	0.9	120	10	89	593/3551
16	DMF	(CH <sub>3</sub> ) <sub>3</sub> COK	2.0	0.9	100	5	78	520/6243
17	DMF	(CH <sub>3</sub> ) <sub>3</sub> COK	2.0	0.9	100	15	91	606/2424
18	DMF	(CH <sub>3</sub> ) <sub>3</sub> COK	2.0	0.9	100	20	91	606/1820
19	DMF	(CH <sub>3</sub> ) <sub>3</sub> COK	2.0	0.9	100	25	90	600/1429
20	DMF	(CH <sub>3</sub> ) <sub>3</sub> COK	2.0	0.9	100	30	91	606/1212

<sup>a</sup>Reaction conditions: **1a** (3.0 mmol), **2a** (1.0 mmol), air atmosphere.

<sup>b</sup>5 mL aliquot of solvent was used in all the reactions.

<sup>c</sup>GC yield.

<sup>d</sup>TON/TOF [TON = the amount of product (mol)/the amount of active sites; TOF = TON/time (h)].

Among the various solvents tested, DMF was found to be more effective (Table 3.1, entries 1-4). It was found that (CH<sub>3</sub>)<sub>3</sub>COK was a more efficient base (Table 3.1, entries 3, 5-8). The amount of base has played a crucial role in the efficiency of present

catalytic system. 2.0 mmol of  $(\text{CH}_3)_3\text{COK}$  was found to be an optimal (Table 3.1, entry 3). When the amount of base was decreased to 1.5 mmol, the reaction was very slow (Table 3.1, entry 9). Subsequently, amount of catalyst was optimized (Table 3.1, entries 3, 11 and 12). A 5.0 mg (0.9 mol% of Ru) of  $\text{RuO}_2/\text{SWCNT}$  was found to be the optimal amount of catalyst with an excellent yield of 91% (Table 3.1, entry 3). To our delight, this is the lowest amount of Ru catalyst (0.9 mol%) used to perform the Heck olefination of aryl halides. In the temperature optimization (Table 3.1, entries 13-15), an excellent yield of 91% was obtained when the reaction was stirred at  $100^\circ\text{C}$  (Table 3.1, entry 3). To the best of our knowledge, among the Ru-based catalytic systems for Heck olefination of aryl halides, the present one requires the lowest reaction temperature. In the time optimization (Table 3.1, entries 16-20), 91% yield of product was obtained after 10 minutes. Further increase in the reaction time did not enhance the yield of product. Moreover, under the optimized reaction conditions, the present catalytic system achieved a good yield of 91% with a highest turnover number (TON) of 606 and turnover frequency (TOF) of  $3651\text{ h}^{-1}$  (Table 3.1, entry 3). The optimal reaction conditions were adopted to extend the scope of the Heck olefination of aryl halides.

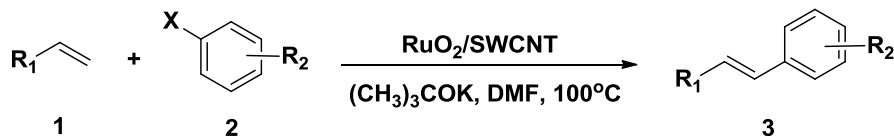
### 3.3.3 Substrate scope

As seen from Table 3.2, a wide range of aryl halides have been effectively coupled to give the olefinated products in moderate to good yields. The yield of the products was fairly affected by various substituents on the aromatic ring of aryl halides. Aryl iodides gave slightly higher yields compared to aryl bromides and aryl chlorides. In the olefination of iodobenzene with styrene, the present catalytic system gave a better

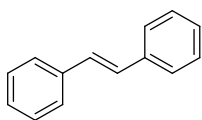
yield of 91% (**3a**) when compared to silylated Pd–NHC system [25]. Interestingly, aryl iodides containing electron donating group such as  $-\text{OCH}_3$  and  $\text{CH}(\text{CH}_3)_2$  at *para* position were also effectively coupled with styrene to give the olefinated products in excellent yields (**3b** and **3d**) whereas the same substrates exhibited lower yields with ethyl acrylate (**3c**). In the olefination of 1-iodo-3-nitrobenzene with styrene, an excellent yield of 92% was achieved (**3e**). Similarly, the present system affords 92% of ethyl 3-(3-nitrophenyl)acrylate (**3f**) from the reaction of 1-iodo-3-nitrobenzene with ethyl acrylate. It was found that a moderate yield of 64% (**3g**) was obtained from the coupling reaction of 1-iodo-4-benzoic acid with ethyl acrylate. The good yields obtained from aryl iodides are due to the better leaving nature of the iodo group.

The present catalytic system worked well also for the olefination of less reactive chloro- and bromoarenes. As seen from Table 3.2, a wide range of chloro- and bromoarenes have been olefinated (**3h-3p**). Particularly, bromoarenes react faster than chloroarenes. For example, in the coupling of 4-bromobenzonitrile with styrene, the product [**3h(i)**] was obtained in 78% yield just after 10 minutes whereas the coupling of 4-chlorobenzonitrile with styrene gave 79% of the desired product [**3h(ii)**] only after 30 minutes. In the same way, an excellent yield of 87% [**3i(i)**] was achieved from the coupling of 4-bromobenzonitrile with ethyl acrylate in 15 minutes, but similar olefination of 4-chlorobenzonitrile yielded 81% of ethyl 3-(4-cyanophenyl)acrylate [**3i(ii)**] after 30 minutes. The present  $\text{RuO}_2/\text{SWCNT}$  system gave a moderate yield of 61% [**3j(i)** and **3j(ii)**] from the coupling of 4-bromobenzaldehyde or 4-chlorobenzaldehyde with styrene.

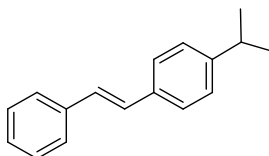
**Table 3.2 – Substrate Scope of the RuO<sub>2</sub>/SWCNT-catalyzed Heck-type Olefination of aryl halides<sup>a</sup>**



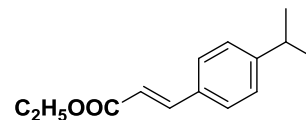
$\text{R}_1 = \text{C}_6\text{H}_5 \text{ or } \text{COOC}_2\text{H}_5$   
 $\text{R}_2 = \text{OCH}_3, \text{CN}, \text{CH}(\text{CH}_3)_2, \text{CH}_3, \text{NO}_2, \text{CHO} \text{ or } \text{COOH}$   
 $\text{X} = \text{I, Br or Cl}$



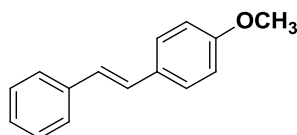
**3a**, (91%)<sup>b</sup>, (86%)<sup>c</sup>, 15 min, (606/3651 h<sup>-1</sup>)<sup>d</sup>



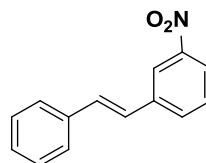
**3b**, (91%)<sup>b</sup>, (80%)<sup>c</sup>, 20 min, (606/1820 h<sup>-1</sup>)<sup>d</sup>



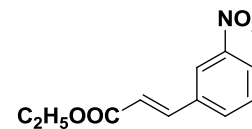
**3c**, (50%)<sup>b</sup>, 10 min (333/1994 h<sup>-1</sup>)<sup>d</sup>



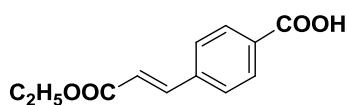
**3d**, (90%)<sup>b</sup>, (79%)<sup>c</sup>, 10 min, (600/3592 h<sup>-1</sup>)<sup>d</sup>



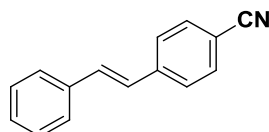
**3e**, (92%)<sup>b</sup>, (84%)<sup>c</sup>, 10 min, (613/3671 h<sup>-1</sup>)<sup>d</sup>



**3f**, (92%)<sup>b</sup>, (87%)<sup>c</sup>, 10 min, (613/3671 h<sup>-1</sup>)<sup>d</sup>

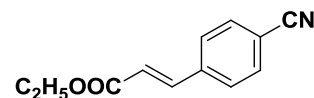


**3g**, (64%)<sup>b</sup>, 10 min (427/2557 h<sup>-1</sup>)<sup>d</sup>



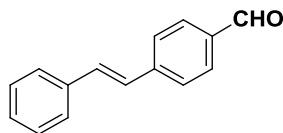
**3h(i)**, (78%)<sup>b</sup>, 10 min, (520/3114 h<sup>-1</sup>)<sup>d</sup>

**3h(ii)**, (77%)<sup>b</sup>, 20min, (513/1541 h<sup>-1</sup>)<sup>d</sup>



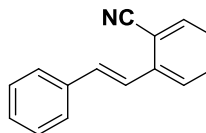
**3i(i)**, (87%)<sup>b</sup>, 10 min, (580/3473 h<sup>-1</sup>)<sup>d</sup>

**3i(ii)**, (81%)<sup>b</sup>, 20 min, (485/1456 h<sup>-1</sup>)<sup>d</sup>

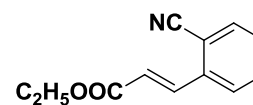


**3j(i)**, (61%)<sup>b</sup>, 20min, (406/1219 h<sup>-1</sup>)<sup>d</sup>

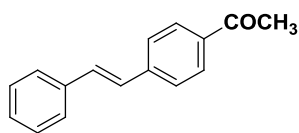
**3j(ii)**, (61%)<sup>b</sup>, 50min, (406/487 h<sup>-1</sup>)<sup>d</sup>



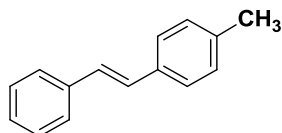
**3k**, (61%)<sup>b</sup>, 15 min, (406/1624 h<sup>-1</sup>)<sup>d</sup>



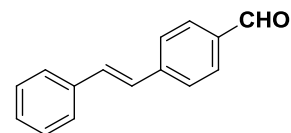
**3l**, (86%)<sup>b</sup>, 20 min, (573/1720 h<sup>-1</sup>)<sup>d</sup>



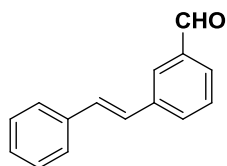
**3m**, (71%)<sup>b</sup>, 10 min,  
(473/2832 h<sup>-1</sup>)<sup>d</sup>



**3n**, (28%)<sup>b</sup>, 20 min,  
(187/562 h<sup>-1</sup>)<sup>d</sup>



**3o**, (31%)<sup>b</sup>, 15 min,  
(207/828 h<sup>-1</sup>)<sup>d</sup>



**3p**, (28%)<sup>b</sup>, 10 min,  
(187/1124 h<sup>-1</sup>)<sup>d</sup>

---

<sup>a</sup>Reaction conditions: **1** (3.0 mmol), **2** (1.0 mmol), RuO<sub>2</sub>/SWCNT (0.9 mol%), (CH<sub>3</sub>)<sub>3</sub>COK (2.0 mmol), DMF (5.0 mL), air atmosphere, 10-50 min, 110°C.

<sup>b</sup>GC yield. <sup>c</sup>Isolated yield. <sup>d</sup>TON/TOF.

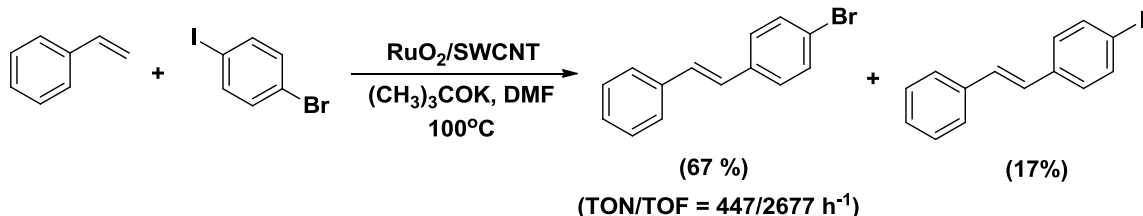
---

The present catalytic system required just 20 minutes to yield 61% of the desired product (**3k**) from the coupling of 2-bromobenzonitrile with styrene whereas the CuO/aluminosilicate yielded the same product after 20 h [8]. Interestingly, a good yield of 86% (**3l**) was obtained from the olefination of 2-bromobenzonitrile with ethyl acrylate. This showed the effectiveness of the present catalytic system towards the olefination of bromo- and chloroarenes. With a 0.9 mol% RuO<sub>2</sub>/SWCNT under optimal conditions, the olefination of 4-bromoacetophenone with styrene gave a better yield of 71% (**3m**) when compared to Pd-catalyzed coupling [26]. However, the olefination of aryl bromide containing -CH<sub>3</sub> at *para* position afforded a lower yield of 28% (**3n**). When processing the aryl halides containing -CHO group (**3o** and **3p**), the GC analyses showed the presence of side products: bromo- or chloro benzoic acid and styrylbenzoic acid. Importantly, for the Ru-catalyzed Heck coupling reactions, this is the highest TON and

TOF values (TON: from 187 to 613; TOF: from 3671 to 1120 h<sup>-1</sup>) reported to date. The excellent catalytic activity of RuO<sub>2</sub>/SWCNT is due to three most important reasons: (i) the ultrafine nature of the RuO<sub>2</sub>NPs, (ii) specific high surface area of RuO<sub>2</sub>/SWCNT, and (iii) an effective dispersion of the RuO<sub>2</sub>/SWCNT in the reaction medium.

### 3.3.4 Regioselectivity

To study the regioselectivity of the present catalytic system, coupling between styrene and 1-bromo-4-iodobenzene was carried out under the optimized reaction conditions (Scheme 3.1). As expected, 1-bromo-4-styrylbenzene was selectively formed in 67% yield with a higher TON (447) and TOF (2677 h<sup>-1</sup>), whereas only 17% of 1-iodo-4-styrylbenzene was obtained. This can be explained by the better leaving nature of the iodo group compared to the bromo group.

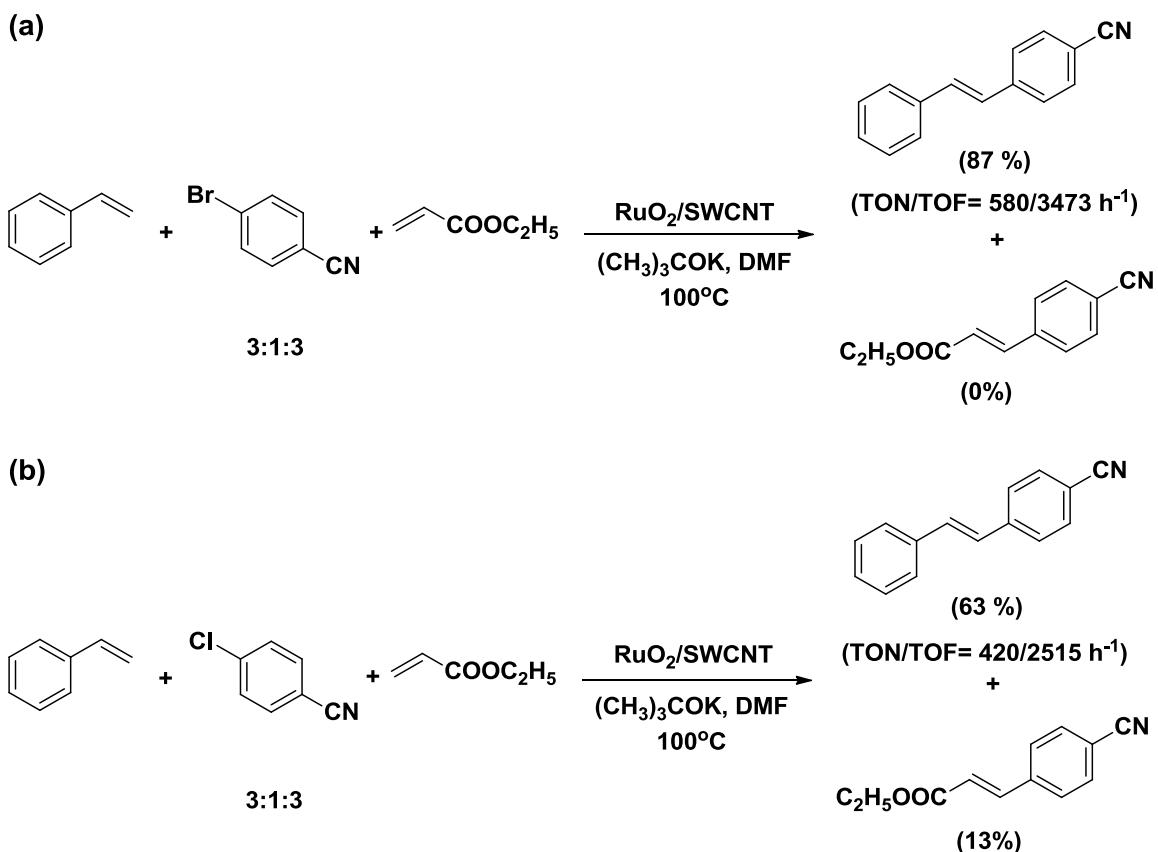


**Scheme 3.1** – Regioselectivity of RuO<sub>2</sub>/SWCNT-catalyzed Heck olefination reaction.

### 3.3.5 Chemoselectivity

When a mixture of styrene (3 mmol), 4-bromobenzonitrile [scheme 3.2 (a)] or 4-chlorobenzonitrile (1.0 mmol) [scheme 3.2 (b)] and ethyl acrylate (3.0 mmol) was allowed to stir under optimized reaction conditions, aryl halide selectively coupled with

styrene to give 4-styrylbenzonitrile in good yields with higher TON (580) and TOF (3473 h<sup>-1</sup>) in the presence of ethyl acrylate.



**Scheme 3.2** – Chemoselectivity of RuO<sub>2</sub>/SWCNT-catalyzed Heck olefination reaction.

### 3.3.6 Heterogeneity, Reusability and Stability of RuO<sub>2</sub>/SWCNT

Well known that several heterogeneous catalysts, particularly in Heck type olefination reaction, are suffered by the leaching of active species from the catalyst and, therefore, the stability and reusability of the catalyst are highly limited [3-6]. To check whether the RuO<sub>2</sub> active species leached out from the SWCNT support during the reaction, a heterogeneity test was performed.

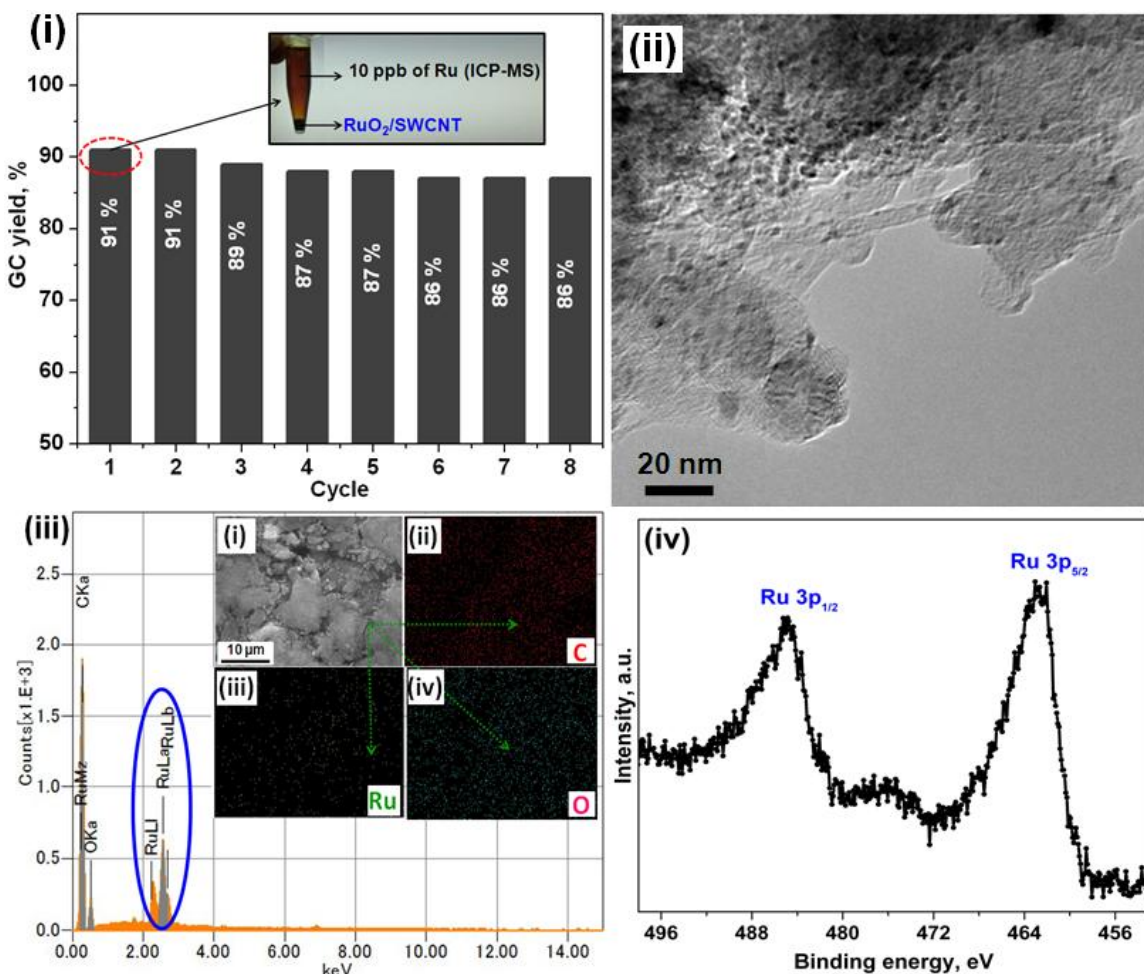


**Figure 3.6** – (i) Heterogeneity and (ii) recyclability test of RuO<sub>2</sub>/SWCNT [styrene (343 μL, 3.0 mmol), iodobenzene (111 μL, 1.0 mmol), (CH<sub>3</sub>)<sub>3</sub>COK (224 mg, 2.0 mmol) and RuO<sub>2</sub>/SWCNT (5 mg, 0.9 mol% of Ru) at 100°C in 5 mL of DMF], (iii) SEM and corresponding EDS spectrum of *u*-RuO<sub>2</sub>/SWCNT, and (iv) Ru 3p XPS spectrum of *u*-RuO<sub>2</sub>/SWCNT.

In a typical test, a mixture of styrene (343 μL, 3.0 mmol) and iodobenzene (111 μL, 1.0 mmol) was stirred under optimized reaction conditions. After the reaction was completed, the solid RuO<sub>2</sub>/SWCNT was separated out from the reaction mixture by centrifugation and then the filtrate was analyzed by ICP-MS [Figure 3.6(i)]; a very low content of Ru (~10 ppb) confirmed that the leaching of active species (RuO<sub>2</sub>) from the

SWCNTs support is negligible. Inspired by this result, subsequently, reusability of the catalyst was investigated. After the first use, the catalyst was separated out by centrifugation, washed, dried at 60°C, and then reused. The catalyst was reused eight times and the yields of product are shown in Figure 3.6(i). Merit of the proposed catalytic system can be realized from the reusability of RuO<sub>2</sub>/SWCNT that shows an excellent yield of 86% with a higher TON (573) and TOF (3431 h<sup>-1</sup>) at eighth cycle. Moreover, to confirm the stability of the catalyst, the used RuO<sub>2</sub>/SWCNT (*u*-RuO<sub>2</sub>/SWCNT) was analyzed by TEM, XPS and SEM-EDS [Figure 3.6(ii-iv)]. It can be seen that there is no significant change was found in the morphology of the *u*-RuO<sub>2</sub>/SWCNT when compared to the fresh RuO<sub>2</sub>/SWCNT. It was found that the oxidation state and the weight percentage of Ru in *u*-RuO<sub>2</sub>/SWCNT were +4 and 13.01 wt% respectively. The results indicate that the RuO<sub>2</sub>/SWCNT is physically as well as chemically stable.

### 3.3.7 Proposed mechanism

In order to understand the mechanism of RuO<sub>2</sub>/SWCNT-catalyzed Heck olefination of aryl halides, FT-IR and XPS spectra (data not shown) were recorded for RuO<sub>2</sub>/SWCNT (pure nanocatalyst) and *h*-RuO<sub>2</sub>/SWCNT (the catalyst after stirring with styrene and iodobenzene in 5 mL of DMF at 100°C for 5 min). In comparison to pure RuO<sub>2</sub>/SWCNT, both the FT-IR and C 1s XPS spectra of *h*-RuO<sub>2</sub>/SWCNT showed extra peaks which may be attributed to the adsorption of aryl halide on the active sites of RuO<sub>2</sub>NPs. In addition, XPS spectrum of *h*-RuO<sub>2</sub>/SWCNT confirmed the formation of KI (I 3p and K 2p XPS spectrum) during the reaction. Furthermore, GC analysis showed the formation of *t*BuOH during the Heck coupling reaction.

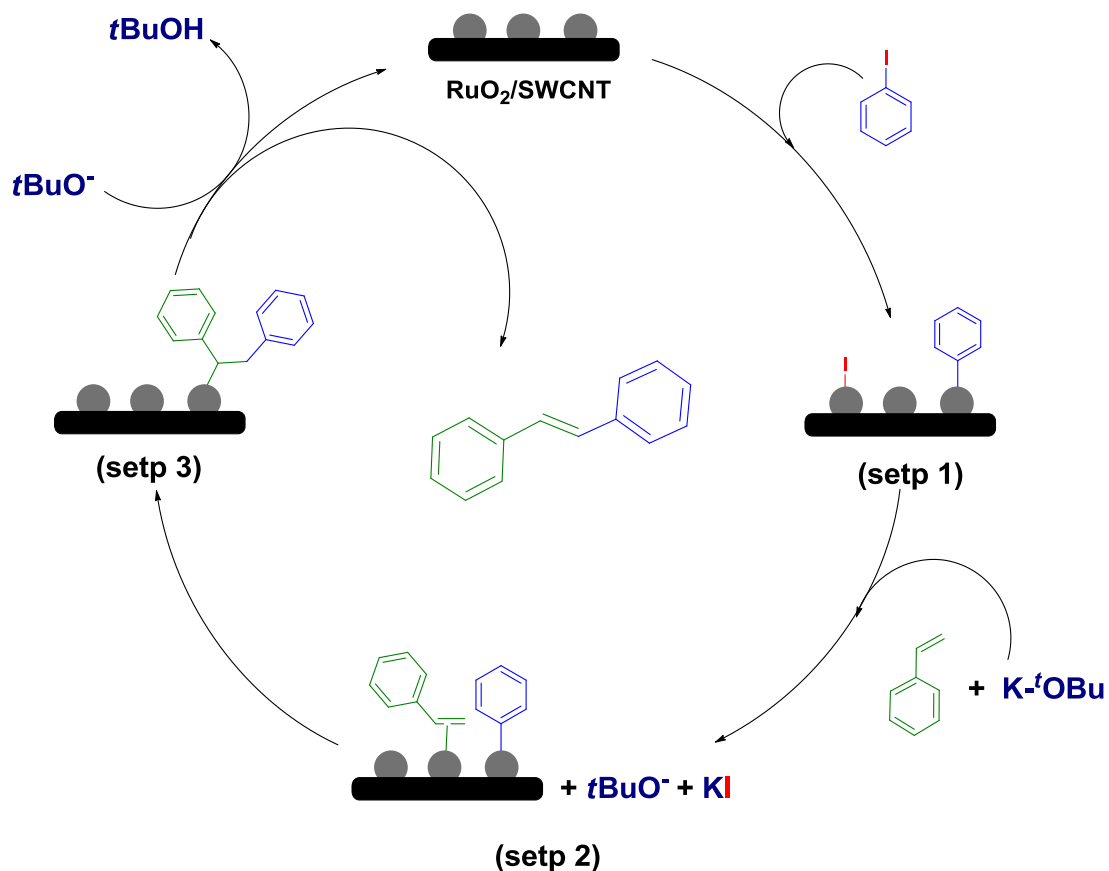


**Figure 3.7** – Proposed mechanism for Heck olefination of iodobenzene with styrene.

Based on the results obtained from the XPS, FT-IR and GC analysis, we concluded that the catalytic reaction might be taken place *via* adsorption followed by desorption. In step (i), heating the mixture of RuO<sub>2</sub>/SWCNT and aryl halide lead to the adsorption of the aryl halide on the active sites of the RuO<sub>2</sub>NPs. Owing to the adsorption of aryl halide on RuO<sub>2</sub>NPs, the positive charge was developed and the excess charge might be shared among the RuO<sub>2</sub>NPs. Since the SWCNT is highly conductive, the created excess charge might assist good dispersion of charged RuO<sub>2</sub>NPs on SWCNT support and consequently exhibit more adsorption of the aryl halide species on the surface of RuO<sub>2</sub>NPs [27]. In step (ii), the adsorbed aryl halide undergoes reaction with olefin and

base. Subsequently, in step (iii), the catalytic cycle is completed by the desorption of coupled product. Finally, RuO<sub>2</sub>/SWCNT was regenerated for the further coupling reaction.

### **3.4 Conclusions**

In conclusion, a mild and highly efficient SWCNT-supported RuO<sub>2</sub>NPs based catalytic system for the Heck olefination of aryl halides is developed. The substrate scope of the reaction could be efficiently carried out with as low as 0.9 mol % of the supported RuO<sub>2</sub> catalyst over a wide range of substrates in moderate to excellent yields with a very high TON and TOF values. In addition to the iodoarenes, less reactive bromo- and chloroarenes can also be effectively olefinated using the present catalytic system. To the best of our knowledge, the RuO<sub>2</sub>/SWCNT is the most active Ru-based heterogeneous catalyst for the Heck olefination of aryl halides among those reported so far. The RuO<sub>2</sub>/SWCNT is highly regioselective and chemoselective for the Heck olefination reaction. Heterogeneity, reusability and stability of RuO<sub>2</sub>/SWCNT were found to be good. Overall, the simple synthesis and excellent activity make RuO<sub>2</sub>/SWCNT as an alternate choice to the existing Ru based catalysts for Heck coupling reactions.

## Reference

- [1] Baur, J. A.; Sinclair, D. A. Therapeutic Potential of Resveratrol: The In Vivo Evidence. *Nat. Rev. Drug Discov.* **2006**, *5*, 493–506.
- [2] Beletskaya, I. P.; Cheprakov, A. V. The Heck Reaction as a Sharpening Stone of Palladium Catalysis *Chem. Rev.* **2000**, *100*, 3009–3066.
- [3] Denmark, S. E.; Sweis, R. F. Design and Implementation of New, Silicon-Based, Cross-Coupling Reactions: Importance of Silicon–Oxygen Bonds. *Acc. Chem. Res.* **2002**, *35*, 835–846.
- [4] Qingwei, Y.; Elizabeth, P. K.; Zhi, Y. Ligand-Free Heck Reaction: Pd(OAc)<sub>2</sub> as an Active Catalyst Revisited. *J. Org. Chem.* **2003**, *68*, 7528–7531.
- [5] Bhanage, B. M.; Shirai, M.; Arai, M. Heterogeneous Catalyst System for Heck Reaction Using Supported Ethylene Glycol Phase Pd/TPPTS Catalyst with Inorganic Base. *J. Mol. Catal. A: Chem.* **1999**, *145*, 69–74.
- [6] Mori, K.; Yamaguchi, K.; Hara, T.; Mizugaki, T.; Ebitani, K.; Kaneda, K. Controlled Synthesis of Hydroxyapatite-Supported Palladium Complexes as Highly Efficient Heterogeneous Catalysts. *J. Am. Chem. Soc.* **2002**, *124*, 11572–11573.
- [7] Reetz, M. T.; Westermann, E. Phosphane-Free Palladium-Catalyzed Coupling Reactions: The Decisive Role of Pd Nanoparticles. *Angew. Chem., Int. Ed.* **2000**, *39*, 165–168.
- [8] Iyer, S.; Ramesh, C.; Sarkar, A.; Wadgaonkar, P. P. The Vinylation of Aryl and Vinyl Halides Catalyzed by Copper Salts. *Tetrahedron Lett.* **1997**, *38*, 8113–8116.
- [9] Lipshutz, B. H.; Sclafani, J. A.; Blomgren, P. A. Biaryls via Suzuki Cross-Couplings Catalyzed by Nickel on Charcoal. *Tetrahedron* **2000**, *56*, 2139–2144.

- [10] Furstner, A.; Leitner, A.; Mendez, M.; Krause, H. Iron-Catalyzed Cross-Coupling Reactions. *J. Am. Chem. Soc.* **2002**, *124*, 13856–13863.
- [11] Oi, S.; Honma, Y.; Inoue, Y. Conjugate Addition of Organosiloxanes to  $\alpha,\beta$ -Unsaturated Carbonyl Compounds Catalyzed by a Cationic Rhodium Complex. *Org. Lett.* **2002**, *4*, 667–669.
- [12] Iyer, S. The Vinylation of Aryl Iodides Catalysed by Co, Rh and Ir Complexes. *J. Organomet. Chem.* **1995**, *490*, 27–28.
- [13] Naota, T.; Takaya, H. Murahashi, S.I. Ruthenium-Catalyzed Reactions for Organic Synthesis. *Chem. Rev.* **1998**, *98*, 2599–2660.
- [14] Na, Y.; Park, S.; Han, S. B.; Han, H.; Ko, S.; Chang, S. Ruthenium-Catalyzed Heck-Type Olefination and Suzuki Coupling Reactions: Studies on the Nature of Catalytic Species. *J. Am. Chem. Soc.* **2004**, *126*, 250–258.
- [15] Joo, S. H.; Park, J. Y.; Renzas, J. R.; Butcher, D. R.; Huang, W.Y.; Somorjai, G.A. Size Effect of Ruthenium Nanoparticles in Catalytic Carbon Monoxide Oxidation. *Nano Lett.* **2010**, *10*, 2709–2713.
- [16] Gomez-Escalonilla, M. J.; Atienzar, P.; Garcia Fierro, J. L.; Garcia. H.; Langa, F. Heck Reaction on Single-Walled Carbon Nanotubes. Synthesis and Photochemical Properties Of A Wall Functionalized SWNT-Anthracene Derivative. *J. Mater. Chem.* **2008**, *18*, 1592–1600.
- [17] Krashennnikov, A. V.; Lehtinen, P. O.; Foster, A. S.; Pyykko, P.; Nieminen, R. M. Embedding Transition-Metal Atoms in Graphene: Structure, Bonding, and Magnetism. *Phys. Rev. Lett.* **2009**, *102*, 126807–126810.

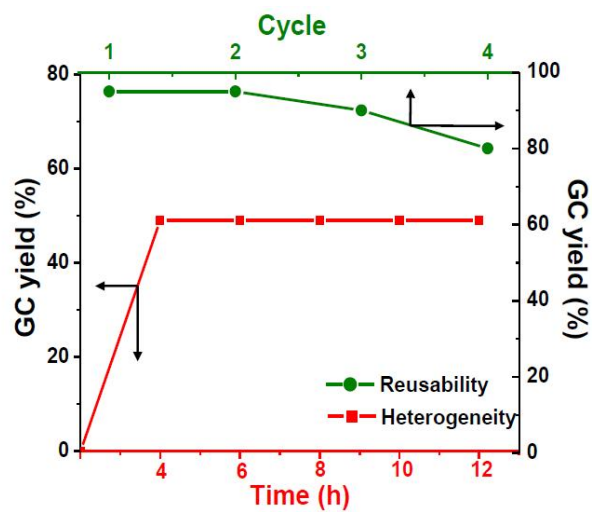
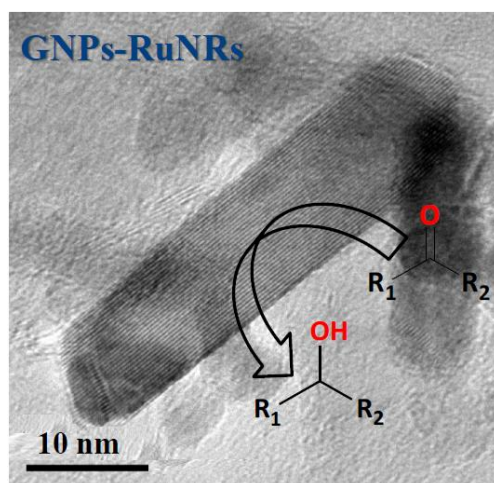
- [18] Tsang, S. C.; Chen, Y. K.; Harris, P. J. F.; Green, M. L. H. A Simple Chemical Method of Opening And Filling Carbon Nanotubes. *Nature* **1994**, *372*, 159–162.
- [19] Dresselhaus, M. S.; Dresselhaus, G.; Saito, R.; Jorio, A. Raman Spectroscopy of Carbon Nanotubes. *Phys. Rep.* **2005**, *409*, 47–99.
- [20] Datsyuk, V.; Kalyva, M.; Papagelis, K.; Parthenios, J.; Tasis, D.; Siokou, A.; Kallitsis, I.; Galiotis, C. Chemical Oxidation of Multiwalled Carbon Nanotubes. *Carbon* **2008**, *46*, 833–840.
- [21] Akhavan, O. The Effect of Heat Treatment on Formation of Graphene Thin Films From Graphene Oxide Nanosheets. *Carbon* **2010**, *48*, 509–519.
- [22] Proton Exchange Membrane Fuel Cells; Fuller, T., Eds.; ECS Transactions; **2008**.
- [23] Chakroune, N.; Viau, G.; Ammar, S.; Poul, L.; Veautier, D.; Chehimi, M. M.; Mangeney, C.; Villain, F.; Fievet, F. Acetate- and Thiol-Capped Monodisperse Ruthenium Nanoparticles: XPS, XAS, and HRTEM Studies. *Langmuir* **2005**, *21*, 6788–6796.
- [24] Gopiraman, M.; Ganesh Babu, S.; Khatri, Z.; Kai, W.; Endo, M.; Karvembu, R.; Kim, I. S. Facile and Homogeneous Decoration of RuO<sub>2</sub> Nanorods on Graphene Nanoplatelets for Transfer Hydrogenation of Carbonyl Compounds. *Catal. Sci. Technol.* **2013**, *3*, 1485.
- [25] Polshettiwar, V.; Hesemann, P.; Moreau, J. J. E. Silica Hybrid Material Containing Pd–NHC Complex as Heterogeneous Catalyst For Mizoroki–Heck Reactions. *Tetrahedron Lett.* **2007**, *48*, 5363–5366.
- [26] Palmisano, G.; Bonrath, W.; Boffa, L.; Garella, D.; Barge, A.; Cravotto, G. Heck Reactions with Very Low Ligandless Catalyst Loads Accelerated by Microwaves

or Simultaneous Microwaves/Ultrasound Irradiation. *Adv. Synth. Catal.* **2007**, *349*, 2338–2344.

- [27] Gopiraman, M.; Ganesh Babu, S.; Khatri, Z.; Kai, W.; Kim, A. Y.; Endo, M.; Karvembu, R.; Kim, I. S. An Efficient, Reusable Copper-Oxide/Carbon-Nanotube Catalyst for N-Arylation of Imidazole. *Carbon* **2013**, *62*, 135–148.

## CHAPTER 4

### Facile and homogeneous decoration of RuO<sub>2</sub> nanorods on graphene nanoplatelets for transfer hydrogenation of carbonyl compounds



## CHAPTER 4

# Facile and homogeneous decoration of RuO<sub>2</sub> nanorods on graphene nanoplatelets for transfer hydrogenation of carbonyl compounds

### 4.1 Introduction

Reduction of carbonyl compounds (C=O) to their corresponding alcohols is a pivotal organic transformation and synthetically important both in industrial and fine chemical processes [1]. There are many methods available to achieve this transformation [2]. Recently most of the studies have focused on the transition metals-catalyzed reduction of carbonyl compounds by hydrogen transfer from 2-propanol. In fact, this method is operationally very simple and these reactions can be carried out in the absence of molecular hydrogen [3]. Hence, there are many homogeneous and heterogeneous catalysts have been developed and investigated for this transformation [4]. For the last few decades, heterogeneous catalysts particularly MNPs are getting more attention from both economic and industrial point of view because they are highly recyclable and easily separable from the reaction mixture [5]. In spite of remarkable catalytic effect, a drawback remains in these catalysts as the MNPs effortlessly agglomerate in the reaction conditions, which lead to low catalytic activity as well as the poor reusability of the catalyst. To overcome this, several inorganic and organic materials have been used as a support for metal catalysts [6]. Recently, owing to the unique properties such as high surface area and chemical inertness, carbon building blocks such as CNTs and carbon

nanofibers have been used as a support for metal catalysts [7]. In this century, graphene has been discovered as a “rising-star” nanomaterial and has attracted vast interest owing to its extraordinary properties such as chemical inertness, thermal stability and a huge surface area. Recently graphene has been used as a support for MNPs in heterogeneous catalysis [8]. Krashennnikov *et al.*, examined the transition metals supported on graphene using density functional theory and found that there is a bonding between the transition metal atom and neighboring carbon atoms of graphene [9]. Hence, the inert graphene may be transformed to a very active catalyst through the interactions between the metal clusters and carbon vacancies. Recently, Baoqiang *et al.*, has investigated the transfer hydrogenation of alkynes, alkenes and nitro aromatics using graphene supported PtNPs [10]. Gil *et al.*, prepared graphite oxide supported PdNPs and used as a catalyst for the Suzuki-Miyaura coupling reaction with higher activity than the commercial Pd-C catalyst [11]. Inspired by these results, we presumed that GNPs supported RuNRs would also exhibit high catalytic activity for the transfer hydrogenation of carbonyl compounds. Herein, we report the preparation of GNPs supported RuNRs and its catalytic property in the transfer hydrogenation of various aldehydes and ketones. In addition, GNPs were successfully recovered from the used GNPs-RuNRs by simple chemical treatment. Chemoselectivity, reusability and heterogeneity of GNPs-RuNRs on transfer hydrogenation of carbonyl compounds were also tested.

## 4.2 Experimental section

### 4.2.1 Materials and characterization

Graphene nanoplatelets (GNPs, purity: >99wt%, surface area: >750m<sup>2</sup>/g, average thickness: 3nm, layers: <3, diameter: 1-2 um) were purchased from Cheap tubes Inc., VT, US. H<sub>2</sub>SO<sub>4</sub> (98%) and HNO<sub>3</sub> (70%) were purchased from Wako pure chemicals, Japan. Ru(acac)<sub>3</sub> (97%) and all other chemicals were purchased from Aldrich and used as received.

To find the actual size of RuNRs on GNPs and to study the morphology of GNPs-RuNRs, TEM images were taken with accelerating voltage of 120 kV using JEM-2100 JEOL Japan. The definite quantity of decorated RuNRs in the GNPs-RuNRs was determined by ICP-MS model (7500CS, Agilent). In addition, the weight percentage of Ru in GNPs-RuNRs was determined by SEM-EDS [Hitachi (model-3000H) Scanning Electron Microscope]. The same field of view was then scanned using an EDS spectrometer to acquire a set of X-ray maps for Ru, C, and O using 1 ms point acquisition for approximately one million counts. To investigate the interaction between RuNRs and GNPs, Raman spectra were recorded using a Raman spectrometer (Hololab 5000, Kaiser Optical Systems Inc., USA), argon laser at 532 nm with a Kaiser holographic edge filter. WAXD experiments were performed at room temperature using a Rotaflex RTP300 (Rigaku.Co., Japan) at 50 kV and 200 mA. Nickel-filtered Cu K $\alpha$  radiation was used for the measurements, along with an angular range of  $10 < 2\theta < 80^\circ$ . To confirm the chemical state of Ru in GNPs-RuNRs, XPS spectrum was recorded in Kratos Axis-Ultra DLD model instrument. The GNPs-RuNRs was irradiated under Mg K $\alpha$  ray source before XPS

analysis. In order to determine the conversion of the reactants and to calculate the yield of resultant products, GC was recorded using Shimadzu-2010 gas chromatograph.

#### 4.2.2 Typical procedure for oxidation of GNPs

In a typical procedure, 0.5 g of as-received GNPs was treated with a 3:1 ratio mixture of concentrated  $\text{H}_2\text{SO}_4$  and  $\text{HNO}_3$ . Then the mixture was sonicated at  $40^\circ\text{C}$  for 3 h in ultrasonic bath for the generation of functional groups ( $-\text{COOH}$ ,  $-\text{C}=\text{O}$ ,  $-\text{C}-\text{O}-\text{C}-$  and  $-\text{OH}$ ) on the GNPs surface. After cooling at room temperature, the reaction mixture was diluted with 500 mL of deionized water and then vacuum-filtered through a filter paper of  $3\ \mu\text{m}$  porosity. The resultant *f*-GNPs were repeatedly washed with deionized water until the pH reached neutral and finally, the solid was dried in *vacuo* at  $60^\circ\text{C}$ .

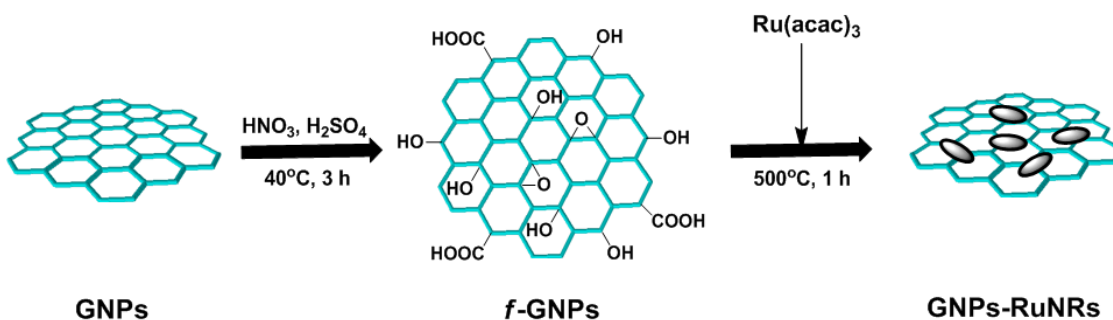


**Figure 4.1** – Preparation of nanocatalyst, GNP-RuNRs.

#### 4.2.3 Preparation of nanocatalyst

To attain a specific nucleation of RuNRs on GNPs with excellent adhesion, initially, GNPs were functionalized by chemical treatment with  $\text{HNO}_3/\text{H}_2\text{SO}_4$  to generate  $-\text{COOH}$ ,  $-\text{C}=\text{O}$ ,  $-\text{C}-\text{O}-\text{C}-$  and  $-\text{OH}$  functional groups on GNPs surface as described in

literature.<sup>12</sup> Then, 0.5 g of functionalized GNPs (*f*-GNPs) were added to 0.2 g of Ru(acac)<sub>3</sub> and mixed well using a mortar and pestle until the mixture was homogeneous. Then the mixture was calcinated at 500°C under argon atmosphere for 1 h (Figure 4.1).

#### 4.2.4 Transfer hydrogenation of carbonyl compounds

A 5.0 mg of GNPs-RuNRs (0.15 mol% of Ru), substrate (1.0 mmol), isopropyl alcohol (4 mL) and potassium *tert*-butoxide ((CH<sub>3</sub>)<sub>3</sub>COK, 1 mmol) were refluxed under air atmosphere at 82°C. The completion of the reaction was checked by TLC. Once the reactions completed, the nanocatalyst was separated out from the reaction mixture by simple centrifugation and the products and unconverted reactants were analyzed by GC without any purification. Selectivity of the product for each reaction was also calculated. Subsequently, the reduced products of selected reactions were separated to compare the isolated yields to those determined by GC. The separated nanocatalyst was washed well with diethyl ether followed by drying in oven at 130°C for 3 h and was reused for the subsequent transfer hydrogenation of carbonyl compounds for testing the reusability of GNPs-RuNRs.

#### 4.2.5 Typical procedure for reusability of GNPs-RuNRs

It is well known that the most excellent advantages of the heterogeneous catalyst are the prospect of reusing and recovering it from reaction mixture. After the first cycle the catalyst was separated out by simple filtration and washed well with diethyl ether, dried in *vacuo* at 130°C for 3 h, and then used for the second cycle under the optimized

reaction condition. The catalytic run was repeated for four cycles with further addition of substrates in appropriate amounts under optimum reaction conditions and the conversion yield of the final products were monitored by GC.

#### **4.2.6 Typical procedure for recovery of GNPs**

After the first cycle, the catalyst was separated out by simple filtration, then washed well with diethyl ether and dried in an oven at 130°C for 3 h. Then the catalyst was chemically treated with Conc. HNO<sub>3</sub> and H<sub>2</sub>SO<sub>4</sub> mixture (1:4 ratios) under sonication for 1 h. Then the solid was filtered and washed well with distilled water followed by drying in *vacuo*. Finally, the resultant sample was characterized by TEM, Raman and XRD.

#### **4.2.7 Product confirmation and analysis**

In order to confirm the formation of the product, samples of both reactant and products were dissolved in ethyl acetate and then analyzed by GC. GC was equipped with 5 % diphenyl and 95 % dimethyl siloxane, Restek capillary column (0.32 mm dia, 60 m in length) and a flame ionization detector (FID). Nitrogen gas was used as a carrier gas. The initial column temperature was increased from 60 to 150°C at the rate of 10°C/min and then to 220°C at the rate of 40°C/min. During the product analysis, the temperatures of the FID and injection port were kept constant at 150 and 250°C, respectively.

## 4.3 Result and discussions

### 4.3.1 Characterization of GNPs-RuNRs

Very small and homogeneously dispersed RuNRs on GNPs were observed by TEM images [Figure 4.2(i)]. The length and diameter of RuNRs were found to be around 25-30 nm and 8-12 nm, respectively. The XPS and XRD were recorded to investigate the chemical state of the RuNRs. The binding energies of Ru 3p<sub>3/2</sub> at 462.5 eV, Ru 3p<sub>1/2</sub> at 485.0 eV and Ru 3d<sub>5/2</sub> at 280.8 eV are attributed to the photoemission from RuO<sub>2</sub> (Ru<sup>4+</sup>) [Figure 4.2(ii)] [16]. The XRD peaks [Figure 4.3(i) and (ii)] observed at 27.5°, 34.9°, 39.9° and 57.5° correspond to the typical crystal faces (110), (101), (200) and (220) of RuO<sub>2</sub> (JCPDS 21-1172), respectively.

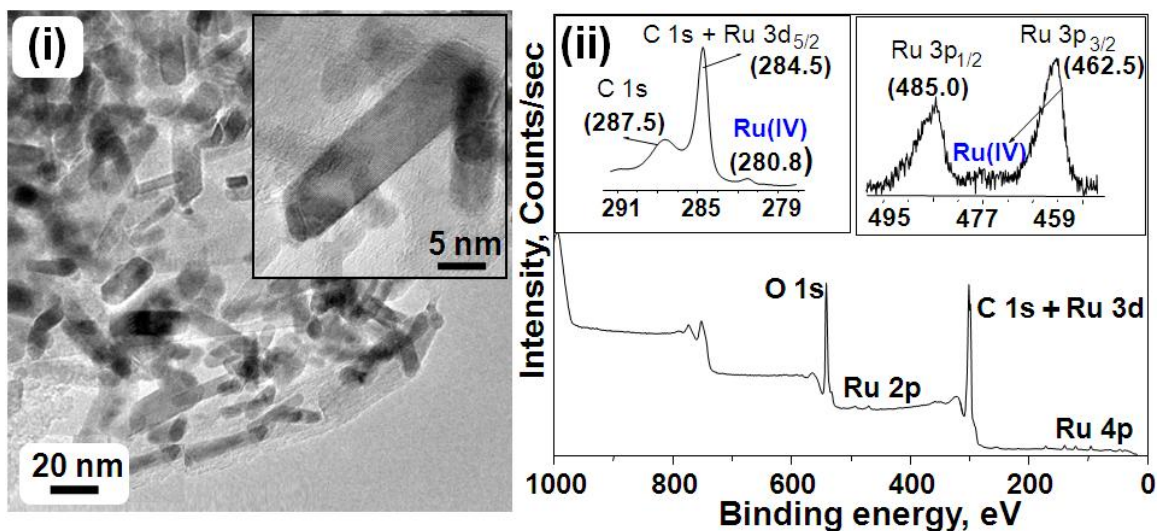


**Figure 4.2** – (i) TEM image of the GNPs-RuNRs (inset: magnified TEM image); (ii) XPS for catalyst (insert, above, right: Ru<sub>1/2</sub> and Ru<sub>3/2</sub> spectrum; left: Ru 3d<sub>5/2</sub> spectrum).

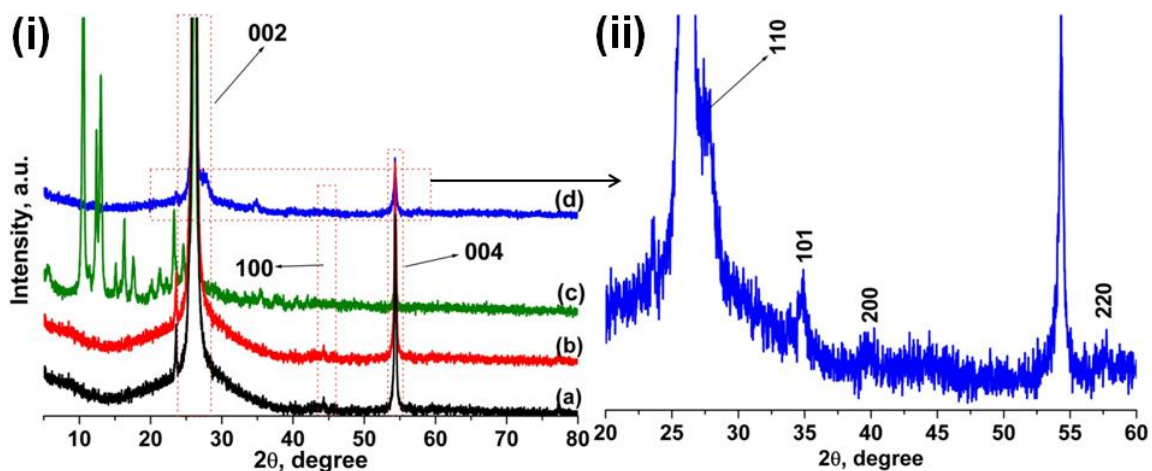


**Figure 4.3** – (i) Full and (ii) magnified (right) region of XRD pattern of GNPs (a), *f*-GNPs (b), GNPs-Ru(acac)<sub>3</sub> (c) and GNPs-RuNRs (d).

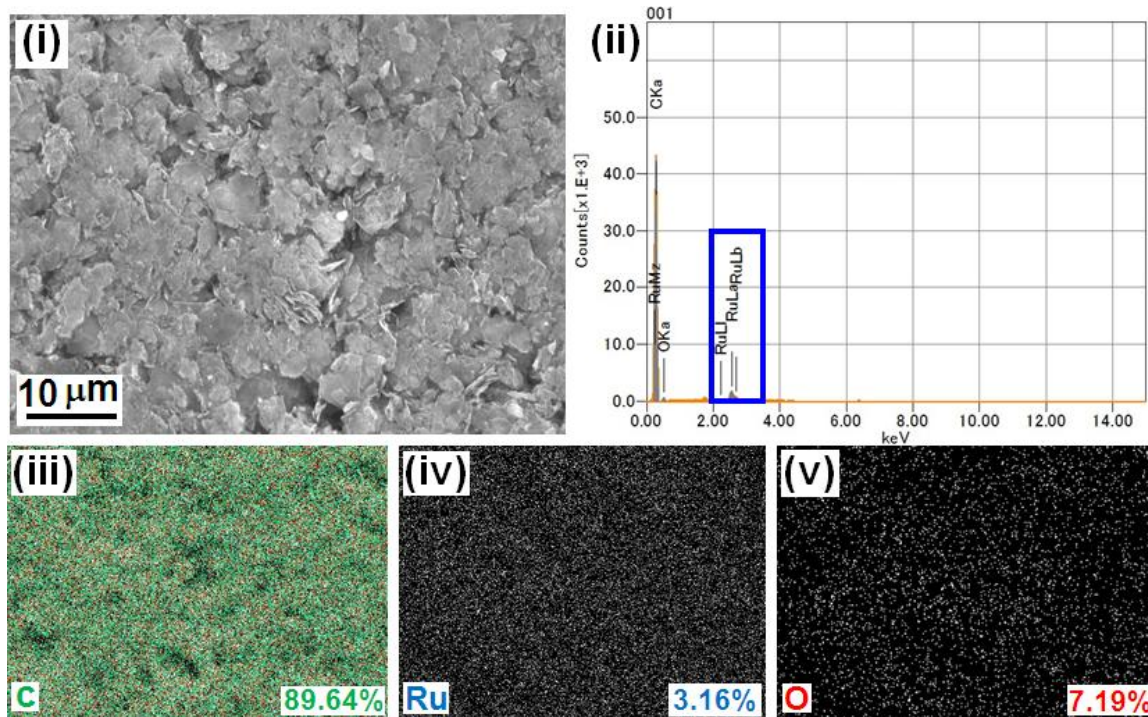


**Figure 4.4** – (i) SEM and (ii) corresponding EDS images of GNPs-RuNRs, and EDX mapping observations of (iii) C, (iv) Ru and (v) O (inset in iii, iv and v, bottom, right: weight percentage).

The actual loading of Ru in GNPs-RuNRs was 2.99 wt%, as determined by ICP-MS. The SEM-EDS and its corresponding elemental mapping were taken for GNPs-RuNRs [Figure 4.4(i) and (ii)]. EDS result revealed the loading of Ru in GNPs-RuNRs as 3.19 wt%, which agrees well with the ICP-MS result. The elemental mapping of GNPs-RuNRs confirmed that the RuNRs are homogeneously distributed on GNPs, which agrees well with TEM results.

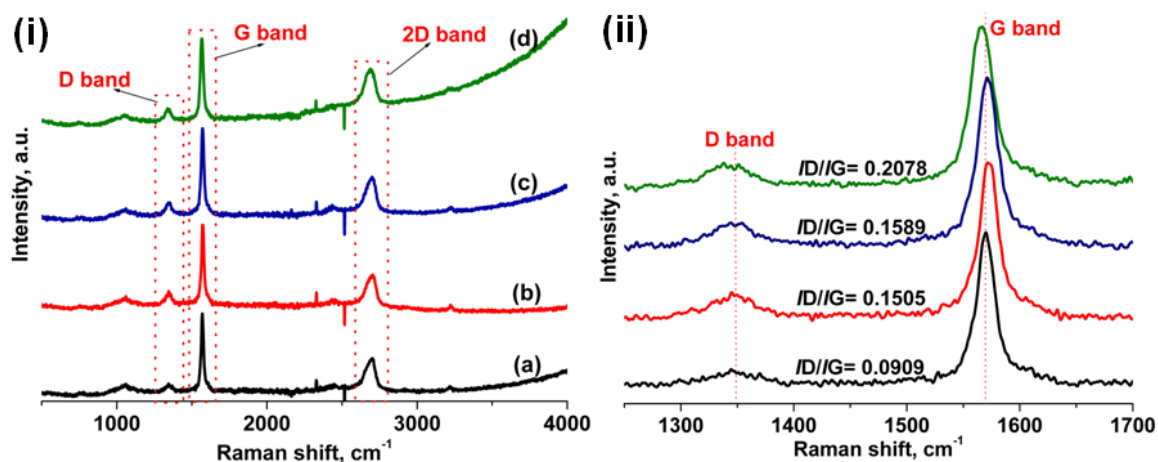


**Figure 4.5** – (i) Full and (ii) magnified region of Raman spectrum of GNPs (a), *f*-GNPs (b), GNPs-Ru(acac)<sub>3</sub> (c) and GNPs-RuNRs (d).

The Raman spectra were recorded for GNPs, *f*-GNPs, GNPs-Ru(acac)<sub>3</sub> [GNPs and Ru(acac)<sub>3</sub> mixture before the calcination] and GNPs-RuNRs [Figure 4.5(i) and (ii)]. The D and G bands observed at 1345 and 1575 cm<sup>-1</sup> respectively corresponding to the sp<sup>3</sup>- and sp<sup>2</sup>- hybridized carbons, indicating the disordered graphite (D band) and the ordered state graphite (G band) of GNPs [13]. The red shift in the G band for *f*-GNPs revealed that the GNPs were chemically functionalized by -COOH, -C=O, -C-O-C- and -OH groups [14]. The intensity ratios (*ID/IG*) were calculated for all the four samples from

Raman peaks. The intensity ratio of GNPs-RuNRs was high ( $ID/IG = 0.2078$ ) when compared to that of GNPs-Ru(acac)<sub>3</sub> ( $ID/IG = 0.1589$ ), which revealed the physical attachment of RuNRs on GNPs [15].

### 4.3.2 Optimization of reaction conditions

The prepared GNPs-RuNRs have been applied as catalyst in the transfer hydrogenation of aldehydes/ketones using 2-propanol as hydrogen donor.

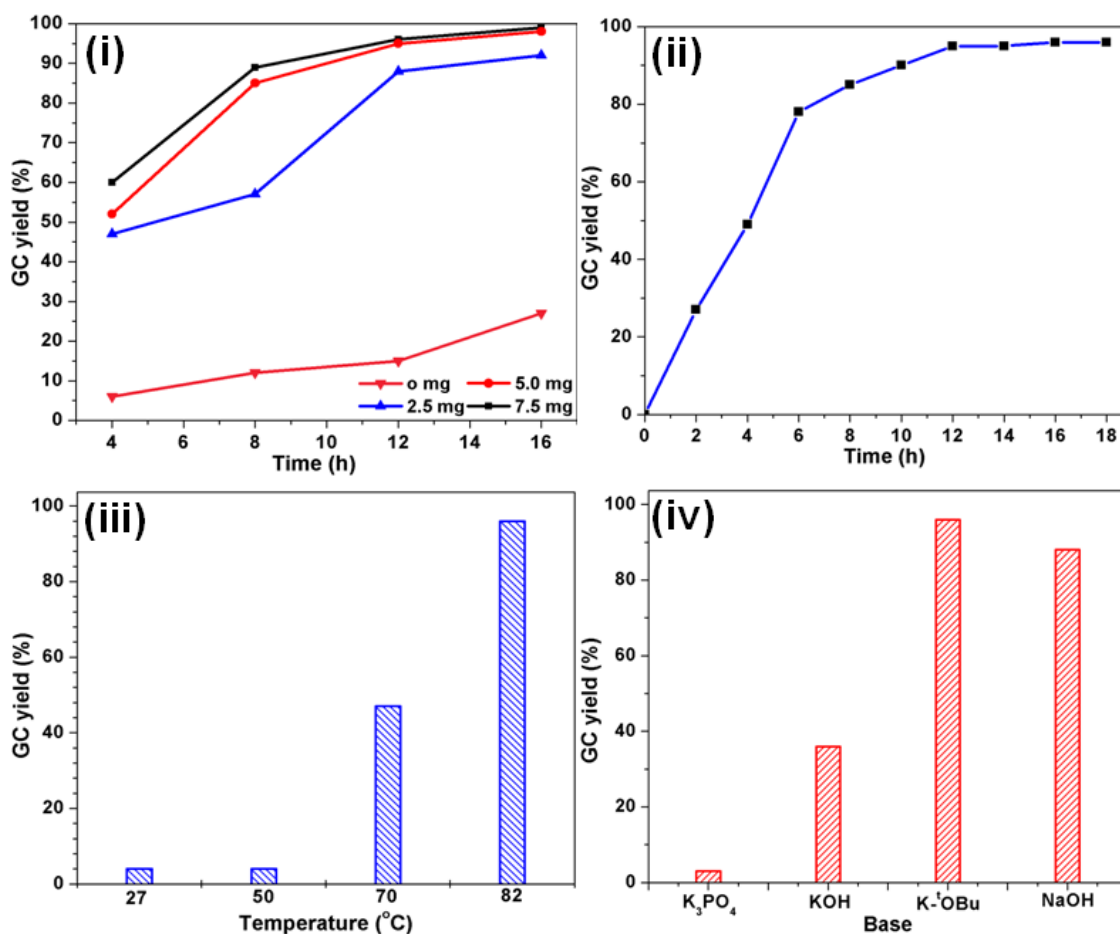


**Figure 4.6** – Effect of (i) catalyst amount, (ii) reaction time, (iii) temperature and (iv) base on transfer hydrogenation of acetophenone.

To find the most effective reaction condition, we have chosen acetophenone as a model substrate and varied the amount of catalyst, reaction time, temperature and base [Figure 4.6(1-iv)]. The conversion was checked by GC. At first, the catalyst amount was optimized; as we anticipated, a very lower conversion (13%) was obtained in the absence of GNPs-RuNRs. A 5.0 mg (0.15 mol %) of GNPs-RuNRs was found to be the optimum amount of catalyst. The optimum reaction time and temperature were 12 h and 82°C respectively. In base optimization, potassium *tert*-butoxide ((CH<sub>3</sub>)<sub>3</sub>COK, 1 mmol) was found to be the most effective one compared to NaOH, K<sub>2</sub>CO<sub>3</sub> and KOH.

### 4.3.3 Extension of scope

To extend the scope, the catalyst was applied to the transfer hydrogenation of wide range of carbonyl compounds in the optimum condition (Table 4.1). The conversion and yield were moderately affected by the substituent on the aromatic ring, but the high selectivity was maintained. Active aryl secondary ketone, acetophenone, was reduced to 1-phenylethanol in excellent yield of 95% with an excellent selectivity of 100% (Table 4.1, entry 1) whereas NiNPs system gave only 80% 1-phenylethanol [17]. In addition, the resultant product (1-phenylethanol) was analyzed by HPLC to understand the chirality of the product and found to be racemic. Similarly, 4-bromo acetophenone (Table 4.1, entry 2) gave the corresponding alcohol in excellent yield (95%) and selectivity (100%). In the conversion of 4-methoxy acetophenone to 1-(4-methoxyphenyl)ethanol (Table 4.1, entry 3), the present catalytic system afforded a better yield of 74% in comparison to the NiNPs system [18].

**Table 4.1 – Transfer hydrogenation of carbonyl compounds catalyzed by GNPs-RuNRs<sup>a</sup>**

entry	substrate (1a)	product (1b)	time (h)	conv. <sup>b</sup> (%)	sel. <sup>b</sup> (%)	yield <sup>b</sup> (%)
1			12	95	100	95
2			10	95	100	95 (89) <sup>c</sup>
3			12	74	100	74
4			8	63	100	63
5			8	87	96	83 (80) <sup>c</sup>
6			10	71	100	71 (68) <sup>c</sup>
7			10	90	86	76 (71) <sup>c</sup>

8			15	95	93	89 (82) <sup>c</sup>
9			9	100	55	55
10			8	90	62	52
11			10	93	94	87
12			10	96	96	92
13			14	99	100	99
14			14	99	98	97
15			18	61	100	61
16			20	25	100	25
17			20	72	100	72
18			20	82	100	82

<sup>a</sup>Reaction conditions: Substrate (1 mmole), GNPs-RuNRs (0.15 mol %), (CH<sub>3</sub>)<sub>3</sub>COK (1 mmole), *i*-PrOH (4 mL), 82° C. <sup>b</sup>Determined by GC analysis. <sup>c</sup>Isolated yield.

In the case of 4-nitro acetophenone, the conversion was less, but the selectivity was high (Table 4.1, entry 4). In the reduction of benzaldehyde to benzyl alcohol (Table 4.1, entry 5), the present catalytic system afforded a better yield compared to NiNPs-catalyzed conversion [17]. In the same way, benzophenone (Table 4.1, entry 6) was transformed into diphenylmethanol in moderate yield (71%) whereas Au/TiO<sub>2</sub> system produced only 44% of the product [19]. It was found that 4-fluoro benzophenone was transformed into its corresponding alcohol in moderate yield of 76% (Table 4.1, entry 7). A good yield of 89% was obtained from the reduction of 4-bromo benzophenone after stirring for 15 h (Table 4.1, entry 8). However, the reduction of 2-amino benzophenone (Table 4.1, entry 9) gave the corresponding alcohol in poor yield (55%) with poor selectivity. This may be due to the steric effect of an amino group at the *ortho* position [20].

Less reactive 2-butanone yielded 2-butanol in moderate yield of 52% (Table 4.1, entry 10). In the transfer hydrogenation of 2-pentanone to form 2-pentanol (Table 4.1, entry 11), the present catalytic system showed a better yield of 87% (94% selectivity) whereas MgO/Al<sub>2</sub>O<sub>3</sub> system showed lower yield of 47% even after stirring for 24 h [20]. Similarly, 2-hexanone was transformed into 2-hexanol in excellent yield (92%) with high selectivity (Table 4.1, entry 12). It is worth to mention that an excellent yield of 99% (100% selectivity) was obtained from the transfer hydrogenation of 2-octanone (Table 4.1, entry 13) whereas Ru(OH)<sub>x</sub>/TiO<sub>2</sub> system produced 2-octanol in 92% yield [21]. In the reduction of cyclohexanone to cyclohexanol, the present catalytic system showed a good yield of 97% with high selectivity (Table 4.1, entry 14) whereas CuNPs catalyzed reduction proceeded to give 88% of the product [23].

**Table 4.2 – Selective transfer hydrogenation of carbonyl compounds catalyzed by GNPs-RuNRs<sup>a</sup>**

entry	substrate	product	time (h)	conv. <sup>b</sup> (%)	sel. <sup>b</sup> (%)	yield <sup>b</sup> (%)
1			9	100	93	93
2			12	93	87	80
3			12	99	100	99

<sup>a</sup>Reaction conditions: Substrate (1 mmole), GNPs-RuNRs (0.15 mol %), (CH<sub>3</sub>)<sub>3</sub>COK (1 mmole), *i*-PrOH (4 mL), 82° C. <sup>b</sup>Determined by GC analysis.

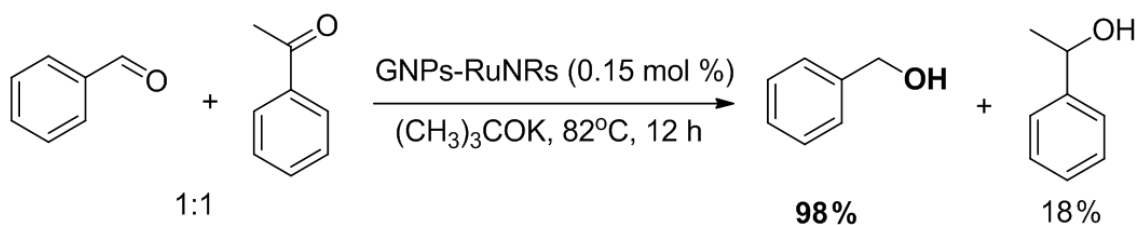
In the same way, cycloheptanone was reduced to cycloheptanol in moderate yield of 62% but the selectivity was high (Table 4.1, entry 15). Alicyclic ketone, 1-cyclohexylethanone was transformed into 1-cyclohexylethanol in poor yield (25%) (Table 4.1, entry 16).

The present GNPs-RuNRs system can be adopted for the reduction of heterocyclic carbonyl compounds as well. 2-Acetylthiophene was reduced to 1-thiophene ethanol (72%) with high selectivity (Table 4.1, entry 17) while nickel aluminosilicate system gave only 48% of the product [24]. Similarly, 1-furyl ethanone yielded 1-furyl ethanol in 82% (Table 4.1, entry 18) whereas MgO/Al<sub>2</sub>O<sub>3</sub> catalyzed reaction yielded only 50% of the product [21]. There can be two possible reasons for the

higher catalytic activity of GNPs-RuNRs: (i) higher surface area of GNPs and (ii) effective dispersion of the GNPs-RuNRs in the reaction medium [25].

#### 4.3.4 Chemoselectivity of GNPs-RuNRs

The present catalytic system was also investigated for the chemoselective reduction of various substrates under optimized reaction condition. The results are presented in Table 4.2. Methyl 4-formylbenzoate (Table 4.2, entry 1), was selectively (93% selectivity) reduced to methyl 4-(hydroxymethyl)benzoate in excellent yield of 93%. Similarly, hydrogenation of 4-acetylbenzoic acid yielded 4-(1-hydroxyethyl)benzoic acid selectively (87%) in 80% (Table 4.2, entry 2). 4-acetylbenzaldehyde was reduced selectively to 1-(4-(hydroxymethyl)phenyl)-ethanone in the present catalytic system (Table 4.2, entry 3). Furthermore, when an equimolar mixture of benzaldehyde and acetophenone was stirred under optimized reaction condition, benzaldehyde yielded benzyl alcohol in excellent yield of 98% whereas acetophenone was reduced to 1-phenylethanol in a lower yield of 18% (Scheme 4.1).



**Scheme 4.1** – Chemoselectivity of catalyst, GNPs-RuNRs.

### 4.3.5 Heterogeneity and reusability of GNPs-RuNRs

In order to inspect the factual heterogeneity of the GNPs-RuNRs, the transfer hydrogenation of acetophenone was carried out for 4 h, then the filtrate after the separation of solid GNPs-RuNRs was stirred for 8 h, no further reduction occurred (Figure 4.7). This clearly indicates the heterogeneous nature of the GNPs-RuNRs. In addition, the filtrate was also analyzed by ICP-MS; absence of Ru further confirmed the above fact.

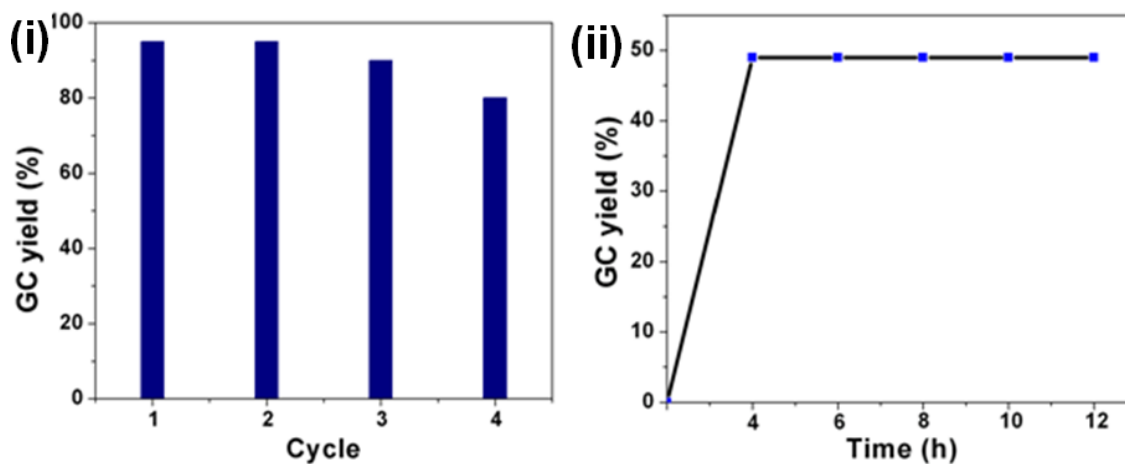


**Figure 4.7** – (i) Reusability test and (ii) heterogeneity test of GNPs-RuNRs for transfer hydrogenation of acetophenone.

The catalyst can be reused for four times (Figure 4.7). Additionally, TEM, XPS, SEM-EDS, XRD and Raman analyses were carried out for the used GNPs-RuNRs. No significant change in the morphology, NRs size and shape, chemical state and weight percentage of Ru was observed. The complete characterization details of used GNPs-RuNRs are shown in Figures 4.7.

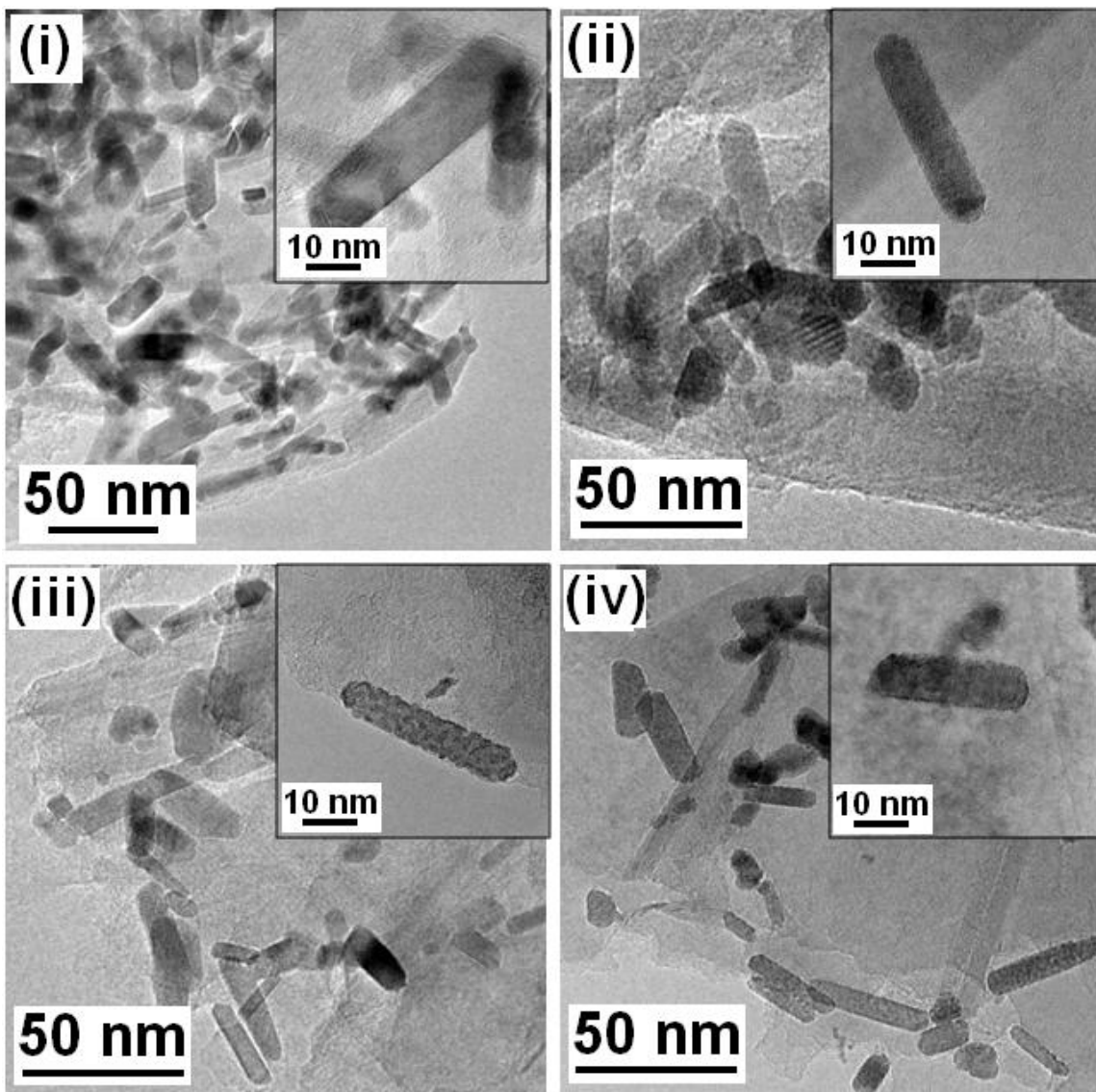


**Figure 4.8** – TEM images of used GNPs-RuNRs: (i) cycle 1, (ii) cycle 2, (iii) cycle 3 and (iv) cycle 4.

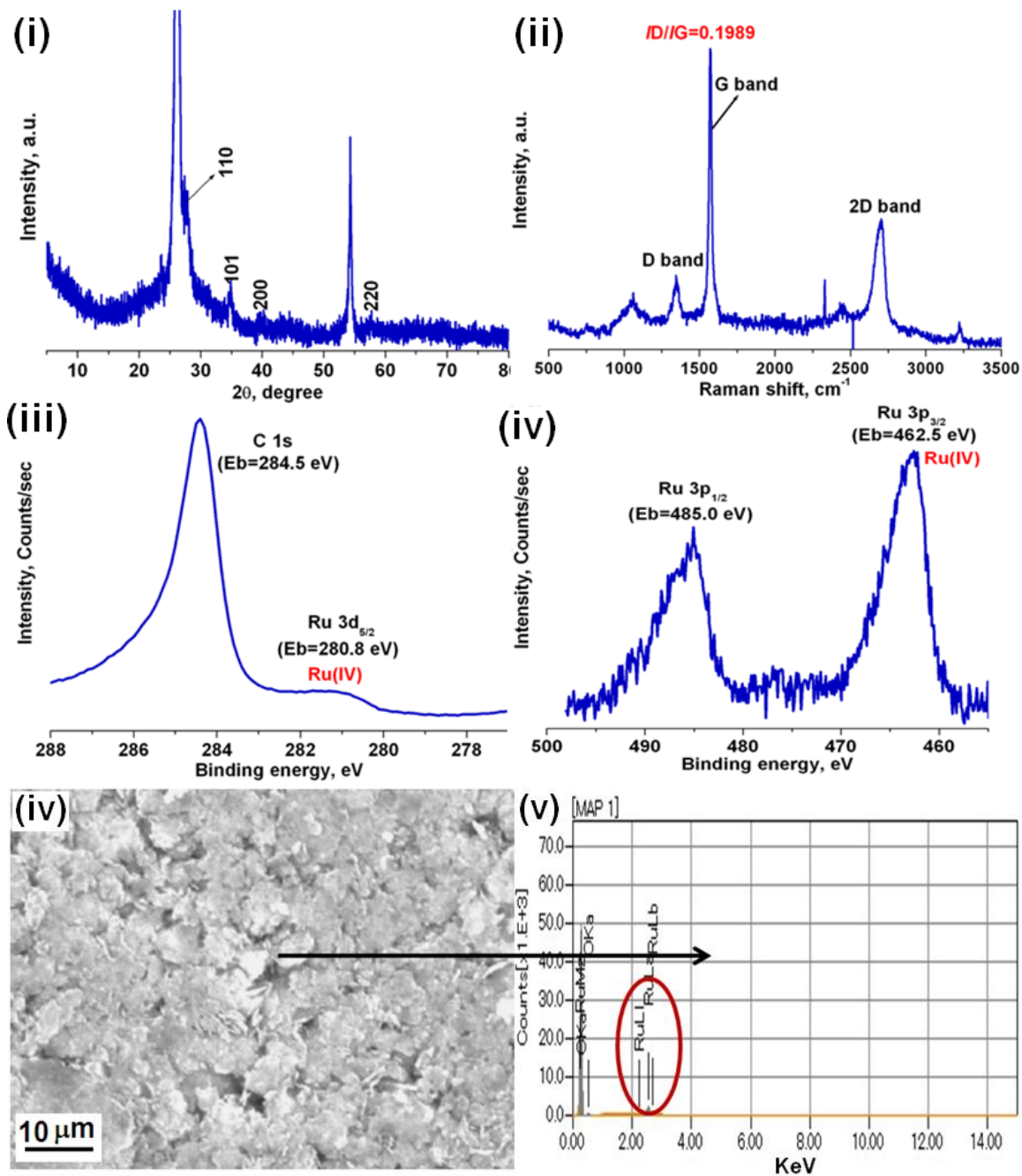


**Figure 4.9** – (i) XRD, (ii) Raman, (iii and iv) XPS and (iv and v) SEM-EDX of used GNPs-RuNRs.

### 4.3.6 Proposed mechanism

The mechanism proposed for the reduction of acetophenone involves metal hydride intermediate (Figure 4.10). First, the base reacts with 2-propanol to form 2-propoxide,  $(\text{CH}_3)_3\text{COH}$  and  $\text{K}^+$ . Subsequently, the formed 2-propoxide coordinates with Ru (**1**) and then hydride migrates from  $\alpha$ -C of 2-propoxide to the Ru to form Ru-H reducing species (**2**). Then coordinated acetone is replaced by acetophenone followed by hydride migration from Ru to  $\alpha$ -C of the substrate to give **4**. Finally, H exchange between  $(\text{CH}_3)_3\text{COH}$  and **4** yields 1-phenylethanol and completes the catalytic cycle.

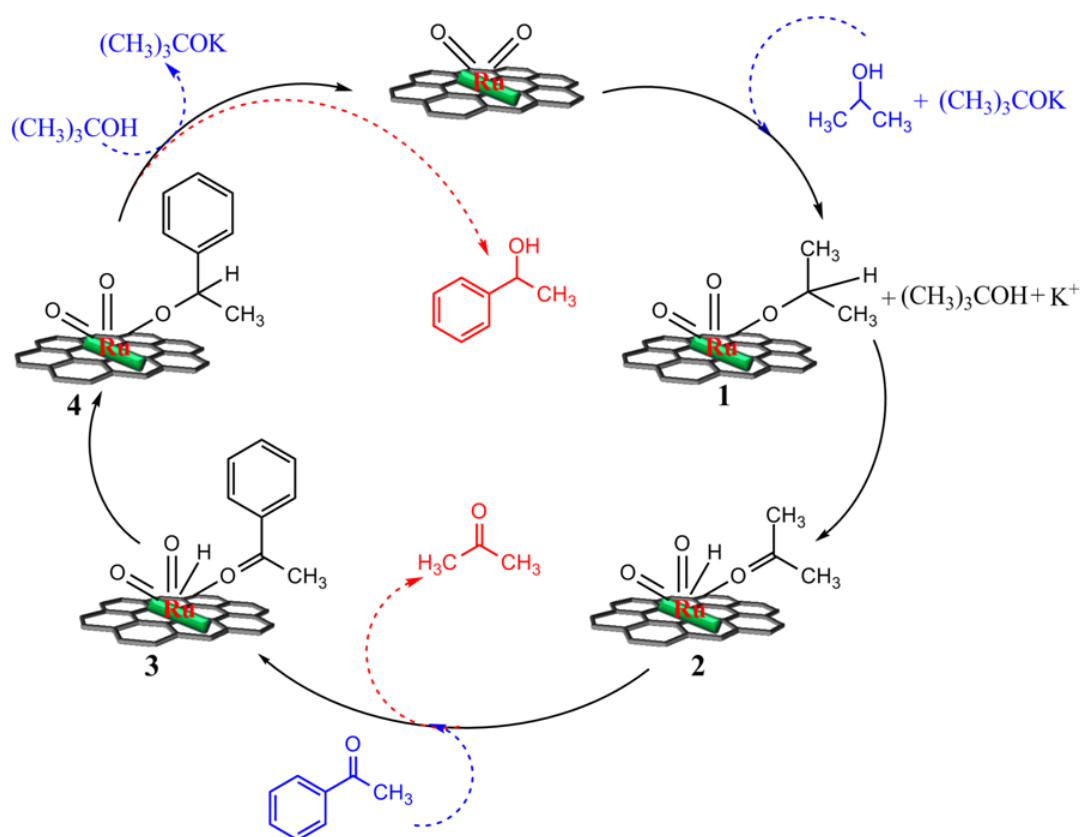


**Figure 4.10** – Proposed catalytic mechanism.

FT-IR and Raman spectra exhibited a weak band at  $\sim 2000\text{ cm}^{-1}$  for the catalyst which was stirred with a mixture of 2-propanol and  $(\text{CH}_3)_3\text{COK}$  at  $82^\circ\text{C}$  for 6 h. This confirmed the formation of Ru–H intermediate during the catalytic reaction (Figures 4.11 and 4.12).

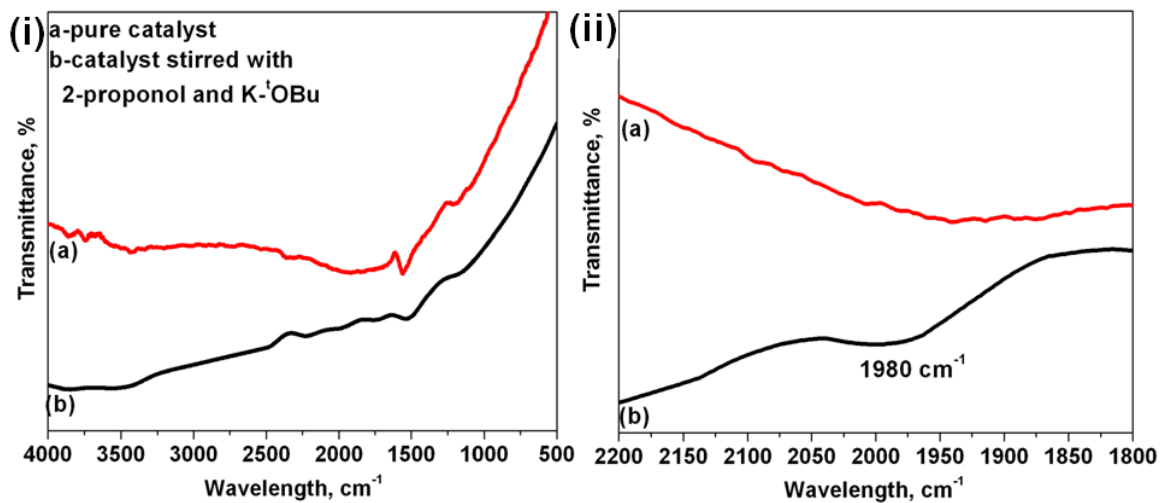


**Figure 4.11** – (i) FT-IR spectra (ii) of pure catalyst (a) and catalyst after stirred with 2-propanol and  $(\text{CH}_3)_3\text{COK}$  for 6 h at  $82^\circ\text{C}$  (b).

Certainly, graphene is a very expensive material and plays a vital role in many fields [8]. Hence the recovery of graphene from the catalyst after being used is very important. In this study, the GNPs were successfully recovered from the used GNPs-RuNRs. The results of TEM, Raman spectrum and XRD (Figure 4.13) of the recovered GNPs were well correlated with the results obtained for fresh GNPs.

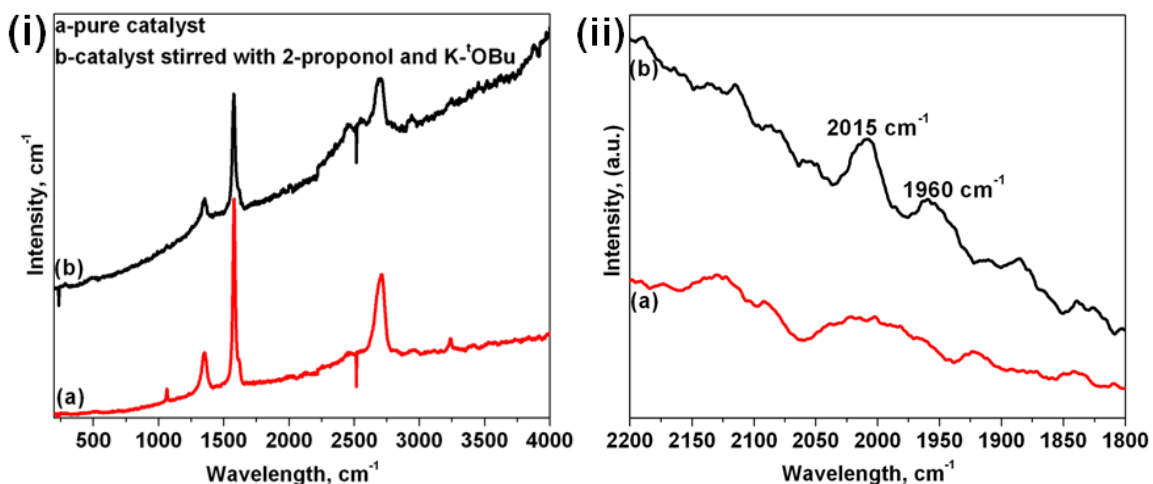


**Figure 4.12** – (i) Raman spectra (ii) of pure catalyst (a) and catalyst after stirred with 2-propanol and  $(\text{CH}_3)_3\text{COK}$  for 6 h at  $82^\circ\text{C}$  (b).

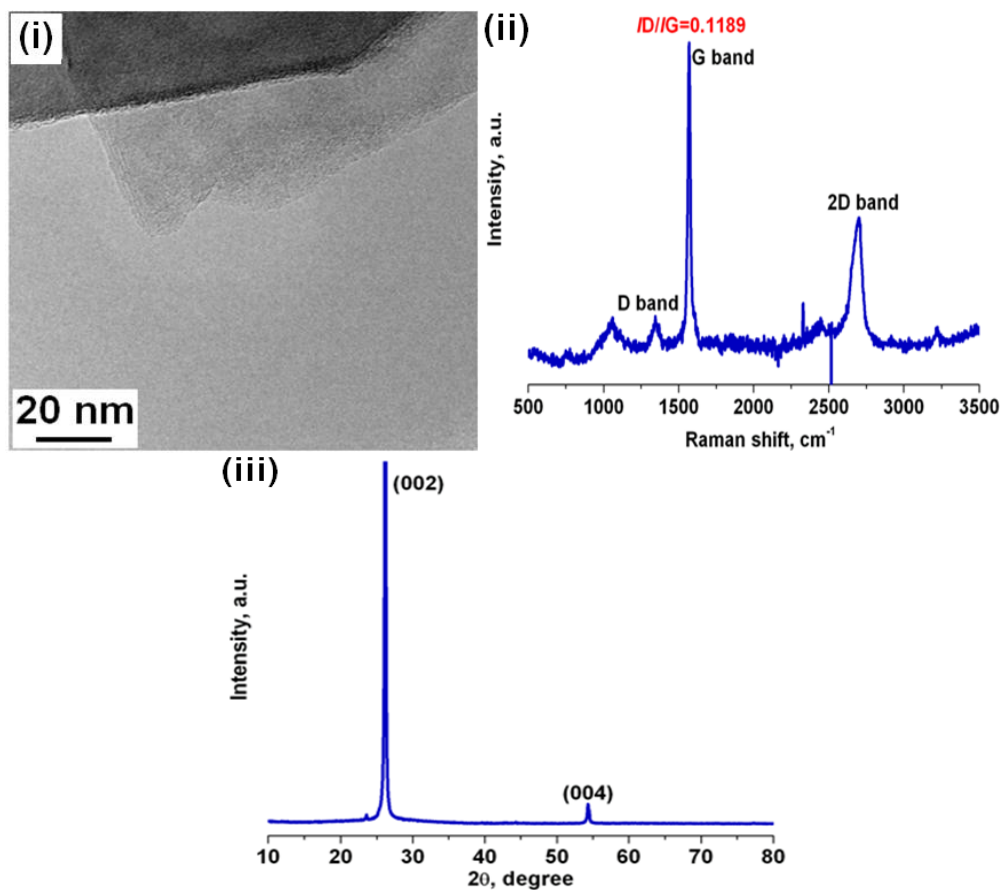


**Figure 4.13** – (i) TEM image, (ii) Raman spectra and (iii) WAXD pattern of recovered GNPs.

## 4.4 Conclusions

In summary, we applied a simple protocol to prepare GNPs supported RuNRs which exhibited excellent catalytic activity, chemoselectivity, stability and reusability in the transfer hydrogenation of aldehydes and ketones. Besides, GNPs were successfully recovered from the used GNPs-RuNRs.

## Reference

- [1] Zassinovich, G.; Mestroni, G.; Gladiali, S. Asymmetric Hydrogen Transfer Reactions Promoted by Homogeneous Transition Metal Catalysts. *Chem. Rev.* **1992**, *92*, 1051–1069.
- [2] Noyori, R.; Hashiguchi, S. Asymmetric Transfer Hydrogenation Catalyzed by Chiral Ruthenium Complexes. *Acc. Chem. Res.* **1997**, *30*, 97–102.
- [3] Sterk, D.; Stephan, M.; Mohar, B. Highly Enantioselective Transfer Hydrogenation of Fluoroalkyl Ketones. *Org. Lett.* **2006**, *8*, 5935–5938.
- [4] Rhyoo, H. Y.; Park, H. J.; Chung, Y. K. The First Ru(II)-Catalysed Asymmetric Hydrogen Transfer Reduction of Aromatic Ketones in Aqueous Media. *Chem. Commun.* **2001**, 2064–2065.
- [5] Johnstone, R. A. W.; Wilby, A. H. Heterogeneous Catalytic Transfer Hydrogenation and Its Relation to Other Methods for Reduction of Organic Compounds. *Chem. Rev.* **1985**, *85*, 129–170.
- [6] Auer, E.; Freund, A.; Pietsch, J. Tacke, T. Carbons as Supports for Industrial Precious Metal Catalysts. *Appl. Catal. A: Gen.* **1998**, *173*, 259–271.
- [7] Yu, W. J.; Hou, P. X.; Li, F.; Liu, C. Improved Electrochemical Performance Of Fe<sub>2</sub>O<sub>3</sub> Nanoparticles Confined in Carbon Nanotubes. *J. Mater. Chem.* **2012**, *22*, 13756–13763.
- [8] Geim, A. K. Graphene: Status and Prospects. *Science* **2009**, *324*, 1530–1534.
- [9] Krashennnikov, A. V.; Lehtinen, P. O.; Foster, A. S.; Pyykko, P.; Nieminen, R. M. Embedding Transition-Metal Atoms in Graphene: Structure, Bonding, and Magnetism. *Phys. Rev. Lett.* **2009**, *102*, 126807–126810.

- [10] Baoqiang, S.; Lei, H.; Tingting, Y.; Xueqin, C.; Hongwei, G. Highly-Dispersed Ultrafine Pt Nanoparticles on Graphene as Effective Hydrogenation Catalysts. *RSC Adv.* **2012**, *2*, 5520–5523.
- [11] Gil, M. S.; Luigi, R.; Peter, S.; Willi, B.; Rolf, M. Palladium Nanoparticles on Graphite Oxide and Its Functionalized Graphene Derivatives as Highly Active Catalysts for the Suzuki-Miyaura Coupling Reaction. *J. Am. Chem. Soc.* **2009**, *131*, 8262–8270.
- [12] Tsang, S. C.; Chen, Y. K.; Harris, P. J. F.; Green, M. L. H. A Simple Chemical Method of Opening and Filling Carbon Nanotubes. *Nature*, **1994**, *372*, 159–162.
- [13] Nabid, M. R.; Bide, Y.; Rezaei, S. J. T. Pd nanoparticles immobilized on PAMAM-grafted MWCNTs hybrid materials as new recyclable catalyst for Mizoraki–Heck cross-coupling reactions. *Appl. Catal. A: Gen.* **2011**, *406*, 124–132.
- [14] Lin, Y.; Watson, K. A.; Fallbach, M. J.; Ghose, S.; Smith, J. G.; Delozier, D. M.; Cao, W.; Crooks, R. E.; Connell, J. W. Rapid, Solventless, Bulk Preparation of Metal Nanoparticle-Decorated Carbon Nanotubes. *ACS Nano* **2009**, *3*, 871–884.
- [15] Filho, A. G. S.; Meunier, V.; Terrones, M.; Sumpter, B. G.; Barros, E. B.; Villalpando-Paez, F.; Filho, J. M.; Kim, Y. A.; Muramatsu, H.; Hayashi, T.; Endo, M.; Dresselhaus, M. S. Selective Tuning of the Electronic Properties of Coaxial Nanocables through Exohedral Doping. *Nano Lett.* **2007**, *7*, 2383–2388.
- [16] Sankar, J.; Sham, T. K.; Puddephatt, R. J. Low Temperature Chemical Vapour Deposition of Ruthenium and Ruthenium Dioxide on Polymer Surfaces. *J. Mater. Chem.* **1999**, *9*, 2439–2444.

- [17] Alonso, F.; Riente, P.; Yus, M. Hydrogen-Transfer Reduction of Carbonyl Compounds Promoted by Nickel Nanoparticles. *Tetrahedron* **2008**, *64*, 1847–1852.
- [18] Michalek, F.; Lagunas, A.; Jimenoa, C.; Pericas, M. A. Synthesis of Functional Cobalt Nanoparticles for Catalytic Applications. Use in Asymmetric Transfer Hydrogenation of Ketones. *J. Mater. Chem.* **2008**, *18*, 4692–4697.
- [19] Su, F. Z.; He, L.; Ni, J.; Cao, Y.; He, H. Y.; Fan, K. N. Efficient and Chemoselective Reduction of Carbonyl Compounds with Supported Gold Catalysts Under Transfer Hydrogenation Conditions. *Chem. Commun.* **2008**, 3531–3533.
- [20] Noyori, R.; Ohkuma, T. Asymmetric Catalysis by Architectural and Functional Molecular Engineering: Practical Chemo- and Stereoselective Hydrogenation of Ketones. *Angew. Chem. Int. Ed.* **2001**, *40*, 40–73.
- [21] Ruiz, J. R.; Sanchidrian, C. J.; Hidalgo, J. M.; Marinas, J. M. Reduction of Ketones and Aldehydes to Alcohols with Magnesium–Aluminium Mixed Oxide and 2-Propanol. *J. Mol. Catal. A: Chem.* **2006**, *246*, 190–194.
- [22] Yamaguchi, K.; Koike, T.; Kim, J. W.; Ogasawara, Y.; Mizuno, N. Highly Dispersed Ruthenium Hydroxide Supported on Titanium Oxide Effective for Liquid-Phase Hydrogen-Transfer Reactions. *Chem. Eur. J.* **2008**, *14*, 11480–11487.
- [23] Subramanian, T.; Pitchumani, K. Transfer Hydrogenation of Carbonyl Compounds and Carbon–Carbon Multiple Bonds by Zeolite Supported Cu Nanoparticles. *Catal. Sci. Technol.* **2012**, *2*, 296–300.
- [24] Neelakandeswari, N.; Sangami, G.; Emayavaramban, P.; Babu, S. G.; Karvembu, R.; Dharmaraj, N. Preparation And Characterization of Nickel Aluminosilicate

Nanocomposites for Transfer Hydrogenation of Carbonyl Compounds. *J. Mol. Catal. A: Chem.* **2012**, *356*, 90–99.

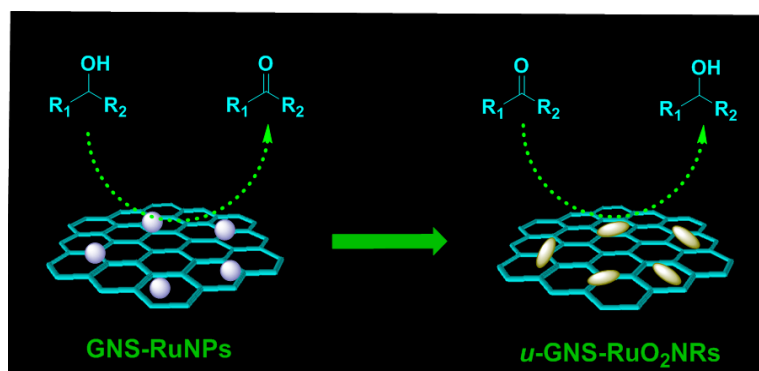
- [25] Kantam, M. L.; Rao, B. P. C.; Choudary, B. M.; Sreedhara, B. Selective Transfer Hydrogenation of Carbonyl Compounds by Ruthenium Nanoclusters Supported on Alkali-Exchanged Zeolite Beta. *Adv. Synth. Catal.* **2006**, *348*, 1970–1976.

## CHAPTER 5

### Dry synthesis of easily tunable nano ruthenium supported on graphene

– novel nanocatalysts for aerial oxidation of alcohols and transfer

hydrogenation of ketones



## CHAPTER 5

### **Dry synthesis of easily tunable nano ruthenium supported on graphene – novel nanocatalysts for aerial oxidation of alcohols and transfer hydrogenation of ketones**

#### **5.1 Introduction**

Carbonyl compounds such as aldehydes and ketones serve as key and versatile intermediates in C–C bond forming reactions and as a high-functional component in perfumery industry and also used for the synthesis of fine chemicals [1–3]. In order to obtain these compounds *via* organic transformation, a selective oxidation of primary and secondary alcohols is the prime route [4–6]. Although there are several homogeneous and heterogeneous metal catalysts have been proposed [7–10], particularly, MNPs based on Pd [11], Au [12], Pt [13] and Ru [14], play a tremendous role in aerial oxidation process due to their high recyclability and easy separation from the reaction mixture. Among the numerous catalytic systems, RuNPs based aerobic system is an effective, inexpensive and extremely versatile synthetic tool to afford selectively oxygenated products [15–17]. Consequently, many RuNPs mediated aerial oxidation systems in mild reaction conditions such as low temperature and shorter reaction time have been developed [18–21]. In spite of the advantages, they often require higher stoichiometric amounts of Ru (typically 10-20 mol %), which lead to environmental hazard as well as less economical feasibility. Besides, high surface energies and strong van der Waals interactions in RuNPs promote unavoidable aggregation, as a consequence, low catalytic

activities as well as poor reusability were observed [11]. To control the aggregation of RuNPs, several inorganic and organic supports have been used but their instability in high basic and acidic reaction conditions limits their use [22–24]. Owing to the better chemical stability and high surface area, activated carbon and CNTs have been used as a support for the active metal catalysts [25–29]. However, they too require higher stoichiometric amounts of Ru (typically 5.0-7.5 mol %) and the catalytic system has a very limited scope in terms of yields and selectivity [30, 31]. Therefore, developing an efficient, selective, stable, recyclable and versatile catalyst for the aerial oxidation process with the use of lesser amount of Ru remains a challenging task.

Very recently, graphene has been receiving a greater attention owing to its astounding properties such as unique structure, high surface area, and chemical as well as electrochemical inertness [32–34]. Graphene plays a remarkable role as support for transition MNPs in the heterogeneous catalysis [35]. Particularly, graphene-supported transition MNPs demonstrated outstanding catalytic activities mainly due to the effective dispersion in various solvents, less aggregation of MNPs and larger surface area of the nanocatalysts [36]. Moreover, the decoration of MNPs onto the GNS support has shown more versatility in carrying out the highly selective catalytic processes [37]. Recently, Gil *et al.*, [38] prepared PdNPs supported graphite oxide and used as a catalyst for the Suzuki-Miyaura coupling reaction with higher activity than the commercial Pd-C catalyst. Kamat *et al.*, [39] have investigated the interaction between graphene oxide and semiconductors (TiO<sub>2</sub>, ZnO), and graphene oxide and metal (Au, Pt) NPs. They have discussed their potential applications in catalysis, light energy conversion and fuel cells. We believe that the RuNPs based on graphene composite could overcome the above

discussed drawbacks especially higher stoichiometric amounts of Ru and the limited scope. In our study, RuNPs have been decorated over graphene nanosheets (GNS) by dry synthesis method and this was used as a nanocatalyst for the oxidation of alcohols. Chemoselectivity, heterogeneity and reusability of the catalyst during the oxidation of alcohols were examined. The influence of the size of RuNPs on the oxidation of alcohols was also studied. Moreover, to investigate the versatility of the GNS-RuNPs, the used catalyst (*u*-GNS-RuNPs) was separated out from the reaction, converted into GNS supported RuO<sub>2</sub> nanorods (*u*-GNS-RuO<sub>2</sub>NRs) by calcination and used as a catalyst in the transfer hydrogenation of ketones. In fact, the reduction of ketones to their corresponding alcohols is also one of the essential organic transformations in both industrial and fine chemical processes [40]. Particularly,  $\alpha,\beta$ -unsaturated alcohols synthesized from this route have a high commercial value [41]. Hence the used catalyst was applied in the transfer hydrogenation of ketones after calcination.

## **5.2 Experimental section**

### **5.2.1 Materials and characterization**

Graphene nanoplatelets (GNPs, purity: >99wt%, surface area: >750m<sup>2</sup>/g, average thickness: 3 nm, layers: <5, diameter: 1-2  $\mu$ m) were purchased from Cheap tubes Inc., VT, US. H<sub>2</sub>SO<sub>4</sub> (98%) and HNO<sub>3</sub> (70%) were purchased from Wako pure chemicals, Japan. Ru(acac)<sub>3</sub> (97%) and all other chemicals were purchased from Aldrich and used as received.

The morphology of the prepared nanocatalysts was investigated by transmission electron microscopy (TEM, JEM-2100 JEOL Japan) with accelerating voltage of 200 kV. The weight percentage and homogeneous decoration of metal NPs on GNS were confirmed by scanning electron microscopy-energy dispersive spectrum [SEM-EDS, Hitachi (model-3000H)]. The same field of view was then scanned using an EDS spectrometer to acquire a set of X-ray maps at 1 ms point acquisition for approximately one million counts. Nature of interaction between MNPs and GNS was examined by Raman spectrometer (Hololab 5000, Kaiser Optical Systems Inc., USA) using argon laser at 532 nm with a Kaiser holographic edge filter. Wide angle X-ray diffraction (WAXD) experiments were performed at room temperature using a Rotaflex RTP300 instrument (Rigaku.Co., Japan) at 50 kV and 200 mA. Nickel-filtered Cu K $\alpha$  radiation was used for the measurements, along with an angular range of  $10 < 2\theta < 80^\circ$ . To confirm the chemical state of metal NPs in nanocatalysts, X-ray photoelectron spectrum was recorded in Kratos Axis-Ultra DLD model instrument. The samples were irradiated under Mg K $\alpha$  ray source before XPS analysis. In order to determine the conversion of the reactants, Gas chromatograms (GC) was recorded using Shimadzu-2010 gas chromatograph. The specific surface area (BET method), specific pore volume and average pore diameter (BJH method) of the sample were measured by N<sub>2</sub> adsorption-desorption isotherms using Quantochrome Autosorb 1 sorption analyzer. Before the measurements, the samples were outgassed at 250 °C under vacuum (10<sup>-5</sup> mbar) for 3 h. Ru content during heterogeneity test was determined by ICP-mass spectrometer (7500CS, Agilent).

### 5.2.2 Dry synthesis of nanocatalyst (GNS-RuNPs)

Owing to the hydrophobic nature and chemical inertness of the graphene [42], the decoration of MNPs over graphene is a very difficult task. All previous studies so far reported: used solution-based techniques i.e. wet synthesis [43–45]. In order to obtain a homogeneous distribution and very good adhesion of MNPs on graphene, many factors such as solvent, concentration of metal precursor, reducing agent, deposition time and temperature need to be controlled very carefully, therefore, a wet synthesis approach has limitations [46–48]. In contrast to wet synthesis, the solventless bulk synthesis so called ‘dry synthesis’ has been attracting greater interest due to its simplicity, better adhesion and has an advantage of least parameters to be controlled [49]. Therefore, a straight forward dry synthesis method was adopted to decorate the RuNPs on GNS.

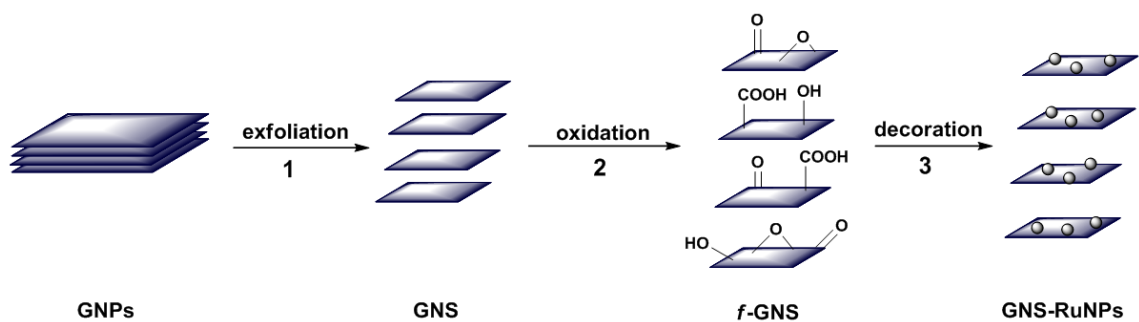


**Figure 5.1** – Schematic illustration for the preparation of GNS-RuNPs.

Initially, the bi and few layered graphene nanosheets (GNS) were obtained from graphene nanoplatelets (GNPs) by a solution phase exfoliation (SPE) method. In a typical procedure, 500 mL of *N*-methylpyrrolidone (NMP) containing 0.5 g of GNPs was sonicated for 12 h at 4°C (Figure 5.1, step 1). The GNPs-dispersed NMP solution was

centrifuged and vacuum dried. Then the resultant graphene nanosheets (GNS, 0.5 g) were chemically treated with a 3:1 volume ratio mixture of concentrated  $\text{H}_2\text{SO}_4$  and  $\text{HNO}_3$ . The mixture was sonicated at  $40^\circ\text{C}$  for 3 h in an ultrasonic bath for the generation of functional groups ( $-\text{COOH}$ ,  $-\text{C}=\text{O}$ ,  $-\text{C}-\text{O}-\text{C}-$  and  $-\text{OH}$ ) on the GNS surface (Figure 5.1, step 2). After cooling to room temperature, the reaction mixture was diluted with 500 mL of deionized water and then vacuum-filtered through a filter paper of  $3\ \mu\text{m}$  porosity. The resultant *f*-GNS were repeatedly washed with deionized water until the pH reached neutral and finally, the solid was vacuum dried at  $60^\circ\text{C}$ . After that, 0.13 g of  $\text{Ru}(\text{acac})_3$  was added into 0.5 g of *f*-GNS and mixed well by a mortar and pestle under ambient condition. The homogeneous mixture of *f*-GNS and  $\text{Ru}(\text{acac})_3$  was obtained within 10-15 minutes. The impregnated  $\text{Ru}(\text{acac})_3$  was thermally decomposed into metallic RuNPs by calcination at  $300^\circ\text{C}$  for 3 h under argon atmosphere (Figure 5.1, step 3). Figure 5.1 shows a schematic illustration of the procedure for the preparation of GNS-RuNPs.

### 5.2.3 Aerial oxidation of alcohols

GNS-RuNPs (5 mg, 0.036 mol%) were stirred in 4 mL of toluene taken in a round-bottomed flask equipped with a condenser and a stirring bar. The substrate (1 mmol) was added to the stirring solution and then the mixture was refluxed at  $110^\circ\text{C}$  under atmospheric pressure of air. The oxidation reaction was monitored by TLC. After the completion of the reaction, the nanocatalyst was separated out from the reaction mixture by simple centrifugation, and the products and unconverted reactants were analyzed by GC. Selectivity of the product formed in each reaction was also calculated. Subsequently, the products of the selected oxidation reactions were isolated. The

separated nanocatalyst was washed well with diethyl ether, dried at 130°C for 3 h and reused. Yield of the product, conversion and selectivity were calculated by using the equations (1), (2) and (3), respectively.

$$\text{GC yield (\%)} = \% \text{ of product formed} \quad (1)$$

$$\text{GC conversion (\%)} = 100 - \% \text{ of reactant remains} \quad (2)$$

$$\text{Selectivity (\%)} = 100 - (\text{conversion} - \text{yield}) \quad (3)$$

## 5.2.4 Transfer hydrogenation of ketones

A mixture of *u*-GNS-RuO<sub>2</sub>NRs (5.0 mg, 0.033 mol% of Ru), substrate (1.0 mmol), 2-propanol (4 mL) and potassium *tert*-butoxide (112.21 mg, 1 mmol) were refluxed at 82°C. The nanocatalyst was separated out from the reaction mixture after the completion of the reaction by simple centrifugation, and the products and unconverted reactants were analyzed by GC. Selectivity of the product was also calculated.

## 5.3 Result and discussions

### 5.3.1 Characterization of GNS-RuNPs

To investigate the morphology and fairly accurate number of GNS layers (bi or few layers), TEM images were taken for pure GNPs, GNS, *f*-GNS and GNS-RuNPs (Figure 5.2). The TEM image [Figure 5.2(i)] showed that the GNPs were two-dimensional and pure. As seen from the magnified TEM images [Figure 5.2(i) and (v)], most of the GNPs were found as irregular ultra thin sheets having size ranging from 0.5

$\mu\text{m}$  to  $2\ \mu\text{m}$ . Further, GNPs showed a multi layer with an average thickness of about 7-9 nm. Whereas the GNPs after the SPE process with NMP [Figure 5.2(ii)] exhibited a continuous, wrinkled and transparent sheet with an average thickness of about 0.8-2 nm, indicating the successful generation of GNS [50]. In order to confirm the formation of GNS, Brunauer–Emmett–Teller (BET) surface area was determined for GNPs and GNS. It was found that the BET surface area of GNS was obviously higher ( $103.1\ \text{m}^2\text{g}^{-1}$ ) than that of the GNPs ( $62.5\ \text{m}^2\text{g}^{-1}$ ). These results are consistent with one of our previous reports [51]; Raman, XRD and XPS results also substantiate the existence of GNS (few) layers. For more details, refer the TEM images in the supporting information (Figure 5.3). Ultra-fine RuNPs were homogeneously dispersed on the surface of GNS [Figure 2(iv)]. The factual size of these attached RuNPs was found to be around 0.5-3.0 nm. Referring to the TEM images [Figures 5.2(vii) and (viii)], RuNPs were adhered on the anchoring sites of GNS with a very narrow particle size distribution ranging from 0.5 to 3 nm. The mean diameter of RuNPs was found to be ca. 1.7 nm. Furthermore, no free RuNPs were found in the background of the TEM images [Figures 5.2(iv), (vii) and (viii)], which confirmed the complete utilization of RuNPs. The GNS-RuNPs has a BET surface area of  $83.3\ \text{m}^2\text{g}^{-1}$  with a pore volume of  $0.392\ \text{cm}^3\text{g}^{-1}$  and a BJH desorption average pore diameter of 19 nm. In addition, the surface area per unit mass ( $S$ ) of RuNPs was calculated to be  $283.42\ \text{m}^2\text{g}^{-1}$  based on the equation  $S = 6000/(\rho \times d)$ , where  $d$  is the mean diameter of RuNPs (1.7 nm), and  $\rho$  is the density of Ru ( $12.45\ \text{gcm}^{-3}$ ) [52].

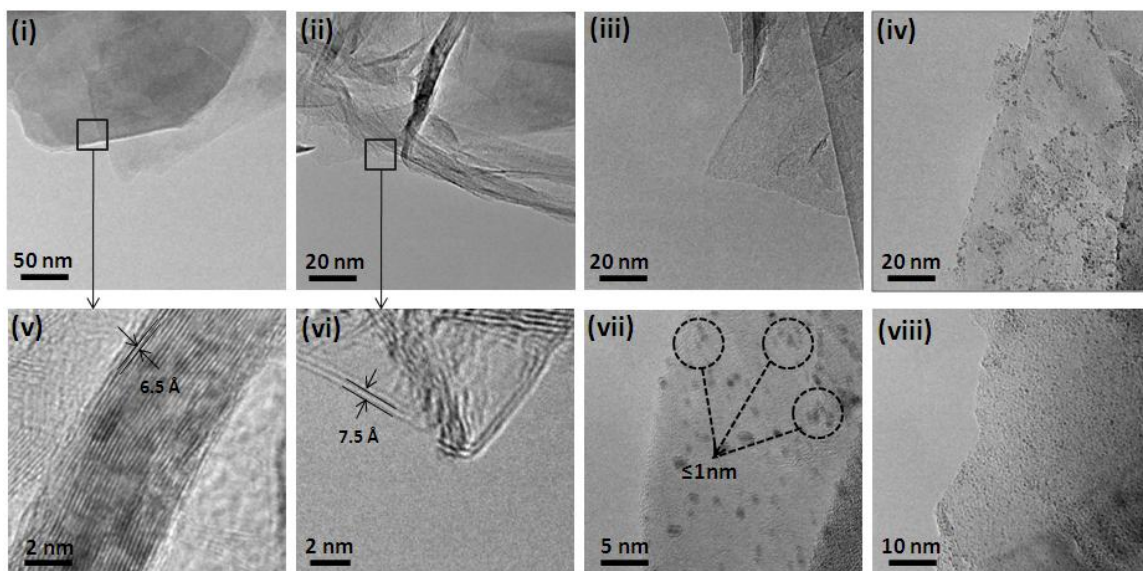


**Figure 5.2** – (i and v) TEM images of GNPs, (ii and vi) GNS, (iii) *f*-GNS and (iv, vii and viii) GNS-RuNPs.

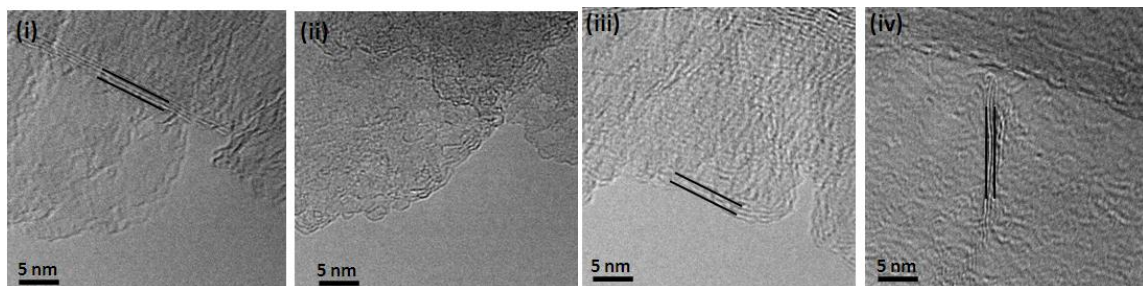


**Figure 5.3** – High resolution TEM images of GNS.

Figure 5.4 shows the SEM-EDS and their corresponding elemental mapping images of GNS-RuNPs. The weight percentage of Ru in GNS-RuNPs was 3.31, as determined by EDS analysis [Figure 5.4(ii)]. From Figure 5.4(v), the weight percentage of oxygen was found to be 3.52 which indicate the presence of –OH groups in GNS-RuNPs. Figures 5.4(iv) and (v) depict the homogeneous distribution of RuNPs in GNS-RuNPs. The credibility of the proposed method can be recognized from the purity of

GNS-RuNPs that contain only carbon, ruthenium and oxygen elements as confirmed by EDS analysis (Figure 5.4).

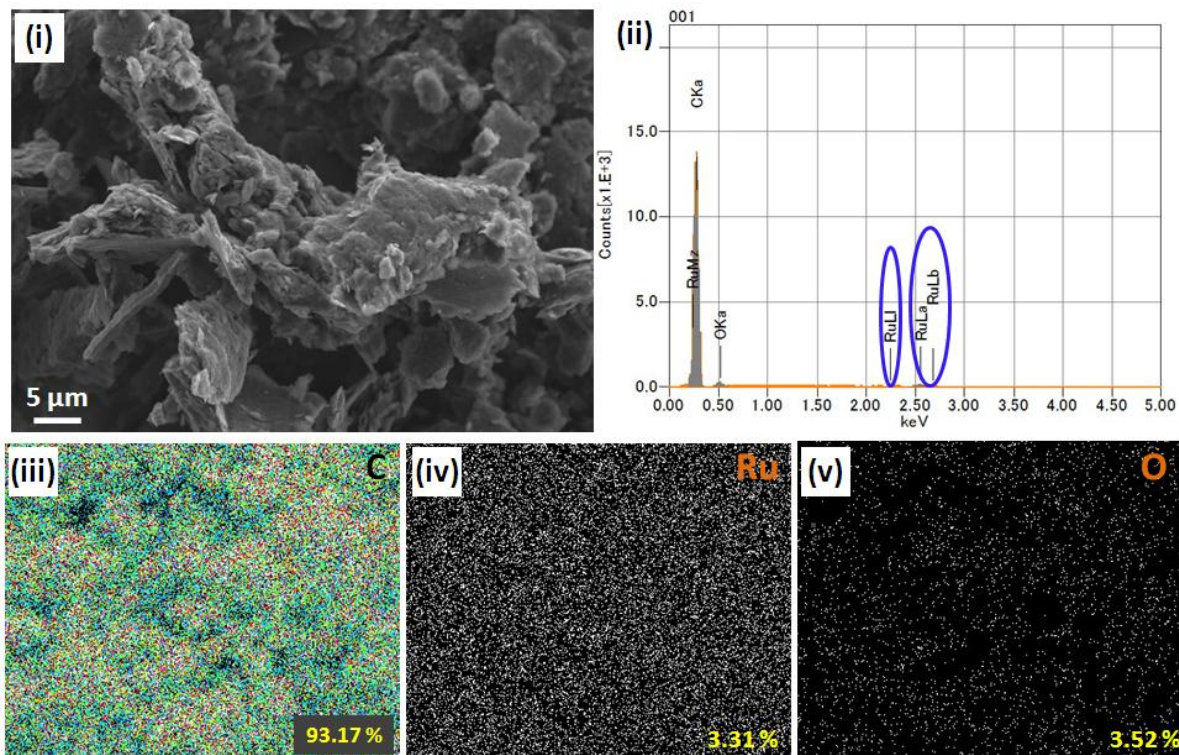


**Figure 5.4** – (i) SEM image and (ii) EDS spectra of GNS-RuNPs, and corresponding elemental mapping observations of (iii) C, (iv) Ru and (v) O.

Raman spectra were recorded for GNPs (**a**), GNS (**b**), *f*-GNS (**c**), GNS-Ru(acac)<sub>3</sub> [Ru(acac)<sub>3</sub> and GNS mixture before calcination] (**d**) and GNS-RuNPs (**e**), under 514.5 nm excitation over the Raman shift interval of 250-4000 cm<sup>-1</sup> (Figure 5.5). Well known that, graphene shows Raman features in the region 800-2000 cm<sup>-1</sup> [53]. As expected, all the five samples (**a-e**) exhibited three main Raman features, corresponding to the well-defined D-band line at ~1345 cm<sup>-1</sup>, G-band line at ~1570 cm<sup>-1</sup> and 2D-band line at ~2700 cm<sup>-1</sup> [54]. The G-band line was originated from the in-plane vibration of sp<sup>2</sup>

carbon atoms, which represented the relative degree of graphitization [55]. The D-band line was related to the amount of disorder which arises only in the presence of defects, indicating the presence of  $sp^3$  carbon atoms or defect sites in graphene [56]. The 2D-band line at  $2700\text{ cm}^{-1}$  is an overtone of the D band. Obviously, the intensity ratios of D, G and 2D bands ( $I_D/I_G$  and  $I_{2D}/I_G$ ) are often used as a diagnostic tool to evaluate the number of layers and defects concentration in graphene [57]. The calculated intensity ratios for all the five samples are shown in Figures 5.5(iii) and (iv). The  $I_D/I_G$  (0.1475) and  $I_{2D}/I_G$  (0.4032) values of GNS were found higher than the  $I_D/I_G$  (0.0909) and  $I_{2D}/I_G$  (0.3809) of GNPs, which indicated the effective exfoliation of GNPs. Besides, the shape of the 2D band [Figure 5.5(iv)] was also significantly changed [51]. These changes confirmed the successful generation of bi- and few-layered GNS, as a consequence, the surface area has been increased [51]. Figure 5.4(iii) confirms the chemical functionalization of GNS surface by  $-\text{COOH}$ ,  $-\text{C}=\text{O}$ ,  $-\text{C}-\text{O}-\text{C}-$  and  $-\text{OH}$  groups as the  $I_D/I_G$  (0.1505) and  $I_{2D}/I_G$  (0.4206) ratios were high for *f*-GNS when compared to that of pure GNS ( $I_D/I_G=0.0909$  and  $I_{2D}/I_G=0.3809$ ). Indeed, these functional groups act as effective nucleation centers for RuNPs, which assist homogeneous decoration as well as better adhesion of RuNPs on GNS [58]. It is noteworthy that the  $I_D/I_G$  (0.5320) ratio of sample **e** was about four times higher than that of *f*-GNS (**c**), and in comparison to the *f*-GNS (**c**), a positive shift in G band ( $1570$  to  $1578\text{ cm}^{-1}$ ) was observed in **e**, which confirmed the attachment of RuNPs on the surface of GNS. Apart from these relative intensity ratios, the Raman spectrum of sample **d** showed four new peaks at  $462$ ,  $506$ ,  $625$  and  $692\text{ cm}^{-1}$  [Figure 5.5(ii)], which are attributed to the presence of acetylacetonate

groups. However, these peaks were completely disappeared in sample **e** which revealed that Ru(acac)<sub>3</sub> was converted into metallic Ru [59].

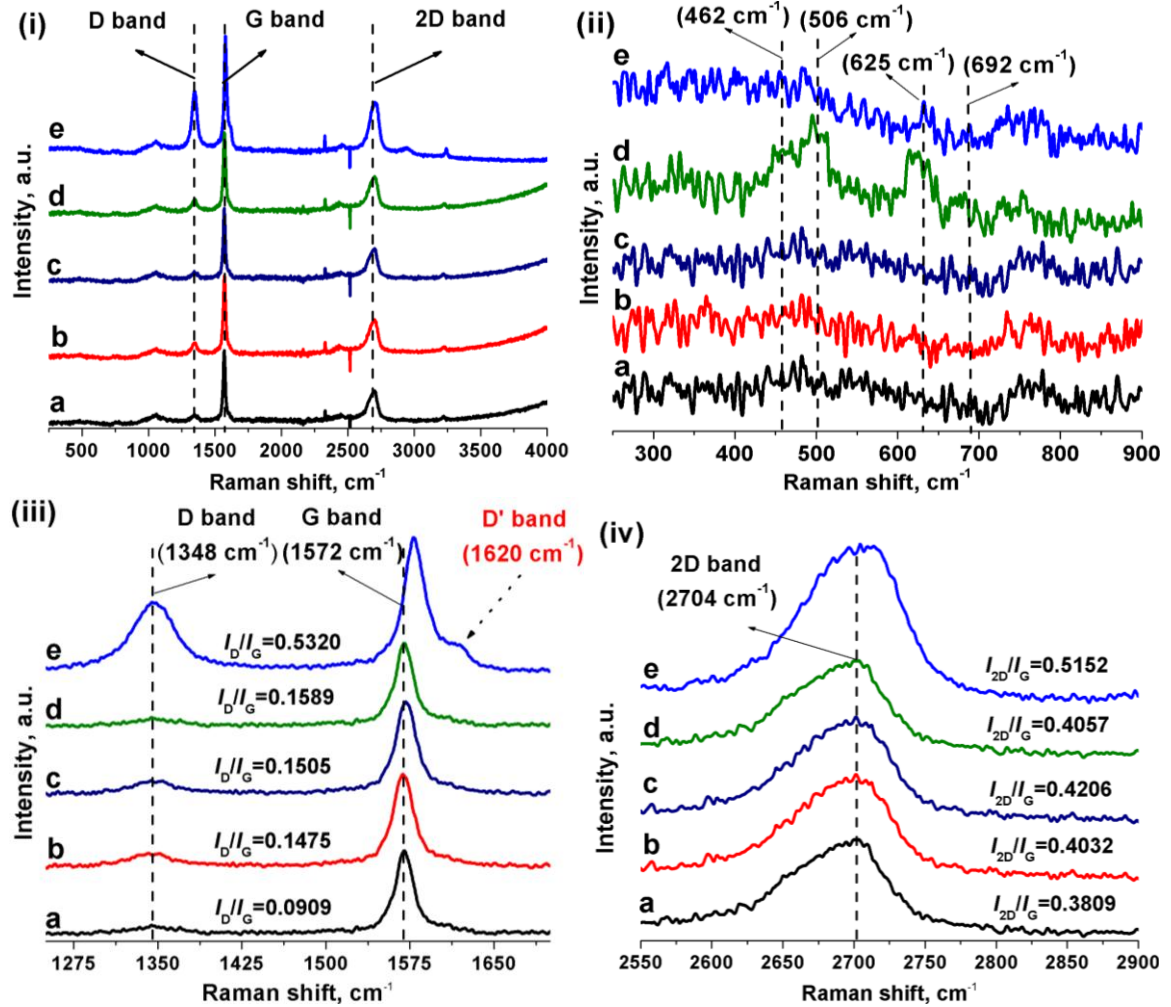


**Figure 5.5** – (i) Full and (ii, iii and iv) magnified Raman spectra of GNPs (a), GNS (b), *f*-GNS (c), GNS+Ru(acac)<sub>3</sub> (d), and GNS-RuNPs (e).

Furthermore, the presence of a shoulder peak at 1620 cm<sup>-1</sup> in sample **e** indicated the presence of larger defect sites in GNS; this may be due to a very strong attachment of RuNPs and/or may be caused by further fragmentation of GNS into smaller sheets during the preparation process [60].

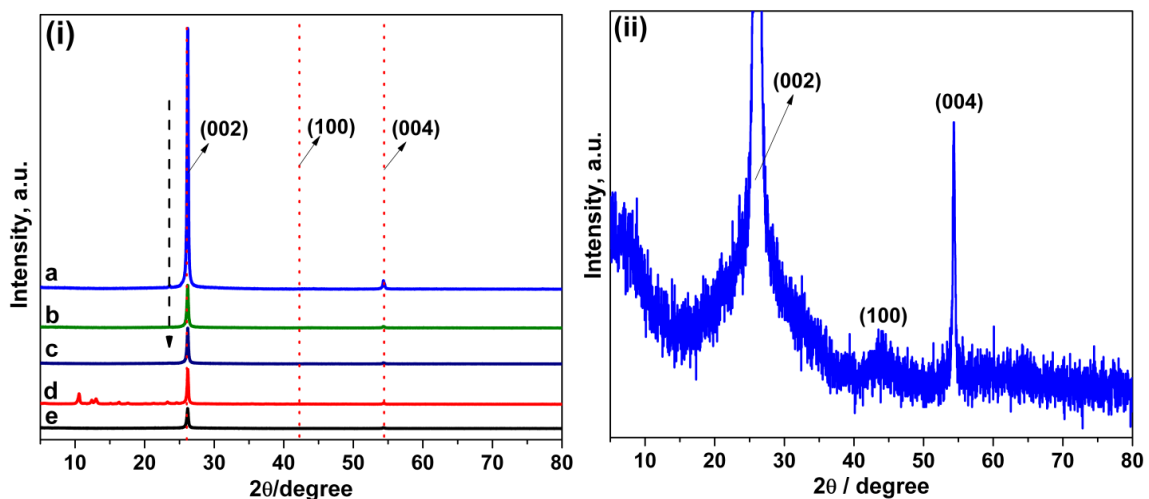


**Figure 5.6** – (i) XRD pattern of GNPs (a), GNS (b), *f*-GNS (c), (d) GNS+Ru(acac)<sub>3</sub> and (e) GNS-RuNPs, and (ii) magnified XRD pattern of GNS-RuNPs.

Figure 5.6 shows XRD patterns of pure GNPs (a), GNS (b), *f*-GNS (c), GNS-Ru(acac)<sub>3</sub> (d), and GNS-RuNPs (e). All the five samples (a-e) showed diffraction peaks at 26.5°, 44.2°, and 54.8°, corresponding to the (002), (100), and (004) crystal planes of graphite respectively, which are attributed to the hexagonal graphite structures of GNS [61]. As a result of SPE process, a significant decrease in the intensity of diffraction peak at 26.5° was observed in b compared to a, which confirmed the generation of layered GNS [Figure 5.6(i)] [62, 63]. A further decrease in the intensity of this peak in sample c might be due to the presence of functional groups in *f*-GNS. In fact, the inter-layers of carbon stacked by van der Waals forces have interaction energy of about 2 eV/nm<sup>2</sup> [64]. In order to break this energy, typically ~300 nN/lm<sup>2</sup> magnitude of force is required [64]. This extremely weak force might be achieved during the mixing/grinding process. The sample d exhibited a typical XRD pattern for acetylacetonate groups of Ru(acac)<sub>3</sub> (JCPDS No. 14-0733), whereas the sample e showed no diffraction peaks for Ru (Figure 3), which implied that Ru particles were of nano-crystalline nature [65]. Moreover, the

absence of acetylacetonate peaks at around  $12.0^\circ$  in the sample **e** confirmed that  $\text{Ru}(\text{acac})_3$  was completely converted into Ru on the surface of GNS.

In order to investigate the functionalization on GNS and the chemical state of Ru in GNS-RuNPs, XPS spectra were recorded for GNS, *f*-GNS and GNS-RuNPs; the results are shown in Figure 5.7. As expected, all the three samples showed a C 1s peak and a O 1s peak at 284.6 and 532.8 eV respectively [Figure 5.7(i)]. In order to find the shift in the peak, curve fitting was performed on C 1s and O 1s spectra of *f*-GNS and GNS-RuNPs using a Gaussian-Lorentzian peak shape. Prior to peak fitting, a Shirley baseline correction was done.

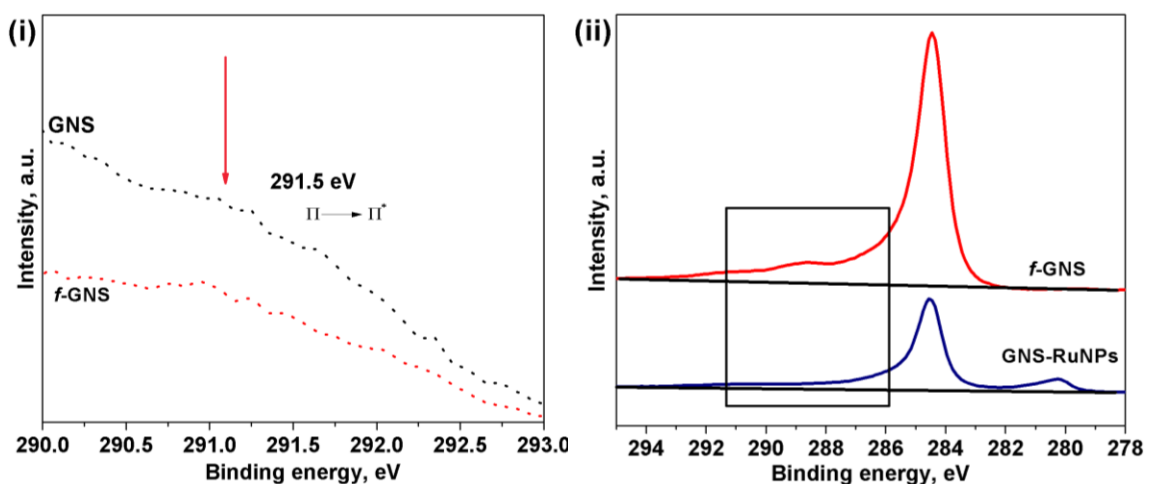


**Figure 5.7** – Magnified C 1s peaks of (i) GNS and *f*-GNS, and (ii) *f*-GNS and GNS-RuNPs.

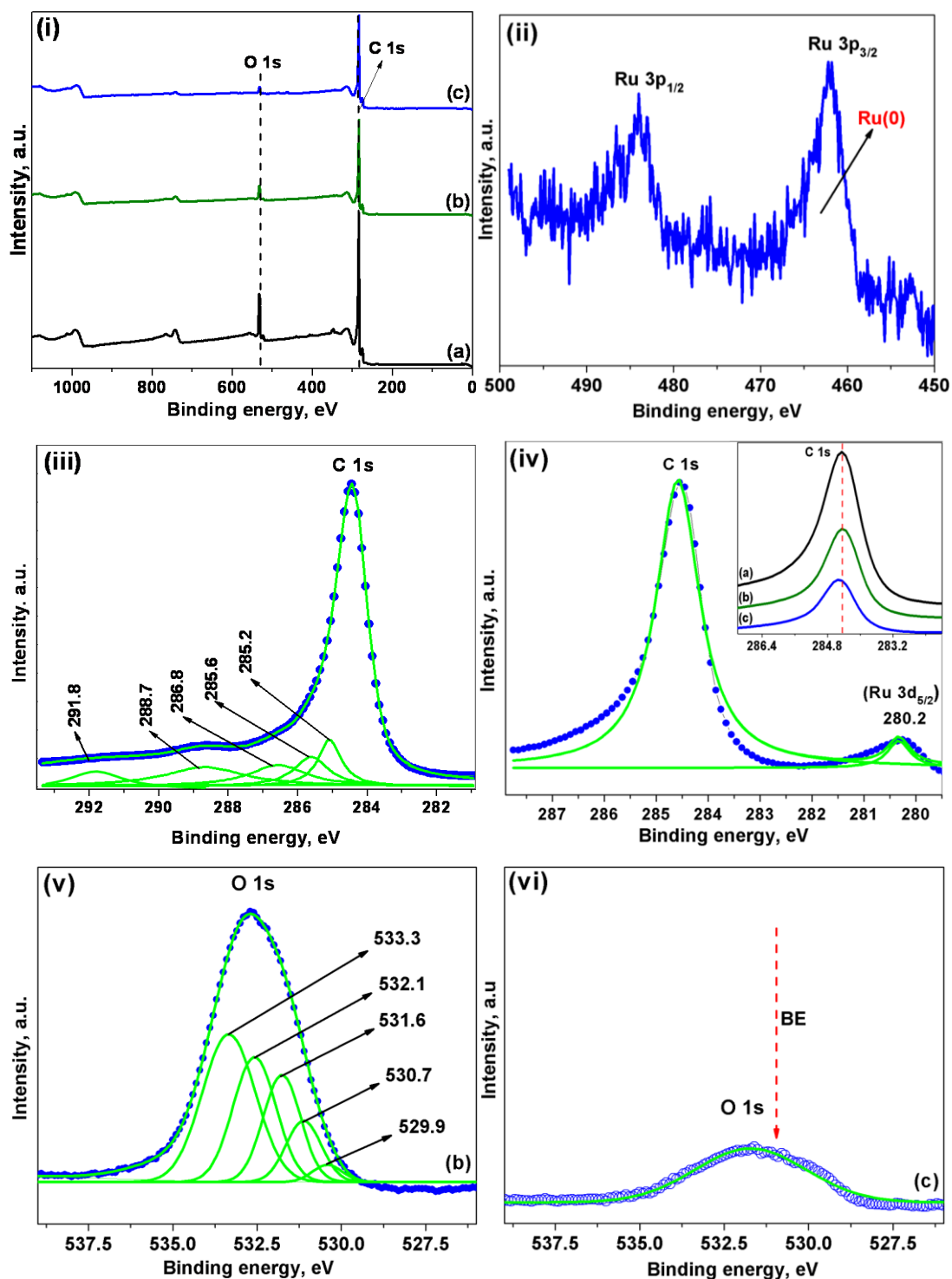


**Figure 5.8** – (i) (i) XPS spectra of (a) GNSs, (b) *f*-GNSs and (c) GNS-RuNPs, (ii) main peaks of Ru 3p of GNS-RuNPs, (iii) C 1s peak of *f*-GNSs, (iv) main peaks of Ru 3d and O 1s of GNS-RuNPs [insert: C 1s peak of (a), (b) and (c)], and (v and vi) magnified O 1s peak of *f*-GNS and GNS-RuNPs.

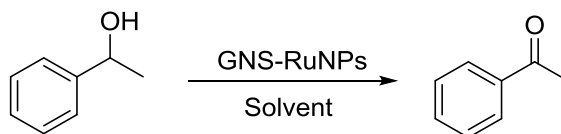
The binding energy (BE) of the C–C and C–H bonds were assigned at 284.5–285 eV and the peaks at 285.2, 285.6, 286.8 and 288.7 eV were ascribed to C–OH, –C–O–C–, C=O and –COOH groups respectively [Figure 5.8(iii)] [65]. Similarly, deconvolution of the O 1s spectra of *f*-GNS [Figure 5.8(v)] resulted in five peaks located at 529.9, 530.7, 531.6, 532.1 and 533.3 eV, which were assigned to the C=O, –COOH, C–OH, –C–O–C– and H<sub>2</sub>O respectively [66]. In comparison to the C 1s spectrum of GNS [Figure 5.7(i)], the intensity of  $\pi \rightarrow \pi^*$  shake-up satellite peak at 291.5 eV significantly decreased, which supports the successful functionalization of GNS [67]. In fact, the presence of carboxylic groups makes GNS hydrophilic and assists homogeneous decoration and good adhesion of RuNPs [68]. Mainly, –COOH group plays a bridging role between the RuNPs and GNS by exchanging the proton of carboxyl group (–COOH) of the *f*-GNS with RuNPs, hence, a strong attachment of RuNPs on the surface of GNS was achieved [68]. The XPS spectrum of the GNS-RuNPs in Ru 3p region [Figure 5.8(ii)] showed BE for Ru 3p<sub>3/2</sub> at 461.0 eV and Ru 3p<sub>1/2</sub> at 483.2 eV, which correspond to the photoemission from metallic Ru [69].

In Figure 5.8(vi), GNS-RuNPs showed Ru 3d<sub>5/2</sub> peak at 280.2 eV which was attributed to the metallic Ru [69]. The overlapping of the C 1s and the Ru 3d<sub>3/2</sub> peaks at ~285 eV made it difficult to assign the BE of Ru 3d<sub>3/2</sub>. Referring the O 1s spectrum of GNS-RuNPs [Figure 5.8(vi)], all the deconvoluted peaks (529.9, 530.7, 532.1 and 533.3 eV) were disappeared except the weak one related to the C–OH bond (~531.6 eV) as compared with the O 1s spectrum of *f*-GNS [Figure 5.8(v)]. Alike, in the C 1s spectrum of GNS-RuNPs [Figure 5.8(vi)], the deconvoluted peaks at the binding energies of 285.6, 286.8 and 288.7 eV were completely disappeared. The disappearance of the deconvoluted

peaks in both O 1s and C 1s spectra of GNS-RuNPs showed a virtually complete reduction of the oxygen functional groups (C=O, -COOH and -C-O-C-) [66]. Interestingly, a positive shift in C 1s peak was observed for GNS-RuNPs when compared with that of the *f*-GNS; this confirmed the strong interaction between GNS and RuNPs [70]. Furthermore, the decrease in the intensity of C 1s peak in GNS-RuNPs, in comparison to GNS, is an indication of generation of few layered GNS [71]. These results are in well agreement with the results of TEM, Raman and XRD.

### 5.3.2 Optimization of reaction conditions for the oxidation of alcohols

In order to find the optimum reaction conditions for the oxidation of alcohols, we used 1-phenylethanol as a substrate and results are given in Table 5.1. Various organic solvents such as *N,N*-dimethylacetamide (DMAc), *N,N*-dimethylformamide (DMF), toluene and dimethyl sulfoxide (DMSO) were tested in the oxidation reaction (Table 5.1, entries 1–4). The high yield of 99% was achieved when the reaction was carried out in toluene. As expected, no oxidized product was obtained in the absence of GNS-RuNPs (Table 5.1, entry 5). The optimum amount of GNS-RuNPs catalyst was found to be 5 mg (0.036 mol %) (Table 5.1, entries 3, 6–8). To the best of our knowledge, this is the lowest amount of Ru catalyst reported for the aerial oxidation of alcohols till to date. In temperature optimization, a maximum yield of 99% was obtained when the reaction was stirred at 110°C (Table 5.1, entries 3, 9–11). The reaction time of 16 h was found to be an optimum (Table 5.1, entries 3, 12–21).

**Table 5.1– Optimization of the reaction conditions for oxidation of 1-phenylethanol<sup>a</sup>**

entry	solvent <sup>b</sup>	amount of catalyst (mol %)	temp. (°C)	time (h)	yield <sup>c</sup> (%)
1	DMAc	0.036	110	16	48
2	DMF	0.036	110	16	35
<b>3</b>	<b>toluene</b>	<b>0.036</b>	<b>110</b>	<b>16</b>	<b>99</b>
4	DMSO	0.036	110	16	61
5	toluene	0	110	16	0
6	toluene	0.018	110	16	14
7	toluene	0.054	110	16	99
8	toluene	0.072	110	16	99
9	toluene	0.036	25	16	2
10	toluene	0.036	50	16	14
11	toluene	0.036	80	16	91
12	toluene	0.036	110	0	0
13	toluene	0.036	110	2	3
14	toluene	0.036	110	4	4
15	toluene	0.036	110	6	5
16	toluene	0.036	110	8	5
17	toluene	0.036	110	10	15
18	toluene	0.036	110	12	17
19	toluene	0.036	110	14	18
20	toluene	0.036	110	18	99
21	toluene	0.036	110	20	99

<sup>a</sup>All the reactions were performed with 1.0 mmol (117.0  $\mu$ L) of 1-phenylethanol.

<sup>b</sup>A 4 mL of solvent was used in all the reactions.

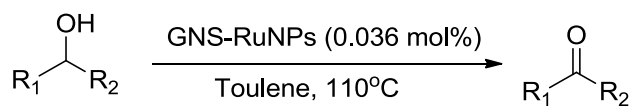
<sup>c</sup>GC yield.

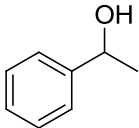
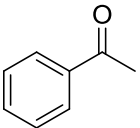
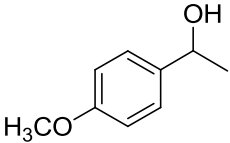
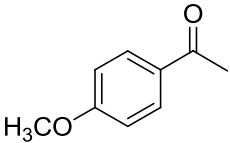
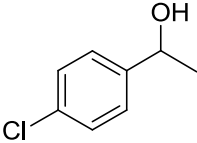
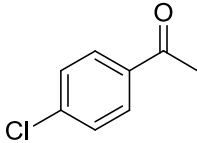
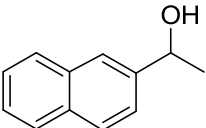
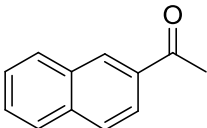
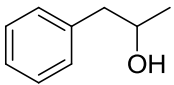
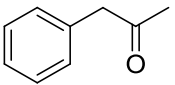
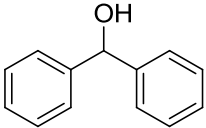
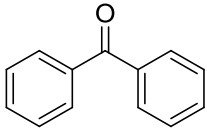
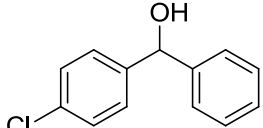
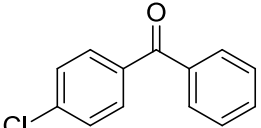
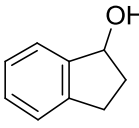
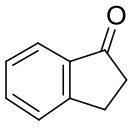
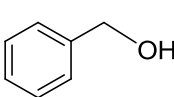
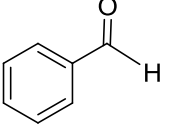
Finally, to confirm the reaction to be aerobic, the reaction was performed under N<sub>2</sub> atmosphere using the optimized reaction conditions. A very low conversion (13%) was observed under N<sub>2</sub> atmosphere; this confirmed that GNS-RuNPs oxidize the alcohols using atmospheric O<sub>2</sub>.

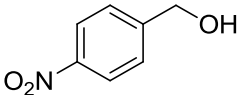
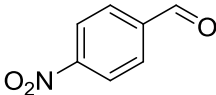
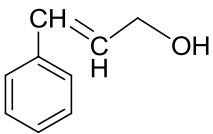
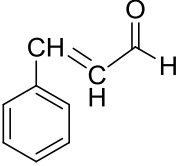
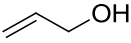
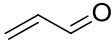
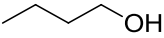
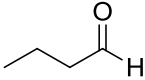
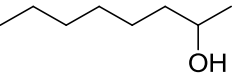
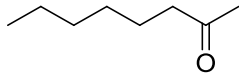
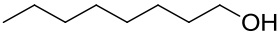
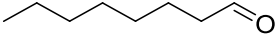
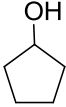
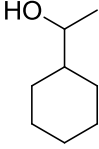
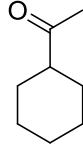
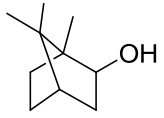
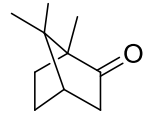
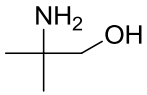
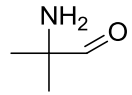
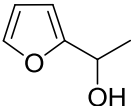
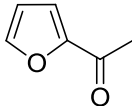
### 5.3.3 Extension of scope

The optimized reaction conditions were applied to the oxidation of various aliphatic, aromatic, alicyclic, benzylic, allylic, amino and heterocyclic alcohols (Table 5.2). Results in Table 5.2 revealed that a variety of alcohols could be oxidized into their corresponding carbonyl compounds in good to excellent yields with high selectivity. Active aryl secondary alcohol, 1-phenylethanol, was oxidized to acetophenone quantitatively with an excellent selectivity of 100% (Table 5.2, entry 1) whereas Ru/CNTs catalytic system gave only 64% of acetophenone [31]. Generally, the substrates with electron donating substituents such as methoxy, bromo or chloro, are less reactive due to mesomeric effect, and therefore, often exhibit lower yields [72]. However, in the present case, 1-phenylethanol containing electron donating substituent such as methoxy or chloro at the *para* position was effectively oxidized to the corresponding ketone in good yield without affecting the selectivity (Table 5.2, entries 2 and 3). In contrast to CrO<sub>3</sub>/H<sub>5</sub>IO<sub>6</sub> oxidation [73], the 2-naphthyl ethanol was oxidized to 2-acetylnaphthalene in good yield (98%) without oxidizing the naphthalene ring (Table 5.2, entry 4). It was found that 1-phenyl-2-propanol was transformed to its corresponding ketone in moderate yield of 59% with 100% selectivity (Table 5.2, entry 5). In the conversion of diphenylcarbinol to benzophenone (Table 5.2, entry 6), the present catalytic system produced a better yield of 83% in comparison to the 28.2% yield of Pd/C system [74]. Diphenylcarbinol with chloro group at the *para* position also gave its corresponding ketone in excellent yield (93%) (Table 5.2, entry 7). In the same way, 1-indanol was converted into 1-indanone in 86% yield after 22 h (Table 5.2, entry 8).

**Table 5.2 – Oxidation of alcohols<sup>a</sup>**



entry	substrate	product	time (h)	conv. <sup>b</sup> (%)	sel. <sup>b</sup> (%)	yield <sup>b</sup> (%)
1			16	99	100	99
2			16	86	100	86 (80) <sup>c</sup>
3			24	90	88	78
4			18	98	100	98 (95) <sup>c</sup>
5			18	59	100	59
6			20	83	100	83(79) <sup>c</sup>
7			22	93	100	93(86) <sup>c</sup>
8			22	86	77	63
9			18	95	100	95 (89) <sup>c</sup>

10			24	99	96	95 (93) <sup>c</sup>
11			21	81	100	81
12			9	67	100	67
13			22	93	100	93
14			20	56	100	56
15			20	93	100	93
16			24	63	94	60
17			22	70	73	43
18			19	100	61	61
19			22	89	76	65
20			22	76	73	49

<sup>a</sup>Reaction conditions: Substrate (1 equiv.), GNS-RuNPs (0.036 mol%), toluene (4 mL), 110°C. <sup>b</sup>Determined by GC analysis. <sup>c</sup> Isolated yield is given in paranthesis.

The present catalytic system is also competent to oxidize the primary benzylic alcohols to the corresponding aldehydes effectively. Referring entry 9 in Table 5.2, benzyl alcohol yielded benzaldehyde in excellent yield (95%) and selectivity (100%) without over-oxidation to benzoic acid whereas Ru-substituted silicotungstate catalytic system gave a poor yield of 64% with an over-oxidation of benzyl alcohol to benzoic acid [75]. For the transformation of 4-nitrobenzyl alcohol to 4-nitro benzaldehyde (Table 5.2, entry 10), the present GNS-RuNPs catalyst was very effective (95% yield after 24 h) compared to V<sub>2</sub>O<sub>5</sub> which gave only 79% of the desired product after 25 h [76]. Moreover, inspection of entry 11 in Table 5.2 revealed that cinnamyl alcohol yielded cinnamaldehyde in good yield of 81% (100% selectivity) without intramolecular hydrogen transfer or geometrical isomerization of the double bond.

Several existing Ru based oxidation systems are mainly suffered by the over-oxidation of allylic and aliphatic alcohols to their corresponding carboxylic acids, which leads to lower selectivity and therefore hinders its industrial applications. It is worth to mention that the present catalytic system showed a high selectivity (100%) toward the oxidation of allylic and aliphatic alcohols (Table 5.2, entries 12-15) without over-oxidation. Allylic and aliphatic alcohols such as 2-propenol and 1-butanol were converted into the corresponding aldehydes in good to excellent yields (Table 5.2, entries 12 and 13). Less reactive 1-octanol was transformed into 1-octanone in good yield of 93% (Table 5.2, entry 14) without any over oxidation whereas Ru-substituted silicotungstate-catalyzed oxidation of the same substrate gave only 14% of 1-octanone even after stirring for 48 h [75]. In the conversion of 2-octanol to 2-octanone (Table 5.2, entry 15), the present catalytic system gave a better yield of 56% (100% selectivity) whereas

hydroxyapatite-supported palladium (PdHAP)-catalyzed oxidation yielded only 10.5% of 2-octanone [77].

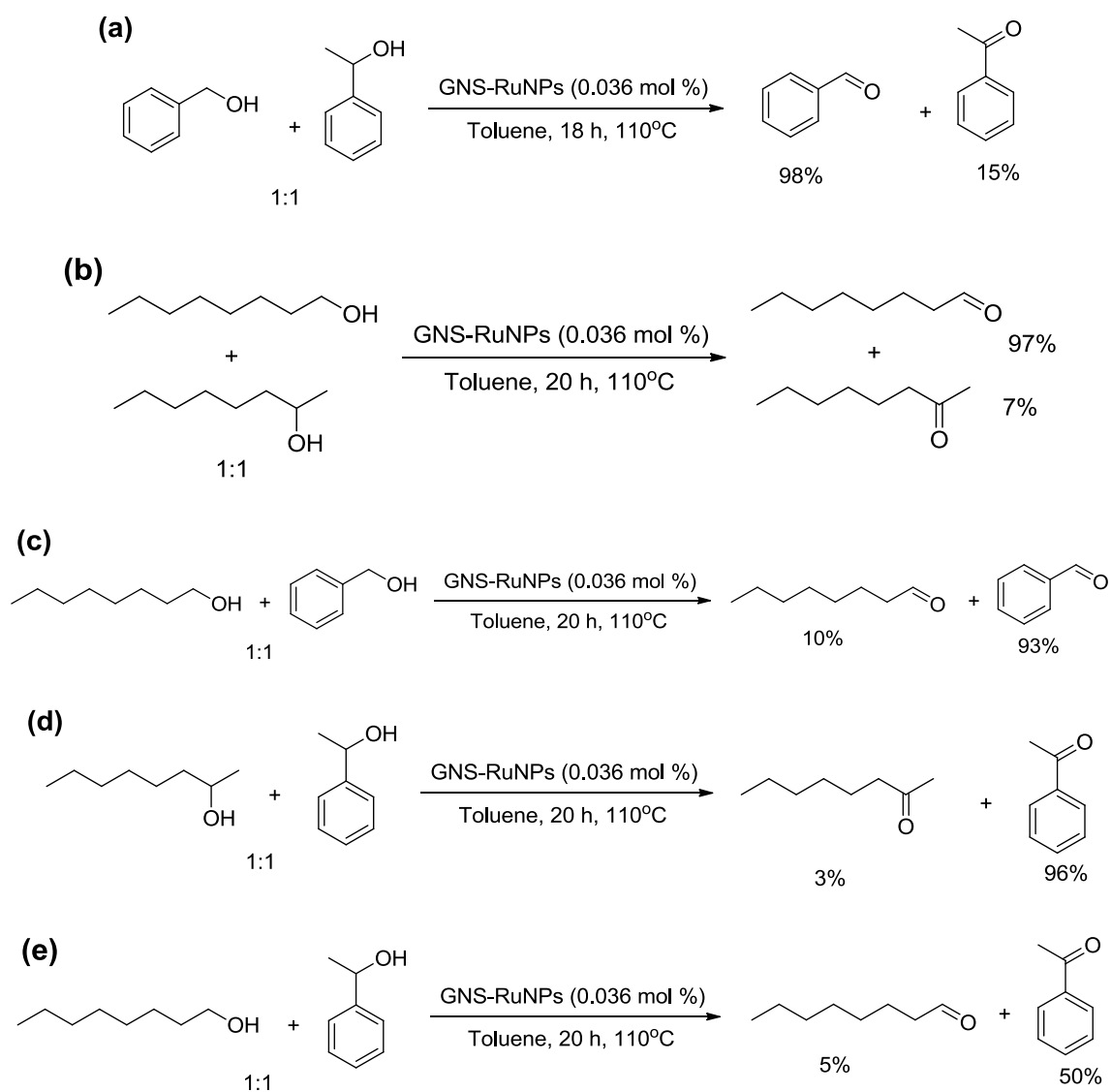
Less reactive cyclopentanol was converted into cyclopentanone in moderate yield of 60% whereas Au/Fe<sub>3</sub>O<sub>4</sub>@SiO<sub>2</sub> system produced only 42% yield (Table 5.2, entry 16) [78]. A moderate yield (43%) of ketone was obtained from the oxidation of 1-cyclohexylethanol after stirring for 24 h (Table 5.2, entry 17). More interestingly, the sterically hindered alcohols such as 2-amino-2-methylpropan-1-ol and DL-isoborneol (Table 5.2, entries 18 and 19) were efficiently oxidized to their corresponding ketones. In spite of possessing heterocyclic ring, 2-furyl ethanol (Table 5.2, entry 20) is capable of being oxidized to 2-acetyl furan in moderate yield (49%) in the present catalytic system.

Under the optimized reaction condition, active ruthenium oxo-species forms on the surface of GNS. Obviously, the active species is unstable and its formation is faster, which favor higher activity of the present catalytic system. The formation of ruthenium oxo-species was confirmed by XPS, Raman and FT-IR (Figure 5.12), which has been discussed in section 6.3.8 (proposed mechanism). In addition to the role played by ruthenium oxo-species, the excellent catalytic activity of GNS-RuNPs is due to three most important reasons: (i) the smaller size of the RuNPs, (ii) higher surface area of the GNS-RuNPs, and (iii) an effective dispersion of the GNS-RuNPs in the reaction medium.

### **5.3.4 Chemoselective nature of GNS-RuNPs**

To examine the chemoselectivity of the GNS-RuNPs, a series of reactions were carried out (Scheme 5.1). The present catalytic system can selectively oxidize the primary alcohol (benzyl alcohol or 1-octanol) in the presence of secondary alcohol (1-

phenylethanol or 2-octanol). Oxidation of benzyl alcohol was faster compared to 1-octanol. Among 1-phenylethanol and 2-octanol, 1-phenyl ethanol undergoes oxidation faster. On contrary, 1-phenylethanol was chemoselectively oxidized to obtain acetophenone in the presence of 1-octanol. This may be due to the better reactivity of 1-phenylethanol when compared to 1-octanol.



**Scheme 5.1** – Chemoselectivity of nanocatalyst, GNS-RuNPs.

### 5.3.5 Heterogeneity of GNS-RuNPs

To inspect the factual heterogeneity of the GNS-RuNPs, a hot filtration test was performed for the oxidation of 1-phenylethanol under optimized reaction conditions. The nanocatalyst was separated out from the reaction mixture by a simple centrifugation after 8 h and the yield of acetophenone determined by GC was 5%. Then the filtrate was continued stirring for another 10 h and the reaction conversion was monitored at 2 h intervals; the results are shown in Figure 5.9. It was noticed, that there was no further conversion occurred after the GNS-RuNPs were separated out; this showed that the oxidation of 1-phenylethanol occurred only in the presence of GNS-RuNPs. In addition, the conversion remained 5% even after 18 h of the reaction time, which confirmed that the Ru was not leached out from GNS-RuNPs during the oxidation reaction. The filtrate was further analyzed by ICP-MS; trace amount of Ru content (9.8 ppb) confirmed the heterogeneous nature of the present catalytic system.

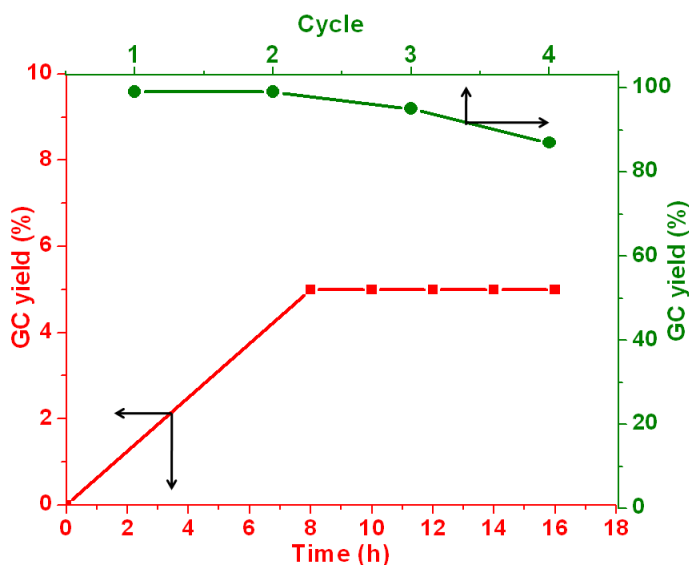


**Figure 5.9** – Heterogeneity and reusability tests of GNS-RuNPs.

### 5.3.6 Reusability of GNS-RuNPs

Indeed, recovery and reusability are the important advantages of nanocatalysts, which make them economically feasible. GNS-RuNPs were separated out from the reaction mixture, washed with diethyl ether and dried in *vacuo* at 130°C. Then the recovered catalyst was reused for the oxidation of 1-phenylethanol; the results are presented in Figure 5.9. It is noteworthy that the present catalytic system provided 87% of acetophenone even at the 4<sup>th</sup> cycle, which confirmed its excellent reusability. Furthermore, used nanocatalyst (*u*-GNS-RuNPs) was characterized by TEM, Raman, XRD and SEM-EDS.

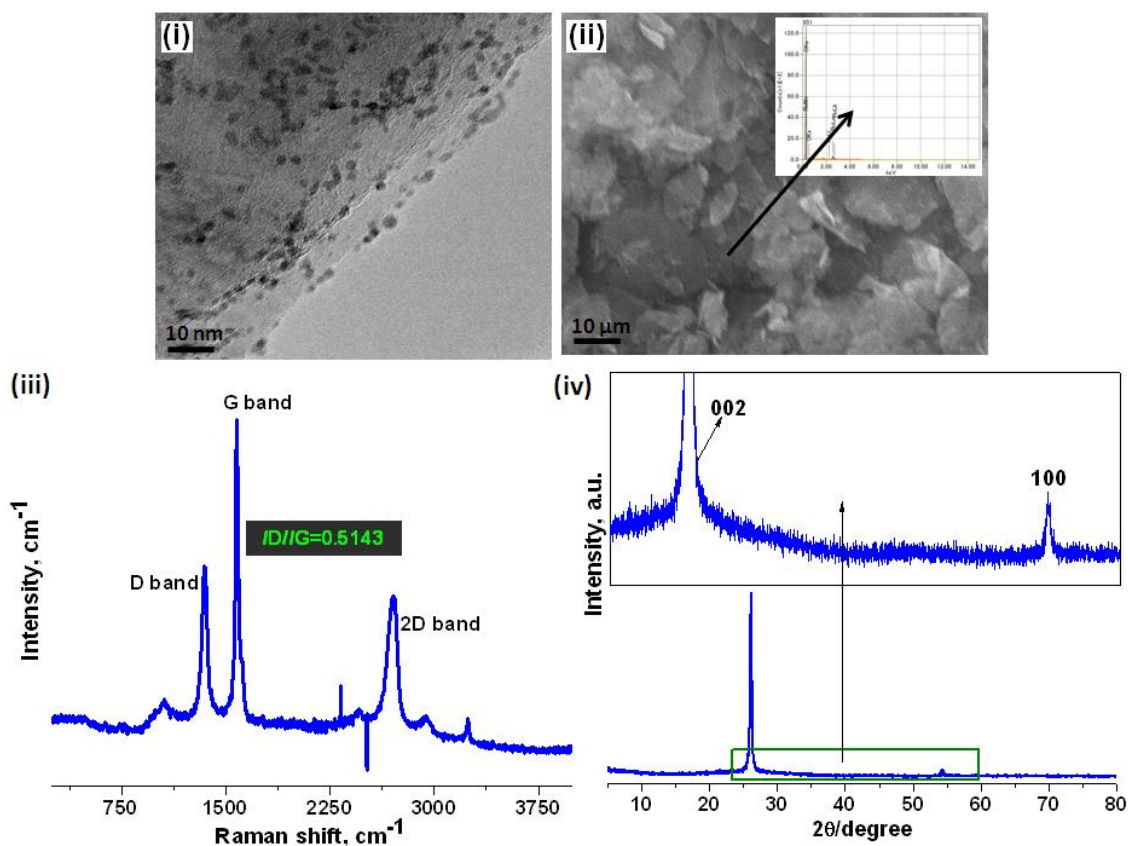


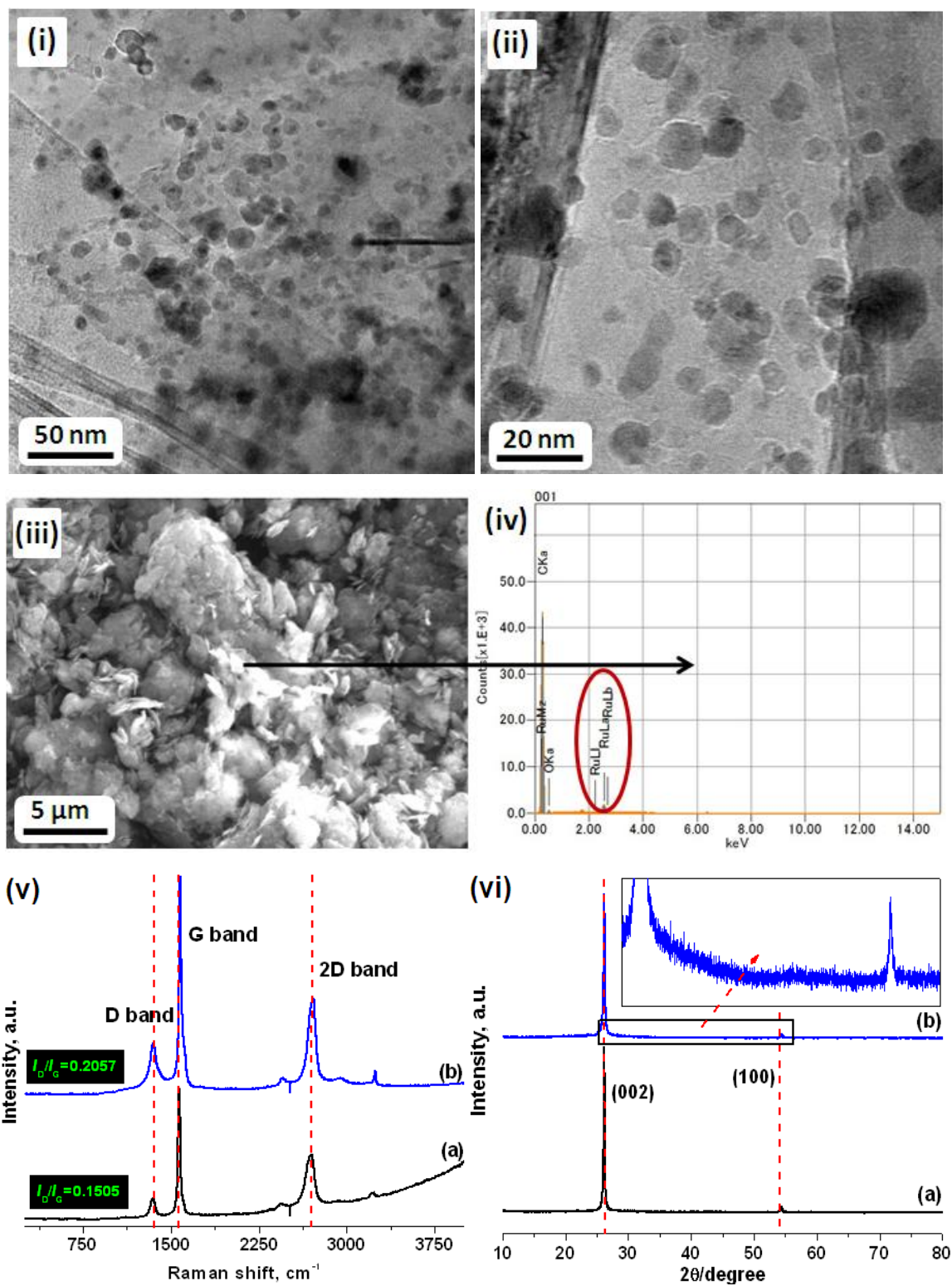
**Figure 5.10** – (i) TEM, (ii) SEM-EDS, (iii) Raman and (iv) XRD of *u*-GNS-RuNPs.

The TEM images showed that the morphology of *u*-GNS-RuNPs remains unchanged [Figure 5.10(i)]. SEM-EDS result revealed that the weight percentage of Ru in *u*-GNS-RuNPs was 3.01 [Figure 5.10(ii)]. The calculated Raman intensity ratio ( $I_D/I_G=0.5143$ ) of *u*-GNPs-RuNPs was still high in comparison to *f*-GNS, which revealed that the RuNPs are still strongly attached to GNS [Figure 5.10 (iii)]. XRD result confirmed that the chemical state of Ru was zero and were in nano-crystalline nature [Figure 5.10(iv)]. Hence we conclude that GNS-RuNPs are physically as well as chemically stable and reusable.

### **5.3.7 Effect of particle size on catalytic activity**

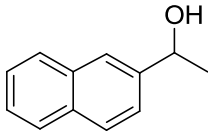
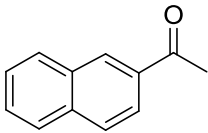
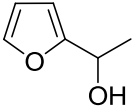
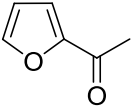
Owing to the high active surface area of MNPs, they are usually employed as a heterogeneous nanocatalyst in various reactions and facilitate better yields. Particularly, the MNPs having size of under 5 nm exhibited a dramatic catalytic activity [79]. Therefore, the effect of Ru particle size on catalytic efficiency in terms of yields has been investigated. For this purpose, another nanocatalyst with RuNPs size of around 10-20 nm was prepared using the procedure pursued for the preparation of GNS-RuNPs, however the mixing time was 5 minutes and the calcination was carried out at 350°C for 3 h. Well known that, MNPs can easily agglomerate to form bigger particles particularly at higher temperature due to their high specific surface energy [80]. Here, we postulate that the RuNPs might be agglomerated to form bigger RuNPs (10-20 nm) at the calcination temperature of 350°C. The increase in the temperature from 300 to 350°C increased the size of RuNPs from 1-3 nm to 10-20 nm; this suggests that the size of the RuNPs depends on the calcination temperature used. The TEM images [Figures 5.11(i) and (ii)] of this

catalyst revealed that the RuNPs were well attached on the surface of GNS with the particle size ranging from 10 to 20 nm. The mean diameter of RuNPs was found to be ca. 15 nm. The weight percentage of Ru was 4.34 in this catalyst [Figures 5.11(iii) and (iv)]. The calculated Raman intensity ratio ( $I_D/I_G$ ) was higher (0.2057) than that of the *f*-GNS; this indicates that the RuNPs were physically attached to GNS surface [Figure 5.11(v)]. The XRD results confirmed that the RuNPs were in the zero oxidation state and having nano-crystalline nature [Figure 5.11(vi)]. The GNS-RuNPs catalyst (10-20 nm) has a BET surface area of  $35.1 \text{ m}^2\text{g}^{-1}$  with a pore volume of  $0.160 \text{ cm}^3\text{g}^{-1}$  and a BJH desorption average pore diameter of 17 nm. The surface area per unit mass ( $S$ ) of RuNPs was found to be  $32.1 \text{ m}^2\text{g}^{-1}$ . After the characterization, this nanocatalyst was employed in the oxidation of alcohols and efficiency was compared with GNS-RuNPs having 0.5-3 nm RuNPs (Table 5.3). As expected, the catalyst with 0.5-3 nm RuNPs exhibited a good catalytic activity in comparison to the one which contains RuNPs of 10-20 nm size. Hence it is inferred that the excellent catalytic activity of GNS-RuNPs toward oxidation of alcohols is mainly due to the ultra-fine structure of RuNPs (Table 5.3). Moreover, the activity of the catalyst in aerial oxidation reaction is obviously dependant on the size of RuNPs. In fact, when the size of RuNPs decreases, the surface area per unit mass ( $S$ ) certainly increases. Consequently, more number of active sites are available. Thus, the GNS-RuNPs having Ru particle size of 0.5-3 nm showed excellent catalytic activity [81]. This argument is well supported by the BET surface area and the surface area per unit mass ( $S$ ) of RuNPs.



**Figure 5.11** – (i and ii) TEM images, (iii and iv) SEM-EDS, (v) Raman and (vi) XRD of GNS-RuNPs having 10-20 nm RuNPs.

**Table 5.3 – Oxidation of alcohols using GNS-RuNPs having 10-20 nm RuNPs<sup>a</sup>**

entry	substrate	Product	time (h)	conv. <sup>b</sup> (%)	sel. <sup>b</sup> (%)	yield <sup>b</sup> (%)
1			18	54	100	54
2			20	39	100	39
3			22	10	100	10

<sup>a</sup>Reaction conditions: Substrate (1 equiv.), GNS-RuNPs having 10-20 nm RuNPs (0.036 mol%), toluene (4 mL), 110°C.

<sup>b</sup>Determined by GC analysis.

### 5.3.8 Proposed mechanism

In order to study the mechanism of GNS-RuNPs catalyzed aerial oxidation of alcohols, FT-IR, Raman and XPS spectra were recorded for GNS-RuNPs (pure nanocatalyst) and *o*-GNS-RuNPs (the nanocatalyst after stirring with 1-phenylethanol in 4 mL of toluene at 110°C for 8 h); results are shown in Figure 5.12. As expected, FT-IR spectra of GNS-RuNPs and *o*-GNS-RuNPs showed a peak at 1600 cm<sup>-1</sup> which was attributed to C=C stretching of GNS. Interestingly, both FT-IR and Raman spectra of *o*-GNS-RuNPs showed a new peak at around 450 cm<sup>-1</sup>, which confirmed the formation of Ru-oxo species (Ru<sup>II</sup>=O) during the catalytic reaction [82]. In comparison to pure GNS-RuNPs, XPS spectra of *o*-GNS-RuNPs showed a positive shift in the O 1s peak with a dramatic increase in the peak intensity at 531.5 eV; this obviously confirmed the formation of Ru<sup>II</sup>=O during the oxidation reaction [82].

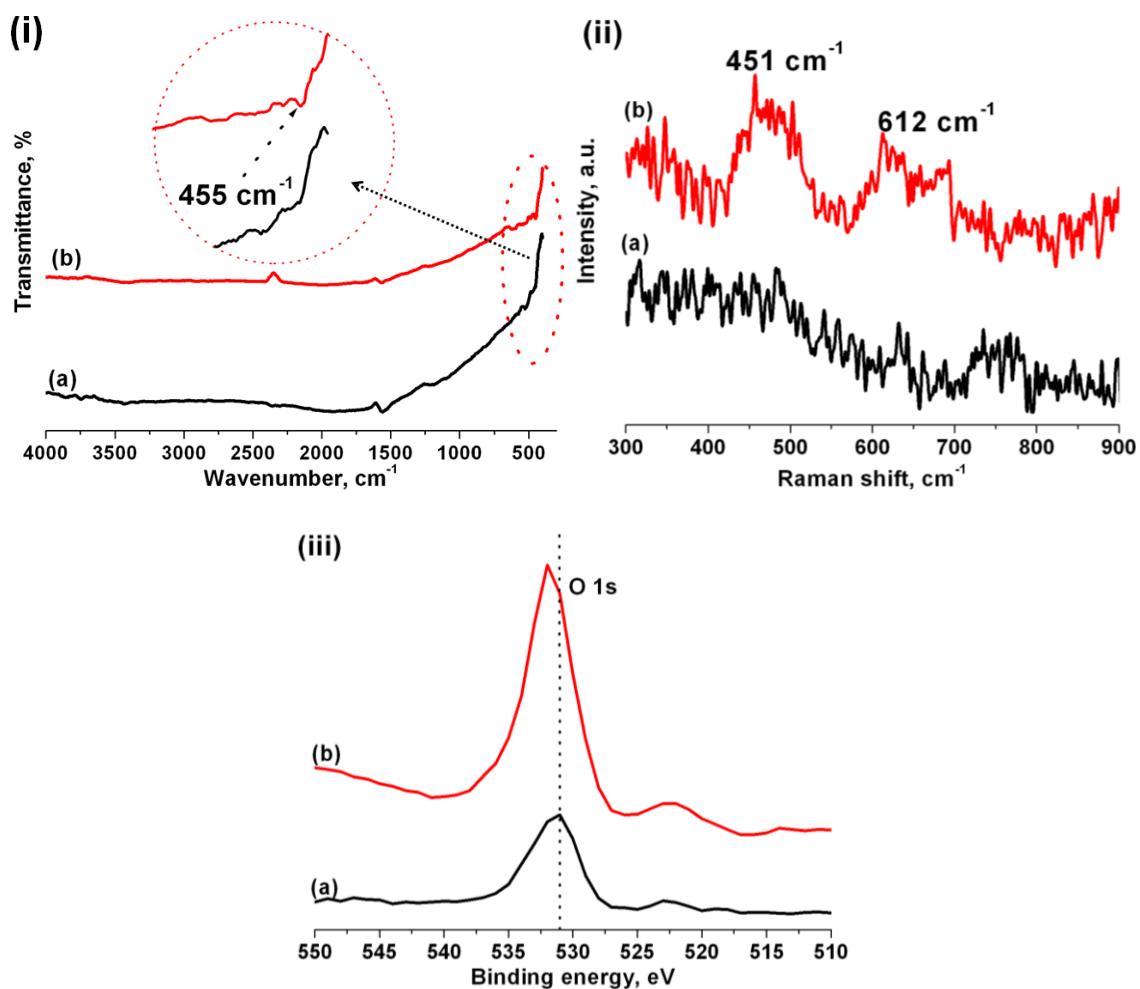


**Figure 5.12** – (i) FT-IR, (ii) Raman and (iii) XPS spectra of pure GNS-RuNPs (a) and *o*-GNS-RuNPs (b).

On the basis of the results obtained, we conclude that the mechanism for the oxidation of alcohols might be involving the Ru-oxo species as an intermediate (Figure 5.13). In the first step, RuNPs form Ru<sup>II</sup>=O species with the help of atmospheric oxygen. In the next step, the formed Ru-oxo species assisted the formation of acetophenone from 1-phenylethanol. Finally, nanocatalyst was regenerated for the further oxidation process.

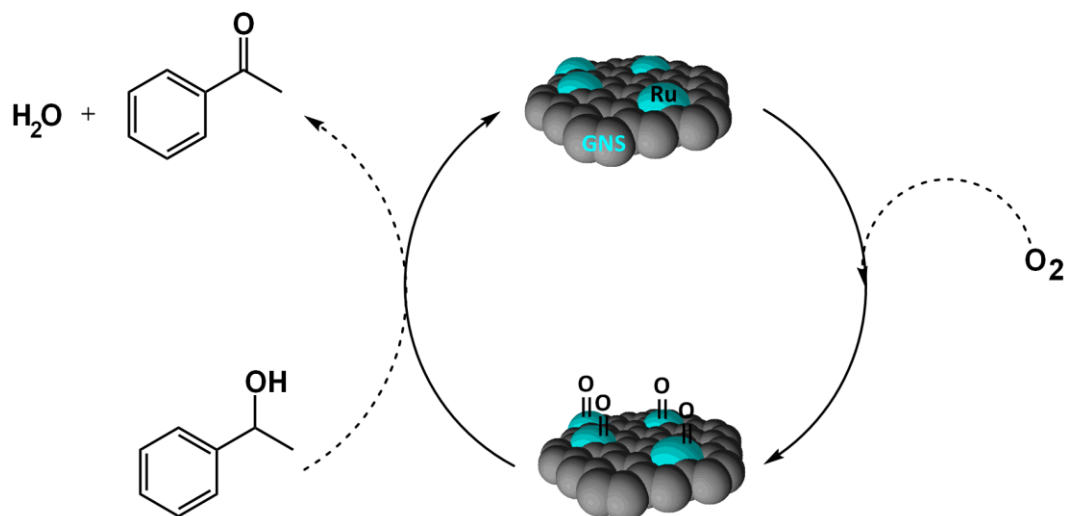


**Figure 5.13** – Proposed mechanism for GNS-RuNPs catalyzed oxidation of alcohols.

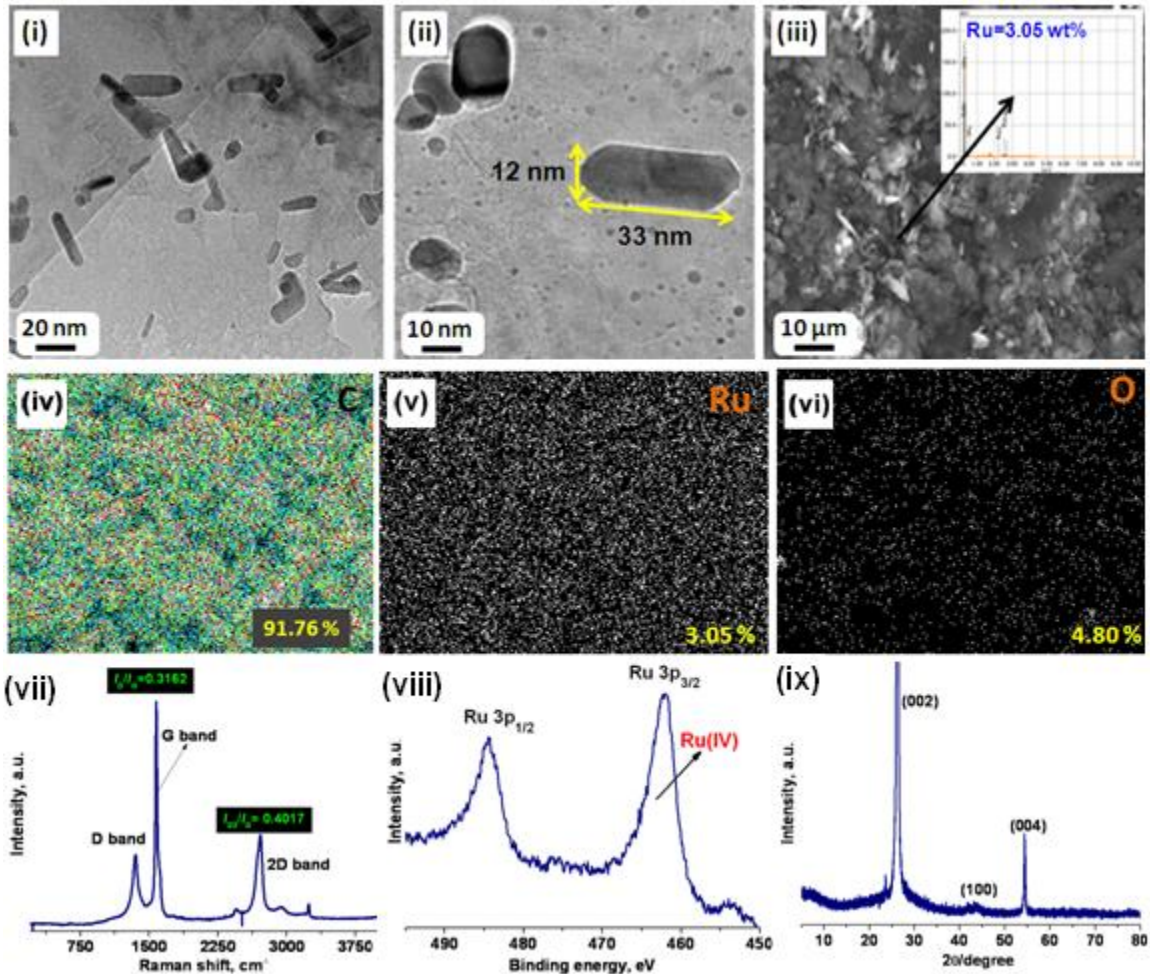
### 5.3.9 Versatility of GNS-RuNPs

The *u*-GNS-RuNPs were used to prepare ruthenium oxide nanorods hybrid GNS (*u*-GNS-RuO<sub>2</sub>NRs) which was characterized by TEM, SEM-EDS, XRD, Raman and XPS. *u*-GNS-RuO<sub>2</sub>NRs were tested as catalyst in the transfer hydrogenation of ketones.

#### 5.3.9.1 Preparation and characterization of *u*-GNS-RuO<sub>2</sub>NRs

In a typical procedure, *u*-GNS-RuO<sub>2</sub>NRs were prepared by the calcination of *u*-GNS-RuNPs under N<sub>2</sub> atmosphere at 600°C for 6 h in a muffle furnace. The calcinated material was characterized and found to be *u*-GNS-RuO<sub>2</sub>NRs which were used as a catalyst for the transfer hydrogenation of ketones. The TEM images showed a very small and uniformly dispersed RuO<sub>2</sub>NRs on GNS [Figures 5.14(i) and (ii)]. The length and diameter of RuO<sub>2</sub>NRs were found in the range of 25-35 and 12-15 nm respectively. The weight percentage of Ru in *u*-GNS-RuO<sub>2</sub>NRs was found to be 3.05 [Figure 5.14(iii)]. The

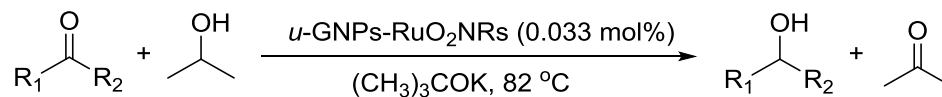
elemental mapping of the *u*-GNS-RuO<sub>2</sub>NRs confirmed that the RuO<sub>2</sub>NRs were distributed uniformly on the surface of GNS [Figure 5.14(iv-vi)]. The intensity ratio ( $I_D/I_G=0.3162$ ) of *u*-GNPs-RuO<sub>2</sub>NRs was higher than that ( $I_D/I_G=0.1505$ ) of *f*-GNS, which revealed that the RuO<sub>2</sub>NRs were attached to the surface of GNS. The BE of Ru 3p<sub>3/2</sub> at 462.5 eV and Ru 3p<sub>1/2</sub> at 485.0 eV were attributed to the photoemission from RuO<sub>2</sub> (Ru<sup>4+</sup>) [Figure 5.14(vii) and (viii)] [84]. No X-ray diffraction peaks corresponding to RuO<sub>2</sub> was observed, which proved the nano-crystalline nature of RuO<sub>2</sub>NRs [85].

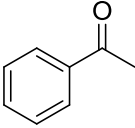
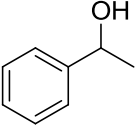
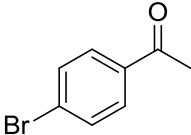
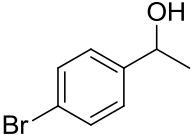
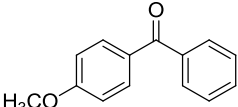
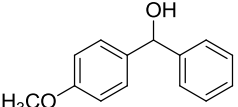
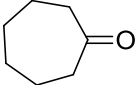
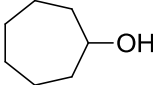
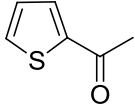
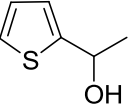
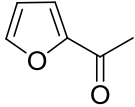
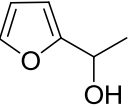


**Figure 5.14** – (i and ii) TEM images, (iii) SEM-EDS, (iv) Raman, (v) XPS and (iv) XRD of *u*-GNS-RuO<sub>2</sub>NRs, and (iv-vi) elemental mapping of C (iv), Ru (v) and O (vi).

### 5.3.9.2 Transfer hydrogenation of ketones catalyzed by *u*-GNS-RuO<sub>2</sub>NRs

The *u*-GNS-RuO<sub>2</sub>NRs were investigated as catalyst for the transfer hydrogenation of ketones using 2-propanol as a hydrogen donor. Fortunately, acetophenone showed a very high conversion of 99% with 100% selectivity. Inspired by this result, the scope of the catalytic system was further extended to investigate a wide range of aromatic, alicyclic and heterocyclic ketones (Table 5.4). The substituents have a moderate influence on the final yields but the higher selectivity was maintained. 4-Bromo acetophenone was converted into its corresponding alcohol in 81% yield after stirring for 10 h (Table 5.4, entry 2). Hydrogenation of 4-methoxy benzophenone (Table 5.4, entry 3) proceeded with moderate yield of 62% (100 % selectivity), which may be due to the presence of bulky substituent [86]. In the reduction of cycloheptanone to cycloheptanol, the present catalytic system showed a good yield of 88% with high selectivity of 100% (Table 5.4, entry 4) whereas HSi(OMe)-catalyzed reduction of cycloheptanone proceeded with the formation of the desired product in 76% yield [87]. Moreover, the present catalytic system can be adopted for the reduction of heterocyclic ketones as well. It is noteworthy that 2-acetylthiophene was transformed to 1-thiophene ethanol (90%) with high selectivity while silica-bound RhCl(PPh<sub>3</sub>)<sub>3</sub>-catalyzed reduction gave only 4% of the product [88]. Similarly, 1-furyl ethanone yielded 1-furyl ethanol in 76% yield whereas Pt/Al<sub>2</sub>O<sub>3</sub>-catalyzed reaction yielded only 50% of the product [89]. The results concluded that the *u*-GNS-RuO<sub>2</sub>NRs effectively reduces various ketones; this confirms that the proposed catalyst (GNS-RuNPs) is highly stable and versatile.

**Table 5.4 – Transfer hydrogenation of ketones catalyzed by *u*-GNPs-RuO<sub>2</sub>NRs<sup>a</sup>**

entry	substrate	product	time (h)	conv. <sup>b</sup> (%)	sel. <sup>b</sup> (%)	yield <sup>b</sup> (%)
1			12	99	100	99
2			10	81	100	81
3			16	62	100	62
4			24	88	100	88
5			20	95	95	90
6			20	92	84	76

<sup>a</sup>Reaction conditions: Substrate (1 mmole), *u*-GNPs-RuO<sub>2</sub>NRs (0.033 mol%), (CH<sub>3</sub>)<sub>3</sub>COK (1 mmole), 2-propanol (4 mL), 82°C.

<sup>b</sup>Determined by GC analysis.

## 5.4 Conclusions

In summary, we have successfully achieved bi- and few layered GNS from GNPs by a SPE method. The RuNPs were decorated on GNS by a straight forward dry synthesis method and TEM images confirmed good adhesion of RuNPs with a very narrow particle

size distribution on GNS. The weight percentage of Ru in GNS-RuNPs was 3.31, as determined by EDS analysis. Raman intensity ratios confirmed the attachment of RuNPs on the surface of GNS. XRD and XPS revealed the metallic as well as nano-crystalline nature of RuNPs. The prepared GNS-RuNPs were able to oxidize effectively a wide range of alcohols into their corresponding carbonyl compounds in the presence of air. The nanocatalyst can also be used for selective oxidation of various aliphatic and aromatic alcohols. The amount of GNS-RuNPs catalyst used for oxidation of alcohols was found as low as 5 mg (0.036 mol%), the lowest to the best of our knowledge. The ICP-MS result of the filtrate after the separation of the catalyst revealed the heterogeneous nature of the present catalysis. The excellent reusability of the GNS-RuNPs can be realized from the good yield of acetophenone (87 %) from 1-phenylethanol even at the 4<sup>th</sup> run. The used GNS-RuNPs were transformed into  $\mu$ -GNS-RuO<sub>2</sub>NRs which showed good catalytic activity toward the transfer hydrogenation of various ketones. Overall, the simple synthesis, versatility and good activity make GNS-RuNPs as an alternate choice to the existing Ru based catalysts.

## References

- [1] Punniyamurthy, T.; Velusamy, S.; Iqbal, J. Recent Advances in Transition Metal Catalyzed Oxidation of Organic Substrates with Molecular Oxygen. *Chem. Rev.* **2005**, *105*, 2329–2364.
- [2] Lawrence, Q.; Tolman, W. B. Biologically Inspired Oxidation Catalysis. *Nature* **2008**, *455*, 333–340.
- [3] Arakawa, H. Catalysis Research of Relevance to Carbon Management: Progress, Challenges, and Opportunities. *Chem. Rev.* **2011**, *101*, 953–996.
- [4] Hill, C. L. *Advances in Oxygenated Processes*; Baumstark, A. L., Eds.; JAI: London, 1988.
- [5] Hudlicky, M. *Oxidations in Organic Chemistry*; ACS Monograph Series; American Chemical Society: Washington, DC, 1990.
- [6] Sheldon, R. A.; Kochi, J. K. *Metal Catalyzed Oxidations of Organic Compounds*, Academic Press, New York, 1981.
- [7] Zhan, B. Z.; Thompson, A. Recent Developments in the Aerobic Oxidation of Alcohols. *Tetrahedron* **2004**, *60*, 2917–2935.
- [8] Rhule, J. T.; Neiwert, W. A.; Hardcastle, K. I.; Do, B. T.; Hill, C. L.  $\text{Ag}_5\text{PV}_2\text{Mo}_{10}\text{O}_{40}$ , A Heterogeneous Catalyst for Air-Based Selective Oxidation at Ambient Temperature. *J. Am. Chem. Soc.* **2001**, *123*, 12101–12102.
- [9] Choudary, B. M.; Kantam, M. L.; Rahman, A.; Reddy, C. V.; Rao, K. K. The First Example of Activation of Molecular Oxygen by Nickel in Ni-Al Hydrotalcite: A Novel Protocol for the Selective Oxidation of Alcohols. *Angew. Chem. Int. Ed.* **2001**, *40*, 763–766.

- [10] Nishibayashi, Y.; Yamauchi, A.; Onodera, G.; Uemura, S. Oxidative Kinetic Resolution of Racemic Alcohols Catalyzed by Chiral Ferrocenyloxazolinylphosphine–Ruthenium Complexes. *J. Org. Chem.* **2003**, *68*, 5875–5880.
- [11] Karimi, B.; Abedi, S.; Clark, J. H.; Budarin, V. Highly Efficient Aerobic Oxidation of Alcohols Using a Recoverable Catalyst: The Role of Mesoporous Channels of SBA-15 in Stabilizing Palladium Nanoparticles. *Angew. Chem. Int. Ed.* **2006**, *45*, 4776–4779.
- [12] Oliveira, R. L.; Kiyohara, P. K.; Rossi, L. M. High Performance Magnetic Separation of Gold Nanoparticles for Catalytic Oxidation of Alcohols. *Green Chem.* **2010**, *12*, 144–149.
- [13] Yamada, Y. M. A.; Arakawa, T.; Hocke, H.; Uozumi, Y. A Nanoplatinum Catalyst for Aerobic Oxidation of Alcohols in Water. *Angew. Chem. Int. Ed.* **2007**, *119*, 718–720.
- [14] Mori, K.; Kanai, S.; Hara, T.; Mizugaki, T.; Ebitani, K.; Jitsukawa, K.; Kaneda, K. Development of Ruthenium–Hydroxyapatite-Encapsulated Superparamagnetic  $\gamma$ -Fe<sub>2</sub>O<sub>3</sub> Nanocrystallites as an Efficient Oxidation Catalyst by Molecular Oxygen. *Chem. Mater.* **2007**, *19*, 1249–1256.
- [15] Tomioka, H.; Takai, K.; Nozaki, H.; Oshima, K. Selective Oxidation of a Primary Hydroxyl in the Presence of Secondary One. *Tetrahedron Lett.* **1981**, *22*, 1605–1608.

- [16] Kanemoto, S.; Matsubara, S.; Takai, K.; Oshima, K. Transition-Metal Catalyzed Oxidation of Alcohols to Aldehydes and Ketones by means of  $\text{Me}_3\text{SiOOSiMe}_3$ . *Tetrahedron Lett.* **1983**, *24*, 2185–2188.
- [17] Backvall, J. E.; Chowdhury, R. L.; Karlsson, U. Ruthenium-Catalysed Aerobic Oxidation of Alcohols *via* Multistep Electron Transfer. *J. Chem. Soc., Chem. Commun.* **1991**, 473–475.
- [18] Pagliaro, M.; Campestrini, S.; Ciriminna, R. Ru-based Oxidation Catalysis. *Chem. Soc. Rev.* **2005**, *34*, 837–845.
- [19] Bleloch, A.; Johnson, B. F. G.; Ley, S. V.; Price, A. J.; Shepard, D. S.; Thomas, A. W. Modified Mesoporous Silicate MCM-41 Materials: Immobilised Perruthenate – A New Highly Active Heterogeneous Oxidation Catalysts for Clean Organic Synthesis Using Molecular Oxygen. *Chem. Commun.*, **1999**, *1999*, 1907–1908.
- [20] Parmeggiani, C.; Cardona, F. Transition Metal Based Catalysts in the Aerobic Oxidation of Alcohols, *Green Chem.* **2012**, *14*, 547–564.
- [21] Yamaguchi, K.; Mori, K.; Mizugaki, T.; Ebitani, K.; Kaneda, K. Creation of a Monomeric Ru Species on the Surface of Hydroxyapatite as an Efficient Heterogeneous Catalyst for Aerobic Alcohol Oxidation. *J. Am. Chem. Soc.* **2000**, *122*, 7144–7145.
- [22] Yamaguchi, K.; Mizuno, N. Supported Ruthenium Catalyst for the Heterogeneous Oxidation of Alcohols with Molecular Oxygen. *Angew. Chem. Int. Ed.* **2002**, *41*, 4538–4542.
- [23] Sheldon, R. A.; Arends, R. A.; Dijkman, A. New Developments in Catalytic Alcohol Oxidations for Fine Chemicals Synthesis. *Catal. Today* **2000**, *57*, 157–166.

- [24] Yamaguchi, K.; Mizuno, N. Scope, Kinetics, and Mechanistic Aspects of Aerobic Oxidations Catalyzed by Ruthenium Supported on Alumina. *Chem. Eur. J.* **2003**, *9*, 4353–4361.
- [25] Matsumoto, M.; Ito, S. Ruthenium-Catalyzed Aerobic Oxidation of Pantoyl Lactone to Ketopantoyl Lactone. *Synth. Commun.* **1984**, *14*, 697–700.
- [26] Murahashi, S. I.; Oda, Y.; Komiya, N.; Naota, T. Ruthenium-Catalyzed Oxidation of Alkanes with Peracids. *Tetrahedron Lett.* **1994**, *35*, 7953–7956.
- [27] Choi, E.; Lee, C.; Na, Y.; Chang, S. [RuCl<sub>2</sub>(p-cymene)]<sub>2</sub> on Carbon: An Efficient, Selective, Reusable, and Environmentally Versatile Heterogeneous Catalyst. *Org. Lett.* **2002**, *4*, 2369–2371.
- [28] Komiya, N.; Nakae, T.; Sato, H.; Naota, T. Water-Soluble Diruthenium Complexes Bearing Acetate and Carbonate Bridges: Highly Efficient Catalysts for Aerobic Oxidation of Alcohols in Water. *Chem. Commun.* **2006**, 4829–4831.
- [29] Csajernyik, G.; Ell, A. H.; Fadini, L.; Pugin, B.; Backvall, J. E. Efficient Ruthenium-Catalyzed Aerobic Oxidation of Alcohols Using a Biomimetic Coupled Catalytic System. *J. Org. Chem.*, **2002**, *67*, 1657–1662.
- [30] Mori, S.; Takubo, M.; Makida, K.; Yanase, T.; Aoyagi, S.; Maegawa, T.; Monguchi, Y.; Sajiki, H. A Simple and Efficient Oxidation of Alcohols with Ruthenium on Carbon. *Chem. Commun.* **2009**, 5159–5161.
- [31] Yanga, X.; Wang, X.; Qiu, J. Aerobic Oxidation of Alcohols over Carbon Nanotube-Supported Ru Catalysts Assembled at the Interfaces of Emulsion Droplets. *Appl. Catal. A: Gen.* **2010**, *382*, 131–137.

- [32] Geim, A. K.; Novoselov, K. S. The Rise of Graphene. *Nat. Mater.* **2007**, *6*, 183–191.
- [33] Geim, A. K. Graphene: Status and Prospects. *Science* **2009**, *324*, 1530–1534.
- [34] Stankovich, S.; Dikin, D. A.; Dommett, G. H. B.; Kohlhaas, K. M.; Zimney, E. J.; Stach, E. A.; Piner, R. D.; Nguyen, S. D.; Ruoff, R. S. Graphene-Based Composite Materials. *Nature* **2006**, *442*, 282–286.
- [35] Machadoa, B. F.; Serp, P. Graphene-Based Materials for Catalysis. *Catal. Sci. Technol.* **2012**, *2*, 54–75.
- [36] Schaetz, A.; Zeltner, M.; Stark, W. J. Carbon Modifications and Surfaces for Catalytic Organic Transformations. *ACS Catal.* **2012**, *2*, 1267–1284.
- [37] Nethravathi, C.; Anumol, E. A.; Rajamathi, M.; Ravishankar, N. Highly Dispersed Ultrafine Pt and PtRu Nanoparticles on Graphene: Formation Mechanism and Electrocatalytic Activity. *Nanoscale* **2011**, *3*, 569–571.
- [38] Gil, M. S.; Luigi, R.; Peter, S.; Willi, B.; Rolf, M. Palladium Nanoparticles on Graphite Oxide and its Functionalized Graphene Derivatives as Highly Active Catalysts for the Suzuki–Miyaura Coupling Reaction. *J. Am. Chem. Soc.* **2009**, *131*, 8262–8270.
- [39] Kamat, P. V. Graphene-Based Nanoarchitectures. Anchoring Semiconductor and Metal Nanoparticles on a Two-Dimensional Carbon Support. *J. Phys. Chem. Lett.* **2010**, *1*, 520–527.
- [40] Noyori, R.; Hashiguchi, S. Asymmetric Transfer Hydrogenation Catalyzed by Chiral Ruthenium Complexes. *Acc. Chem. Res.* **1997**, *30*, 97–102.

- [41] Johnstone, R. A. W.; Wilby, A. H.; Entwistle, I. D. Heterogeneous Catalytic Transfer Hydrogenation and its Relation to other Methods for Reduction of Organic Compounds. *Chem. Rev.* **1985**, *85*, 129–170.
- [42] Sanjib, B.; Lawrence, T. D. A Novel Approach to Create a Highly Ordered Monolayer Film of Graphene Nanosheets at the Liquid–Liquid Interface. *Nano Lett.* **2009**, *9*, 167–172.
- [43] Xiaozhu, Z.; Xiao, H.; Xiaoying, Q.; Shixin, W.; Can, X.; Freddy, Y. C. B.; Qingyu, Y.; Peng, C.; Hua, Z. In Situ Synthesis of Metal Nanoparticles on Single-Layer Graphene Oxide and Reduced Graphene Oxide Surfaces. *J. Phys. Chem. C* **2009**, *113*, 10842–10846.
- [44] Yang, J.; Tian, C.; Wang, L.; Fu, H. An Effective Strategy for Small-Sized and Highly-Dispersed Palladium Nanoparticles Supported on Graphene with Excellent Performance for Formic Acid Oxidation. *J. Mater. Chem.* **2011**, *21*, 3384–3390.
- [45] Li, Y.; Fan, X.; Qi, J.; Ji, J.; Wang, S.; Zhang, G.; Zhang, F. Palladium Nanoparticle-Graphene Hybrids as Active Catalysts for the Suzuki Reaction. *Nano Res.* **2010**, *3*, 429–437.
- [46] Li, J.; Liu, C. Y. Ag/Graphene Heterostructures: Synthesis, Characterization and Optical Properties. *Eur. J. Inorg. Chem.* **2010**, *2010*, 1244–1248.
- [47] Tien, H. W.; Huang, Y. L.; Yang, S. Y.; Wang, J. Y.; Ma, C. C. M. The Production of Graphene Nanosheets Decorated with Silver Nanoparticles for use in Transparent, Conductive Films. *Carbon* **2011**, *49*, 1550–1560.
- [48] Bai, S.; Shen, X. Graphene–Inorganic Nanocomposites. *RSC Adv.* **2012**, *2*, 64–98.

- [49] Lin, Y.; Watson, K. A.; Fallbach, M. J.; Ghose, S.; Smith, J. G.; Delozier, D. M.; Cao, W.; Crooks, R. E.; Connell, J. W. Rapid, Solventless, Bulk Preparation of Metal Nanoparticle-Decorated Carbon Nanotubes. *ACS Nano* **2009**, *3*, 871–884.
- [50] Hu, H.; Zhao, Z.; Zhou, Q.; Gogotsi, Y.; Qiu, J. The Role of Microwave Absorption on Formation of Graphene from Graphite Oxide. *Carbon* **2011**, *50*, 3267–3273.
- [51] Yong, C. J.; Jin, H. K.; Takuya, H.; Yoong, A. K.; Morinobu, E.; Mauricio, T.; Mildred, S. D. Fabrication of Transparent, Tough, and Conductive Shape-Memory Polyurethane Films by Incorporating a Small Amount of High-Quality Graphene. *Macromol. Rapid Commun.* **2012**, *33*, 628–634.
- [52] Lu, J.; Do, I.; Drzal, L. T.; Worden, R. M.; Lee, I. Nanometal-Decorated Exfoliated Graphite Nanoplatelet Based Glucose Biosensors with High Sensitivity and Fast Response. *ACS Nano* **2008**, *2*, 1825–1832.
- [53] Liu, L. H.; Zorn, G.; Castner, D. G.; Solanki, R.; Lerner, M. M.; Yan, M. A Simple and Scalable Route to Wafer-Size Patterned Graphene. *J. Mater. Chem.* **2010**, *20*, 5041–5046.
- [54] Zhou, X.; Huang, X.; Qi, X.; Wu, S.; Xue, C.; Boey, F. Y. C.; Yan, Q.; Chen, P.; Zhang, H. In Situ Synthesis of Metal Nanoparticles on Single-Layer Graphene Oxide and Reduced Graphene Oxide Surfaces. *J. Phys. Chem. C* **2009**, *113*, 10842–10846.
- [55] Cancado, L. G.; Jorio, A.; Martins Ferreira, E. H.; Stavale, F.; Achete, C. A.; Capaz, R. B.; Moutinho, M. V. O.; Lombardo, A.; Kulmala, T. S.; Ferrari, A. C.

- Quantifying Defects in Graphene *via* Raman Spectroscopy at Different Excitation Energies. *Nano Lett.* **2011**, *11*, 3190–3196.
- [56] Tjoa, V.; Jun, W.; Dravid, V.; Mhaisalkarad, S.; Mathews, N. Hybrid Graphene–Metal Nanoparticle Systems: Electronic Properties and Gas Interaction. *J. Mater. Chem.* **2011**, *21*, 15593–15599.
- [57] Dresselhaus, M. S.; Dresselhaus, G.; Saito, R.; Jorio, A. Raman Spectroscopy of Carbon Nanotubes. *Phys. Rep.* **2005**, *409*, 47–99.
- [58] Sheng, Z. H.; Shao, L.; Chen, J. J.; Bao, W. J.; Wang, F. B.; Xia, X. H. Catalyst-Free Synthesis of Nitrogen-Doped Graphene via Thermal Annealing Graphite Oxide with Melamine and its Excellent Electrocatalysis. *ACS Nano* **2011**, *5*, 4350–4358.
- [59] North, J. M.; Van de Burgt, L. J.; Dalal, N. S. A Raman Study of the Single Molecule Magnet Mn<sub>12</sub>-Acetate and Analogs. *Solid State Commun.* **2002**, *123*, 75–79.
- [60] Thomsen, C.; Reich, S. Double Resonant Raman Scattering in Graphite. *Phys. Rev. Lett.* **2000**, *85*, 5214–5217.
- [61] Michael, J. M.; Je-Luen, Li.; Douglas, H. A.; Hannes, C. S.; Ahmed, A. A.; Jun, L.; Margarita, H. A.; David, L. M.; Roberto, C.; Robert, K. P.; Ilhan, A. A. Single Sheet Functionalized Graphene by Oxidation and Thermal Expansion of Graphite. *Chem. Mater.* **2007**, *19*, 4396–4404.
- [62] Wei, T.; Fan, Z.; Zheng, C.; Yao, C.; Li, W. Movement-Induced Voltage Properties of Stable Graphite Nanoplatelet Suspensions. *Mater. Lett.* **2009**, *63*, 1608–1610.

- [63] Soldano, C.; Mahmood, A.; Dujardin, E. Production, Properties and Potential of Graphene. *Carbon* **2010**, *48*, 2127–2150.
- [64] Zhang, Y. B.; Small, J. P.; Pontius, W. V.; Kim, P. Fabrication and Electric-Field-Dependent Transport Measurements of Mesoscopic Graphite Devices. *Appl. Phys. Lett.* **2005**, *86*, 073104–073107.
- [65] Liu, C.; Kim, W. S.; Baek, J.; Cho, Y.; Han, S.; Kim, S. W.; Min, N. K.; Choie, Y.; Kim, J. U.; Leea, C. J. Improved Field Emission Properties of Double-walled Carbon Nanotubes Decorated with Ru Nanoparticles. *Carbon* **2009**, *47*, 1158–1164.
- [66] Akhavan, O. The Effect of Heat Treatment on Formation of Graphene Thin Films from Graphene Oxide Nanosheets. *Carbon* **2010**, *48*, 509–519.
- [67] Fan, X.; Peng, W.; Li, J.; Li, X.; Wang, S.; Zhang, G.; Zhang, F. Deoxygenation of Exfoliated Graphite Oxide under Alkaline Conditions: A Green Route to Graphene Preparation. *Adv. Mater.* **2008**, *20*, 4490–4493.
- [68] Kuila, T.; Bhadra, S.; Yao, D.; Kim, N. H.; Bose, S.; Lee, J. H. Recent Advances in Graphene Based Polymer Composites. *Prog. Polym. Sci.* **2010**, *35*, 1350–1375.
- [69] Chakroune, N.; Viau, G.; Ammar, S.; Poul, L.; Veautier, D.; Chehimi, M. M.; Mangeney, C.; Villain, F.; Fievet, F. Acetate- and Thiol-Capped Monodisperse Ruthenium Nanoparticles: XPS, XAS, and HRTEM Studies. *Langmuir* **2005**, *21*, 6788–6796.
- [70] Akhavan, O. Graphene Nanomesh by ZnO Nanorod Photocatalysts. *ACS Nano* **2010**, *4*, 4174–4180.

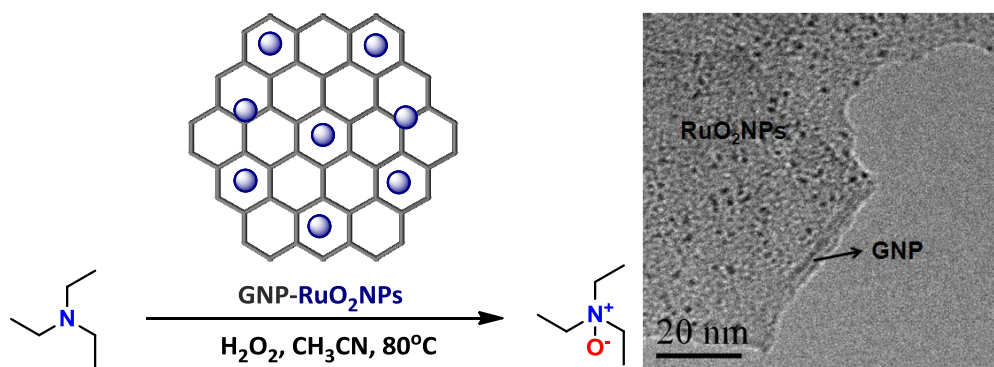
- [71] Kuila, T.; Bose, S.; Hong, C. E.; Uddin, M. E.; Khanra, P.; Kim, N. H.; Lee, J. H. Preparation of Functionalized Graphene/Linear Low Density Polyethylene Composites by a Solution Mixing Method. *Carbon* **2011**, *49*, 1033–1051.
- [72] Kerber, R. C. If it's Resonance, What is Resonating?. *J. Chem. Educ.* **2006**, *83*, 223–227.
- [73] Zhao, M.; Li, J.; Song, Z.; Desmond, R.; Tschaen, D. M.; Grabowski, E. J. J.; Reider, P. J. A Novel Chromium Trioxide Catalyzed Oxidation of Primary Alcohols to the Carboxylic Acids. *Tetrahedron Lett.* **1998**, *39*, 5323–5326.
- [74] Hronec, M.; Cvenegrova, Z.; Kizlink, J. Competitive Oxidation of Alcohols in Aqueous Phase Using Pd/C Catalyst. *J. Mol. Catal.* **1993**, *83*, 75–82.
- [75] Yamaguchi, K.; Mizuno, N. Heterogeneously Catalyzed Liquid-Phase Oxidation of Alkanes and Alcohols with Molecular Oxygen. *New J. Chem.* **2002**, *26*, 972–974.
- [76] Velusamy, S.; Punniyamurthy, T. Novel Vanadium-Catalyzed Oxidation of Alcohols to Aldehydes and Ketones under Atmospheric Oxygen. *Org. Lett.* **2004**, *6*, 217–219.
- [77] Su, F. Z.; Liu, Y. M.; Wang, L. C.; Cao, Y.; He, H. Y.; Fan, K. N. Ga–Al Mixed-Oxide-Supported Gold Nanoparticles with Enhanced Activity for Aerobic Alcohol Oxidation. *Angew. Chem. Int. Ed.* **2008**, *120*, 340–343.
- [78] Oliveira, R. L.; Kiyohara, P. K.; Rossi, L. M. High Performance Magnetic Separation of Gold Nanoparticles for Catalytic Oxidation of Alcohols. *Green Chem.* **2010**, *12*, 144–149.

- [79] Joo, S. H.; Park, J. Y.; Renzas, J. R.; Butcher, D. R.; Huang, W.; Somorjai, G. A. Size Effect of Ruthenium Nanoparticles in Catalytic Carbon Monoxide Oxidation. *Nano Lett.* **2010**, *10*, 2709–2713.
- [80] Arvela, P. M.; Murzin, D. Y. Effect of Catalyst Synthesis Parameters on the Metal Particle Size. *Appl. Catal. A: Gen.* **2013**, *451*, 251–281.
- [81] Bell, A. T. The Impact of Nanoscience on Heterogeneous Catalysis. *Science* **2003**, *299*, 1688–1691.
- [82] Hirai, Y.; Kojima, T.; Mizutani, Y.; Shiota, Y.; Yoshizawa, K.; Fukuzumi, S. Ruthenium-Catalyzed Selective and Efficient Oxygenation of Hydrocarbons with Water as an Oxygen Source. *Angew. Chem. Int. Ed.* **2008**, *120*, 5856–5860.
- [83] Rochefort, D.; Dabo, P.; Guay, D.; Sherwood, P. M. A. XPS Investigations of Thermally Prepared RuO<sub>2</sub> Electrodes in Reductive Conditions. *Electrochim. Acta.* **2003**, *48*, 4245–4252.
- [84] Sankar, J.; Sham, T. K.; Puddephatt, R. J. Low Temperature Chemical Vapour Deposition of Ruthenium and Ruthenium Dioxide on Polymer Surfaces. *J. Mater. Chem.* **1999**, *9*, 2439–2444.
- [85] Mirosław, Z.; Janina, O. Synthesis and Structure Characterization of Ru Nanoparticles Stabilized by PVP or  $\gamma$ -Al<sub>2</sub>O<sub>3</sub>. *Mater. Res. Bull.* **2008**, *43*, 3111–3121.
- [86] Noyori, R.; Ohkuma, T. Asymmetric Catalysis by Architectural and Functional Molecular Engineering: Practical Chemo- and Stereoselective Hydrogenation of Ketones. *Angew. Chem. Int. Ed.* **2001**, *40*, 40–73.

- [87] Hosomi, A.; Hayashida, H.; Kohra, S.; Tominaga, Y. J. Penta Coordinate Silicon Compounds in Synthesis: Chemo- and Stereo-Selective Reduction of Carbonyl Compounds Using Trialkoxy-Substituted Silanes and Alkali Metal Alkoxides. *J. Chem. Soc. Chem. Commun.* **1986**, 1986, 1411–1412.
- [88] Bogar, K.; Krumlinde, P.; Bacsik, Z.; Hedin, N.; Backvall, J. E.; Ruiz, J. R.; Sanchidrian, C. J.; Hidalgo, J. M.; Marinas, J. M. Heterogenized Wilkinson-Type Catalyst for Transfer Hydrogenation of Carbonyl Compounds. *Eur. J. Org. Chem.* **2011**, 2011, 4409–4414.
- [89] Kijenski, J.; Winiarek, P.; Paryjczak, T.; Lewicki, A.; Mikołajska, A. Platinum Deposited on Monolayer Supports in Selective Hydrogenation of Furfural to Furfuryl Alcohol. *Appl. Catal. A: Gen.* **2002**, 233, 171–182.

## CHAPTER 6

### Catalytic *N*-oxidation of tertiary amines on RuO<sub>2</sub>NPs anchored graphene nanoplatelets



## CHAPTER 6

# Catalytic *N*-oxidation of tertiary amines on RuO<sub>2</sub>NPs anchored graphene nanoplatelets

### 6.1 Introduction

Aliphatic and aromatic *tert*-amine oxides (amine *N*-oxides) are essential and key components in the formulation of several cosmetic products as well as in biomedical applications [1, 2]. Particularly, *N*-oxides of aromatic amines are extensively used as protecting groups, auxiliary agents, and oxidants in various organic reactions [3, 4]. They often used as potential cytotoxins for the treatment of solid tumors and also as ligands for the preparation of useful transition metal complexes [5, 6]. As a catalyst, especially in epoxidation reactions, amine *N*-oxides displayed a wide range of advantages in chemical industries [7]. Notably, enantiopure chiral *N*-oxides, found to play a substantial role as a Lewis base catalyst in asymmetric transformation [8]. However, traditionally, these amine *N*-oxides are prepared *via* a noncatalytic oxidation processes using  $\alpha$ -azo hydroperoxides [9], activated H<sub>2</sub>O<sub>2</sub> [10], Caro's acid (H<sub>2</sub>SO<sub>5</sub>) [11], dioxiranes [12], peracids [13], and magnesium monophthalate [14]. These reagents are not only expensive and toxic, but also produce large amount of effluents during the reaction, which often lead to the environmental problem of waste disposal. To prevent this issue, catalytic oxidation processes using environmental friendly oxidants such as air, O<sub>2</sub> and H<sub>2</sub>O<sub>2</sub> have been developed. Silica supported vanadium [15], biomimetic methyltrioxorhenium(VII) or manganese porphyrin [16], titanium molecular sieves [TiMCM-41 and TiZSM-5(30)]

[17], tungsten-based polyperoxometalates [18], tungstate-exchanged Mg/Al-layered double hydroxide acid (LDH-WO<sub>4</sub>) [19], vanadium-silicate molecular sieve [20], and titanium silicalite (TS-1) materials [21] have been proposed as heterogeneous catalysts for the oxidation of tertiary amines to their corresponding *N*-oxides using H<sub>2</sub>O<sub>2</sub> as an oxidant. Owing to the recyclability and easy separation from the reaction mixture, metal nanoparticles (MNPs), particularly supported MNPs, played a tremendous role in heterogeneous catalysis. There are very few MNPs supported on carbon materials, particularly carbon black, employed as a catalyst for this oxidation reaction. Unfortunately, most of them have shown less activity in *N*-oxidation of tertiary amines [22]. Pina *et al.*, investigated the activity of gold-based mono- and bi-metallic catalysts in the oxidation of tertiary amines to afford the corresponding *N*-oxides [23]. They found that Au/C catalyst showed an excellent catalytic activity for the oxidation of tertiary amines to the corresponding *N*-oxides; however, other catalysts namely Rh/C, Pt/C, AuRh/C and AuPt/C are less effective and often require alkali as a promoter to improve the activity of the catalysts [23]. In addition to the high cost of the Au, Pt and Rh catalysts, they often require higher stoichiometric amount of catalyst for the *N*-oxidation reaction. Therefore, developing an efficient and recyclable catalytic system with the use of lower amount of catalyst remains a challenging task.

Among the noble metal catalysts, ruthenium has shown high catalytic activity mainly in oxidation reactions [24-27]. Very recently, due to the astounding properties of graphene such as high surface area and chemical inertness, it has been receiving a great deal of attention as a support for active metal catalysts including RuNPs in heterogeneous catalysis [28]. According to Krasheninnikov *et al.*, the inert graphene can be transformed

into a very active catalyst through the interactions between the active metal clusters and carbon vacancies [29]. In our previous work on the aerial oxidation of alcohols, we found that RuNPs decorated GNS catalyst is efficient, reusable, chemically as well as physically very stable and the catalytic system required a low amount of Ru (0.036 mol%) [30]. Inspired by these results, we believed that the RuO<sub>2</sub>NPs/GNP composite could also show a very good catalytic activity with use of lower amount of supported Ru catalyst in N-oxidation reactions. Herein, we report the simple preparation of graphene nanoplatelets (GNP) supported RuO<sub>2</sub>NPs catalyst and its catalytic property towards *N*-oxidation of tertiary amines.

## 6.2 Experimental section

### 6.2.1 Materials and characterization

GNP (purity: >99 wt%, surface area: >750 m<sup>2</sup>/g, average thickness: 3 nm, layers: <5, diameter: 1-2 μm) were purchased from Cheap Tubes Inc., VT, US. Ru(acac)<sub>3</sub> (97%) and all other chemicals were purchased from Aldrich and used as received.

The morphology of the prepared nanocatalysts (GNP-RuO<sub>2</sub>NPs) was investigated by TEM (JEM-2100 JEOL Japan) with accelerating voltage of 200 kV. The weight percentage and homogeneous decoration of RuO<sub>2</sub>NPs on GNP were confirmed by SEM-EDS (Hitachi 3000H). The same field of view was then scanned using an EDS spectrometer to acquire a set of X-ray maps at 1 ms point acquisition for approximately one million counts. The interaction of RuO<sub>2</sub>NPs with GNP was examined by Raman spectrometer (Hololab 5000, Kaiser Optical Systems Inc., USA) using argon laser at 532

nm with a Kaiser holographic edge filter. Wide angle XRD experiments were performed at room temperature using a Rotaflex RTP300 (Rigaku.Co., Japan) instrument at 50 kV and 200 mA. Nickel-filtered Cu K $\alpha$  radiation ( $5^\circ > 2\theta < 80^\circ$ ) was used for the XRD measurements. To confirm the chemical state of Ru, XPS spectrum was recorded in Kratos Axis-Ultra DLD instrument. The samples were irradiated under Mg K $\alpha$  ray source before XPS analysis. NMR spectra were recorded on a 400 MHz Bruker spectrometer in CDCl<sub>3</sub> using tetramethylsilane as a standard. FT-IR spectra were recorded using a Horiba FT-720 IR spectrophotometer.

### **6.2.2 Dry synthesis of nanocatalyst (GNP-RuO<sub>2</sub>NPs)**

In order to introduce oxygen functional groups on GNP, initially, chemical treatment was carried out for the pure GNP according to the literature procedure [31]. In a typical procedure, the GNP (1.0 g) was chemically treated with a 3:1 ratio mixture of concentrated H<sub>2</sub>SO<sub>4</sub> and HNO<sub>3</sub>. Subsequently, the resulting mixture was sonicated at 40°C for 3 h in an ultrasonic bath. After cooling to room temperature, the mixture was diluted with 750 mL of double distilled water and then vacuum-filtered. The resultant solid (*f*-GNP) was repeatedly washed with double distilled water until the pH reached neutral and then vacuum dried at 60°C. After that, 50 mg of Ru(acac)<sub>3</sub> was added into 500 mg of *f*-GNP and mixed well by a mortar and pestle under ambient condition. The homogeneous mixture of *f*-GNP and Ru(acac)<sub>3</sub> was obtained within 10-15 minutes. Finally, the impregnated Ru(acac)<sub>3</sub> was thermally decomposed into RuO<sub>2</sub>NPs by calcinating at 350°C for 6 h under nitrogen atmosphere. Figure 6.1 shows a schematic illustration of the procedure for preparation of the GNP-RuO<sub>2</sub>NPs.

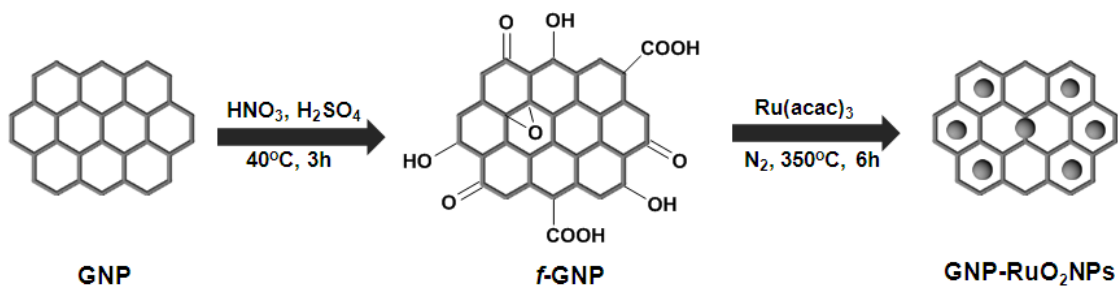


**Figure 6.1** – Schematic diagram of the preparation of GNP-RuO<sub>2</sub>NPs.

### 6.2.3 Oxidation of tertiary amines

10 mg of GNP-RuO<sub>2</sub>NPs (0.13 mol%) was stirred with 3 mL of CH<sub>3</sub>CN taken in a round-bottomed flask equipped with a condenser and a stirring bar. To the above mixture, substrate (2 mmol) was added followed by a slow dropwise addition of 30% H<sub>2</sub>O<sub>2</sub> (5 mmol). Then the solution mixture was heated at 80°C under atmospheric pressure of air. The completion of the *N*-oxidation reaction was monitored by TLC. Once the reaction completed, the nanocatalyst was separated out from the reaction mixture by simple centrifugation, washed well with diethyl ether followed by drying in oven at 80°C for 3 h and was reused for the subsequent *N*-oxidation of tertiary amines to test the reusability of the nanocatalyst. In other hand, the centrifugate was dried over anhydrous MgSO<sub>4</sub> to afford the product which was purified by passing through a column of silica gel using dichloromethane-MeOH (90:10) as an eluent. The products (amine *N*-oxides) were identified by <sup>1</sup>H NMR and FT-IR spectral data.

Triethylamine *N*-oxide (Table 6.1, entry 1): Yellow liquid; <sup>1</sup>H-NMR (400 MHz, DMSO-d<sub>6</sub>): δ 1.10-1.14 (t, 9H), 2.99-3.05 (m, 6H); FT-IR (cm<sup>-1</sup>): 3145, 1685, 1392, 1150, 825.

N,N-Dimethyl aniline *N*-oxide (Table 6.1, entry 2): Yellow solid;  $^1\text{H-NMR}$  (400 MHz, DMSO- $\text{d}_6$ ):  $\delta$  2.65 (s, 6H), 6.62-6.64 (m, 1H), 6.71-7.73 (m, 3H), 7.15-7.19 (m, 2H); FT-IR ( $\text{cm}^{-1}$ ): 2933, 1591, 1500, 1341, 1223, 1190, 1164, 1063, 1030, 1000, 943, 750, 689.

N,N-Dimethyl-*p*-toluidine *N*-oxide (Table 6.1, entry 3): Yellow solid;  $^1\text{H-NMR}$  (400 MHz, DMSO- $\text{d}_6$ ):  $\delta$  2.25 (s, 3H), 2.89 (s, 6H), 6.68-6.70 (d,  $J = 8$  Hz, 2H), 7.04-7.06 (d,  $J = 8$  Hz, 2H); FT-IR ( $\text{cm}^{-1}$ ): 3389, 2932, 2879, 2868, 1676, 1623, 1523, 1330, 1154, 1050, 952, 799, 713, 687.

N,N-Dimethyl-*o*-toluidine *N*-oxide (Table 6.1, entry 4): Yellow solid;  $^1\text{H-NMR}$  (400 MHz, DMSO- $\text{d}_6$ ):  $\delta$  2.25 (s, 3H), 2.61 (s, 6H), 6.91-7.14 (m, 4H); FT-IR ( $\text{cm}^{-1}$ ): 2967, 1569, 1493, 1450, 1310, 1185, 1155, 1117, 1050, 950, 760, 723.

N,N-Dimethyl-*m*-toluidine *N*-oxide (Table 6.1, entry 5): Yellow solid;  $^1\text{H-NMR}$  (400 MHz, DMSO- $\text{d}_6$ ):  $\delta$  2.24 (s, 3H), 2.86 (s, 6H), 6.46-6.48 (m, 1H), 6.48-6.51 (m, 1H), 6.53 (s, 1H), 7.03-7.07 (m, 1H); FT-IR ( $\text{cm}^{-1}$ ): 2935, 2825, 1679, 1626, 1518, 1339, 1157, 1059, 960, 810, 773, 689.

4-Bromopyridine *N*-oxide (Table 6.1, entry 8): Pale brown solid;  $^1\text{H-NMR}$  (400 Hz, DMSO- $\text{d}_6$ ):  $\delta$  7.85-7.86 (d,  $J = 4.0$  Hz, 2H), 8.73-8.74 (d,  $J = 4.0$  Hz, 2H); FT-IR ( $\text{cm}^{-1}$ ): 3023, 2531, 1619, 1475, 1360, 1342, 1102, 1084, 794, 725.

2-Bromopyridine *N*-oxide (Table 6.1, entry 9): Pale brownish yellow liquid;  $^1\text{H-NMR}$  (400 Hz, DMSO- $\text{d}_6$ ):  $\delta$  7.44-7.47 (m, 1H), 7.64-7.66 (d,  $J = 8.0$  Hz, 1H),  $\delta$  7.75-7.79 (m, 1H), 8.39-8.41 (m, 1H); FT-IR ( $\text{cm}^{-1}$ ): 3050, 1560-1580, 1451, 1410, 1100-1080, 991, 758, 699.

Quinoline *N*-oxide (Table 6.1, entry 11): Colorless solid;  $^1\text{H-NMR}$  (400 MHz, DMSO- $\text{d}_6$ ):  $\delta$  7.51-8.05 (m, 5H), 8.35-8.37 (d,  $J = 8$  Hz, 1H), 8.91-8.92 (m, 1H); FT-IR ( $\text{cm}^{-1}$ ):

3562, 3029, 1492, 1428, 1388, 1298, 1265, 1219, 1204, 1176, 1136, 1086, 1052, 1010, 877, 829, 763, 732.

Quinoxaline N-dioxide (Table 6.1, entry 12): Yellow solid;  $^1\text{H-NMR}$  (400 MHz, DMSO- $d_6$ ):  $\delta$  7.74-7.87 (m, 2H), 8.12 (m, 2H), 8.86 (s, 2H); FT-IR ( $\text{cm}^{-1}$ ): 3411, 3046, 1675, 1485, 1372, 1202, 1126, 1020, 950, 863, 750.

2,2'-Bipyridyl N-dioxide (Table 6.1, entry 13): Gray solid;  $^1\text{H-NMR}$  (400 Hz, DMSO- $d_6$ ):  $\delta$  7.45-7.47 (m, 2H), 7.95-7.97 (m, 2H), 8.38-8.40 (d,  $J = 8.0$  Hz, 2H), 8.69-8.70 (d,  $J = 4.0$  Hz, 2H); FT-IR ( $\text{cm}^{-1}$ ): 2900, 2825, 2201, 1622, 1520-1530, 1503, 1350-1370, 1225, 1100, 1060, 980, 789, 657.

4-(Dimethylamino)pyridine N-dioxide (Table 6.1, entry 17): Colorless solid;  $^1\text{H-NMR}$  (400 Hz, DMSO- $d_6$ ):  $\delta$  2.94 (s, 6H), 6.57-6.59 (d,  $J = 8.0$  Hz, 2H), 8.09-8.11 (d,  $J = 8.0$  Hz, 2H); FT-IR ( $\text{cm}^{-1}$ ): 2901, 2832, 1520-1532, 1432, 1350-1374, 1225, 1108, 1064, 985, 806, 745, 655.

1-Phenylpiperazine N-dioxide (Table 6.1, entry 18): Yellow liquid;  $^1\text{H-NMR}$  (400 Hz, DMSO- $d_6$ ):  $\delta$  1.8 (s, 1H), 3.01-3.03 (m, 2H), 3.12-3.15 (m, 2H), 6.83-6.94 (m, 3H), 7.24-7.28 (m, 2H); FT-IR ( $\text{cm}^{-1}$ ): 2900, 2825, 1594, 1500-1530, 1434, 1350-1374, 1225, 1114, 1064, 980, 799.

## 6.3 Results and discussion

### 6.3.1 Characterization of GNP-RuO<sub>2</sub>NPs

To investigate the morphology of GNP-RuO<sub>2</sub>NPs, TEM images were taken for pure GNP and GNP-RuO<sub>2</sub>NPs [Figure 6.2(i-v)]. The TEM image of pure GNP confirmed

the presence of irregular ultra thin sheets of size ranging from 0.5 to 2  $\mu\text{m}$ . GNP also has multi layers with an average thickness of about 7-9 nm. As can be seen from the TEM images of GNP-RuO<sub>2</sub>NPs, an ultra-fine RuO<sub>2</sub>NPs were homogeneously dispersed on the surface of GNP. High magnified TEM images of GNP-RuO<sub>2</sub>NPs showed good adhesion of RuO<sub>2</sub>NPs on anchoring sites of GNP with very narrow particle size distribution. The histogram of RuO<sub>2</sub>NPs reveals that the RuO<sub>2</sub>NPs have a very narrow size distribution ranging from 0.5 to 3.0 nm with a peak centered at *ca.* 1.3 nm [Figure 6.2(vi)]. It is worth to mention that there was no free RuO<sub>2</sub>NPs were observed in the background of the TEM images, which confirmed the complete utilization of the RuO<sub>2</sub>NPs by the GNP.

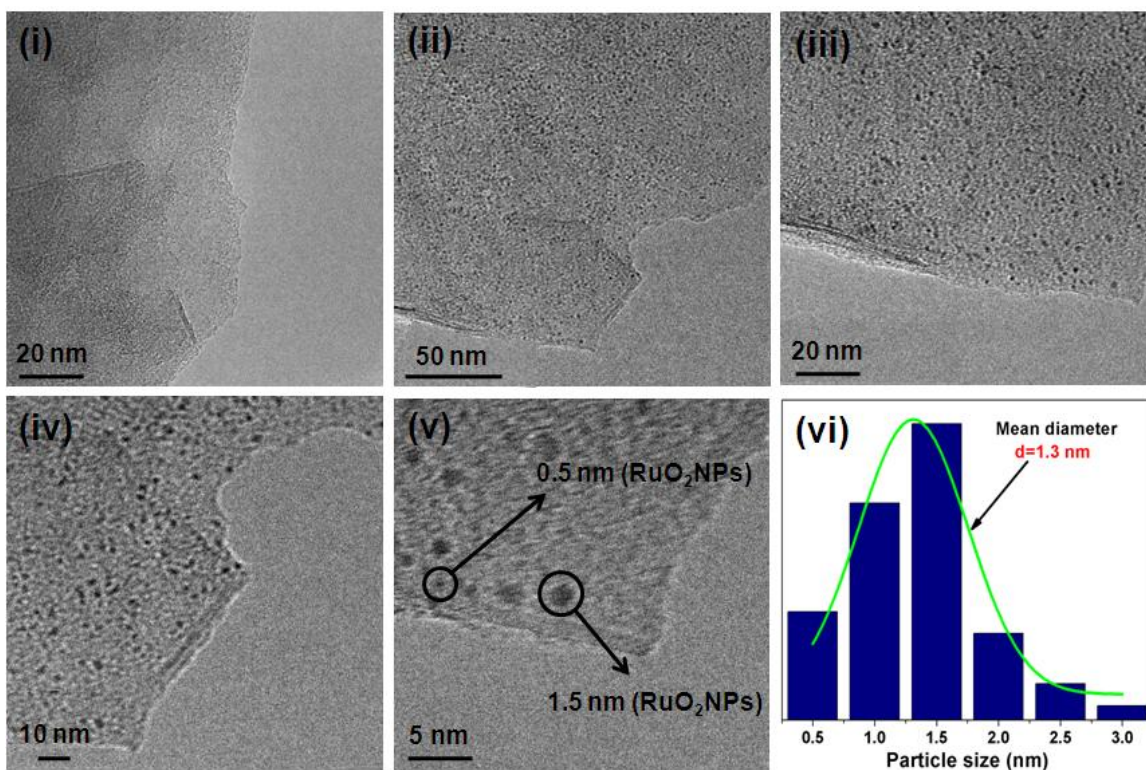


**Figure 6.2** – TEM images of (i) pure GNP and (ii, iii, iv and v) GNP-RuO<sub>2</sub>NPs, and (vi) the particle size distribution of RuO<sub>2</sub>NPs.

In addition, the surface area per unit mass ( $S$ ) of RuO<sub>2</sub>NPs was calculated by using the equation [30],  $S = 6000/(\rho \times d)$  where  $d$  is the mean diameter of RuO<sub>2</sub>NPs (1.3 nm), and  $\rho$  is the density of RuO<sub>2</sub> (6.97 gcm<sup>-3</sup>) and it was found to be 1119.40 m<sup>2</sup>g<sup>-1</sup>. Figure 6.3 shows the SEM-EDS and corresponding elemental mapping images of GNP-RuO<sub>2</sub>NPs. The weight percentage of Ru in GNP-RuO<sub>2</sub>NPs was 2.68 as determined by EDS analysis [Figure 6.3(ii)]. As expected, EDS mapping analysis confirms the homogeneous distribution of RuO<sub>2</sub>NPs in GNP-RuO<sub>2</sub>NPs. The credibility of the proposed method can be understood from the purity of GNP-RuO<sub>2</sub>NPs that contains only carbon, ruthenium and oxygen elements as confirmed by EDS analysis.

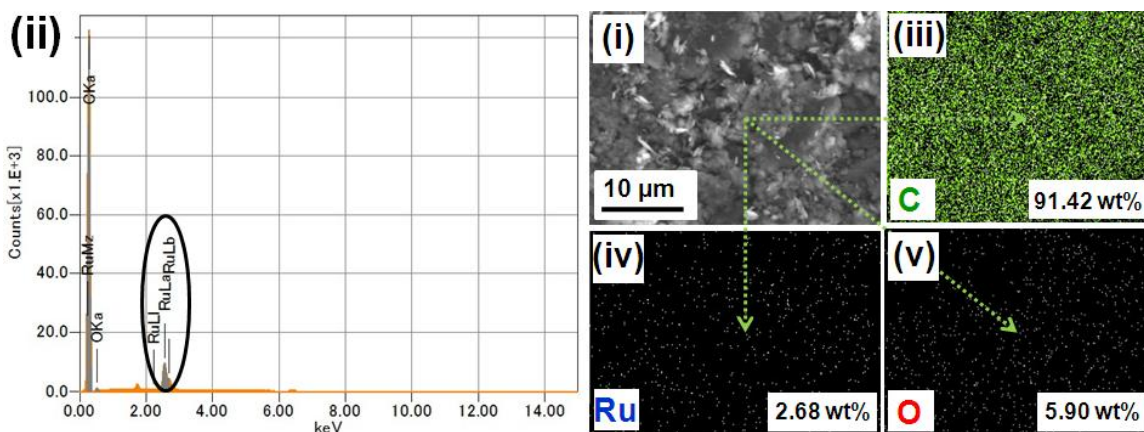


**Figure 6.3** – (i) SEM images and (ii) corresponding EDS spectrum of GNP-RuO<sub>2</sub>NPs, and EDS mapping of (iii) C, (iv) Ru and (v) O.

XPS spectra were recorded for *f*-GNP and GNP-RuO<sub>2</sub>NPs in order to confirm the functionalization of GNP and the chemical state of Ru in GNP-RuO<sub>2</sub>NPs; the results are shown in Figure 6.4(i and ii) and Figure 6.5(i and ii). As expected, both *f*-GNP and GNP-RuO<sub>2</sub>NPs showed a C 1s peak and O 1s peak at 284.5 and 532.5 eV respectively [Figure 6.4(i and ii) and Figure 6.5(i)]. The binding energy of C–C, C–O–C, C=O and –COOH

groups is assigned at 285.2, 285.6, 286.8 and 288.7 eV respectively [32]. Deconvolution of the O 1s spectrum of *f*-GNP [Figure 6.5(ii)] resulted in five peaks located at 530.1, 531.2, 531.7, 532.6 and 533.5 eV, which were assigned to the C=O, –COOH, C–OH, –C–O–C– and H<sub>2</sub>O respectively [33]. According to Gil *et al.*, [34] oxygen functional groups on graphene act as effective nucleation centers for MNPs, which assist homogeneous decoration as well as better adhesion of MNPs on graphene. Likewise in the present case, the homogeneous as well as better adhesion of RuO<sub>2</sub>NPs on GNP [Figure 6.2(i-v)] is due to the presence of oxygen functional groups on GNP. Particularly, –COOH group assists good adhesion of RuO<sub>2</sub>NPs on GNP by replacing the proton of –COOH [35]. The XPS spectrum of GNP-RuO<sub>2</sub>NPs [Figure 6.5(i and ii)] showed binding energy (BE) of Ru 3p<sub>3/2</sub> at 462.5 eV, Ru 3p<sub>1/2</sub> at 485.0 eV and Ru 3d<sub>5/2</sub> at 280.8 eV, which correspond to the photoemission from RuO<sub>2</sub> [36]. The overlapping of the C 1s and the Ru 3d<sub>3/2</sub> peaks at ~285 eV makes it difficult to assign BE of Ru 3d<sub>3/2</sub>. The chemical state of Ru was also confirmed by XRD [Figure 6.6(i)]. The diffraction peaks at 26.5, 44.2 and 54.8°, corresponding to the (002), (100), and (004) crystal planes of graphite respectively, attributed to the hexagonal graphite structures of GNP [37]. The very weak XRD peaks at 27.5, 34.9, 39.9 and 57.5° correspond to the typical crystal faces (110), (101), (200) and (220) of RuO<sub>2</sub> (JCPDS 21-1172) respectively, confirmed the nanocrystalline nature of RuO<sub>2</sub> [37].

The Raman spectroscopy is a precise and quick analysis method to investigate the nature of interaction between various MNPs and graphene. Therefore, Raman spectrum was recorded for GNP-RuO<sub>2</sub>NPs under 514.5 nm excitation over the Raman shift interval of 250-4000 cm<sup>-1</sup> [Figure 6.6(ii)]. As expected, both *f*-GNP and GNP-RuO<sub>2</sub>NPs exhibited

two main Raman features, corresponding to the well-defined D-band line at  $\sim 1345\text{ cm}^{-1}$  and G-band line at  $\sim 1570\text{ cm}^{-1}$ . The G-band line is originated from in-plane vibration of  $\text{sp}^2$  carbon atoms, which represents the relative degree of graphitization [38]. The D-band line is related to the amount of disorder which arises only in the presence of defects, indicating the presence of  $\text{sp}^3$  carbon atoms or defect sites in GNP [38]. Since the ratio of D and G band ( $I_D/I_G$ ) intensities is often used as a diagnostic tool to evaluate the defects concentration in graphene, it was calculated for *f*-GNP and GNP-RuO<sub>2</sub>NPs. It is noteworthy that the  $I_D/I_G$  (0.1801) ratio of GNP-RuO<sub>2</sub>NPs was higher than that of *f*-GNP (0.1515), which confirmed that the RuO<sub>2</sub>NPs are attached on the surface of GNP with good adhesion. In the XPS spectrum [Figure 6.5(i)], a significant positive shift in C 1s peak was observed for GNP-RuO<sub>2</sub>NPs when compared to that of the *f*-GNP; this too confirms there has been a very strong interaction between GNP and RuO<sub>2</sub>NPs [39].

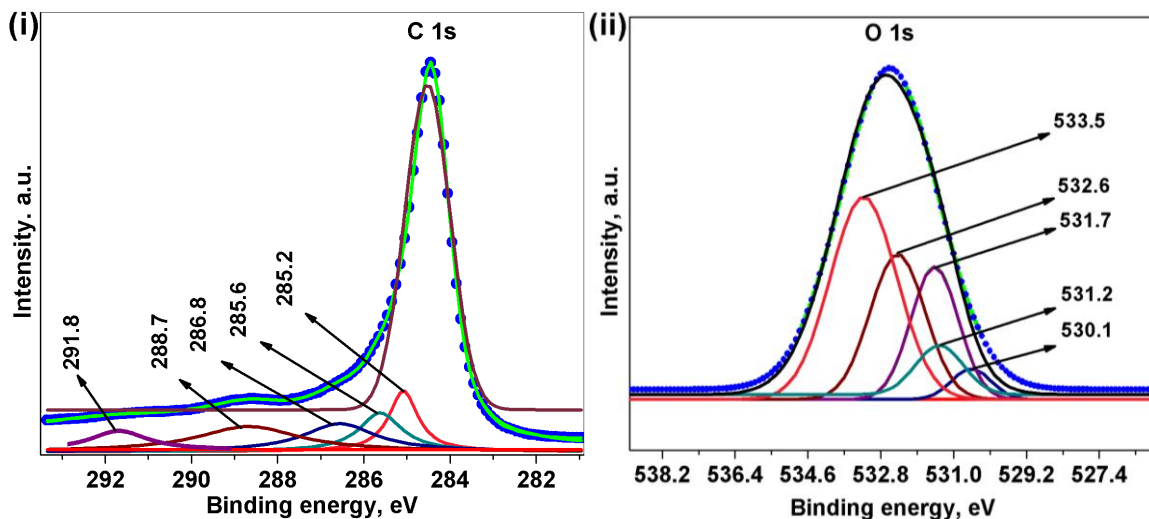


**Figure 6.4** – XPS spectrum of *f*-GNP; magnified (i) C 1s and (ii) O 1s peaks.

The XPS spectrum of the GNP-RuO<sub>2</sub>NPs in Ru 3p region [Figure 6.5(ii)] showed BE of Ru 3p<sub>3/2</sub> at 462.5 eV and Ru 3p<sub>1/2</sub> at 485.0 eV which correspond to the photoemission from RuO<sub>2</sub> [36]. In Figure 6.5(i), GNP-RuO<sub>2</sub>NPs show Ru 3d<sub>5/2</sub> peak at 280.8 eV which attributed to the ruthenium dioxide [36]. The overlapping of the C 1s and the Ru 3d<sub>3/2</sub> peaks at ~285 eV makes it difficult to assign BE of Ru 3d<sub>3/2</sub>. The chemical state of Ru was also confirmed by XRD [Figure 6.6(i)]. The diffraction peaks at 26.5°, 44.2°, and 54.8°, corresponding to the (002), (100), and (004) crystal planes of graphite respectively, which attributed to the hexagonal graphite structures of GNP [37]. The very weak XRD peaks were observed at 27.5°, 34.9°, 39.9° and 57.5° correspond to the typical crystal faces (110), (101), (200) and (220) of RuO<sub>2</sub> (JCPDS 21-1172), respectively; it is confirmed that the RuO<sub>2</sub> are of nano-crystalline nature [37].

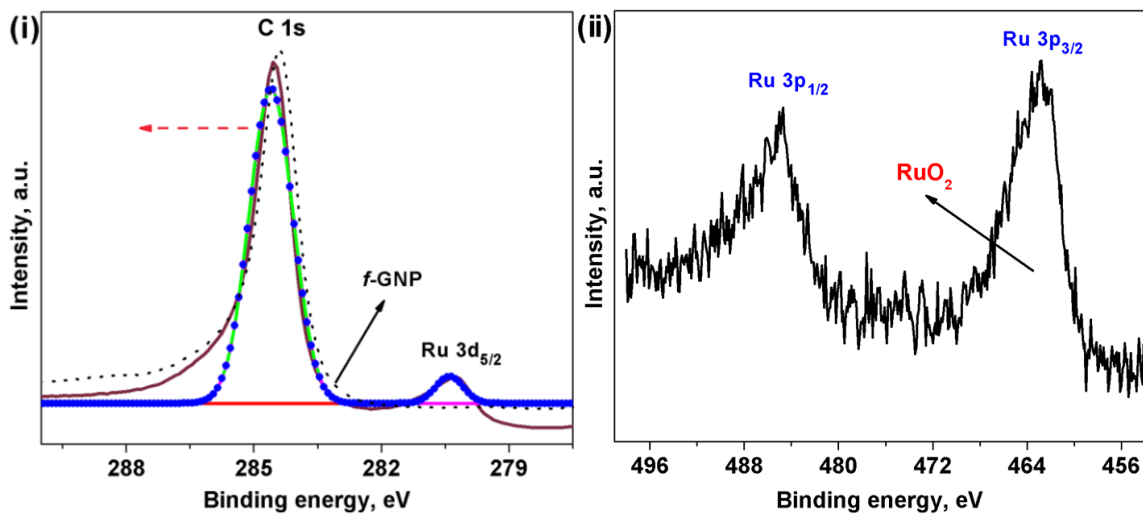


**Figure 6.5** – XPS spectrum of GNP-RuO<sub>2</sub>NPs; magnified (i) C 1s and (ii) Ru 3p peaks.

The Raman spectroscopy is a precise and quick analysis method to investigate the nature of interactions between various MNPs and graphene. Therefore, Raman spectrum

was recorded for GNP-RuO<sub>2</sub>NPs under 514.5 nm excitation over the Raman shift interval of 250-4000 cm<sup>-1</sup> [Figure 6.6(ii)]. As expected, both GNP and GNP-RuO<sub>2</sub>NPs exhibit two main Raman features, corresponding to the well-defined D-band line at ~1345 cm<sup>-1</sup> and G-band line at ~1570 cm<sup>-1</sup>. The G-band line is originated from in-plane vibration of -sp<sup>2</sup> carbon atoms which, represents the relative degree of graphitization [38]. The D-band line is related to the amount of disorder which arises only in the presence of defects, indicating the presence of sp<sup>3</sup> carbon atoms or defect sites in GNP [38].

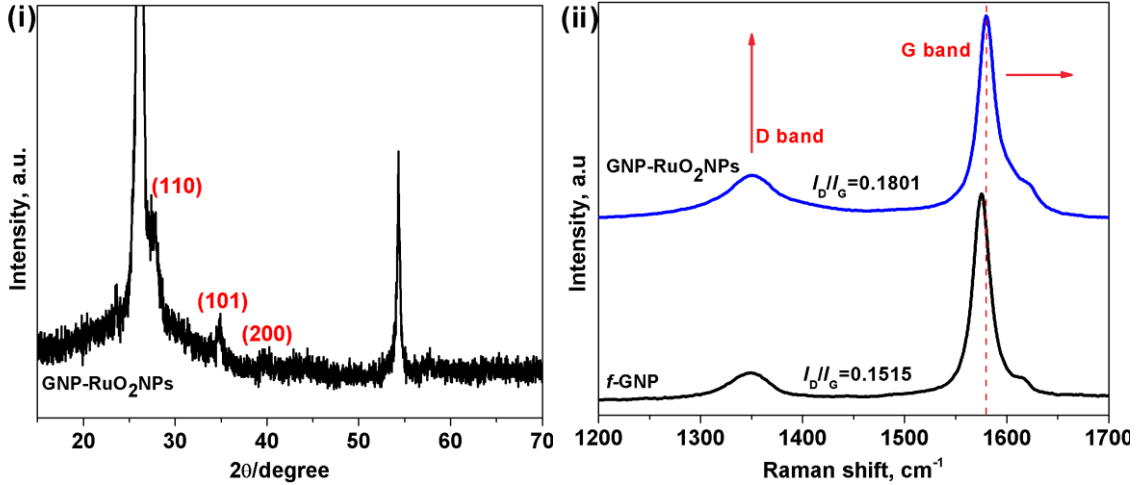


**Figure 6.6** – (i) XRD pattern of GNP-RuO<sub>2</sub>NPs and (ii) Raman spectra of *f*-GNP and GNP-RuO<sub>2</sub>NPs.

Since the ratio of D and G band ( $I_D/I_G$ ) intensities are often used as a diagnostic tool to evaluate the defects concentration in graphene, it was calculated for *f*-GNP and of GNP-RuO<sub>2</sub>NPs [Figure 6.6(iv)]. It is noteworthy that the  $I_D/I_G$  (0.1801) ratio for GNP-RuO<sub>2</sub>NPs was higher than that of *f*-GNP (0.1515) which confirmed that the RuO<sub>2</sub>NPs are attached on the surface of GNP with good adhesion. In case of XPS spectrum [Figure 6.6(i)], a significant positive shift in C 1s peak was observed for GNP-RuO<sub>2</sub>NPs when

compared with that of the *f*-GNP, this too confirms there has been a very strong interaction between GNP and RuO<sub>2</sub>NPs [39].

### 6.3.2 Optimization of reaction conditions

To find out the most effective reaction condition for the N-oxidation of tertiary amines, in a preliminary study, we used triethylamine as a substrate and varied the solvent, amount of catalyst, time, amount of oxidant and temperature [Figure 6.7(i-iv)].

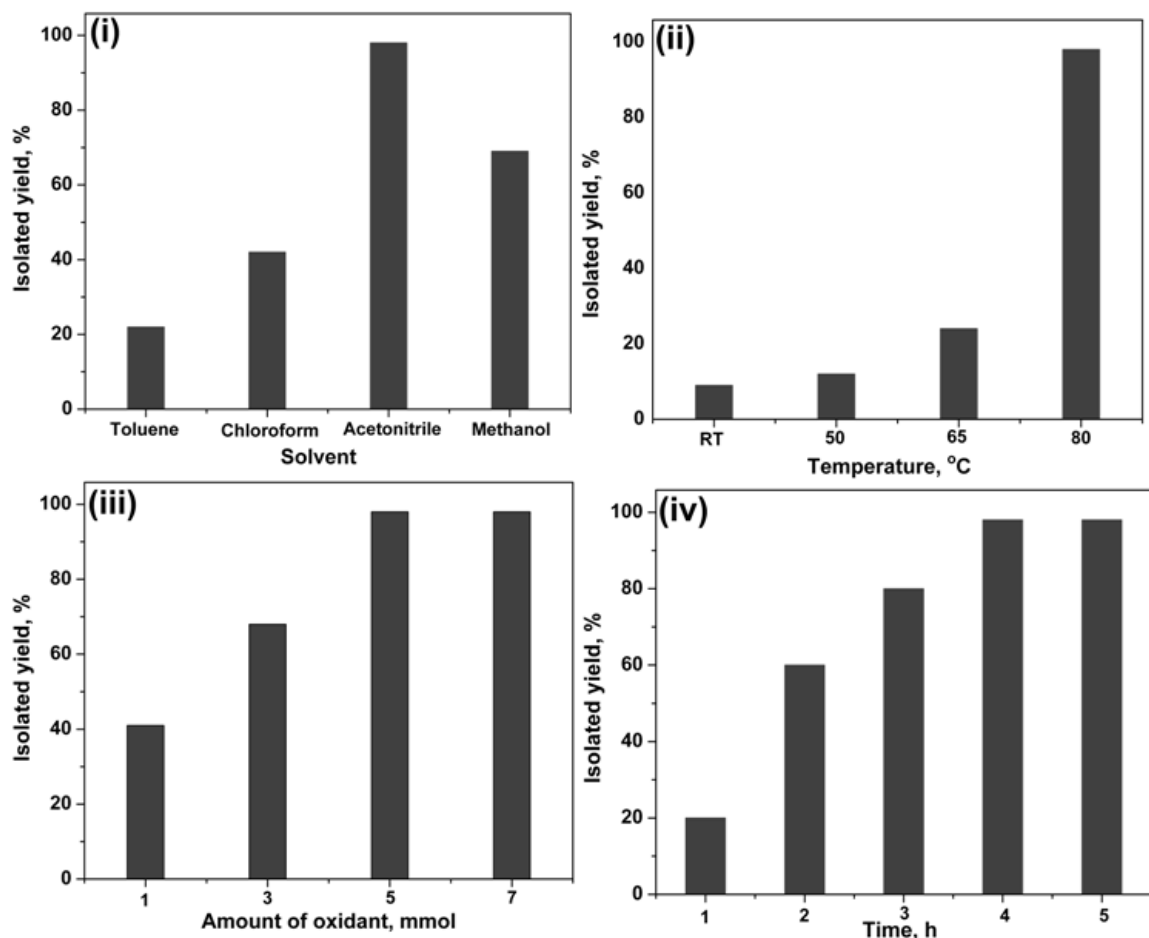


**Figure 6.7** – Effect of (i) solvent, (ii) temperature, (iii) amount of oxidant and (iv) time on the oxidation of triethylamine.

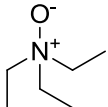
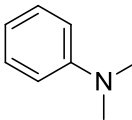
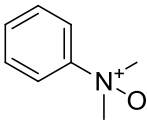
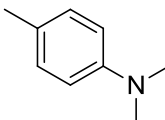
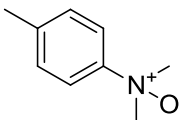
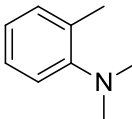
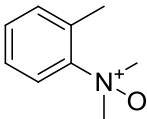
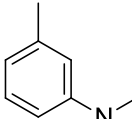
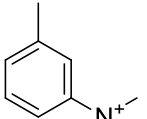
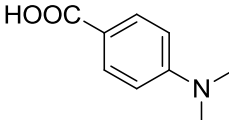
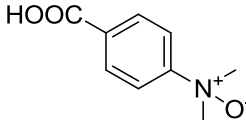
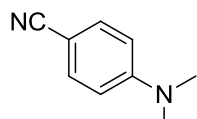
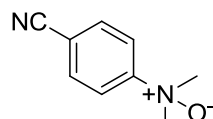
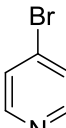
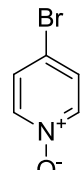
In solvent optimization, various solvents such as toluene,  $\text{CHCl}_3$  and  $\text{CH}_3\text{OH}$  were used but they were less effective compared to  $\text{CH}_3\text{CN}$  [Figure 6.7(i)]. As expected, only a very less amount of triethylamine *N*-oxide was obtained in the absence of the catalyst. 10 mg of the catalyst (0.13 mol% of Ru) was enough for the *N*-oxidation of triethylamine; this is the lowest amount of Ru catalyst reported for the *N*-oxidation of tertiary amines till to date. In temperature optimization, a maximum yield of 98% was obtained when the reaction was stirred at  $80^\circ\text{C}$  [Figure 6.7(ii)]. Amount of oxidant played a significant role in the *N*-oxidation process. It was found that 5 mmol of  $\text{H}_2\text{O}_2$  was an optimum amount of oxidant [Figure 6.7(iii)]. An excellent yield of 98% was obtained when the reaction mixture was stirred for 4 h [Figure 6.7(iv)]. The optimized reaction condition was opted to extend the scope of the *N*-oxidation of tertiary amines.

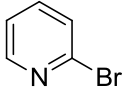
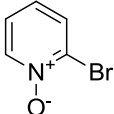
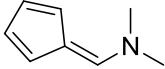
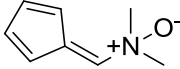
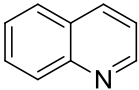
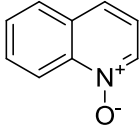
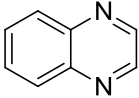
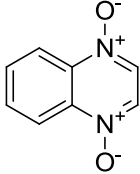
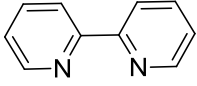
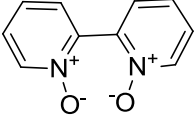
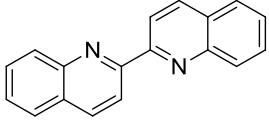
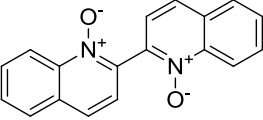
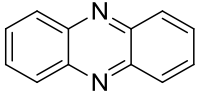
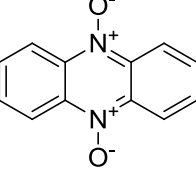
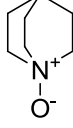
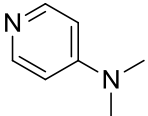
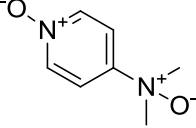
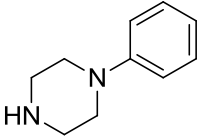
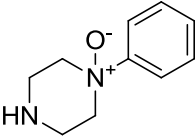
### 6.3.3 Extension of scope

Table 6.1 shows a variety of tertiary amines which were oxidized to their corresponding *N*-oxides in good to excellent yields. The yield of products was moderately affected by the substituent in the substrate. Aliphatic tertiary amine, triethylamine, was oxidized to triethylamine *N*-oxide in excellent yield of 99% (Table 6.1, entry 1) whereas Pt/C gave a lower yield of 66% [23]. Similarly, *N,N*-dimethyl aniline (DMA) gave the corresponding *N*-oxide in a better yield of 98% (Table 6.1, entry 2) in comparison to the Ti-MCM-41 system [40]. It was found that the DMA containing electron donating group such as methyl ( $-\text{CH}_3$ ), reacted faster whereas DMA with electron withdrawing group ( $-\text{CN}$  or  $-\text{COOH}$ ) required extended reaction time to afford even the less amount of corresponding *N*-oxide, which may be due to the mesomeric

effect (Table 6.1, entries 3-7). The present catalytic system showed a better yield for these substrates in comparison to the Pd catalytic system [41].

**Table 6.1 – N-oxidation of tertiary amines catalyzed by GNP-RuO<sub>2</sub>NPs<sup>a</sup>**

entry	substrate	product	time (h)	yield <sup>b</sup> (%)
1			4.0	98
2			4.0	98
3			5.0	97
4			4.5	89
5			4.5	90
6			8.0	76
7			5.0	66
8			8.0	93

9			9.0	84
10			6.0	92
11			4.5	82
12			4.0	62
13			4.0	91
14			7.0	68
15			6.0	86
16			4.5	94
17			6.0	80
18			6.0	56

<sup>a</sup>Reaction conditions: Amine (2 mmol), GNP-RuO<sub>2</sub>NPs (0.13 mol%), H<sub>2</sub>O<sub>2</sub> (5 mmol), acetonitrile (3 mL), 80°C. <sup>b</sup>Isolated yield.

Very recently, pyridine *N*-oxides have been recognized as a new class of anti-HIV compounds [42]. Therefore, the present catalytic system was adopted to prepare some pyridine *N*-oxide derivatives. Interestingly, pyridine containing electron withdrawing group such as -Br at *para* position gave the corresponding *N*-oxide in excellent yield of 93% (Table 6.1, entry 8) whereas  $H_{14}P_5Mo$  system afforded only a trace amount of the same product [42]. Alike, 2-bromopyridine was also oxidized to the corresponding *N*-oxide in a good yield of 87% (Table 6.1, entry 9). In the oxidation of 6-(dimethylamino)fulvene, the present catalytic system gave an excellent yield of 92% after stirring for 6 h (Table 6.1, entry 10). For the transformation of quinoline to quinoline *N*-oxide (Table 6.1, entry 11), the present GNP-RuO<sub>2</sub>NPs catalyst is very effective (yielded 82 % after 4.5 h) compared to the  $V_xSi_{4x}O_{6.4x}$  system which gave 71% of the desired product after 8 h [15]. It was found that the present catalytic system gave a moderate yield of 62% in the oxidation of quinoxaline to quinoxaline *N*-dioxide (Table 6.1, entry 12). A good yield of 91% was obtained from the oxidation of 2,2'-bipyridine after stirring for 4 h (Table 6.1, entry 13). The present catalytic system is less effective for the oxidation of sterically hindered heterocyclic amine. 2,2'-Biquinoline was oxidized to the corresponding *N*-dioxide in lower yield of 68% after stirring for 7 h (Table 6.1, entry 14). On contrary, in the oxidation of phenazine to the corresponding *N*-dioxide, the present catalytic system afforded a good yield of 86% (Table 6.1, entry 15). Alicyclic tertiary amine, quinuclidine, was oxidized to the corresponding amine oxide in an excellent yield of 94% (Table 6.1, entry 16). A good yield of 80% was obtained from the oxidation of 4-(dimethylamino)pyridine to the corresponding amine oxide after stirring for 6 h (Table 6.1, entry 17). Interestingly, the present catalytic system is highly selective towards the

tertiary amine than the secondary one. In the oxidation of 1-phenylpiperazine (Table 6.1, entry 18), the catalytic system selectively oxidized the tertiary amine (56%). The excellent catalytic activity of the GNP-RuO<sub>2</sub>NPs with lower amount of Ru catalyst (0.13 mol%) is due to three most obvious reasons: (i) the smaller size of the RuO<sub>2</sub>NPs, (ii) higher surface area of the GNP-RuO<sub>2</sub>NPs and (iii) an effective dispersion of the GNP-RuO<sub>2</sub>NPs in the reaction medium.

#### 6.3.4 Heterogeneity and reusability of GNP-RuO<sub>2</sub>NPs

To study the heterogeneity of the GNP-RuO<sub>2</sub>NPs, the nanocatalyst was separated out from the reaction mixture by a simple centrifugation and then the filtrate was analyzed by ICP-MS; no Ru content confirmed the heterogeneous nature of the GNP-RuO<sub>2</sub>NPs. Since the reusability of nanocatalyst is an important advantage, the separated GNP-RuO<sub>2</sub>NPs were washed with diethyl ether and dried in *vacuo* at 80°C. Then the recovered GNP-RuO<sub>2</sub>NPs were reused for the oxidation of triethylamine [Figure 6.8(i)]. Interestingly, the present catalytic system afforded 94% of triethylamine *N*-oxide even at the 5<sup>th</sup> cycle, which confirmed its excellent reusability. Additionally, used nanocatalyst (*u*-GNP-RuO<sub>2</sub>NPs) was characterized by TEM, SEM-EDS and XPS analysis. The TEM image [Figure 6.8(ii)] showed that the morphology of *u*-GNP-RuO<sub>2</sub>NPs remains unchanged. SEM-EDS result [Figure 6.8(iii)] revealed that the weight percentage of Ru in *u*-GNP-RuO<sub>2</sub>NPs was 2.24. The chemical state of Ru in *u*-GNP-RuO<sub>2</sub>NPs was +4, as confirmed by XPS analysis [Figure 6.8(iv)]. Therefore, GNP-RuO<sub>2</sub>NPs are physically as well as chemically stable and reusable.

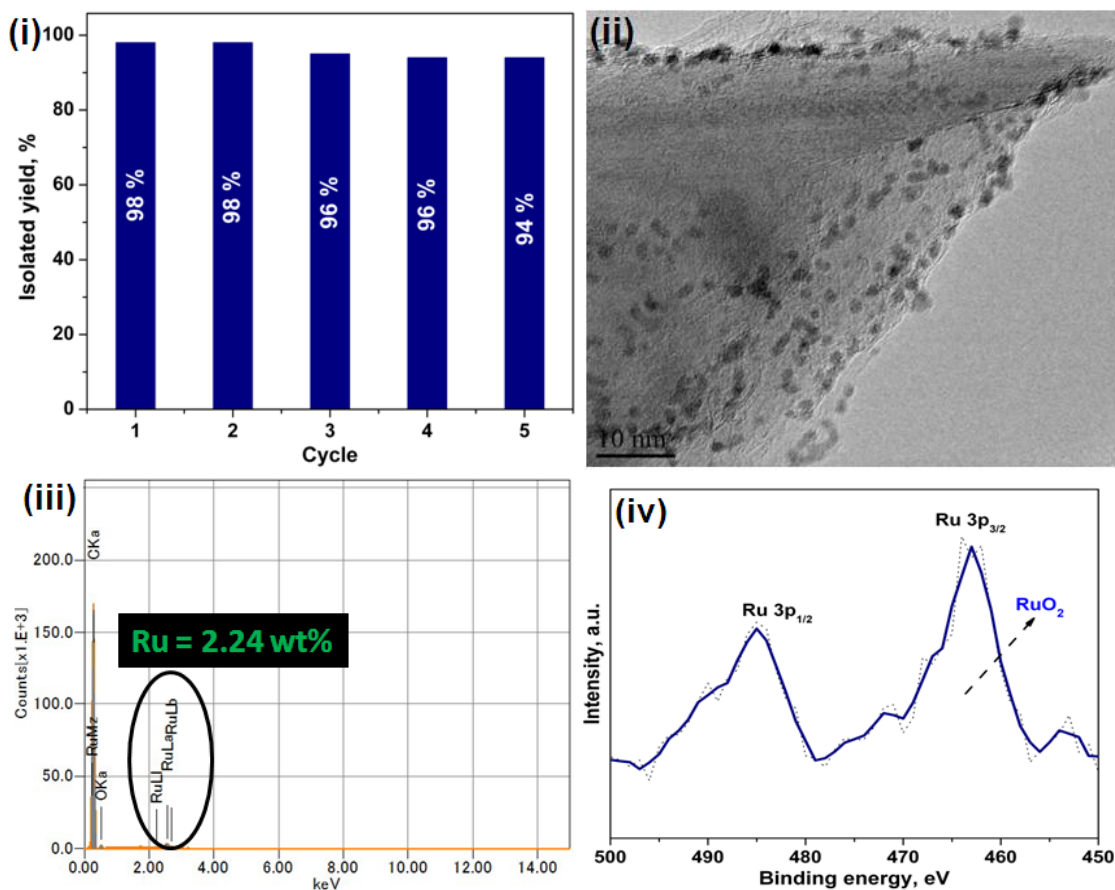


**Figure 6.8** – (i) Reusability of GNP-RuO<sub>2</sub>NPs, (ii) TEM image, (iii) EDS and (iv) XPS of *u*-GNP-RuO<sub>2</sub>NPs.

### 6.3.5 Proposed mechanism

In order to understand the mechanism of GNP-RuO<sub>2</sub>NPs-catalyzed *N*-oxidation of tertiary amines, XPS spectrum was recorded for pure GNP-RuO<sub>2</sub>NPs and *o*-GNP-RuO<sub>2</sub>NPs (the catalyst after stirring with H<sub>2</sub>O<sub>2</sub> in CH<sub>3</sub>CN at 80°C for 4 h); results are shown in Figure 6.9. In comparison to pure GNP-RuO<sub>2</sub>NPs, O1s spectrum of *o*-GNP-RuO<sub>2</sub>NPs showed a dramatic increase in the peak intensity at 531.0 eV; this clearly confirmed the formation of Ru<sup>VI</sup>=O species during the *N*-oxidation reaction [43]. The results concluded that the mechanism for the *N*-oxidation of tertiary amines might be

involving the Ru-oxo species as an intermediate (Figure 6.9). In step (i),  $\text{H}_2\text{O}_2$  helps for the formation Ru-oxo species by transferring its oxygen. Subsequently, in step (ii), the formed Ru-oxo species assists the formation of triethylamine *N*-oxide from triethylamine. Finally, GNP-RuO<sub>2</sub>NPs were regenerated for the further *N*-oxidation process.

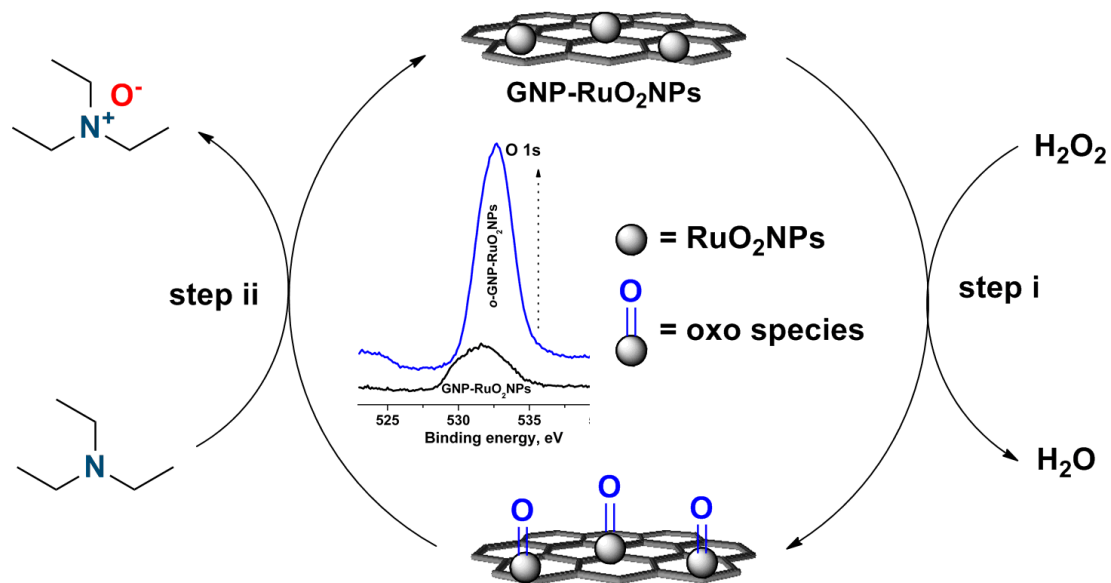


**Figure 6.9** – Proposed catalytic mechanism for the *N*-oxidation of triethyl amine using GNP-RuO<sub>2</sub>NPs.

## 6.4 Conclusions

RuO<sub>2</sub>NPs with a mean diameter of 1.3 nm were decorated on *f*-GNP by a straight forward “dry synthesis” method. TEM images showed an excellent attachment and homogeneous dispersion of RuO<sub>2</sub>NPs on GNP. The weight percentage of Ru in GNP-RuO<sub>2</sub>NPs was 2.68 wt%, as determined by EDS analysis. Raman intensity ratios confirmed the good attachment of RuO<sub>2</sub>NPs on the surface of GNP. XRD and XPS

revealed that the Ru was in +4 oxidation state with a nano-crystalline nature of RuO<sub>2</sub>NPs. The *N*-oxidation of tertiary amines could be carried out effectively with as low as 0.13 mol% of supported Ru catalyst for a wide range of substrates. To the best of our knowledge, this is the lowest amount of Ru used for the *N*-oxidation reaction. The proposed catalyst was chemically as well as physically very stable, heterogeneous in nature and could be reused up to 5 cycles. In summary, we have developed a heterogeneous Ru based nanocatalytic system for the *N*-oxidation of tertiary amines, which requires only a lower amount of catalyst (0.13 mol% of Ru) for efficient reaction.

## References

- [1] Othmer, K. Encyclopedia of Chemical Technology, 4<sup>th</sup> ed., John Wiley and Sons, Wiley Interscience, New York, **1997**.
- [2] Boyer, J. H. Increasing the Index of Covalent Oxygen Bonding at Nitrogen Attached To Carbon. *Chem. Rev.* **1980**, *80*, 495–561.
- [3] Campeau, L. C.; Stuart, D. R.; Leclerc, J. P.; Laperle, M. B.; Villemure, E.; Sun, H. Y.; Lasserre, S.; Guimond, N.; Lecavallier, M.; Fagnou, K. Palladium-Catalyzed Direct Arylation of Azine and Azole *N*-Oxides: Reaction Development, Scope and Applications in Synthesis. *J. Am. Chem. Soc.* **2009**, *131*, 3291–3306.
- [4] VanRheenen, V. .; Cha, D. Y.; Hartley, W. M. Catalytic Osmium Tetroxide Oxidation of Olefins: *cis*-1,2-Cyclohexanediol. *Org. Synth.* **1988**, *6*, 342–348.
- [5] Priyadarsini, K. I.; Dennis, M. F.; Naylor, M. A.; Stratford, M. R. L.; Wardman, P. Free Radical Intermediates in the Reduction of Quinoxaline *N*-Oxide Antitumor Drugs: Redox and Prototropic Reactions. *J. Am. Chem. Soc.* **1996**, *118*, 5648–5654.
- [6] Malkov, A. V.; Bell, M.; Castelluzzo, F.; Kocovsky, P. METHOX: A New Pyridine *N*-Oxide Organocatalyst for the Asymmetric Allylation of Aldehydes with Allyltrichlorosilanes. *Org. Lett.* **2005**, *7*, 3219–3222.
- [7] Schroder, M. Osmium Tetraoxide Cis Hydroxylation of Unsaturated Substrates. *Chem. Rev.* **1980**, *80*, 187–213.
- [8] Malkov, A. V.; Kocovsky, P. Chiral *N*-Oxides in Asymmetric Catalysis. *Eur. J. Org. Chem.* **2007**, 29–36.
- [9] Baumstark, A. L.; Dotrong, M.; Vasquez, P. C. Oxygen-Atom Transfer Reagents: New, Reactive *A*-Azohydroperoxides. *Tetrahedron Lett.* **1987**, *28*, 1963–1966.

- [10] Payne, G. B.; Deming, P. H.; Williams, P. H. Reactions of Hydrogen Peroxide. VII. Alkali-Catalyzed Epoxidation and Oxidation Using a Nitrile as Co-reactant. *J. Org. Chem.* **1961**, *26*, 659–663.
- [11] Wei, Z.; Chunxia, Y. A green catalytic procedure for oxidation of pyridines catalyzed by a lacunary polyoxometalate in water at room temperature. *New J. Chem.* **2013**, *37*, 1867–1870.
- [12] Ferrer, M.; Sanchez-Baeza, F.; Messgure, A. On The Preparation of Amine *N*-Oxides by Using Dioxiranes. *Tetrahedron* **1997**, *53*, 15877–15888.
- [13] Edward, J. T.; Josephine, W. Reactions of Amine Oxides and Hydroxylamines with Sulfur Dioxide. *Can. J. Chem.* **1971**, *49*, 3502.
- [14] Brougham, P.; Cooper, M. S.; Cummerson, D. A.; Heaney, H.; Thomson, N. Oxidation Reactions Using Magnesium Monoperphthalate: A Comparison with *m*-Chloroperoxybenzoic Acid. *Synthesis* **1987**, 1015–1017.
- [15] Rout, L.; Punniyamurthy, T. Silica-Supported Vanadium-Catalyzed *N*-Oxidation of Tertiary Amines with Aqueous Hydrogen Peroxide. *Adv. Synth. Catal.* **2005**, *347*, 1958–1960.
- [16] Coperet, C.; Adolfsson, H.; Khuong, T. A. V.; Yudin, A. K.; Sharpless, K. B. A Simple and Efficient Method for the Preparation of Pyridine *N*-Oxides. *J. Org. Chem.* **1998**, *63*, 1740–1741.
- [17] Prasad, M. R.; Kamalakar, G.; Madhavi, G.; Kulkarni, S. J.; Raghavan, K. V. An Efficient Synthesis of Heterocyclic *N*-Oxides Over Molecular Sieve Catalysts. *Chem. Commun.* **2000**, 1577–1578.

- [18] Bailey, A. J.; Griffith, W. P.; Parkin, B. C. Heteropolyperoxo- and Isopolyperoxo-Tungstates and-Molybdates as Catalysts for the Oxidation of Tertiary Amines, Alkenes and Alcohols. *J. Chem. Soc. Dalton Trans.* **1995**, 1833–1837.
- [19] Choudary, B. M.; Bharathi, B.; Reddy, C. V.; Kantam, M. L. The First Example of Heterogeneous Oxidation of Secondary Amines by Tungstate-Exchanged Mg-Al Layered Double Hydroxides: A Green Protocol. *Green Chem.* **2002**, *4*, 279–284.
- [20] Phukan, P.; Khisti, R. S.; Sudalai, A. Green Protocol for the Synthesis of *N*-Oxides from Secondary Amines Using Vanadium Silicate Molecular Sieve Catalyst. *J. Mol. Catal. A: Chem.* **2006**, *248*, 109–112.
- [21] Robinson, D. J.; McMorn, P.; Bethell, D.; Bulman-Page, P. C.; Sly, C.; King, F.; Hancock, F. E.; Hutchings, G. J. *N*-Oxidation of Pyridines by Hydrogen Peroxide in the Presence of TS-1. *Catal. Lett.* **2001**, *72*, 233–234.
- [22] Comotti, M.; Della Pina, C.; Rossi, M.; Mono- and Bimetallic Catalysts for Glucose Oxidation. *J. Mol. Catal. A: Chem.* **2006**, *251*, 89–92.
- [23] Della Pina, C.; Falletta, E.; Rossi, M.; Selective Oxidation of Tertiary Amines on Gold Catalysts. *Top. Catal.* **2007**, *44*, 325–329.
- [24] Pagliaro, M.; Campestrini, S.; Ciriminna, R.; Ru-Based Oxidation Catalysis. *Chem. Soc. Rev.* **2005**, *34*, 837–845.
- [25] Veerakumar, P.; Balakumar, S.; Velayudham, M.; Luc, K. L.; Rajagopal, S.; Ru/Al<sub>2</sub>O<sub>3</sub> Catalyzed *N*-Oxidation of Tertiary Amines by using H<sub>2</sub>O<sub>2</sub>. *Catal. Sci. Technol.* **2012**, *2*, 1140–1145.

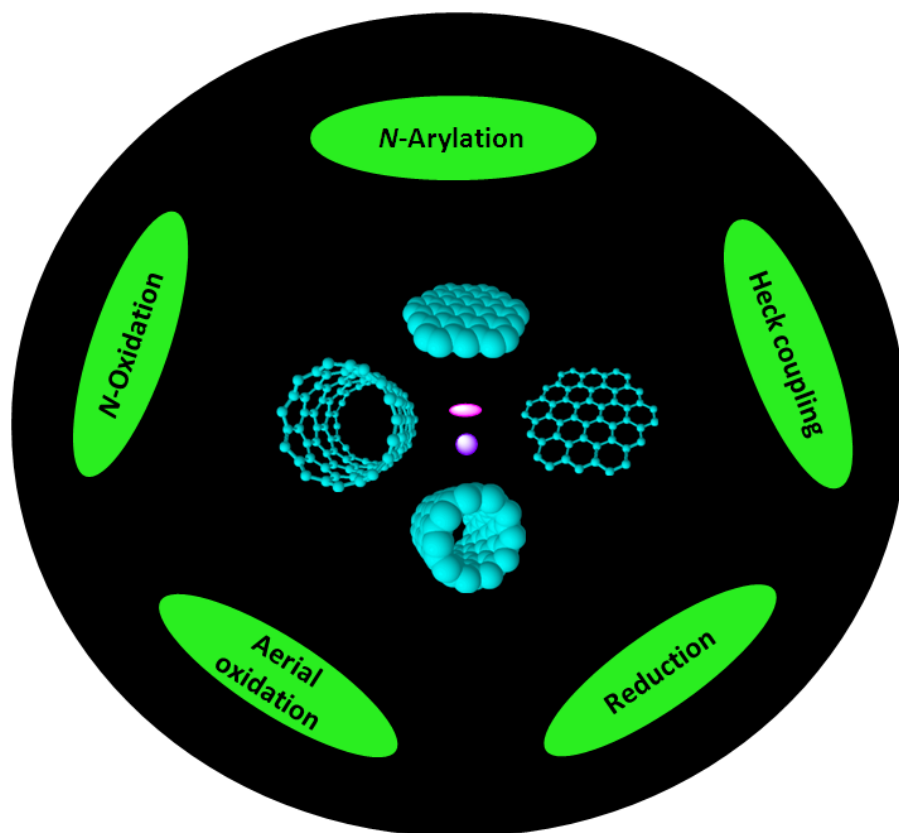
- [26] Yanga, X.; Wanga, X.; Qiua, J.; Aerobic Oxidation of Alcohols over Carbon Nanotube-Supported Ru Catalysts Assembled At the Interfaces of Emulsion Droplets. *Appl. Catal. A: Gen.* **2010**, *382*, 131–137.
- [27] Joo, S. H.; Park, J. Y.; Renzas, J. R.; Butcher, D.R.; Huang, W. Y.; Somorjai, G. A. Size Effect of Ruthenium Nanoparticles in Catalytic Carbon Monoxide Oxidation. *Nano Lett.* **2010**, *10*, 2709–2713.
- [28] Machadoab, B. F.; Serp, P. Graphene-Based Materials for Catalysis. *Catal. Sci. Technol.* **2012**, *2*, 54–75.
- [29] Krashennnikov, A. V.; Lehtinen, P. O.; Foster, A. S.; Pyykko, P.; Nieminen, R. M. Embedding Transition-Metal Atoms in Graphene: Structure, Bonding, and Magnetism. *Phys. Rev. Lett.* **2009**, *102*, 126807–126810.
- [30] Gopiraman, M.; Ganesh Babu, S.; Khatri, Z.; Kai, W.; Kim, A. Y.; Endo, M.; Karvembu, R.; Kim, I. S. Dry Synthesis of Easily Tunable Nano Ruthenium Supported on Graphene: Novel Nanocatalysts for Aerial Oxidation of Alcohols and Transfer Hydrogenation of Ketones. *J. Phys. Chem. C* **2013**, *117*, 23582–23596.
- [31] Lin, Y.; Watson, K. A.; Fallbach, M. J.; Ghose, S.; Smith, J. G.; Delozier, D. M.; Cao, W.; Crooks, R. E.; Connell, J. W. Rapid, Solventless, Bulk Preparation of Metal Nanoparticle-Decorated Carbon Nanotubes. *ACS Nano* **2009**, *3*, 871–884.
- [32] Akhavan, O. The Effect of Heat Treatment on Formation of Graphene Thin Films from Graphene Oxide Nanosheets. *Carbon* **2010**, *48*, 509–519.
- [33] Datsyuk, V.; Kalyva, M.; Papagelis, K.; Parthenios, J.; Tasis, D.; Siokou, A.; Kallitsis, I.; Galiotis, C. Chemical Oxidation of Multiwalled Carbon Nanotubes. *Carbon* **2008**, *46*, 833–840.

- [34] Gil, G.; Marques, P. A. A. P.; Granadeiro, C. M.; Nogueira, H. I. S.; Singh, M. K.; Gracio, J. Surface Modification of Graphene Nanosheets with Gold Nanoparticles: The Role of Oxygen Moieties at Graphene Surface on Gold Nucleation and Growth. *Chem. Mater.* **2009**, *21*, 4796–4802.
- [35] Shrestha, S.; Choi, W. C.; Song, W.; Kwon, Y. T.; Shrestha, S.P.; Park, C. Y. Preparation and Field Emission Properties of Er-Decorated Multiwalled Carbon Nanotubes. *Carbon* **2010**, *48*, 54–59.
- [36] Sankar, J.; Sham, T. K.; Puddephatt, R. J. Low Temperature Chemical Vapour Deposition of Ruthenium and Ruthenium Dioxide on Polymer Surfaces. *J. Mater. Chem.* **1999**, *9*, 2439–2444.
- [37] Gopiraman, M.; Ganesh Babu, S.; Khatri, Z.; Kai, W.; Endo, M.; Karvembu, R.; Kim, I. S. Facile and Homogeneous Decoration of RuO<sub>2</sub> Nanorods on Graphene Nanoplatelets for Transfer Hydrogenation of Carbonyl Compounds. *Catal. Sci. Technol.* **2013**, *3*, 1485–1489.
- [38] Zhou, X.; Huang, X.; Qi, X.; Wu, S.; Xue, C.; Boey, F. Y. C.; Yan, Q.; Chen, P.; Zhang, H. In Situ Synthesis of Metal Nanoparticles on Single-Layer Graphene Oxide and Reduced Graphene Oxide Surfaces. *J. Phys. Chem. C* **2009**, *113*, 10842–10846.
- [39] Akhavan, O. Graphene Nanomesh by ZnO Nanorod Photocatalysts. *ACS Nano* **2010**, *4*, 4174–4180.
- [40] Prasad, M. R.; Kamalakar, G.; Madhavi, G.; Kulkarni, S. J.; Raghavan, K. V. An Efficient Synthesis of Heterocyclic N-Oxides over Molecular Sieve Catalysts. *J. Mol. Catal. A: Chem.* **2002**, *186*, 109–120.

- [41] Marco, C.; Alessandro, S.; Giorgio, S. Mild Catalytic Oxidation of Secondary and Tertiary Amines to Nitrones and *N*-Oxides with H<sub>2</sub>O<sub>2</sub> Mediated by Pt(II) Catalysts. *Green Chem.* **2008**, *10*, 793–798.
- [42] Bamoharrama, F. F.; Heravi, M. M.; Roshani, M.; Tavakoli, N. *N*-Oxidation of Pyridine Carboxylic Acids Using Hydrogen Peroxide Catalyzed by a Green Heteropolyacid Catalyst: Preyssler's Anion, [NaP<sub>5</sub>W<sub>30</sub>O<sub>110</sub>]<sup>14-</sup>. *J. Mol. Catal. A: Chem.* **2006**, *252*, 219–225.
- [43] Hirai, Y.; Kojima, T.; Mizutani, Y.; Shiota, Y.; Yoshizawa, K.; Fukuzumi, S.; Ruthenium-Catalyzed Selective and Efficient Oxygenation of Hydrocarbons with Water as an Oxygen Source. *Angew. Chem. Int. Ed.* **2008**, *120*, 5856–5860.

# CHAPTER 7

## Conclusions



## CHAPTER 7

### Conclusions

We have shown that the carbon materials decorated metal nanostructures can be successfully prepared by a straightforward ‘dry synthesis’ method. All the prepared materials have shown an excellent catalytic activity in various organic transformation reactions.

CuONPs were decorated on MWCNTs by a ‘dry synthesis’ method. The resultant material (CuO/MWCNT) behaves as efficient catalysts for *N*-arylation of imidazole with various aryl halides. The stoichiometric amount of CuO/MWCNT catalyst was found as low as 5 mg (0.98 mol % of Cu) and to the best of our knowledge, this is the lowest amount of Cu used for this reaction. The good yields of products are mainly due to the smaller particle size of the CuONPs. The proposed catalyst is chemically as well as physically very stable, heterogenous in nature and reusable. The main feature of CuO/MWCNT nanocatalysts is the recovery of pure MWCNTs from the used nanocatalyst by the simple acid treatment. The recovered MWCNTs can be used for any further applications. In summary, we have developed a ligand free and heterogeneous Cu based nanocatalytic system for *N*-arylation of imidazole, which requires a lower amount of catalyst (0.98 mol% of Cu) to be effective.

Ultrafine RuO<sub>2</sub>NPs with mean diameter of about 0.9 nm were decorated on SWCNTs. It was found that the RuO<sub>2</sub>/SWCNTs is highly efficient towards the Heck-type olefination of aryl halides. The substrate scope of the reactions could be efficiently carried out with as low as 0.9 mol % of the supported RuO<sub>2</sub> catalyst over a wide range of

substrates in short reaction times. Unreactive bromo- and chloroarenes are also effectively olefinated under the present catalytic reaction condition. The RuO<sub>2</sub>/SWCNT is highly regioselective and chemoselective for the Heck-type olefination reaction. Heterogeneity, reusability and stability of RuO<sub>2</sub>/SWCNT were found to be excellent.

GNPs supported RuNRs were successfully prepared for the very first time by simple “mix and heat” method, and it was found to be an effective and reusable heterogeneous catalyst for the transfer hydrogenation of aromatic aldehydes and ketones in good yield with excellent selectivity. The catalyst is highly chemoselective, stable and reusable. Besides, GNPs were successfully recovered from the used GNPs-RuNRs.

Bi- and few layered GNS were achieved from GNPs by a solution phase exfoliation (SPE) method. The RuNPs were decorated on GNS by a straight forward dry synthesis method and TEM images confirmed good adhesion of RuNPs with a very narrow particle size distribution on GNS. The weight percentage of Ru in GNS-RuNPs was 3.31 wt%, as determined by EDS analysis. Raman intensity ratios confirmed the attachment of RuNPs on the surface of GNS. XRD and XPS revealed the metallic as well as nano-crystalline nature of RuNPs. The prepared GNS-RuNPs were able to oxidize effectively a wide range of alcohols into their corresponding carbonyl compounds in the presence of air. The nanocatalyst can also be used for selective oxidation of various aliphatic and aromatic alcohols. The amount of GNS-RuNPs catalyst used for oxidation of alcohols was found as low as 5 mg (0.036 mol%), the lowest to the best of our knowledge. The ICP-MS result of the filtrate after the separation of the catalyst revealed the heterogeneous nature of the present catalysis. The excellent reusability of the GNS-RuNPs can be realized from the good yield of acetophenone (87 %) from 1-

phenylethanol even at the 4<sup>th</sup> run. The used GNS-RuNPs were transformed into *u*-GNS-RuO<sub>2</sub>NPs which showed good catalytic activity toward the transfer hydrogenation of various ketones. Overall, the simple synthesis, versatility and good activity make GNS-RuNPs as an alternate choice to the existing Ru based catalysts.

RuO<sub>2</sub>NPs with a mean diameter of 1.3 nm was decorated on *f*-GNP by a straight forward “dry synthesis” method. TEM images showed an excellent attachment and homogeneous dispersion of RuO<sub>2</sub>NPs on GNP. The weight percentage of Ru in GNP-RuO<sub>2</sub>NPs was 2.68%, as determined by EDS analysis. Raman intensity ratios confirmed the good attachment of RuO<sub>2</sub>NPs on the surface of GNP. XRD and XPS revealed that the Ru was in +4 oxidation state with a nano-crystalline nature of RuO<sub>2</sub>NPs. The scope of the reactions could be carried out effectively with as low as 0.13 mol% of supported Ru catalyst for a wide range of substrates. To the best of our knowledge, this is the lowest amount of Ru used for this *N*-oxidation reaction. The proposed catalyst was chemically as well as physically very stable, heterogenous in nature and the catalyst could be reused up to 5 cycles. In summary, we have developed a heterogeneous Ru based nanocatalytic system for *N*-oxidation of tertiary amines, which requires a lower amount of catalyst (0.13 mol% of Ru) to be efficient.

## Accomplishments



## Accomplishments

### List of papers published/submitted

- [1] Ru and TiO<sub>2</sub> Mono and Bi-metallic Graphene Nanocatalysts for Aerial Oxidation of Primary Alcohols and Photodegradation of Dyes  
**M. Gopiraman**, S.G. Babu, Z. Khatri, K. Wei, B.S. Kim, R. Karvembu, I. S. Kim  
*Catalysis Communications* (To be submitted).
- [2] Efficient RuO<sub>2</sub> Nanostructures Supported MWCNTs-Catalyzed Transfer Hydrogenation of Carbonyl Compounds and Aerial Oxidation of Alcohols  
**M. Gopiraman**, S. Ganesh Babu, R. Karvembu, I.S. Kim  
*Applied Catalysis A: General* (Under review).
- [3] Highly Active, Selective and Reusable RuO<sub>2</sub>/SWCNT Catalyst for Heck Olefination of Aryl Halides  
**M. Gopiraman**, R. Karvembu, I.S. Kim  
*ACS Catalysis* (Under revision).
- [4] Catalytic N-Oxidation of Tertiary Amines on RuO<sub>2</sub>NPs Anchored Graphene Nanoplatelets  
**M. Gopiraman**, H. Bang, S. Ganesh Babu, K. Wei, R. Karvembu, I.S. Kim  
*Catalysis Science and Technology* (Under revision).
- [5] Dry Synthesis of Easily Tunable Nano Ruthenium Supported on Graphene – Novel Nanocatalysts for Aerial Oxidation of Alcohols and Transfer Hydrogenation of Ketones  
**M. Gopiraman**, S. Ganesh Babu, Z. Khatri, K. Wei, Y.A. Kim, M. Endo, R. Karvembu, I.S. Kim  
*Journal of Physical Chemistry C* 117 (2013) 23582–23596.

- [6] An Efficient, Reusable Copper-oxide/Carbon-nanotube Catalyst for *N*-arylation of Imidazole  
**M. Gopiraman**, S.G. Babu, Z. Khatri, W. Kai, Y.A. Kim, M. Endo, R. Karvembu, I.S. Kim  
*Carbon* 62 (2013) 135–148.
- [7] Facile and Homogeneous Decoration of RuO<sub>2</sub> Nanorods on Graphene Nanoplatelets for Transfer Hydrogenation of Carbonyl Compounds  
**M. Gopiraman**, S.G. Babu, Z. Khatri, K. Wei, E. Morinobu, R. Karvembu, I.S. Kim  
*Catalysis Science and Technology* 3 (2013) 1485–1489.
- [8] Structural and Mechanical Properties of Cellulose Acetate/Graphene Hybrid Nanofibers: Spectroscopic Investigations  
**M. Gopiraman**, K. Fujimori, K. Zeeshan, B.S. Kim, I.S. Kim  
*Express in Polymer Letters* 7 (2013) 554–563.
- [9] Mechanical and Electromagnetic Interference Shielding Properties of Poly (vinyl alcohol)/Graphene and Poly (vinyl alcohol)/Multi-Walled Carbon Nanotube Composite Nanofiber Mats and the Effect of Cu Top-Layer Coating  
K. Fujimori, **M. Gopiraman**, H.K. Kim, B.S. Kim, I.S. Kim  
*Journal of Nanoscience and Nanotechnology* 13 (2013) 1759–1764.
- [10] Cationic-Cellulose Nanofibers: Preparation and Dyeability with Anionic Reactive Dyes for Apparel Application  
Z. Khatri, **M. Gopiraman**, Y. Hirata, K. Wei, I.S. Kim  
*Carbohydrate polymers* 91 (2013) 434–443.
- [11] Physicochemical Studies of Glucose, Gellan gum, and Hydroxypropyl Cellulose-Inhibition of Cast Iron Corrosion  
V. Rajeswari, D. Kesavan, **M. Gopiraman**, P. Viswanathamurthi  
*Carbohydrate polymers* 95 (2013) 288–294.

- [12] Synthesis of Novel Photosensitive Polymers for the Protection of Mild Steel from Acid Corrosion  
B. Ramaganthan, D. Kesavan, **M. Gopiraman**, K. Subramanian  
*RSC Advances* 3 (2013) 17039–17047.
- [13] Structural, Optical, and Multiferroic Properties of Single Phased BiFeO<sub>3</sub>  
M. Muneeswaran, P. Jegatheesan, **M. Gopiraman**, I.S. Kim, N.V. Giridharan  
*Applied Physics A* (2013) 1–7.
- [14] Pad Dyeing of Cellulose Acetate Nanofibres with Disperse Dyes  
Z. Khatri, A. Khatri, U. Saleem, **M. Gopiraman**, B.S. Kim, K. Wei, I.S. Kim  
*Coloration Technology* 129 (2013) 159–163.
- [15] Dyeing and Characterization of Cellulose Nanofibers to Improve Color Yields by Dual Padding Method  
Z. Khatri, R.A. Arain, A.W. Jatoi, **M. Gopiraman**, K. Wei, I.S. Kim  
*Cellulose* 20 (2013) 1469–1476.
- [16] Preparation and Characterization of Electrospun Poly ( $\epsilon$ -Caprolactone)-Poly (l-Lactic acid) Nanofiber Tubes  
Z. Khatri, R. Nakashima, **M. Gopiraman**, K.H. Lee, Y.H. Park, K. Wei, I.S. Kim  
*Journal of Materials Science* 48 (2013) 3659–3664.
- [17] Inhibition of Cast Iron Corrosion in Acid, Base, and Neutral Media Using Schiff Base Derivatives  
V. Rajeswari, D. Kesavan, **M. Gopiraman**, P. Viswanathamurthi  
*Journal of Surfactants and Detergents* 16 (2013) 571–580.

- [18] Chemical and Electrochemical Investigations of High Carbon Steel Corrosion Inhibition in 10% HCl Medium by Quinoline Chalcones  
G. Ayyannan, K. Karthikeyan, S.S. Vivekananthan, **M. Gopiraman**, A. Rathinavelu  
*Ionics* 19 (2013) 919–932.
- [19] Spectroscopic Investigations of Physicochemical Interactions on Mild Steel in an Acidic Medium by Environmentally Friendly Green Inhibitors  
P. Sakunthala, S.S. Vivekananthan, **M. Gopiraman**, N. Sulochana, A.R. Vincent  
*Journal of Surfactants and Detergents* 16 (2013) 251–263.
- [20] Effects of pH on Electrospun PVA/Acid-Treated MWNT Composite Nanofibers  
H. Bang, **M. Gopiraman**, B.S. Kim, S.H. Kim, I.S. Kim  
*Colloids and Surfaces A: Physicochemical and Engineering Aspects* 409 (2012) 112–117.
- [21] An Investigation of Mild Carbon Steel Corrosion Inhibition in Hydrochloric Acid Medium by Environment Friendly Green Inhibitors  
**M. Gopiraman**, P. Sakunthala, D. Kesavan, V. Alexramani, I.S. Kim, N. Sulochana  
*Journal of Coatings Technology and Research* 9 (2012) 15–26.
- [22] Effect of Green Inhibitors on Acid Corrosion of AISI 1022 Steel  
V.S. Sundaram, S. Pitchai, K. Devarayan, **M. Gopiraman**, A. Vincent, S. Nagarajan  
*Chemical Science Reviews and Letters* 1 (2013) 195–200.
- [23] Chemical and Physical Interactions of 1-Benzoyl-3,3-Disubstituted Thiourea Derivatives on Mild Steel Surface: Corrosion Inhibition in Acidic Media  
**M. Gopiraman**, N. Selvakumaran, D. Kesavan, I.S. Kim, R. Karvembu  
*Industrial Engineering Chemistry Research* 51 (2012) 7910–7922.

- [24] Adsorption and Corrosion Inhibition Behaviour of *N*-(Phenylcarbamothioyl) Benzamide on mild steel in acidic medium  
**M. Gopiraman**, N. Selvakumaran, D. Kesavan, R. Karvembu  
*Progress in Organic Coatings* 73 (2012) 104–111.
- [25] Green Inhibitors for Corrosion of Metals: A Review  
D. Kesavan, M. Gopiraman, N. Sulochana  
*Chemical Science Reviews and Letters* 1 (2012) 1–8.
- [26] Physicochemical Studies of 4-Substituted *N*-(2-Mercaptophenyl)-Salicylideneimines: Corrosion Inhibition of Mild Steel in an Acid medium  
D. Kesavan, M.M. Tamizh, **M. Gopiraman**, N. Sulochana, R. Karvembu  
*Journal of Surfactants and Detergents* 15 (2012) 567–576.
- [27] Synthesis, Characterization and Electrochemical Studies of Novel Bi-phenyl Based Compounds  
R. Baskar, **M. Gopiraman**, D. Kesavan, I.S. Kim, K. Subramanian  
*Industrial & Engineering Chemistry Research* 51 (2012) 3966–3974.
- [28] Influence of 2,3-Dihydroxyflavanone on Corrosion Inhibition of Mild Steel in Acidic Medium  
**M. Gopiraman**, C. Sathya, S. Vivekananthan, D. Kesavan, N. Sulochana  
*Journal of Materials Engineering and Performance* 21 (2012) 240–246.
- [29] 2-Acetylpyridine *N*(4)-Morpholine Thiosemicarbazone (HAcPMTSc) as a Corrosion Inhibitor on Mild Steel in HCl  
S.L.A. Kumar, **M. Gopiraman**, S.K. Moorthy, S. Anandaram  
*Industrial & Engineering Chemistry Research* 50 (2011) 7824–7832.

- [30] Inhibitive Action of Clematis Gouriana Extract on the Corrosion of Mild Steel in Acidic Medium  
**M. Gopiraman**, P. Sakunthala, R. Kanmani, A.R. Vincent, N. Sulochana  
*Ionics* 17 (2011) 843–852.

## Presentations in conferences

- [1] An Efficient Copper-Oxide/Carbon-Nanotube Catalyst for *N*-Arylation of Imidazole  
**M. Gopiraman**, R. Karvembu, I.S. Kim  
The International Conference on Nanoscience and Nanotechnology (ICONN 2014), to be held at the Adelaide Convention Centre, South Australia, from February 2<sup>nd</sup> to 6<sup>th</sup> 2014.
- [2] RuO<sub>2</sub> Nanorods on Graphene Nanoplatelets Catalyst for Transfer Hydrogenation of Carbonyl Compounds  
**M. Gopiraman**, R. Karvembu, I.S. Kim  
The 7<sup>th</sup> Asian Conference on Electrochemical Power Sources (ACEPS-7), to be held in Osaka, Japan, from November 24<sup>th</sup> to 27<sup>th</sup>, 2013.
- [3] Preparation and Characterization of Graphene Incorporated Cellulose Acetate Nanofibers, their Structural and Mechanical Properties  
**M. Gopiraman**, K. Fujimori, B.S. Kim, I.S. Kim  
3<sup>rd</sup> International Conference on Multifunctional, Hybrid and Nanomaterials at Naples, Italy, during 3-7<sup>th</sup> March 2013.
- [4] CuO Nanoparticles Decorated on CNT as an Effective Nanohybrid Catalyst for *N*-Arylation of Heterocycles  
**M. Gopiraman**, S. Ganesh Babu, B.S. Kim, R. Karvembu, I.S. Kim  
ICNANO-2011 (An international conference on Nanomaterials & Nanotechnology) held at University of Delhi, New Delhi during 18-21 December 2011.

- [5] Enhanced Mechanical Properties of Cellulose Acetate/Graphite Hybrid Nanofibers  
**M. Gopiraman**, B.S. Kim, I.S. Kim  
Advances in Textile, Machinery Nonwoven and Technical Textile held at Kumaraguru College of Technology, Coimbatore during 15-17<sup>th</sup> December 2011.
- [6] Enhanced Mechanical Properties and EMI Shielding Effectiveness of PVA/Graphite and PVA/MWCNT Hybrid Nanofibers  
**M. Gopiraman**, K. Fujimori, B.S. Kim, I.S. Kim  
IUPAC 9<sup>th</sup> International Conference on Advanced Polymers via Macromolecular Engineering (APME 2011) held at Cappadocia, Turkey during 5-8<sup>th</sup> September, 2011.
- [7] Adsorption and Inhibition Effect of Environment Friendly Green Inhibitor on Mild Steel in Acidic Medium  
**M. Gopiraman**, K. Fujimori, B.S. Kim, R. Karvembu, I.S. Kim  
The 4<sup>th</sup> International Symposium on High-Tech Fiber Engineering for Young Researchers held at Shinshu University, Nagano, Japan from August 29<sup>th</sup> to September 4<sup>th</sup>, 2011.
- [8] Studies on Corrosion Inhibition Nature of 2-Acetylpyridine *N* (4) Morpholine Thiosemicarbazone on Mild Steel in HCl  
**M. Gopiraman**, B.S. Kim, I.S. Kim  
The 11<sup>th</sup> Asian Textile Conference held at EXCO, Daegu, Korea during 1-4 November 2011.

## Patents

- [1] Graphene: A superior and recoverable solid support for transition metal nanoparticles to catalyze organic transformations  
**M. Gopiraman**, W. Kai, R. Karvembu, I.S. Kim (to be submitted).
  
- [2] Human hair – A novel and green support for metal nanoparticles catalyst  
**M. Gopiraman**, W. Kai, R. Karvembu, I.S. Kim (to be submitted).
  
- [3] Cellulose nanofibers – A green support for metal nanoparticles  
**M. Gopiraman**, W. Kai, K. Watanabe, I.S. Kim (to be submitted).
  
- [4] Breathable waterproof membrane for automotive lamp  
I.S. Kim, K. Wei, Z. Khatri, **M Gopiraman**  
JP Patent, application number 2012-170687.
  
- [5] Breathable waterproof membrane for electronic components  
I.S. Kim, K. Wei, Z. Khatri, **M. Gopiraman**  
JP Patent, application number 2012-170688.

## BRIEF CURRICULUM VITAE

Name : M. Gopiraman  
Father's name : G. Mayakrishnan  
Mother's name : M. Valli  
Nationality : Indian  
Date of birth : 29<sup>th</sup> June 1987  
Marital Status : Unmarried  
Address : Pudur kallan kutur  
Mariamman kovil back side  
Astham patty post  
Salem – 636007  
Tamilnadu  
India.

---

### Academic qualifications

**Master of Chemistry** - National Institute of Technology, Tiruchirappalli - July 2008 to May 2010 - First class with 7.28 CGPA of marks

**Bachelor of Education** - Lisieux College of Education, Coimbatore - June 2007 to May 2008 - First class with 76.77% of marks

**Bachelor of Chemistry** – Sri Rama Krishnan Mission Vidyalaya, Coimbatore - June 2004 to May 2007 - First class with 70.96% of marks

**H.S.C** – Little Flower Higher Secondary School, Salem - June 2002 to April 2004 - First class with 79.66 % of marks

**S.S.L.C** - Little Flower Higher Secondary School, Salem - June 2001 to April 2002 - First class with 79.80 % of marks

### Other qualifications

**Diploma in Computer Applications (DCA)** – Acetech Coomputer Education, Coimbatore – July 2006 to January 2007 - ‘A’ grade

**Diploma in Yoga (DIY)** - Sri Rama Krishnan Mission Vidyalaya, Coimbatore - January 2004 to January 2007 - First class

## **Projects**

Carried out a project on “**Pedaliun murexlinn an effective hurb for the corrosion inhibition of kidney stones**” at Sri Rama Krishnan Mission Vidyalaya, Coimbatore during December 2006 – May 2007.

Carried out a project on “**Studies on the corrosion inhibition nature of 2-acetyl pyridine N (4) morpholine thiosemicarbozone on mild steel in HCl**” at National Institute of Technology, Tiruchirappalli during June 2008 – May 2009.

## **Achievements**

**Received Best Oral Presentation Award** in the 4<sup>th</sup> International Symposium on for High-tech Fiber engineering of young researches held at Shinshu University, Japan during 1-3 September 2011.

**First Place in District Level Firing Competition** in Combined Annual Training Camp 2005-2006 (SD and JD) held at Marudhamalai Sri Subramania Swamy Devasthanam Higher Secondary School, Vadavalli, Coimbatore during 6-17 January 2006.